TECHNISCHE UNIVERSITÄT WIEN
Vienna | Austria

DISSERTATION

Modeling and Control of Optical Pulse Amplifiers for Ultra-Short Laser Pulses

Ausgeführt zum Zwecke der Erlangung des akademischen Grades eines
Doktors der technischen Wissenschaften (Dr.techn.)

unter der Leitung von
Univ.-Prof. Dipl.-Ing. Dr.techn. Andreas Kugi
E376
Institut für Automatisierungs- und Regelungstechnik

eingereicht an der
Technischen Universität Wien
Fakultät für Elektrotechnik und Informationstechnik

von
Dipl.-Ing. Andreas Deutschmann
Matrikelnummer: 00825712

Wien, im Juni 2019

Die approbierte Originalversion dieser Dissertation ist in der TU Wien Bibliothek verfügbar.
The approved original version of this doctoral thesis is available at the TU Wien Bibliothek.
TU Bibliothek Your knowledge hub

Die approbierte Originalversion dieser Dissertation ist in der TU Wien Bibliothek verfügbar.
The approved original version of this doctoral thesis is available at the TU Wien Bibliothek.

Die approbierte Originalversion dieser Dissertation ist in der TU Wien Bibliothek verfügbar.
The approved original version of this doctoral thesis is available at the TU Wien Bibliothek.
TU WIEN Bibliothek Your knowledge hub

Studiendekan:	Univ.-Prof. Dr.-Ing. Wolfgang Gawlik
Tag des Kolloquiums:	3. September 2019
Betreuer:	Univ.-Prof. Dr.techn. Andreas Kugi
Erster Gutachter:	Univ.-Prof. Dr. Pierre Rouchon
Zweiter Gutachter:	Univ.-Prof. Dr.rer.nat. Georg Reider

Die approbierte Originalversion dieser Dissertation ist in der TU Wien Bibliothek verfügbar.
The approved original version of this doctoral thesis is available at the TU Wien Bibliothek.

Vorwort

Die vorliegende Arbeit entstand während meiner Anstellung am Institut für Automatisierungs- und Regelungstechnik (ACIN) an der Technischen Universität Wien. Der Prozess einer Dissertation gleicht manchmal einer emotionalen Achterbahnfahrt, die auf chaotischen Bahnen über Höhen und Tiefen immer weiter ins Unbekannte führt. Ist das Ziel schließlich erreicht, haben sich die einstigen Fragmente zu einem großen Ganzen zusammengefügt und die Perspektive der Erzählung lässt die Wege erscheinen, als wusste man immer, wohin es sich zu gehen lohnt. Schlussendlich bleibt das Gefühl, etwas geschafft zu haben – vielleicht sogar, etwas geschaffen zu haben –, welches einem mit größter Leichtigkeit zur retrospektiven Geschichtsfälschung antreibt und all die Zweifel und Sorgen vergessen lässt.

Wie jede Unternehmung, so wäre auch der Erfolg dieser nicht ohne die Unterstützung unzähliger Personen möglich gewesen, denen ich an dieser Stelle meinen herzlichsten Dank aussprechen möchte. In erster Linie gilt mein Dank Univ.-Prof. Andreas Kugi für die Möglichkeit, thematisch einen Schritt ins Ungewisse zu wagen. Ohne seine fachliche Unterstützung, seinen Optimismus und sein Vertrauen in meine Fähigkeiten über eigene Zweifel hinweg hätte diese Arbeit nicht gelingen können. Zudem möchte ich mich bei Univ.-Prof. Andrius Baltuška, Dr. Pavel Malevich und Tobias Flöry vom Institut für Photonik bedanken, die dieses Wagnis angeregt und mit Rat und Tat unterstützt haben. Mein weiterer Dank gilt Univ.-Prof. Pierre Rouchon und Univ.-Prof. Georg Reider für die gewissenhafte Begutachtung. Letzterem bin ich darüber hinaus für das offene Ohr, die Bestärkungen über die letzten Jahre und die spannenden Unterhaltungen sehr dankbar.

Zu besonderem Dank bin ich meinen aktuellen und ehemaligen Kolleginnen und Kollegen am Institut verpfichtet. Ihre Neugierde, Hilfsbereitschaft, und nicht zuletzt fachliche Expertise sind mir Vorbild und Motivation und ich freue mich auf jeden weiteren Tag in ihrer Gemeinschaft. Gesondert bedanken möchte

Die approbierte Originalversion dieser Dissertation ist in der TU Wien Bibliothek verfügbar.
The approved original version of this doctoral thesis is available at the TU Wien Bibliothek.
TU Bibliothek Your knowledge hub WIEN

ich mich bei Assoc. Prof. Wolfgang Kemmetmüller, der nie um eine kluge Idee verlegen ist, bei Assist. Prof. Andreas Steinböck, dessen intellektuelle Rigorosität seines gleichen sucht, sowie bei Dr. Tobias Glück, der mir einen Pfad durch ein Dickicht namens ILC schlug. Besonderer Dank gilt Katharina Schrom, die Teile dieser Arbeit während ihrer Anstellung als studentische Mitarbeiterin maßgeblich unterstützte.

Nicht zuletzt möchte ich mich bei meinen Eltern Sigrid und Berthold bedanken, die mir all dies erst ermöglicht haben und mich stets darin bestärkten, meinen Interessen und meinem Herzen zu folgen. Mein größter Dank gilt schließlich meiner Verlobten Karin für ihren Trost an schlechten und ihre geteilte Freude an guten Tagen, ihre bedingungslose Unterstützung und ihre unermessliche Liebe.

Die approbierte Originalversion dieser Dissertation ist in der TU Wien Bibliothek verfügbar.
The approved original version of this doctoral thesis is available at the TU Wien Bibliothek.
TU Bibliothek WIEN Your knowledge hub

Abstract

The amplification of high-energy laser pulses is usually done using regenerative amplifiers. The population inversion due to continuous pumping over a comparatively long period is transferred into an incoming laser pulse in very short time by cycling it through the excited laser medium several times.

While the total energy of the resulting pulses in essentially limited by the storage capacity of the laser medium, the extremely high power densities of short pulses can destroy the medium due to self-focusing effects at significantly lower energies. This limitation can be avoided by using known chirped pulse amplification techniques, where the incoming pulse is spread in time using positive dispersion first and amplified in a spectrally homogeneous way afterwards. Finally, the amplified pulse is recompressed using negative dispersion. The assumption of spectrally homogeneous amplification profiles is increasingly violated for ultrashort pulses due to their required spectral bandwidth. Additionally, the optical nonlinearities of the laser medium lead to self-induced phase distortions, wherefore suitable input filters are used to counter the increasingly incomplete recompression.

If regenerative amplifiers are operated at fast repetition rates, the intrinsic coupling of subsequent pulses can destabilize the amplifier's dynamics and lead to so-called period-doubling bifurcations above a critical pumping power. For safety reasons, those operational regimes are typically avoided despite their potentially beneficial properties.

Alternative methods for the generation of high-energy pulses rely on the coherent superposition of the individual pulses of a pulse burst. Ensuring high efficiency of this so-called "pulse stacking" requires precise amplitude and phase relations between subsequent pulses. A promising technique to simultaneously generate and amplify such pulse bursts relies on the Vernier effect by operating regenerative amplifiers with a slightly detuned resonator. However, the nonlinear coupling of all individual pulses significantly complicates the precise control of the pulse burst's energy distribution.

Die approbierte Originalversion dieser Dissertation ist in der TU Wien Bibliothek verfügbar.
The approved original version of this doctoral thesis is available at the TU Wien Bibliothek.
TU WIEN Bibliothek Your knowledge hub

In all those cases, the availability of programmable optical filters strongly suggests the application of automatic control concepts. The overall goal of this thesis is thus to take a look at optical amplifiers from a dedicated control engineering perspective and investigate suitable control methods.

First, a detailed nonlinear infinite-dimensional model of such amplifiers is derived based on the nonlinear Schrödinger equation and the description of the interaction of the pulses with the doped ions of the laser medium. This mathematical model is subsequently used to create arbitrarily shaped pulses using iterative learning control methods. To this end, the coupling of subsequent pulses due to the complex population dynamics is neglected to describe the spectral input-output behavior by a reduced linear model. Using a Wiener-filtering-based learning approach, adaptive learning control laws are developed that do not rely on precisely calibrated (atomic) models or a chosen operating point.

In a second step, the previously neglected pulse-to-pulse dynamics are investigated by ignoring the spectral properties of the laser medium to obtain a simplified energy-based description in form of a nonlinear discrete-time system. Depending on the available measurement quantities, different feedback schemes are developed to stabilize otherwise unstable operating points. This allows to operate pulse amplifiers with very high gains that can be safely steered into (or through) otherwise unstable regions.

Finally, these methods are transferred to the generation and amplification of pulse bursts. By extending the energy-based description one is able to obtain settings of the input filter that produce the desired steady-state pulse bursts by solving a constrained optimization problem. Possible deviations due to model or parameter uncertainties can be eliminated using iterative learning control methods while the pulse-to-pulse dynamic can be influenced by feedback methods simultaneously.

Die approbierte Originalversion dieser Dissertation ist in der TU Wien Bibliothek verfügbar.
The approved original version of this doctoral thesis is available at the TU Wien Bibliothek.
TU Bibliothek WIEN Your knowledge hub

Kurzzusammenfassung

Zur Erzeugung energiereicher Laserpulse werden üblicherweise regenerative Verstärker verwendet, welche die durch kontinuierliches Pumpen über einen vergleichsweise langen Zeitraum aufgebaute Besetzungsinversion in kurzer Zeit auf einen eintreffenden Laserpuls übertragen, indem dieser mehrfach durch das angeregte Lasermedium geführt wird.

Während die Gesamtenergie des erzeugten Laserpulses im Wesentlichen durch die Speicherfähigkeit des Lasermediums limitiert ist, führen bei kurzen Pulsen die enormen Leistungsdichten zur Selbstzerstörung des Mediums bereits bei wesentlich kleineren Pulsenergien. Um diese Limitierung zu umgehen, wurde auf bekannte Techniken der gechirpten Pulsverstärkung übergegangen. Dabei wird der zu verstärkende Laserpuls zuerst durch positive Dispersion zeitlich gedehnt, danach spektral homogen verstärkt und letztlich durch entsprechende negative Dispersion wieder rekomprimiert. Die Annahme spektral homogener Verstärkungsprofile ist für ultrakurze Laserpulse durch die benötigte spektrale Bandbreite zunehmend verletzt. Zudem induzieren optische Nichtlinearitäten des Lasermediums zusätzliche Phasenverzerrungen in den sich ausbreitenden Laserpulsen, weshalb versucht wird, durch geeignete Eingangsfilter einer zunehmend unvollständigen Rekompression entgegenzuwirken.

Werden regenerative Verstärker mit hohen Repetitionsraten betrieben, kann die intrinsische Verkopplung aufeinanderfolgender Pulse zu einer Destabilisierung des Verstärkers führen. Dabei treten jenseits einer kritischen Pumpleistung sogenannte Periodenverdopplungsbifurkationen auf, welche einen sicheren Betrieb bei hohen Ausgangsleistungen verhindern, obwohl dieser Bereich zum Teil günstige Eigenschaften aufweisen würde.

Alternative Methoden zur Erzeugung energiereicher Laserpulse nutzen die kohärente Überlagerung der einzelnen Pulse eines Pulszuges, wobei jedoch genaue Amplituden- und Phasenrelationen der Pulse zueinander eingehalten werden müssen. Eine vielversprechende Möglichkeit zur gleichzeitigen Erzeugung und Ver-

Die approbierte Originalversion dieser Dissertation ist in der TU Wien Bibliothek verfügbar.
The approved original version of this doctoral thesis is available at the TU Wien Bibliothek.
TU WIEN Bibliothek Your knowledge hub

stärkung derartiger Pulszüge besteht in der Verwendung regenerativer Verstärker mit verstimmten Resonatoren. Durch die nichtlineare Verkopplung der einzelnen Pulse ist die Beeinflussung der Energieverteilung innerhalb eines Pulszuges ungleich komplizierter.

Die Verfügbarkeit programmierbarer optischer Filter legt in all diesen Fällen die Anwendung regelungstechnischer Konzepte nahe. Ziel dieser Arbeit ist es daher, optische Pulsverstärker aus regelungstechnischer Perspektive zu betrachten und damit Lösungen für die auftretenden Problemstellungen zu finden.

Dazu wird zuerst ein detailliertes, verteilt-parametrisches Modell des Verstärkers hergeleitet, welches auf der nichtlinearen Schrödingergleichung zusammen mit einer Beschreibung der atomaren Interaktion mit dem Lichtfeld basiert. Darauf aufbauend soll eine gewünschte Pulsform der Ausgangspulse durch iterativ lernende Regelungsmethoden erzeugt werden. Hierfür wird die Kopplung aufeinanderfolgender Pulse durch die komplexen atomaren Populationsdynamiken vernachlässigt, um das spektrale Eingangs-Ausgangsverhalten durch ein reduziertes lineares Modell zu beschreiben. Mittels eines iterativen Lerngesetzes auf Basis eines akausalen Wiener-Filters kann daraus eine adaptiv lernende Regelung entwickelt werden, welche unabhängig von einem identifizierten (atomaren) Modell oder einem gewählten Arbeitspunkt funktioniert.

In einem zweiten Schritt soll die Puls-zu-Puls-Dynamik unter Vernachlässigung der spektralen Eigenschaften durch ein energiebasiertes Modell beschrieben werden, welches sich in Form eines nichtlinearen, zeitdiskreten Systems darstellen lässt. Abhängig von den verfügbaren Messgrößen können auf Basis dieses Modells instabile Arbeitsbereiche durch Regelung stabilisiert werden, womit Pulsverstärker trotz sehr hohen Verstärkungen sicher in (und durch) ansonsten instabile Bereiche geführt werden können.

Letztlich sollen diese Methoden auf regenerative Verstärker zur Erzeugung von Pulszügen übertragen werden. Durch Erweiterung des energiebasierten Modells lassen sich die benötigten Einstellungen des Eingangsfilters zur Erzeugung eines gewünschten Pulszuges durch ein beschränktes Optimierungsproblem ermitteln. Allfällige Abweichungen durch Modell- und Parameterunsicherheiten lassen sich iterativ durch lernende Regelungsmethoden eliminieren während die Puls-zu-Puls-Dynamik gleichzeitig durch eine klassische Regelung gezielt beeinflusst werden kann.

Die approbierte Originalversion dieser Dissertation ist in der TU Wien Bibliothek verfügbar.
The approved original version of this doctoral thesis is available at the TU Wien Bibliothek.
TU Bibliothek WIEN Your knowledge hub

Contents

1 Introduction **1**
- 1.1 Amplification of laser pulses . . . 1
- 1.2 Applications of control theory to photonics . . . 3
- 1.3 Contributions and outline of this thesis . . . 4

2 Modeling of Chirped Pulse Amplifiers for Ultra-Short Laser Pulses **7**
- 2.1 Stretcher, filter and compressor . . . 9
- 2.2 Regenerative amplifier (RA) . . . 10
  - 2.2.1 Pulse propagation in gain media (pulse model) . . . 12
  - 2.2.2 Interaction with pumping field (pump model) . . . 17
  - 2.2.3 Coupling of pulse and pump model . . . 18
- 2.3 Validity of the CPA model . . . 20

3 Stochastic Iterative Learning Control for Lumped- and Distributed-Parameter Systems: A Wiener-Filtering Approach **25**
- 3.1 Problem statement . . . 26
- 3.2 A Wiener-Filtering approach . . . 27
- 3.3 Choosing the input error PSD . . . 31
  - 3.3.1 A sub-optimal iteration-invariant learning law . . . 31
  - 3.3.2 An optimal iteration-varying learning law . . . 33
- 3.4 Numerical implementation of the learning law . . . 35
- 3.5 Simulation examples . . . 37
  - 3.5.1 A sub-optimal ILC for a system of parabolic PDEs . . . 37
  - 3.5.2 Comparing the sub-optimal with the optimal ILC scheme . 41

Die approbierte Originalversion dieser Dissertation ist in der TU Wien Bibliothek verfügbar.
The approved original version of this doctoral thesis is available at the TU Wien Bibliothek.
TU WIEN Bibliothek Your knowledge hub

4 Iterative Pulse-Shape Control for Ultra-Short Laser Pulses 45
4.1 Reduced linear input-output behavior 47
4.2 Wiener-Filter-based ILC 49
4.3 Adaptive ILC 51
4.4 Simulation results for the experimentally validated model 54
4.4.1 Mildly saturating pulses (1 mJ) 55
4.4.2 Limiting input constraints (3 mJ) 55
4.4.3 Fully saturating pulses (3 mJ) 57
4.4.4 Triple pulse 60
4.5 Pulse-to-pulse dynamics 60

5 Active Feedback Stabilization of Regenerative Amplifiers 65
5.1 Dynamical Frantz-Nodvik model of regenerative amplifiers 67
5.1.1 Four-level and Quasi-three-level laser materials 68
5.1.2 Full description of the amplification and pumping process . 71
5.1.3 Amplification during a single passage (pulse model) 72
5.1.4 Gain regeneration due to pumping (pump model) 74
5.1.5 Discrete-time dynamical model 76
5.2 Stability analysis of the uncontrolled amplifier 77
5.3 Feedback stabilization of unstable operating points 83
5.3.1 Feedback stabilization using pump light measurements . . 83
5.3.2 Feedback stabilization using pulse energy measurements . 86
5.4 Variable pumping power 90
5.5 Experimental results 98

6 Control of the Formation and Amplification of Pulse Bursts in Regenerative Amplifiers using the Vernier Effect 105
6.1 A dynamical model of pulse burst formation and amplification . . 106
6.2 Optimization-based input shaping 110
6.3 Tracking of desired pulse bursts using ILC 112
6.4 Combined tracking control and feedback stabilization 118
6.4.1 Combined tracking and state-feedback control 118
6.4.2 Combined tracking and output-feedback control 123

7 Conclusions and Outlook 127
7.1 Conclusions 127
7.2 Outlook 129

A Efficient numerical solution strategies for CPAs 133

B Parameter identification strategies for CPAs 141
B.1 Partial decoupling of the population dynamics by parameter reduction 142
B.2 Linear propagation model 142

Die approbierte Originalversion dieser Dissertation ist in der TU Wien Bibliothek verfügbar.
The approved original version of this doctoral thesis is available at the TU Wien Bibliothek.
TU WIEN Bibliothek Your knowledge hub

B.3 Semi-automatic identification algorithm 144

C Extensions of the dynamic model to multi-pass pumping and linear cavities 145

C.1 Differences for linear cavities 146

C.2 Description of multi-pass pumping 147

D Proof of Identity (3.35) 151

E Parameter values 153

Die approbierte Originalversion dieser Dissertation ist in der TU Wien Bibliothek verfügbar.
The approved original version of this doctoral thesis is available at the TU Wien Bibliothek.
TU Bibliothek WIEN Your knowledge hub

Die approbierte Originalversion dieser Dissertation ist in der TU Wien Bibliothek verfügbar.
The approved original version of this doctoral thesis is available at the TU Wien Bibliothek.

Die approbierte Originalversion dieser Dissertation ist in der TU Wien Bibliothek verfügbar.
The approved original version of this doctoral thesis is available at the TU Wien Bibliothek.
TU WIEN Bibliothek Your knowledge hub

CHAPTER 1

Introduction

Over the last several decades, the systematic generation, detection, and manipulation of light opened a novel and rapidly growing field of research now commonly known as photonics. This interdisciplinary field of research is closely related to classical optics as well as modern fields of quantum optics [1, 2] and quantum optomechanics [3, 4]. While the latter can be attributed to be predominantly inclined towards basic research, photonics has been an applied branch of research from the beginning by virtue of its programmatic name: let light perform actions prior done by electronics. As a result, many of its developments - starting with the invention of the laser [5] - are now among the essential tools and building blocks of scientific advances not only in optical sciences and physics but also in biology (e.g., optical tweezers [6]) or chemistry (e.g., laser spectroscopy and cooling [7], STED microscopy beyond the diffraction limit [8]). The availability and readiness of these technologies ultimately laid the foundation for sophisticated quantum experiments and the amazing ability to play with quantum states in real time [2, 9] that seemed unimaginable only a few decades ago. In some way, being able to understand phenomena and being able to control them, i.e. the disciplines of science and engineering, have come closer to each other in practise and in theory [10–12]. What great time to be a control engineer!

1.1 Amplification of laser pulses

One particular task in photonic applications is the amplification of light pulses, especially for ultra-short high-energy pulses as used in strong field physics [13], for coherent control [14], for pumping of optical parametric amplifiers [15] and free electron lasers [16], for ablation-based material processing of micro-mechanical

devices [17–19], for X-ray nano-cristallography of proteins [20] and laser-based eye surgery [21].

The amplification of high-energy pulses is usually done by multipass amplification [22] using regenerative amplifiers (RAs), where a (usually) continuously pumped gain medium (also called laser medium) is placed inside an optical resonator. The pulse is then cycled several times until the stored energy of the gain medium is extracted and the amplified pulse is released. Since the amplification of intense laser pulses in active gain media is limited in its maximum energy due to self-focusing effects, a common technique to amplify high-energy pulses is to use so-called optical chirped pulse amplifiers (CPAs) [23]. The idea of CPAs is to stretch the incident pulse temporally to reduce its power density and amplify the stretched pulse. This stretching can be achieved by introducing large amounts of artificial positive dispersion and thus convert the incident pulse into a chirped pulse. Afterwards, one wishes to recompress the chirped pulse by applying negative dispersion [24]. While this is possible for RAs with spectrally uniform gain, the quality of the amplified pulse after recompression is degrading rapidly for non-uniform gains due to the amplitude [25] and phase modulations applied to the pulse's spectral components spread in time. This effect is particularly relevant for broad-band amplifiers required for ultra-short pulse amplification. Additionally, high intensity pulses are subject to complex propagation phenomena such as self-phase modulation [26, 27] due to the optical nonlinearities of the laser material. To approximately compensate for these effects, spectral filters in front of the RA [15] or within the resonator [28] have been successfully applied to achieve spectrally broad and thus temporally short pulses after recompression.

RAs and CPAs are usually driven by so-called seed (input) pulses provided at a certain repetition rate by a dedicated pulse source such as a mode-locked laser [29, 30]. Since the pumping process is typically not strong enough to fully charge the laser medium between two consecutive pulses, the amplification characteristics of the following pulse somewhat depend on the previous pulse and a pulse-to-pulse dynamic emerges. Since the seed pulses are injected into the resonator with a given periodicity, the amplifier approaches a steady state where the pumping process perfectly compensates the energy extracted by the previous pulse. When trying to exploit the full potential of a given laser medium, the amplifier is operated close to the damage threshold given by the self-focusing tendency of high-intensity pulses. Excitation of the pulse-to-pulse dynamics are thus potentially hazardous as they can generate pulses of an intensity that destroys the laser medium. The coupling described above can be so severe that it eventually renders the amplifier unstable [31] in certain operational regions. Unfortunately, those regions usually include the operating points of highest energy extraction and highest energy efficiency. A simple solution to this problem is to increase the available seed energy by using dedicated pre-amplifers [32, 33].

Spreading the pulse's spectral components in time as done in CPAs is not the only option to reduce the power density. Recently, a more direct approach has

Die approbierte Originalversion dieser Dissertation ist in der TU Wien Bibliothek verfügbar.
The approved original version of this doctoral thesis is available at the TU Wien Bibliothek.
TU WIEN Bibliothek Your knowledge hub

been presented [34] where a sequence of similar pulses - a so-called pulse burst - is coherently "stacked" together into a single pulse by injecting them into a resonant cavity. To let all injected pulses interfere in a constructive way, precise amplitude and phase relations between the individual pulses of the pulse burst have to be maintained. Adjusting a single pulse within a narrowly spaced pulse burst is very demanding in terms of timing and actuation. To combine the amplification and generation of the required arbitrary pulse bursts, a slightly detuned cavity design using the Vernier effect has been proposed recently [35]. However, due to nonlinear saturation effects of the underlying amplifier this approach significantly complicates the precise adjustment of the individual pulse amplitudes, i.e., the distribution of the total energy of the pulse burst.

1.2 Applications of control theory to photonics

Reading the above from the perspective of a control engineer it is clear that there is plenty of potential to apply a variety of automatic control techniques to such systems. The timing requirements of modern photonic systems already largely relies on computerized control methods to be available, many actuators are programmable [36, 37] (e.g., acousto-optic programmable dispersive filters (AOPDFs) and spatial light modulators (SLMs)) and measurement equipment often requires algorithmic post-processing of the acquired data (e.g., frequency resolved optical gating (FROG) techniques [38]). Thus, the basic ingredients for advanced automatic control schemes are already present in many experimental setups.

Nevertheless, the number of publications on that topic is rather scarce compared to other application domains where the presence of automatic control schemes is almost ubiquitous. One major reason - apart from the relative novelty of the field itself - might be the usually very complex mathematical models combined with a high degree of uncertainty in both model quality and parameters. Many quantities are inaccessible to direct measurement or can only be measured with highly sophisticated equipment. As a result, the majority of existing literature relies on model-free concepts. However, the control engineering community has a long tradition in dealing with exactly these kind of challenges.

One of the earliest application of control methods to a problem in the realm of what would later be called photonics arrived shortly after the invention of the laser by trying to compensate so-called laser spiking in continuously operated lasers [39, 40]. As it turned out, the tight limits on the acceptable feedback delay are rather critical. Similar concepts were applied to pulsed amplifiers where an adjustable absorber inside the resonator keeps the circulating pulse at a well-defined energy level before starting the amplification phase by eliminating

Die approbierte Originalversion dieser Dissertation ist in der TU Wien Bibliothek verfügbar.
The approved original version of this doctoral thesis is available at the TU Wien Bibliothek.
TU WIEN Bibliothek Your knowledge hub

the added losses [41]. In [42], the spectral power output of a Raman optical amplifier for optical communication systems is regulated using extremum seeking control (ESC) methods. The generation of short optical pulses using mode-locked lasers received some interest using ESC [43] and was also combined with machine learning concepts in [44]. Later, the ESC concept was extended to use model predictive control based on a data-driven model [45].

Some more effort has been dedicated to shape laser pulses by adaptively adjusting some kind of input pulse or optical filter using automatic control methods. Nonlinear phase distortions in fibre-based CPAs were experimentally corrected using genetic algorithms [46]. A similar approach based on genetic algorithms was used in [47] to obtain desired pulses from an optical transmission fibre. A differential-evolution-type algorithm was employed in [48] to learn amplitude and phase corrections for each pixel of an SLM directly. Using amplitude modulations to correct the SPM in fibre-based CPAs was demonstrated in [49]. Amplitude-shaping of intensity-based models has been approach by inversion of the analytical solution [50], model-free iterative learning control (ILC) schemes [51] and, again, ESC methods [52]. Finally, the pulse shape for communication systems was optimized from a high-level perspective by using feedback of the resulting bit error rate in [53].

1.3 Contributions and outline of this thesis

For all kinds of systems, there is a lot to be gained by deriving tailored mathematical models and utilizing the extracted model knowledge to design model-based control schemes and carefully augment them with model-free or data-driven concepts where needed and suitable[1]. The main motivation for this thesis is thus to look at optical pulse amplifiers from a dedicated control perspective and develop novel control concepts that are increasing the expected performance or allow operations that have not been possible before.

Given the existing literature, there are very few contributions with a dedicated control background, such as [42] on Raman optical amplifiers and in particular the series of papers due to Brunton and coworkers [43–45] on mode-locked lasers. Most relevant for this thesis, a simple pulse-shaping approach for optical amplifiers using ILC and ESC methods was proposed in [51, 52] considering intensity-based models to describe the laser medium's gain saturation. For ultra-short pulses and their amplification using CPA systems, however, gain saturation is only one aspect among many others that significantly distort the resulting pulse shape and the proposed model-free learning law cannot be directly extended to cover such phenomena. The proposed extremum seeking schemes and genetic algorithms take considerable time to converge towards a desired solution. The genetic algorithm

[1] While this seems like conventional wisdom, it shall be emphasized at times where a focus on data and data-driven methods resonates so strongly with the current scientific zeitgeist.

Die approbierte Originalversion dieser Dissertation ist in der TU Wien Bibliothek verfügbar.
The approved original version of this doctoral thesis is available at the TU Wien Bibliothek.
TU Bibliothek WIEN Your knowledge hub

in [48] requires several hundreds of iterations on the experimental setup using steady-state measurements of the output pulses. The ESC in [52] even required tens of thousands of iterations to find an energetic optimum. Additionally, using such schemes can be potentially dangerous if the search space is not suitably limited to prevent damage to the laser material. Since our experimental partners from the Ultrafast Laser Group at TU Wien were able to provide measurement data from an existing CPA setup [15] with a pronounced spectrally inhomogeneous gain characteristic, the investigation of suitable pulse shaping methods for such systems provided an ideal starting point for further investigations.

As this thesis aims at exploiting model information to design suitable control concepts, Chapter 2 starts by deriving a mathematical model of CPAs. In particular, a detailed nonlinear model of the underlying regenerative amplifier (RA) is derived to describe the complex evolution of the light field and its interaction with the gain medium. While the modeling procedure itself can be considered quite generic and covers (or can easily be extended to cover) all major effects concerning the pulse amplification process for arbitrary gain media, it is exemplarily derived for a holmium-doped yttrium aluminum garnet. The resulting model is finally validated by measurement data from the experimental system described in [15]. Parts of this chapter are already published in [54].

In order to be able to apply ILC methods to the resulting mathematical model, special learning laws are required that are able to learn in a spectrally selective way and that can be applied to infinite-dimensional systems (i.e., systems described by partial differential equations) with reasonable computational effort. Both aspects provided the motivation to investigate stochastically optimal learning laws in Chapter 3. The proposed learning law can be considered a generalization of existing optimal PD-type learning laws. Moreover, the resulting learning operator turns out to be the solution of the well-known non-causal Wiener-Hopf equation that can be solved numerically irrespective of a potentially infinite-dimensional nature of the system. For clarity, some parts of the main proof are presented separately in Appendix D. This chapter is closely aligned to the results published in [55].

Chapter 4 applies a tailored Wiener-filtering-based learning law to the mathematical model given in Chapter 2. Since the full model is too complex for the proposed ILC scheme, it is simplified to obtain a reduced linear model. The resulting learning operator depends on a few quantities that can be extracted from corresponding input and output measurements. This yields an adaptive pulse-shape control that is able to track desired pulses without requiring a precisely calibrated model. The main results of this chapter are published in [54].

One of the main limitations of the (adaptive) learning law in terms of convergence speed and stability is closely linked to the dynamic coupling of subsequent pulses. As noted above, the underlying pulse-to-pulse dynamics of the regenerative amplifier result in unstable operational regimes that can even damage the laser medium. To further investigate this issue, a simplified energy-based description

Die approbierte Originalversion dieser Dissertation ist in der TU Wien Bibliothek verfügbar.
The approved original version of this doctoral thesis is available at the TU Wien Bibliothek.
TU WIEN Bibliothek Your knowledge hub

of regenerative amplifiers is introduced in Chapter 5, based on the assumption of mono-chromatic light. Furthermore, it is shown that such amplifiers can be stabilized by feedback using measurements of the pump light or the output pulse's energy, respectively. Such feedback laws ultimately allow to operate and safely steer regenerative amplifiers into arbitrary operational regimes.

Chapter 6 investigates the formation and amplification of pulse bursts using regenerative amplifiers with a detuned cavity design. Building on an extension of the energy-based description introduced in Chapter 5, one can calculate input pulse sequences that yield the desired output pulse bursts by using optimization-based methods. Deviations from the desired energy distribution are subsequently eliminated by transferring the learning methods from Chapter 4 to the simpler energy-based description and augmenting them by feedback methods developed in Chapter 5.

Finally, Chapter 7 summarizes the results of this thesis and discusses open issues and further research directions.

Further material on numerical simulation and parameter identification methods for the mathematical model derived in Chapter 2 is given in Appendix A and Appendix B, as originally published in [56]. Possible model extensions to linear cavities and multi-pass pumping schemes are presented in Appendix C. All parameters required to produce the various simulation scenarios throughout this thesis are summarized in Appendix E for completeness.

Die approbierte Originalversion dieser Dissertation ist in der TU Wien Bibliothek verfügbar.
The approved original version of this doctoral thesis is available at the TU Wien Bibliothek.
TU Bibliothek WIEN Your knowledge hub

CHAPTER 2

Modeling of Chirped Pulse Amplifiers for Ultra-Short Laser Pulses

Before beginning to derive a complete mathematical model of a chirped pulse amplifier (CPA), some preliminary statements shall be made. In ultra-fast optics, it is common to represent field quantities as real parts of complex quantities $\mathcal{A}$ that are described by complex envelope representations. The standard tool for the description of optical beams and their interaction with optical components is the so-called Gaussian beam as a solution of the paraxial wave equation [30, Cha. 16]. For collimated light on comparatively short propagation distances it is sufficient to describe the beam as a plane wave with a fixed cross section of the beam A_{B}. Such a plane wave with a homogeneous transversal profile and a fixed polarization propagating along the z axis can be written as

$$\mathcal{A}(z,t) = A(z,t)\mathrm{e}^{-i(k_0 z - \omega_0 t)}, \tag{2.1}$$

with the complex pulse envelope $A(z,t)$ of a carrier wave, the time t, the spatial coordinate z, the imaginary unit i, the angular frequency ω_0, and the spatial wave number k_0.

Remark 1. *While one could assume an arbitrary transversal profile $F(x,y)$, this would require to describe the change of the transversal profile over the propagation direction z due to spatial saturation effects, which is more complicated and beyond the scope of this work. However, recent results show that both the temporal* and *spatial pulse shape is important for ablation and micro-machining applications using femtosecond pulses [19] and such extensions may be useful for future work.*

Since the pulses of interest are typically signals where the spatial and temporal variations of the complex pulse envelope are slow compared to the carrier

Die approbierte Originalversion dieser Dissertation ist in der TU Wien Bibliothek verfügbar.
The approved original version of this doctoral thesis is available at the TU Wien Bibliothek.
TU WIEN Bibliothek Your knowledge hub

oscillations, the following approximations

$$\left|\frac{\partial^2 A(z,t)}{\partial z^2}\right| \ll \left|k_0 \frac{\partial A(z,t)}{\partial z}\right| \tag{2.2a}$$

and

$$\left|\frac{\partial^2 A(z,t)}{\partial t^2}\right| \ll \left|\omega_0 \frac{\partial A(z,t)}{\partial t}\right| \ll \left|\omega_0^2 A(z,t)\right|, \tag{2.2b}$$

usually called slowly varying envelope approximation (SVEA), see, e.g., [30, Sec. 24.4] or [29], are applied. To analyze a pulse spectrally, the Fourier transform

$$\hat{\mathcal{A}}(z,\omega) = \mathcal{F}\left\{\mathcal{A}(z,t)\right\} = \int_{-\infty}^{\infty} \mathcal{A}(z,t)\mathrm{e}^{-i\omega t}\mathrm{d}t \tag{2.3}$$

and its inverse

$$\mathcal{A}(z,t) = \mathcal{F}^{-1}\left\{\hat{\mathcal{A}}(z,\omega)\right\} = \frac{1}{2\pi}\int_{-\infty}^{\infty} \hat{\mathcal{A}}(z,\omega)\mathrm{e}^{i\omega t}\mathrm{d}\omega \tag{2.4}$$

are used. All considered pulses at some location z_0 are bounded and of finite energy and thus $\mathcal{A}(z_0,\cdot) \in L^2 \cap L^\infty$ with the common norms

$$\|\mathcal{A}(z_0,\cdot)\|_2 = \|A(z_0,\cdot)\|_2 = \left(\int_{-\infty}^{\infty} |A(z_0,t)|^2 \mathrm{d}t\right)^{\frac{1}{2}} \tag{2.5a}$$

$$\|\mathcal{A}(z_0,\cdot)\|_\infty = \|A(z_0,\cdot)\|_\infty = \sup_{t\in\mathbb{R}} |A(z_0,t)| \ . \tag{2.5b}$$

Following the convention to describe the light pulse in terms of the electric field $\mathcal{E}$, its pulse energy at z_0 is given by

$$\begin{aligned} W &= \frac{A_\mathrm{B}}{2Z_0}\int_{-\infty}^{\infty} |E(z_0,t)|^2 \mathrm{d}t = \frac{A_\mathrm{B}}{2Z_0}\|E(z_0,\cdot)\|_2^2 \\ &= \frac{A_\mathrm{B}}{4\pi Z_0}\int_{-\infty}^{\infty} \left|\hat{E}(z_0,\omega)\right|^2 \mathrm{d}\omega, \end{aligned} \tag{2.6}$$

where Z_0 denotes the impedance of free space and A_B is the cross section of the laser beam. In the sequel, spatial mean values over the length of the gain medium L are denoted by an overline, i.e.

$$\overline{N} = \frac{1}{L}\int_0^L N(z)\mathrm{d}z \ . \tag{2.7}$$

Apart from the source of input pulses, a CPA system consists of three main components: a pulse stretcher with a spectral filter afterwards, a regenerative amplifier (RA) and a pulse compressor at the end. Such CPA systems are usually operated in a repetitive fashion, where identical seed pulses $E_\mathrm{seed}(t)$ at a repetition frequency f_rep are fed into a (typically grating-based) pulse stretcher. Depending

Die approbierte Originalversion dieser Dissertation ist in der TU Wien Bibliothek verfügbar.
The approved original version of this doctoral thesis is available at the TU Wien Bibliothek.
TU Bibliothek WIEN Your knowledge hub

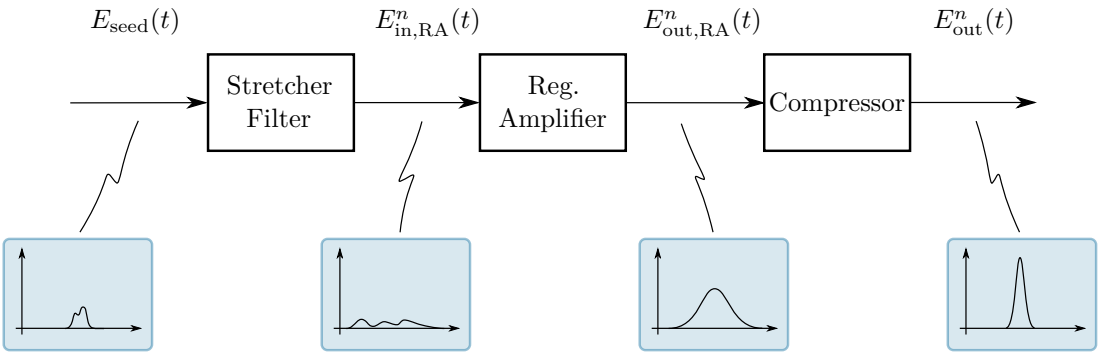

Figure 2.1: Components of a CPA system and associated pulses. The schematic graphs in blue illustrate the ideal temporal pulse shapes for a desired Gaussian output pulse.

on the settings of the spectral filter and the state of the regenerative amplifier (RA), this gives a heavily chirped pulse $E^n_{\text{in,RA}}(t)$ which is amplified to $E^n_{\text{out,RA}}(t)$ and compressed back to yield the output pulse $E^n_{\text{out}}(t)$. The overall goal is to adjust the amplitude and phase characteristics of the spectral filter such that $E^n_{\text{out,RA}}(t)$ is compressed back into an unchirped pulse of desired shape $E^{\text{d}}_{\text{out}}(t)$, as indicated in Figure 2.1. While pulse stretchers and compressors can be easily described in terms of their spectral properties, the behavior of RAs is quite complex and requires a more detailed model. Thus, we start by addressing the description of the stretcher, the compressor and the spectral filter in Section 2.1 and then continue with the RA in Section 2.2.

2.1 Stretcher, filter and compressor

The basic idea of grating-based pulse stretchers (and compressors) is to vary the spatial paths depending on the frequency and thus introduce frequency-depending delays. When propagating through the device, each frequency component ω of the complex envelope's Fourier transform $\hat{E}(z,\omega)$ thus receives an additional phase $\varphi_{\text{S}}(\omega)$ that can be approximated around the carrier frequency ω_0 with high accuracy by

$$\varphi_{\text{S}}(\nu) = \varphi_{\text{S},0} + \varphi_{\text{S},1}\nu + \varphi_{\text{S},2}\nu^2 + \varphi_{\text{S},3}\nu^3 \tag{2.8}$$

where $\nu = \omega - \omega_0$. The constants $\varphi_{\text{S},i}$, $i \in \{0,1,2,3\}$ depend on the geometry, the pulse's center frequency ω_0 and the grating constant as shown in [24]. The transfer function of the pulse stretcher can therefore be written as

$$G_{\text{S}}(\omega) = \eta_{\text{S}} \mathrm{e}^{i\varphi_{\text{S}}(\omega-\omega_0)}, \tag{2.9}$$

with the spectrally uniform efficiency coefficient η_{S}.

Die approbierte Originalversion dieser Dissertation ist in der TU Wien Bibliothek verfügbar.
The approved original version of this doctoral thesis is available at the TU Wien Bibliothek.
TU Bibliothek WIEN Your knowledge hub

Remark 2. *In general, the efficiency coefficient η_S will not be uniform for pulses with very high bandwidth due to varying diffraction efficiency. Moreover, some amount of energy loss is introduced by the limited bandwidth of pulse stretchers and compressors due to the finite size of the grating pair, which can be easily accounted for by truncating the spectrum.*

Thus, the input pulse to the RA is given by

$$E^n_{\mathrm{in,RA}}(t) = \mathcal{F}^{-1}\left\{G^n_{\mathrm{F}}(\omega)\, G_{\mathrm{S}}(\omega)\, \hat{E}_{\mathrm{seed}}(\omega)\right\}, \tag{2.10}$$

where $G^n_{\mathrm{F}}(\omega)$ denotes the adjustable transfer function of the spectral filter (set for the n-th pulse). Since the filter is not able to amplify any frequency component, its transfer function has to fulfill the constraint

$$|G^n_{\mathrm{F}}(\omega)| \leq 1 \tag{2.11}$$

for all $\omega \in \mathbb{R}$. Analogously, the compressor can be described by

$$E^n_{\mathrm{out}}(t) = \mathcal{F}^{-1}\left\{G_{\mathrm{C}}(\omega)\, \hat{E}^n_{\mathrm{out,RA}}(\omega)\right\} \tag{2.12}$$

with $G_{\mathrm{C}}(\omega) = \eta_{\mathrm{C}} \mathrm{e}^{i\varphi_{\mathrm{C}}(\omega-\omega_0)}$.

Remark 3. *Analyzing the effect of (2.8) shows that the constant and linear terms introduce a phase shift and a time delay to the incident pulse, which can be neglected when studying the pulse shape, i.e. $\varphi_{C,0} = \varphi_{S,0} = 0$ and $\varphi_{C,1} = \varphi_{S,1} = 0$. The quadratic term produces the desired linear chirp while the cubic term generates a nonlinear chirp that typically becomes relevant for very short pulses below* 20 fs *[57].*

Depending on the source of seed pulses, a general incident pulse $E_{\mathrm{in}}(t)$ is showing some amount of chirp. Thus, the pulse stretcher only adds such an amount of quadratic phase that the desired temporal stretching is achieved. The compressor is then designed such that it compensates the overall quadratic and cubic phase components to achieve a "Fourier-limited" (unchirped) pulse. For simplicity it is assumed that the input pulse exhibits hardly any quadratic or cubic phase components and that stretcher and compressor compensate each other in a perfect way, i.e.

$$\varphi_{\mathrm{C},2} = -\varphi_{\mathrm{S},2}, \quad \varphi_{\mathrm{C},3} = -\varphi_{\mathrm{S},3}\ . \tag{2.13}$$

2.2 Regenerative amplifier (RA)

The central part of a CPA system is the RA, which comprises a (usually) continuously pumped gain medium located inside an optical resonator. Depending on the exact specifications, the optical resonator may be designed such that the pulse

Die approbierte Originalversion dieser Dissertation ist in der TU Wien Bibliothek verfügbar.
The approved original version of this doctoral thesis is available at the TU Wien Bibliothek.
TU WIEN Bibliothek Your knowledge hub

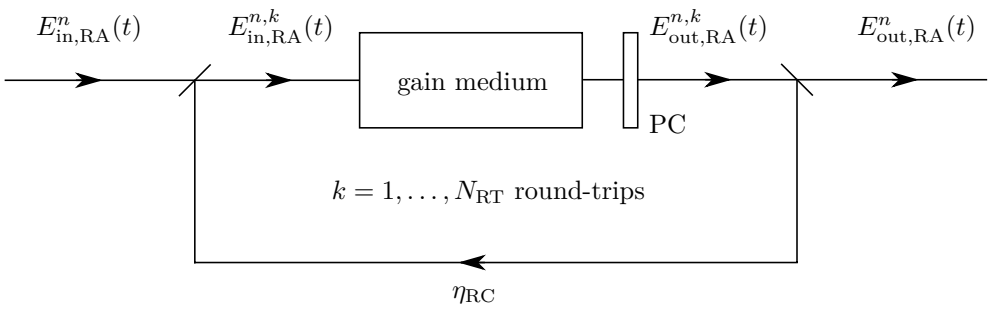

Figure 2.2: Simplified layout of a regenerative amplifier (RA). The n-th chirped input pulse $E^n_{\mathrm{in,RA}}(t)$ is inserted into the ring cavity, amplified by passing the gain medium for N_{RT} times, and finally extracted by switching the polarization via a Pockels cell (PC). All losses are considered to be subsumed in the efficiency coefficient of the resonator cavity η_{RC}.

is injected into the gain medium bidirectionally or unidirectionally, where the first is called a linear cavity and the latter a ring cavity. In the following, we will restrict ourselves to RAs using ring cavities since the case of linear cavities can be treated similarly with slight modifications (compare to Appendix C). According to Figure 2.2, the n-th chirped pulse $E^n_{\mathrm{in,RA}}(t)$ leaving the pulse stretcher and filter is injected into the ring cavity and amplified by the gain medium. The k-th cycle of the n-th pulse is denoted by $E^{n,k}_{\mathrm{in,RA}}(t)$ prior to amplification and $E^{n,k}_{\mathrm{out,RA}}(t)$ after amplification. After N_{RT} round-trips in the resonator cavity, the amplified pulse $E^n_{\mathrm{out,RA}}(t)$ is extracted and passed on to the pulse compressor. Until the next pulse arrives, the depleted population inversion is slowly regenerated (see Figure 2.3 at the top). For simplification, losses of all optical components are combined in the efficiency coefficient η_{RC} acting on the recirculated pulse as shown in Figure 2.2.

A mathematical model describing the amplification process needs to take into account the coupling of the doped ions inside the gain medium with the laser pulse and the continuous pumping light field. Additionally, the propagation of ultra-short and high-energy pulses in dense media is subject to nonlinear and dispersive effects that have to be taken into account. Due to the high energy and the broad spectrum of the amplified pulses, the field-matter interaction while traveling through the gain medium is quite complex and results in fast dynamics of the excited ions. The effect of the several orders of magnitude weaker pumping field is negligible for the comparatively short period it takes the pulse to propagate through the gain medium. In contrast, during the regeneration time or in between cycles where no pulse is present in the gain medium, the pumping field's interaction with the ions is essential, although quite simple and rather slow. Thus, it is advisable to split both domains and use separate pulse and pump models. Since the temporal pulse length is significantly shorter than its round-trip

Die approbierte Originalversion dieser Dissertation ist in der TU Wien Bibliothek verfügbar.
The approved original version of this doctoral thesis is available at the TU Wien Bibliothek.
TU Bibliothek WIEN Your knowledge hub

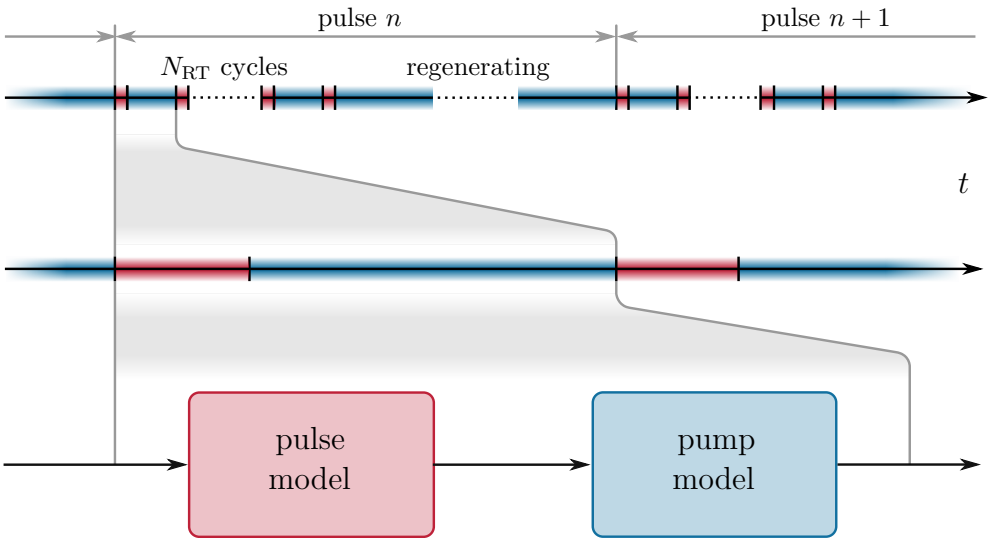

Figure 2.3: Time sequence of a pulse amplification process. Red indicates times where the pulse is traveling through the gain medium while during blue time zones the gain medium is exposed to the pumping laser only. The whole amplification process can thus be described by an alternating chain of pulse and pump models.

time within the cavity this is easily possible in a temporally consecutive fashion as shown in Figure 2.3.

2.2.1 Pulse propagation in gain media (pulse model)

In this section, we want to describe the propagation of a laser pulse through a gain medium including nonlinear and dispersive effects. To keep the presentation short and compact, we will not explicitly specify space or time dependence of any variables unless it is required for the understanding.

The propagation of light within media is determined by Maxwell's equations. Neglecting the magnetization at optical frequencies and splitting the polarization $\mathcal{P}$ into a linear and a nonlinear component $\mathcal{P}_{\mathrm{l}}$ and $\mathcal{P}_{\mathrm{nl}}$, respectively, one obtains the so-called polarization driven wave equation [58, eq. 22.5-18]

$$\frac{\partial^2 \mathcal{E}}{\partial z^2} - \mu_0 \varepsilon_0 \frac{\partial^2 \mathcal{E}}{\partial t^2} = \mu_0 \frac{\partial^2 (\mathcal{P}_{\mathrm{l}} + \mathcal{P}_{\mathrm{nl}})}{\partial t^2} \tag{2.14}$$

for plane waves propagating along the z-direction with the permittivity of free space ε_0 and the permeability of free space μ_0. For dispersive materials, the polarization and the electric field are linked by a dynamical system. Thus, it is customary to describe the linear polarization of the host material in the frequency domain, i.e. $\hat{\mathcal{P}}_{\mathrm{l}}(\omega) = \varepsilon_0 \chi^{(1)}(\omega) \hat{\mathcal{E}}(\omega)$, using the linear electric susceptibility $\chi^{(1)}(\omega)$.

Die approbierte Originalversion dieser Dissertation ist in der TU Wien Bibliothek verfügbar.
The approved original version of this doctoral thesis is available at the TU Wien Bibliothek.
TU Bibliothek WIEN Your knowledge hub

This leads to the Helmholtz equation

$$\frac{\partial^2 \hat{\mathcal{E}}}{\partial z^2} + k^2(\omega)\hat{\mathcal{E}} = -\mu_0\omega^2\hat{\mathcal{P}}_{\mathrm{nl}}, \tag{2.15}$$

with the dispersion relation $k^2(\omega) = \mu_0\varepsilon_0(1+\chi^{(1)}(\omega))\omega^2$. Applying the Fourier transform to the complex pulse envelope representation (2.1), one obtains the relationship

$$\hat{\mathcal{A}}(z,\omega) = \mathrm{e}^{-ik_0 z}\int_{-\infty}^{\infty} A(z,t)\mathrm{e}^{-i(\omega-\omega_0)t}\mathrm{d}\omega = \mathrm{e}^{-ik_0 z}\hat{A}(z,\nu) \tag{2.16}$$

with $\nu = \omega - \omega_0$. Inserting (2.16) into (2.15) yields

$$\frac{\partial^2 \hat{E}}{\partial z^2} - i2k_0\frac{\partial \hat{E}}{\partial z} + (k^2(\omega) - k_0^2)\hat{E} = -\mu_0\omega^2\hat{P}_{\mathrm{nl}}. \tag{2.17}$$

Since the considered pulses $\hat{E}$ are of finite bandwidth, it is sufficient to consider the dispersive effects of $k^2(\omega)$ in the vicinity of $k_0 = k(\omega_0)$. By using $k(\omega) + k_0 \approx 2k_0$ and the second order Taylor expansion $k(\omega) = k_0 + k_1\nu + {}^{k_2}/_{2}\,\nu^2$, we get

$$k^2(\omega) - k_0^2 = (k(\omega)+k_0)(k(\omega)-k_0) \approx 2k_0(k(\omega)-k_0) \approx 2k_0(k_1\nu + {}^{k_2}/_{2}\,\nu^2). \tag{2.18}$$

Utilizing this approximation to simplify (2.17) and transforming the result back into the time domain using the relation

$$\mathcal{F}\left\{\frac{\partial^n A}{\partial t^n}(z,t)\right\} = (i\nu)^n\hat{A}(z,\nu) \tag{2.19}$$

results in

$$\frac{\partial^2 E}{\partial z^2} - i2k_0\frac{\partial E}{\partial z} - i2k_0k_1\frac{\partial E}{\partial t} - 2k_0\frac{k_2}{2}\frac{\partial^2 E}{\partial t^2} = -\mu_0\omega_0^2 P_{\mathrm{nl}} + i2\mu_0\omega_0\frac{\partial P_{\mathrm{nl}}}{\partial t} + \mu_0\frac{\partial^2 P_{\mathrm{nl}}}{\partial t^2}. \tag{2.20}$$

Due to the SVEA (2.2), one can neglect the second spatial derivative of E and both temporal derivatives of P_{nl} to obtain (cp. [58, pp. 991] or [29, Sec. 3.2])

$$i\left[\frac{\partial E}{\partial z} + \frac{1}{v_{\mathrm{g}}}\frac{\partial E}{\partial t}\right] + \frac{k_2}{2}\frac{\partial^2 E}{\partial t^2} = \frac{\mu_0\omega_0^2}{2k_0}P_{\mathrm{nl}}, \tag{2.21}$$

with the group velocity $v_{\mathrm{g}} = {}^{1}/_{k_1}$. Using the transformation $t \mapsto t - \frac{z}{v_{\mathrm{g}}}$ into a time frame traveling with the pulse center and the nonlinear polarization [29, Sec. 8.5]

$$P_{\mathrm{nl}} = \frac{3}{4}\varepsilon_0\chi^{(3)}|E|^2E + P_{\mathrm{at}} \tag{2.22}$$

due to the Kerr effect and the polarization P_{at} induced by the dopant yields the polarization driven version of the nonlinear Schrödinger equation (see [26, 59])

$$i\frac{\partial E}{\partial z} + \frac{k_2}{2}\frac{\partial^2 E}{\partial t^2} - \frac{1}{2}\omega_0\varepsilon_0 n_0 n_2|E|^2E = \frac{\omega_0^2}{2c_0^2\varepsilon_0 k_0}P_{\mathrm{at}}, \tag{2.23}$$

Die approbierte Originalversion dieser Dissertation ist in der TU Wien Bibliothek verfügbar.
The approved original version of this doctoral thesis is available at the TU Wien Bibliothek.
TU Bibliothek WIEN Your knowledge hub

with the refractive indices $n_0 = {}^{k_0 c_0}/_{\omega_0}$, $n_2 = {}^{(3Z_0\chi^{(3)})}/_{(4n_0^2)}$, the impedance of free space $Z_0 = \sqrt{{}^{\mu_0}/_{\varepsilon_0}}$ and $\varepsilon_0\mu_0 c_0^2 = 1$ with the vacuum speed of light c_0.

While equation (2.23) is describing the propagation of the electric field, a model for the atomic polarization of the dopant P_{at} is missing. This could be obtained by invoking the density operator formalism to obtain a full description in terms of quantum theory [60–62]. In this thesis, we apply the more intuitive and standard approach for laser systems and make use of the so-called rate equation modeling together with modified resonant dipole equations, which are quantum mechanically correct [30], but can be more easily related to experimental quantities. Without loss of generality, a Holmium-doped yttrium aluminum garnet (Ho:YAG) gain medium - a promising candidate for mid-infrared laser systems [15] - is chosen for the following demonstration purposes. Taking existing measurement results on the structure of Ho:YAG's ground and first excited state manifold [63, Fig. 1], a simplified energy level diagram can be established as shown in Figure 2.4. Thus, the simplified model assumes that there is one ground state E_0 and one upper state E_5 with four intermediate states E_1 to E_4 where each level is populated by the associated population density N_0 to N_5. Each of the intermediate states is connected to the upper state by a resonant transition that lies within the frequency spectrum of our laser pulse while the resonant transition between the ground and the upper state is used for pumping. Thus, assuming homogeneously broadened line shapes, the polarization at every point z due to the resonant transition $j \leftrightarrow 5, j \in \{1, \ldots, 4\}$, with the population densities N_j and N_5, is given by the resonant dipole equation [30]

$$\frac{\partial^2 \mathcal{P}_j}{\partial t^2} + \Delta\omega_j \frac{\partial \mathcal{P}_j}{\partial t} + \omega_j^2 \mathcal{P}_j = \kappa_j (N_j - N_5)\mathcal{E}, \tag{2.24}$$

with the transition's resonant frequency ω_j, its spectral width $\Delta\omega_j$, $\kappa_j = \frac{\omega_j \varepsilon_0 c_0 \Delta\omega_j \sigma_j}{\omega_0}$, and the transition cross section σ_j. Applying the envelope representation to (2.24) and using the SVEA (2.2) yields

$$\frac{\partial P_j}{\partial t} = -\frac{\omega_j^2 + i\omega_0\Delta\omega_j - \omega_0^2}{\Delta\omega_j + i2\omega_0} P_j + \frac{\kappa_j}{\Delta\omega_j + i2\omega_0}(N_j - N_5)E\ . \tag{2.25}$$

The atomic polarization is then the sum of all four contributions, i.e. $P_{\text{at}} = P_1 + P_2 + P_3 + P_4$.

The time in which the pulse is traveling through the gain medium is significantly shorter than any dynamics of the pumping process or non-radiative relaxation and redistribution processes. Therefore, both can be neglected when describing the evolution of the population densities. Since the total number of the population is given by the dopant density, i.e.

$$\sum N_j = N_0 + N_1 + \ldots + N_5 = N_{\text{dop}}, \tag{2.26}$$

Die approbierte Originalversion dieser Dissertation ist in der TU Wien Bibliothek verfügbar.
The approved original version of this doctoral thesis is available at the TU Wien Bibliothek.
TU Bibliothek WIEN Your knowledge hub

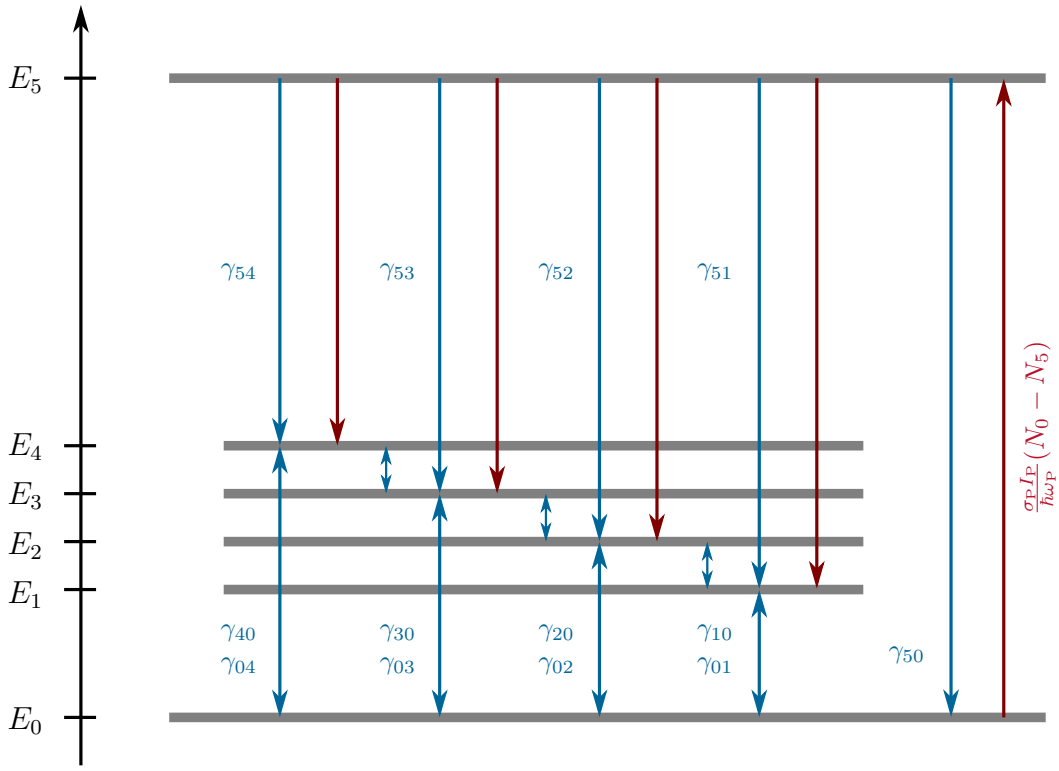

Figure 2.4: Simplified energy level diagram for Ho:YAG with five resonant transitions in red and eleven radiative and non-radiative relaxation transitions in blue (see [63, Fig. 1]). For relaxation transitions, double arrows indicate downward and upward relaxation.

Die approbierte Originalversion dieser Dissertation ist in der TU Wien Bibliothek verfügbar.
The approved original version of this doctoral thesis is available at the TU Wien Bibliothek.
TU Bibliothek Your knowledge hub WIEN

it is sufficient to describe the densities of five energy levels. Thus, an energy conservation argument (see [30, Cha. 24]) gives the atomic rate equations

$$\frac{\partial N_j}{\partial t} = +\frac{1}{2\hbar}\mathrm{Im}\left\{E^* P_j\right\}, \quad j = 1, \ldots, 4 \tag{2.27a}$$

$$\frac{\partial N_5}{\partial t} = -\frac{1}{2\hbar}\mathrm{Im}\left\{E^*(P_1 + P_2 + P_3 + P_4)\right\}, \tag{2.27b}$$

with the reduced Planck constant $\hbar$ and the complex conjugate electric field intensity E^*.

Summing up the results, the propagation of the k-th round-trip in the ring cavity of the n-th pulse can be described by (2.23), (2.25) and (2.27) together with the initial and boundary conditions

$$E(0,t) = E^{n,k}_{\mathrm{in,RA}}(t) \tag{2.28a}$$

$$E(z,0) = 0 \tag{2.28b}$$

$$\left.\frac{\partial E(z,t)}{\partial t}\right|_{t=0} = 0 \tag{2.28c}$$

$$P_j(z,0) = 0 \tag{2.28d}$$

$$N_j(z,0) = N^{n,k}_{j,\mathrm{pulse}}(z), \quad j = 1, \ldots, 5, \tag{2.28e}$$

where $N^{n,k}_{j,\mathrm{pulse}}(z)$ denotes the population density of the j-th energy level at the location z at the time when the n-th pulse enters the gain medium for the k-th cycle. The amplified pulse is given by

$$E^{n,k}_{\mathrm{out,RA}}(t) = E(L,t) \tag{2.29}$$

where L is the length of the gain medium. The depleted population density after the pulse has passed is given by

$$N^{n,k}_{j,\mathrm{dep}}(z) = N^{n,k}_{j}(z, t_{\mathrm{end}}), \tag{2.30}$$

where t_{end} is large enough such that the pulse has completely passed through the gain medium, i.e., that $E(z,t) \equiv 0$ for all $t > t_{\mathrm{end}}$.

Remark 4. *It is diffucult to give an exact a-priori estimate of t_{end} in (2.30) as it depends on the pulse shape of $E^{n,k}_{in,RA}(t)$ as well as on the temporal broadening due to dispersive and nonlinear effects in (2.23). Since we have neglected relaxation and redistribution processes for the pulse model, the population densities remain at a constant value as soon as the pulse has propagated through the gain medium (see (2.27)).*

Remark 5. *The interaction of light with dense media is in general governed by coupling Maxwell's equations with the atomic response of the medium. As indicated*

Die approbierte Originalversion dieser Dissertation ist in der TU Wien Bibliothek verfügbar.
The approved original version of this doctoral thesis is available at the TU Wien Bibliothek.
TU Bibliothek WIEN Your knowledge hub

above, this amounts to solving the von-Neumann equation of the corresponding density operator to obtain a description in quantum-mechanical terms analogous to the derivations above. The resulting mathematical models for a medium with two energy states are usually called Maxwell-Bloch equations (if no dispersion is considered) or Schrödinger-Bloch equations (for linear dispersion as in this section)[1]*. The well-posedness and regularity of the resulting boundary value problem for the nonlinear Schrödinger equation alone has been recently studied in [64]. For more details on the well-posedness of Maxwell-Bloch equations, the reader is referred to [65].*

2.2.2 Interaction with pumping field (pump model)

During times where the light pulse is not present in the gain medium, the dynamics of the regeneration process is determined by the pumping laser and the redistribution of population densities due to non-radiative and radiative relaxation processes. Using the directed relaxation probability γ_{ij} from i to j and describing the pumping field only in terms of its field intensity I_P yields the atomic rate equations (e.g., see [30, Cha. 4])

$$\begin{aligned}
\frac{\partial N_1}{\partial t} &= -(\gamma_{10}+\gamma_{12})N_1+\gamma_{21}N_2+\gamma_{51}N_5+\gamma_{01}N_0\\
\frac{\partial N_2}{\partial t} &= \gamma_{12}N_1-(\gamma_{20}+\gamma_{21}+\gamma_{23})N_2+\gamma_{32}N_3+\gamma_{52}N_5+\gamma_{02}N_0\\
\frac{\partial N_3}{\partial t} &= \gamma_{23}N_2-(\gamma_{30}+\gamma_{32}+\gamma_{34})N_3+\gamma_{43}N_4+\gamma_{53}N_5+\gamma_{03}N_0\\
\frac{\partial N_4}{\partial t} &= \gamma_{34}N_3-(\gamma_{40}+\gamma_{43})N_4+\gamma_{54}N_5+\gamma_{04}N_0\\
\frac{\partial N_5}{\partial t} &= -(\gamma_{50}+\gamma_{51}+\gamma_{52}+\gamma_{53}+\gamma_{54})N_5+\frac{\sigma_\mathrm{P} I_\mathrm{P}}{\hbar\omega_\mathrm{P}}(N_0-N_5),
\end{aligned} \tag{2.31}$$

with the pumping field's cross section σ_P and its angular frequency ω_P. The population of the ground state N_0 can be eliminated by (2.26). Using the Frantz-Nodvik approach [66][30, Cha. 10] for a continuous pumping process and assuming a steady-state solution of the field intensity results in

$$\frac{\partial I_\mathrm{P}}{\partial z} = \sigma_\mathrm{P}(N_5 - N_0)I_\mathrm{P}, \tag{2.32}$$

with the initial and boundary conditions

$$I_\mathrm{P}(0,t) = I_0 \tag{2.33a}$$

[1]Both terms are sometimes used in a more liberal sense to denote the coupled system of equations without necessarily demanding a medium with two energy states, although the reference to Bloch's equations is somewhat odd in that case.

Die approbierte Originalversion dieser Dissertation ist in der TU Wien Bibliothek verfügbar.
The approved original version of this doctoral thesis is available at the TU Wien Bibliothek.
TU Bibliothek WIEN Your knowledge hub

$$N_j(z,0) = N_{j,\text{pump}}^{n,k}(z) \tag{2.33b}$$

where I_0 denotes the incident pumping intensity and $N_{j,\text{pump}}^{n,k}(z)$ denotes the population of the j-th level at the beginning of the k-th cycle of the n-th pulse. The final regenerated population density is given at the time it takes the pulse to complete the round-trip, i.e.

$$N_{j,\text{reg}}^{n,k}(z) = N_j(t_{\text{end}}, z) \tag{2.34}$$

whereby $t_{\text{end}} = {}^{(L_{\text{RC}}-L)}/_{c_0}$ with the length of the resonator cavity L_{RC}.

2.2.3 Coupling of pulse and pump model

From a functional point of view, the pulse model is taking the input pulse $E_{\text{in,RA}}^{n,k}(t)$ and the corresponding initial population distribution $N_{j,\text{pulse}}^{n,k}(z)$ and computes an amplified pulse $E_{\text{out,RA}}^{n,k}(t)$ (that is assumed to be bounded and of finite energy again) and a remaining population distribution $N_{j,\text{dep}}^{n,k}(z)$. The pump model on the other hand is taking this remaining population distribution (and the given incident pumping intensity I_0) and integrates the rate equation (2.31) to obtain $N_{j,\text{reg}}^{n,k}$. Taking into account the concentrated losses of the cavity according to Figure 2.2, the coupling conditions are given by

$$N_{j,\text{pump}}^{n,k}(z) = N_{j,\text{dep}}^{n,k}(z) \tag{2.35a}$$

$$E_{\text{in,RA}}^{n,k+1}(t) = \eta_{\text{RC}} E_{\text{out,RA}}^{n,k}(t) \tag{2.35b}$$

$$N_{j,\text{pulse}}^{n,k+1}(z) = N_{j,\text{reg}}^{n,k}(z). \tag{2.35c}$$

For a given n-th input pulse of the RA

$$E_{\text{in,RA}}^{n}(t) = E_{\text{in,RA}}^{n,1}(t) \tag{2.36}$$

with the corresponding initial population densities

$$N_{j,\text{in}}^{n}(z) = N_{j,\text{pulse}}^{n,1}(z), \tag{2.37}$$

the amplification inside the resonator cavity can be described by an alternating application of the pulse and the pump model with the coupling conditions (2.35) until the output pulse is finally given by

$$E_{\text{out,RC}}^{n}(t) = E_{\text{out,RC}}^{n,N_{\text{RT}}}(t) \tag{2.38}$$

and the remaining populations by

$$N_{j,\text{out}}^{n}(z) = N_{j,\text{dep}}^{n,N_{\text{RT}}}(z)\ . \tag{2.39}$$

Die approbierte Originalversion dieser Dissertation ist in der TU Wien Bibliothek verfügbar.
The approved original version of this doctoral thesis is available at the TU Wien Bibliothek.
TU Bibliothek WIEN Your knowledge hub

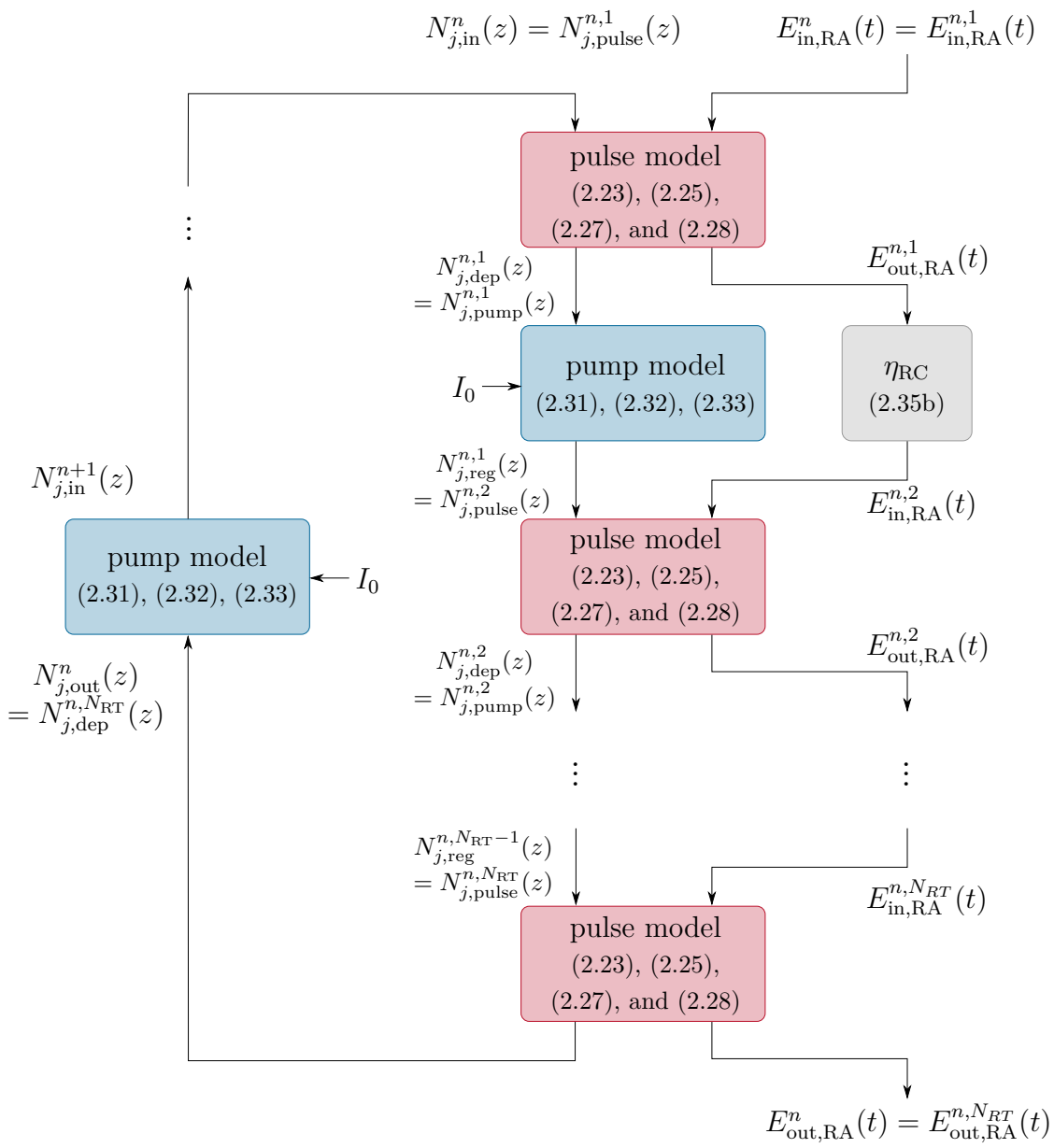

Figure 2.5: Coupling of the pulse and pump models to calculate the amplification of a pulse inside the resonator cavity and the subsequent regeneration phase.

Die approbierte Originalversion dieser Dissertation ist in der TU Wien Bibliothek verfügbar.
The approved original version of this doctoral thesis is available at the TU Wien Bibliothek.
TU WIEN Bibliothek Your knowledge hub

During the following regeneration phase until the $(n+1)$-st pulse arrives, one can simply integrate the pump model for the remaining time t_{reg} to obtain the initial population densities for the following pulse, i.e. $N^n_{j,\mathrm{in}}(z)$. By accounting for the time it takes the pulse to finish N_{RT} round-trips inside the cavity, one obtains

$$t_{\mathrm{reg}} = \frac{1}{f_{\mathrm{rep}}} - N_{\mathrm{RT}}\left[\frac{L_{\mathrm{RC}} - L}{c_0} + \frac{L}{v_{\mathrm{g}}}\right] \tag{2.40}$$

using the repetition frequency f_{rep}, the lengths of the resonator cavity L_{RC} and the gain medium L, and the group velocity v_{g}. A graphical overview of the complete resulting model is given in Figure 2.5.

Remark 6. *Notice that t_{end} as used (2.34) together with (2.40) introduces a slight systematic error since the pumping process is only considered during the times the pump model is used while in reality it is operated continuously. Thus, the total energy supplied to the laser medium is slightly underestimated. As a simple corrective measure, one could approximately attribute the effect of the pumping process during the pulse amplification phases to the following pump phase by replacing t_{end} in (2.34) with the actual round-trip time $t_{RT} = {}^{(L_{RC}-L)}/_{c_0} + {}^{L}/_{v_g}$. Since the difference is negligible for the considered scenario, such a correction has not been used.*

2.3 Validity of the CPA model

In order to investigate the validity of the proposed CPA model, simulation results are compared with actual measurement data from a Ho:YAG system given in [15]. Without going into details of the parameter identification, extracting suitable parameters - especially for the relaxation probabilities γ_{ij} - can be quite challenging and a more detailed treatment of this topic is given in Appendix B. The lifetime of the population N_5 was determined by fluorescence measurements to be approximately $\tau_5 = 8\,\mathrm{ms}$. Under the assumption that each relaxation transition is contributing equally this gives $\gamma_{5j} = {}^{1}/_{5\tau_5} = 25$ for $j \in \{0,\ldots,4\}$. Measurements of the absorption cross section of the pumping process σ_{P} can be found in the literature [63, Table 1]. The losses within the ring cavity are in good approximation spectrally uniform and can be estimated to around 5 % in pulse energy per round-trip. This yields an efficiency coefficient $\eta_{\mathrm{RC}} \approx \sqrt{0.95}$. Neglecting the direct interaction between the intermediate levels, i.e. $\gamma_{ij} = 0$ for $i,j \in \{1,2,3,4\}$, simplifies the problem significantly and allows to identify suitable upward and downward relaxation probabilities γ_{j0} and γ_{0j} together with the unknown transition cross sections σ_j for $j \in \{1,2,3,4\}$.

As shown in Figure 2.6, the observed steady-state gain of the CPA system without any input shaping, i.e.,

$$G(\omega) = \frac{\hat{E}^s_{\mathrm{out}}(\omega)}{\hat{E}_{\mathrm{seed}}(\omega)} \tag{2.41}$$

Die approbierte Originalversion dieser Dissertation ist in der TU Wien Bibliothek verfügbar.
The approved original version of this doctoral thesis is available at the TU Wien Bibliothek.
TU Bibliothek WIEN Your knowledge hub

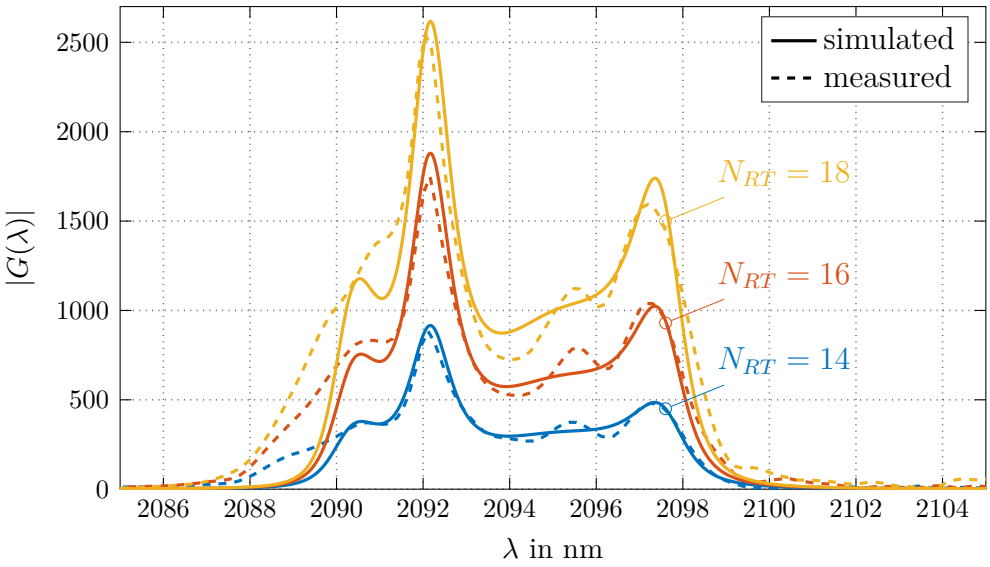

Figure 2.6: Comparing the amplifier gain $|G(\lambda)|$ as a function of the wavelength $\lambda = {}^{2\pi c_0}/_{\omega}$ obtained by simulation of the mathematical model with measurements for $N_{\mathrm{RT}} = 14$ (blue), $N_{\mathrm{RT}} = 16$ (red) and $N_{\mathrm{RT}} = 18$ (yellow).

with the steady-state output pulse $E^s_{\mathrm{out}}(t)$, is adequately reproduced by the proposed mathematical model. Some resonant transitions other than the four considered seem to play only a minor role. In particular the gain for higher frequencies with wavelengths lower then 2090 nm suggests that some levels above the upper state E_5 are populated (see [63]) and contribute slightly to the overall gain. The effects of this additional gain can be seen in Figure 2.7: while the saturation behavior itself in terms of the output energy W^s_{out} of $E^s_{\mathrm{out}}(t)$ according to (2.6) is nicely reproduced, a constant (multiplicative) error remains for various numbers of cycles N_{RT} in the ring cavity. The corresponding depletion in the mean spatial population inversions after the regeneration phase

$$\overline{\Delta N^s_{5j,\mathrm{reg}}} = \frac{1}{L}\int_0^L N^s_{5,\mathrm{reg}}(z) - N^s_{j,\mathrm{reg}}(z)\mathrm{d}z \tag{2.42}$$

is shown in Figure 2.8. Hereby, $\Delta N^s_{5j,\mathrm{reg}}(z)$ denotes the steady state population inversion, i.e. the population inversion has settled at a level where the extraction due to the pulse amplification and the regeneration due to the pumping process cancel each other exactly.

Remark 7. *The identification of the proposed model suffers from two difficulties. First, it is hard to separate the effects of the large number of unknown parameters, in particular of the coefficients of the atomic rate equations (2.31). Moreover, the measurement results shown in Figure 2.6 and Figure 2.7 are steady-state measurements where the population inversion has settled at* $\Delta N^s_{5j,reg}(z)$. *However,*

Die approbierte Originalversion dieser Dissertation ist in der TU Wien Bibliothek verfügbar.
The approved original version of this doctoral thesis is available at the TU Wien Bibliothek.
TU Bibliothek WIEN Your knowledge hub

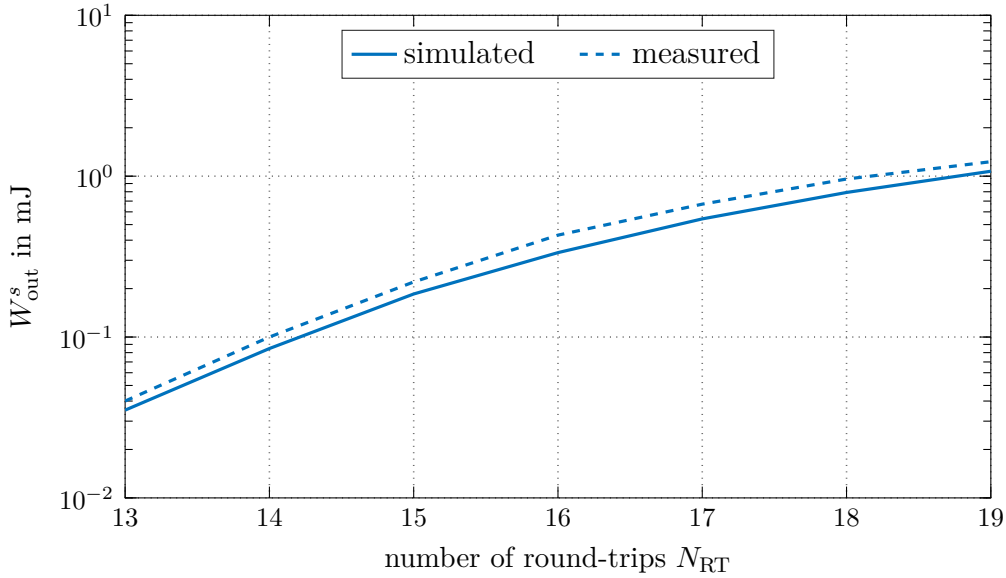

Figure 2.7: Evolution of the output pulse energy W_{out} of the CPA system and the simulated model.

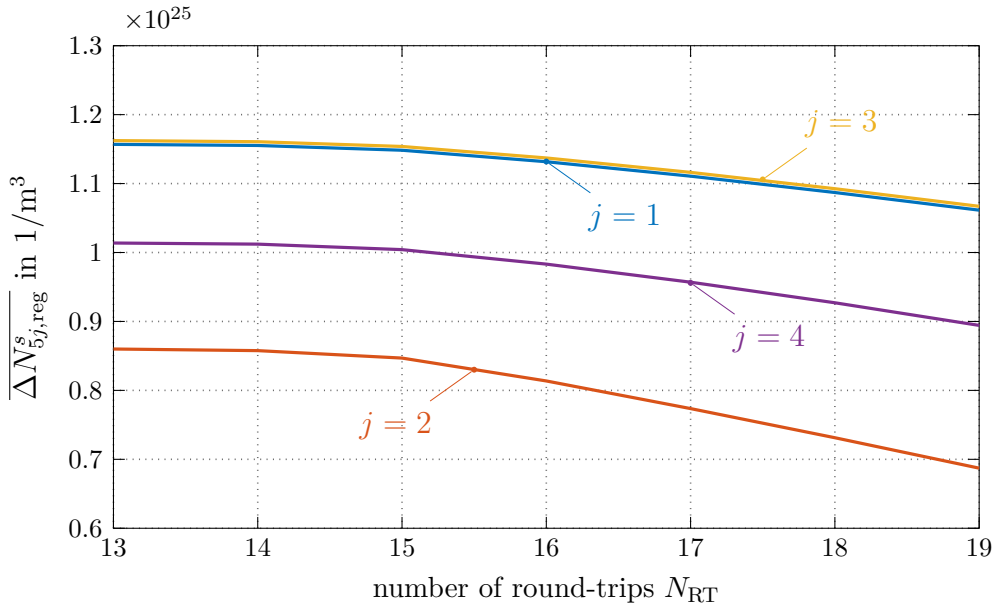

Figure 2.8: Depletion of the mean population inversion $\overline{\Delta N^s_{5j,\text{out}}}$ due to increased power extraction (see Figure 2.7 and Figure 2.6).

Die approbierte Originalversion dieser Dissertation ist in der TU Wien Bibliothek verfügbar.
The approved original version of this doctoral thesis is available at the TU Wien Bibliothek.
TU Bibliothek WIEN Your knowledge hub

this steady state can only be calculated by iterative simulations which is quite time consuming and can only be accomplished by using tailored numerical methods as presented in Appendix B.

The proposed mathematical model for CPAs combines a number of interesting and challenging properties: First of all, the pulse propagation is governed by the antagonistic effects of dispersion and self-steepening due to the nonlinear Schrödinger equation (2.23). CPA systems naturally exhibit a high-gain behavior with a strongly inhomogeneous gain characteristic (see Figure 2.6) that is saturating due to the finite energy stored in the upper energy state. Since the gain characteristic involves several atomic transitions, this saturation effect is acting in a spectrally inhomogeneous fashion - an effect known as spectral hole burning (see, e.g., [29, 30]). The regeneration period is typically not sufficient to fully recover the depleted population inversion. As a result, the gain of the current pulse depends on the amount of energy extracted by the previous pulses. While this is the root cause for the depletion of the steady-state mean spatial population inversion in Figure 2.8, the resulting inter-pulse coupling can be quite significant and – depending on the chosen parameter values – lead to an unstable or even chaotic behavior [31, 67] of the CPA.

Die approbierte Originalversion dieser Dissertation ist in der TU Wien Bibliothek verfügbar.
The approved original version of this doctoral thesis is available at the TU Wien Bibliothek.
TU Bibliothek WIEN Your knowledge hub

Die approbierte Originalversion dieser Dissertation ist in der TU Wien Bibliothek verfügbar.
The approved original version of this doctoral thesis is available at the TU Wien Bibliothek.

CHAPTER 3

Stochastic Iterative Learning Control for Lumped- and Distributed-Parameter Systems: A Wiener-Filtering Approach

The previous chapter presented a detailed mathematical model of CPA system, which we intend to use as a basis for developing suitable control algorithms. Given the problem structure, the measured output pulses should be employed to iteratively correct the current input pulse such that the output pulses converge to a desired pulse shape. From a control engineering perspective, this is a classical task of iterative learning control (ILC) algorithms.

While the last decades of research on ILC algorithms have led to a large number of different concepts, as detailed in Chapter 1, most contributions on ILC focus on certain classes of lumped-parameter systems (LPSs) described by ordinary differential equations (ODEs). The existing literature on ILC for distributed-parameter systems (DPSs) relies either on model-free ILC versions like D-type and PD-type ILC, as presented in [51, 68–70], or on non-constructive concepts as shown in [71]. As a result, an ILC approach directly applicable to DPSs such as the mathematical model derived in the previous chapter is required. Although the mathematical model of the CPA is inherently nonlinear, we restrict ourselves to general linear systems. This can be justified by the fact that it is usually sufficient to use linear models when learning in the vicinity of an operating point. Additionally, one can hope to keep the required computational effort acceptably low.

All types of ILC algorithms try to perform some kind of approximate inversion of the input-output behavior of the system. Since this inversion has to be performed online based on measurements, it is inherently constrained by the presence of stochastic quantities such as process disturbances and measurement

Die approbierte Originalversion dieser Dissertation ist in der TU Wien Bibliothek verfügbar.
The approved original version of this doctoral thesis is available at the TU Wien Bibliothek.
TU WIEN Bibliothek Your knowledge hub

noise. Thus, this chapter systematically investigates minimum mean square error (MMSE) optimal solutions to the iterative learning problem in a stochastic setting applicable to lumped- and distributed-parameter systems.

Following this idea ultimately leads to non-causal Wiener-filters introduced in [72] for the single-input-single-output (SISO) case, which are commonly used in image processing and image restoration, see, e.g., [73], or deconvolution applications as in [74]. The resulting learning law is a generalization of existing stochastically optimal P-type and D-type laws [75–77]. It can be interpreted as a systematic dual to traditional norm-optimal ILC designs that shares their convergence properties but achieves superior asymptotic behavior under stochastic perturbations. Since the resulting non-causal Wiener-Hopf equation can be easily solved regardless of the distributed nature of the system, the proposed learning law constitutes a model-based ILC scheme that directly extends to DPSs in a late-lumping sense. Although the proposed approach is applicable to general linear systems, we restrict ourselves to time-invariant systems for simplicity.

The structure of this chapter is as follows: after the problem setting under consideration is stated in more detail in Section 3.1, a stochastical MMSE optimal learning operator is derived in Section 3.2. The resulting Wiener-filter-based learning operator requires knowledge of the stochastic properties of the input error, which can either be calculated to yield the fully optimal result or roughly estimated by a-priori knowledge to achieve a sub-optimal result. Both approaches are analyzed in Section 3.3 and a simple and efficient numerical solution procedure is presented in Section 3.4. The resulting algorithms are finally evaluated in simulation scenarios for finite- and infinite-dimensional systems in Section 3.5.

In the following, we will make use of the bilateral Laplace transform [74]

$$f(s) = \mathcal{B}\left\{f(t)\right\} = \int_{-\infty}^{\infty} f(t)\exp(-st)\mathrm{d}t \tag{3.1}$$

for all s inside the region of convergence (ROC). If the imaginary axis is included in the ROC, the bilateral Laplace transform is linked to the Fourier transform by $f(s)|_{s=j\omega} = \mathcal{F}\left\{f(t)\right\}$. For two vector-valued stochastic signals $\mathbf{a}^k(t)$ and $\mathbf{b}^l(t)$ with the iteration indices k and l, their cross-correlation function is given by $\mathbf{R}_{a^k b^l}(\tau) = \mathrm{E}\Big\{\mathbf{a}^k(t+\tau)(\mathbf{b}^l(t))^{\mathrm{T}}\Big\}$ where $\mathrm{E}\{\cdot\}$ denotes the expectation operator. The corresponding power spectral density (PSD) reads as $\mathbf{S}_{a^k b^l}(s) = \mathcal{B}\left\{\mathbf{R}_{a^k b^l}(\tau)\right\}$. In case $k = l$, the common index is written as superscript, i.e., $\mathbf{R}^k_{ab}(\tau) = \mathbf{R}_{a^k b^k}(\tau)$ and $\mathbf{S}^k_{ab}(s) = \mathbf{S}_{a^k b^k}(s)$.

3.1 Problem statement

For this chapter, we consider a general class of L^2-stable continuous-time linear systems of potentially distributed character formally described by the input operator $\boldsymbol{\mathcal{G}}_u$ and the disturbance operator $\boldsymbol{\mathcal{G}}_w$. Within an ILC framework, the

Die approbierte Originalversion dieser Dissertation ist in der TU Wien Bibliothek verfügbar.
The approved original version of this doctoral thesis is available at the TU Wien Bibliothek.
TU Bibliothek WIEN Your knowledge hub

iteration k can be described by the input-output relation

$$\mathbf{y}^k(t) = \boldsymbol{\mathcal{G}}_u \mathbf{u}^k(t) + \boldsymbol{\mathcal{G}}_w \mathbf{w}^k(t) + \mathbf{n}^k(t) \tag{3.2}$$

with the system input $\mathbf{u}(t) \in \mathbb{R}^l$, the system output $\mathbf{y}(t) \in \mathbb{R}^m$ and $t \in \mathbb{R}$. The ideal behavior of the plant $\boldsymbol{\mathcal{G}}_u$ is perturbed by exogenous disturbances $\mathbf{w}(t) \in \mathbb{R}^o$ and measurement noise $\mathbf{n}(t) \in \mathbb{R}^m$ which are assumed to be zero-mean wide-sense stationary (WSS) stochastic processes. In the time-invariant case, the input operator $\boldsymbol{\mathcal{G}}_u : L^2(\mathbb{R};\mathbb{R}^l) \to L^2(\mathbb{R};\mathbb{R}^m)$ and the disturbance operator $\boldsymbol{\mathcal{G}}_w : L^2(\mathbb{R};\mathbb{R}^o) \to L^2(\mathbb{R};\mathbb{R}^m)$ can be written as

$$\boldsymbol{\mathcal{G}}_i \mathbf{v}(t) = \int_{-\infty}^{\infty} \mathbf{G}_i(t-\tau)\mathbf{v}(\tau)\mathrm{d}\tau, \quad i \in \{u, w\}, \tag{3.3}$$

with the corresponding impulse response matrices $\mathbf{G}_u(t)$ and $\mathbf{G}_w(t)$.

For a given desired output trajectory $\mathbf{y}^d(t) \in L_2(\mathbb{R};\mathbb{R}^m)$, which is the solution of the unperturbed system

$$\mathbf{y}^d(t) = \boldsymbol{\mathcal{G}}_u \mathbf{u}^d(t), \tag{3.4}$$

with the unknown desired input $\mathbf{u}^d(t)$, we want to iteratively track this desired output trajectory by means of a general linear learning law of the form

$$\mathbf{u}^{k+1}(t) = \mathbf{u}^k(t) + \boldsymbol{\mathcal{L}}^k \boldsymbol{\eta}^k(t), \tag{3.5a}$$

with the output error $\boldsymbol{\eta}^k(t) = \mathbf{y}^d(t) - \mathbf{y}^k(t)$ for the iteration k. The corresponding linear learning operator $\boldsymbol{\mathcal{L}}^k : L^2(\mathbb{R};\mathbb{R}^m) \to L^2(\mathbb{R};\mathbb{R}^l)$ is given by

$$\boldsymbol{\mathcal{L}}^k \boldsymbol{\eta}^k(t) = \int_{-\infty}^{\infty} \mathbf{L}^k(t-\tau)\boldsymbol{\eta}^k(\tau)\mathrm{d}\tau, \tag{3.5b}$$

with the learning kernel $\mathbf{L}^k(t)$. Thus, our goal is to find an optimal learning operator such that the system output asymptotically converges to the desired output, i.e., $\mathbf{y}^k(t) \to \mathbf{y}^d(t)$. Since the system output is a stochastic quantity, we aim at doing this in a stochastically optimal way, i.e. $\mathbf{u}^{k+1}(t)$ should be determined such that it minimizes the expected value of the mean squares output error $\mathrm{E}\left\{\left(\boldsymbol{\eta}^{k+1}(t)\right)^{\mathrm{T}} \boldsymbol{\eta}^{k+1}(t)\right\}$.

3.2 A Wiener-Filtering approach

In view of (3.2) and (3.4), the output error of the iteration k is given by

$$\boldsymbol{\eta}^k(t) = \boldsymbol{\mathcal{G}}_u \boldsymbol{\nu}^k(t) - \boldsymbol{\mathcal{G}}_w \mathbf{w}^k(t) - \mathbf{n}^k(t) \tag{3.6}$$

using the input error $\boldsymbol{\nu}^k(t) = \mathbf{u}^d(t) - \mathbf{u}^k(t)$. Due to the learning law (3.5), the evolution of the input error is described by

$$\boldsymbol{\nu}^{k+1}(t) = \boldsymbol{\nu}^k(t) - \boldsymbol{\mathcal{L}}^k \boldsymbol{\eta}^k(t). \tag{3.7}$$

Die approbierte Originalversion dieser Dissertation ist in der TU Wien Bibliothek verfügbar.
The approved original version of this doctoral thesis is available at the TU Wien Bibliothek.
TU Bibliothek Your knowledge hub WIEN

Thus, the output error of the iteration $k+1$ yields

$$\boldsymbol{\eta}^{k+1}(t) = \left(\boldsymbol{\mathcal{I}} - \boldsymbol{\mathcal{G}}_u \boldsymbol{\mathcal{L}}^k\right) \boldsymbol{\eta}^k(t) + \boldsymbol{\mathcal{G}}_w \mathbf{w}^k(t) - \boldsymbol{\mathcal{G}}_w \mathbf{w}^{k+1}(t) + \mathbf{n}^k(t) - \mathbf{n}^{k+1}(t) \quad (3.8)$$

using the identity operator $\boldsymbol{\mathcal{I}}$. The problem of learning in a stochastically optimal sense can be written as the optimization problem

$$\min_{\boldsymbol{\mathcal{L}}^k} \ \mathrm{E}\left\{\left(\boldsymbol{\eta}^{k+1}(t)\right)^{\mathrm{T}} \boldsymbol{\eta}^{k+1}(t)\right\}. \quad (3.9)$$

Due to the error dynamics (3.6), the stochastic quantities $\boldsymbol{\eta}^k$, $\mathbf{w}^k$ and $\mathbf{n}^k$ appearing on the right-hand side of (3.8) are correlated. Therefore, it is advisable to express $\boldsymbol{\eta}^{k+1}(t)$ as a function of the quantities $\boldsymbol{\nu}^k$, $\mathbf{w}^k$, $\mathbf{w}^{k+1}$, $\mathbf{n}^k$, and $\mathbf{n}^{k+1}$, which yields

$$\begin{aligned}\boldsymbol{\eta}^{k+1}(t) = &\left(\boldsymbol{\mathcal{G}}_u - \boldsymbol{\mathcal{G}}_u \boldsymbol{\mathcal{L}}^k \boldsymbol{\mathcal{G}}_u\right) \boldsymbol{\nu}^k(t) + \boldsymbol{\mathcal{G}}_u \boldsymbol{\mathcal{L}}^k \boldsymbol{\mathcal{G}}_w \mathbf{w}^k(t) \\ &- \boldsymbol{\mathcal{G}}_w \mathbf{w}^{k+1}(t) + \boldsymbol{\mathcal{G}}_u \boldsymbol{\mathcal{L}}^k \mathbf{n}^k(t) - \mathbf{n}^{k+1}(t). \end{aligned} \quad (3.10)$$

Before deriving the optimal solution, we make some reasonable assumptions on the stochastic properties of the measurement noise and the exogenous disturbance:

A1 Instances of the measurement noise from different iterations are uncorrelated, i.e. $\mathrm{E}\left\{\mathbf{n}^i(\mathbf{n}^j)^{\mathrm{T}}\right\} = \mathbf{0}$ for $i \neq j$.

A2 Measurement noise and disturbances are uncorrelated, i.e. $\mathrm{E}\left\{\mathbf{w}^i(\mathbf{n}^j)^{\mathrm{T}}\right\} = \mathbf{0}$ for all i, j.

A3 The input error $\boldsymbol{\nu}^k$ is uncorrelated with the measurement noise and disturbances of the current and the following iteration, i.e. $\mathrm{E}\left\{\boldsymbol{\nu}^k(\mathbf{n}^i)^{\mathrm{T}}\right\} = \mathbf{0}$ and $\mathrm{E}\left\{\boldsymbol{\nu}^k(\mathbf{w}^i)^{\mathrm{T}}\right\} = \mathbf{0}$ for $i \in \{k, k+1\}$.

Remark 8. *While the Assumptions A1 and A2 are standard in the context of Kalman filtering or stochastic ILC (see, e.g., [75, 76]), Assumption A3 essentially truncates the depth of stochastic reasoning. This means that any implicit correlation of the current input error* $\boldsymbol{\nu}^k$ *and the exogenous disturbances* $\mathbf{w}^i$ *with* $i \in \{k, k+1\}$ *due to possible correlations between different instances of the exogenous disturbance in the past, i.e.* $\mathrm{E}\{\mathbf{w}^i(\mathbf{w}^j)^{\mathrm{T}}\} \neq \mathbf{0}$ *with* $i, j < k$ *and* $i \neq j$ *are neglected. If one assumes that* $\mathrm{E}\{\mathbf{w}^i(\mathbf{w}^j)^{\mathrm{T}}\} = \mathbf{0}$ *for* $i \neq j$ *as we will do later in Assumption A4, Assumption A3 is equivalent to* $\mathrm{E}\{\boldsymbol{\nu}^0(\mathbf{w}^i)^{\mathrm{T}}\} = \mathbf{0}$*, which is again quite common in the literature, see, [75, 78].*

Since the system dynamics (3.2) is linear and time invariant and the stochastic quantities $\mathbf{w}^k$ and $\mathbf{n}^k$ are assumed to be WSS, the optimization problem (3.9) can be treated in the Laplace domain (cf. [79]) by applying the bilateral Laplace transform, which yields

$$\min_{\boldsymbol{\mathcal{L}}^k} \ \mathrm{E}\left\{\left(\boldsymbol{\eta}^{k+1}(t)\right)^{\mathrm{T}} \boldsymbol{\eta}^{k+1}(t)\right\} = \min_{\boldsymbol{\mathcal{L}}^k} \mathrm{Tr}\ \left\{\mathbf{R}_{\eta\eta}^{k+1}(0)\right\}$$

Die approbierte Originalversion dieser Dissertation ist in der TU Wien Bibliothek verfügbar.
The approved original version of this doctoral thesis is available at the TU Wien Bibliothek.
TU Bibliothek WIEN Your knowledge hub

$$= \min_{\mathbf{L}^k(s)} \frac{1}{i2\pi} \mathrm{Tr}\left\{ \int_{-i\infty}^{i\infty} \mathbf{S}_{\eta\eta}^{k+1}(s)\mathrm{d}s \right\}, \tag{3.11}$$

where Tr $\{\cdot\}$ denotes the trace operator. In the remainder of this chapter, the Laplace variable s is omitted for brevity unless necessary for the understanding. Due to (3.10) and the assumptions A1 - A3, the PSD of the output error in iteration $(k+1)$ is given by

$$\begin{aligned}\mathbf{S}_{\eta\eta}^{k+1} &= \left(\mathbf{G}_u - \mathbf{G}_u\mathbf{L}^k\mathbf{G}_u\right)\mathbf{S}_{\nu\nu}^k\left(\mathbf{G}_u - \mathbf{G}_u\mathbf{L}^k\mathbf{G}_u\right)^{\mathrm{H}} + \mathbf{G}_w\,\mathbf{S}_{ww}^{k+1}\,\mathbf{G}_w^{\mathrm{H}} \\ &+ \mathbf{G}_u\mathbf{L}^k\mathbf{G}_w\,\mathbf{S}_{ww}^k\,\mathbf{G}_w^{\mathrm{H}}(\mathbf{L}^k)^{\mathrm{H}}\mathbf{G}_u^{\mathrm{H}} + \mathbf{G}_u\mathbf{L}^k\mathbf{S}_{nn}^k(\mathbf{L}^k)^{\mathrm{H}}\mathbf{G}_u^{\mathrm{H}} + \mathbf{S}_{nn}^{k+1} \\ &- \mathbf{G}_u\mathbf{L}^k\mathbf{G}_w\,\mathbf{S}_{w^kw^{k+1}}\,\mathbf{G}_w^{\mathrm{H}} - \mathbf{G}_w\,\mathbf{S}_{w^{k+1}w^k}\,\mathbf{G}_w^{\mathrm{H}}(\mathbf{L}^k)^{\mathrm{H}}\mathbf{G}_u^{\mathrm{H}}\end{aligned} \tag{3.12}$$

with the Hermitian conjugate $(\cdot)^{\mathrm{H}}$. Employing the calculus of variations, the optimization problem (3.11) can be solved analytically by considering the first-order optimality condition, i.e. for the optimal learning kernel $\mathbf{L}^k(s)$ the Gâteaux derivative has to vanish

$$\delta\mathrm{E}\left\{\left(\boldsymbol{\eta}^{k+1}(t)\right)^{\mathrm{T}}\boldsymbol{\eta}^{k+1}(t)\right\} = 0. \tag{3.13}$$

Following the typical variational approach, we substitute $\mathbf{L}^k(s) \to \mathbf{L}^k(s) + \epsilon\boldsymbol{\Gamma}(s)$ into (3.12), whereby $\epsilon\boldsymbol{\Gamma}(s)$ is a small variation of the optimal learning operator $\mathbf{L}^k(s)$. The optimality criterion (3.13) yields after tedious but straightforward computation

$$\begin{aligned}0 = \mathrm{Tr}\Bigg\{ &\int_{-i\infty}^{i\infty} \mathbf{G}_u\boldsymbol{\Gamma}\Big[-\mathbf{G}_u\mathbf{S}_{\nu\nu}^k\left(\mathbf{G}_u - \mathbf{G}_u\mathbf{L}^k\mathbf{G}_u\right)^{\mathrm{H}} + \mathbf{S}_{nn}^k(\mathbf{L}^k)^{\mathrm{H}}\mathbf{G}_u^{\mathrm{H}} \\ &+ \mathbf{G}_w\mathbf{S}_{ww}^k\mathbf{G}_w^{\mathrm{H}}(\mathbf{L}^k)^{\mathrm{H}}\mathbf{G}_u^{\mathrm{H}} - \mathbf{G}_w\mathbf{S}_{w^kw^{k+1}}\mathbf{G}_w^{\mathrm{H}}\Big]\mathrm{d}s + \\ &\int_{-i\infty}^{i\infty}\Big[-\left(\mathbf{G}_u - \mathbf{G}_u\mathbf{L}^k\mathbf{G}_u\right)\mathbf{S}_{\nu\nu}^k\mathbf{G}_u^{\mathrm{H}} + \mathbf{G}_u\mathbf{L}^k\mathbf{S}_{nn}^k \\ &+\mathbf{G}_u\mathbf{L}^k\mathbf{G}_w\mathbf{S}_{ww}^k\mathbf{G}_w^{\mathrm{H}} - \mathbf{G}_w\mathbf{S}_{w^{k+1}w^k}\mathbf{G}_w^{\mathrm{H}}\Big]\boldsymbol{\Gamma}^{\mathrm{H}}\mathbf{G}_u^{\mathrm{H}}\mathrm{d}s\Bigg\}.\end{aligned} \tag{3.14}$$

Since we allow a potentially non-causal solution, $\boldsymbol{\Gamma}(s)$ can vary freely. Using that $\mathrm{Tr}\left(\mathbf{M} + \mathbf{M}^{\mathrm{H}}\right) = 2\,\mathrm{Tr}\left(\mathrm{Re}\left\{\mathbf{M}\right\}\right)$ for any square matrix $\mathbf{M}$ and invoking the fundamental lemma of calculus of variations, the optimal learning operator has to fulfill

$$\mathbf{G}_u\mathbf{L}^k\left[\mathbf{G}_u\mathbf{S}_{\nu\nu}^k\mathbf{G}_u^{\mathrm{H}} + \mathbf{G}_w\mathbf{S}_{ww}^k\mathbf{G}_w^{\mathrm{H}} + \mathbf{S}_{nn}^k\right] = \mathbf{G}_u\mathbf{S}_{\nu\nu}^k\mathbf{G}_u^{\mathrm{H}} + \mathbf{G}_w\mathbf{S}_{w^{k+1}w^k}\mathbf{G}_w^{\mathrm{H}}. \tag{3.15}$$

If the system is square, i.e., $m = l$, and if $\mathbf{G}_u(s)$ is invertible, (3.15) can be solved for $\mathbf{L}^k(s)$ explicitly which yields

$$\mathbf{L}^k = \left(\mathbf{S}_{\nu\nu}^k\mathbf{G}_u^{\mathrm{H}} + \mathbf{G}_u^{-1}\mathbf{G}_w\mathbf{S}_{w^{k+1}w^k}\mathbf{G}_w^{\mathrm{H}}\right)\left[\mathbf{G}_u\mathbf{S}_{\nu\nu}^k\mathbf{G}_u^{\mathrm{H}} + \mathbf{G}_w\mathbf{S}_{ww}^k\mathbf{G}_w^{\mathrm{H}} + \mathbf{S}_{nn}^k\right]^{-1}. \tag{3.16}$$

Die approbierte Originalversion dieser Dissertation ist in der TU Wien Bibliothek verfügbar.
The approved original version of this doctoral thesis is available at the TU Wien Bibliothek.
TU Bibliothek WIEN Your knowledge hub

This type of learning operator takes preemptive actions according to known correlations of the external disturbances given by $\mathbf{S}_{w^{k+1}w^k}$. In practice, a detailed description of the correlation properties of the disturbance $\mathbf{w}$ is hardly known and the constraint that $\mathbf{G}_u(s)$ is invertible drastically limits the scope of the approach. However, there is a more severe implication: The stability of a learning law can be analyzed in the frequency domain using the well known (deterministic) stability criterion [80, 81]

$$\sup_{\omega} \bar{\rho}\left\{\mathbf{I} - \mathbf{G}_u(i\omega)\mathbf{L}(i\omega)\right\} < 1, \tag{3.17}$$

where $\bar{\rho}$ denotes the eigenvalue with the largest absolute value, i.e. the spectral radius. Plugging the general learning operator (3.16) into (3.17), one can easily see that its spectral radius is not necessarily less than one for arbitrary $\mathbf{S}_{w^{k+1}w^k}$. The fact that the learning operator (3.16) does not *necessarily* fulfill the stability condition (3.17) does not imply that the output error PSD may not converge to some finite limit $\mathbf{S}^{\infty}_{\eta\eta}(s) = \lim_{k\to\infty} \mathbf{S}^{k}_{\eta\eta}(s)$ in the nominal case. However, imperfect knowledge of the stochastic properties can destabilize the learning law (3.16), which is not acceptable for robustness reasons. Thus, we neglect correlations of the stochastic disturbances by assuming that

A4 different instances of the disturbance are uncorrelated, i.e. $\mathrm{E}\left\{\mathbf{w}^i(\mathbf{w}^j)^{\mathrm{T}}\right\} = \mathbf{0}$ for $i \neq j$

to obtain the iteration-varying learning operator

$$\mathbf{L}^k = \mathbf{S}^k_{\nu\nu}\mathbf{G}^{\mathrm{H}}_u\left[\mathbf{G}_u\mathbf{S}^k_{\nu\nu}\mathbf{G}^{\mathrm{H}}_u + \mathbf{G}_w\mathbf{S}^k_{ww}\mathbf{G}^{\mathrm{H}}_w + \mathbf{S}^k_{nn}\right]^{-1}. \tag{3.18}$$

The type of solution (3.18) for uncorrelated disturbances is in fact well known in the context of linear filtering problems [74]. By transforming the optimal filter $\mathbf{L}^k(s)$ back into the time domain, one obtains the non-causal Wiener-Hopf equation

$$\int_{-\infty}^{\infty} \mathbf{L}^k(\xi)\mathbf{R}^k_{\eta\eta}(\tau-\xi)\mathrm{d}\xi = \mathbf{R}^k_{\nu\eta}(\tau), \tag{3.19}$$

with the auto-correlation function of the output error

$$\mathbf{R}^k_{\eta\eta}(\tau) = \mathcal{B}^{-1}\left\{\mathbf{G}_u\mathbf{S}^k_{\nu\nu}\mathbf{G}^{\mathrm{H}}_u + \mathbf{G}_w\mathbf{S}^k_{ww}\mathbf{G}^{\mathrm{H}}_w + \mathbf{S}^k_{nn}\right\} \tag{3.20}$$

and the cross-correlation function between input error and output error

$$\mathbf{R}^k_{\nu\eta}(\tau) = \mathcal{B}^{-1}\{\mathbf{S}^k_{\nu\nu}\mathbf{G}^{\mathrm{H}}_u\}. \tag{3.21}$$

Thus, the proposed approach can be understood as the systematic dual to traditional norm-optimal ILC methods, as one is effectively using a non-causal Wiener-filter to *estimate* the input deviation that optimally *explains* the measured output error.

Die approbierte Originalversion dieser Dissertation ist in der TU Wien Bibliothek verfügbar.
The approved original version of this doctoral thesis is available at the TU Wien Bibliothek.
TU Bibliothek WIEN Your knowledge hub

3.3 Choosing the input error PSD

A common problem of Wiener-filter-based approaches is that the optimal solution (3.18) requires knowledge of the input error PSD $\mathbf{S}_{\nu\nu}^k(s)$, which is typically handled using a-priori knowledge of the problem. In the case of ILC, however, the iterative structure of the learning problem can be exploited to obtain an estimate of the current PSD. In the following, two approaches will be presented: first, by assuming a fixed input error PSD, a stochastically sub-optimal but iteration-invariant learning operator is obtained. Second, a forward prediction of the current input error PSD yields an optimal but iteration-varying learning operator.

For the following analysis, the stochastic properties of $\mathbf{w}^k$ and $\mathbf{n}^k$ are assumed independent of the iteration index k, i.e., $\mathbf{S}_{ww}^k(s) = \mathbf{S}_{ww}(s)$ and $\mathbf{S}_{nn}^k(s) = \mathbf{S}_{nn}(s)$ for all k.

3.3.1 A sub-optimal iteration-invariant learning law

As highlighted above, the stochastically optimal learning operator (3.18) depends on the expected input error, i.e., the input error PSD $\mathbf{S}_{\nu\nu}^k(s)$, which is generally unknown. Since iteration-varying learning laws usually increase the effort of implementation, one may prefer to accept the sub-optimal performance of an iteration-invariant learning law by using a fixed input error PSD $\mathbf{S}_{\nu\nu}^k(s) = \mathbf{S}_{\nu\nu}(s)$ according to a-priori knowledge. This yields the iteration-invariant learning operator

$$\mathbf{L} = \mathbf{S}_{\nu\nu}\mathbf{G}_u^{\mathrm{H}}\left[\mathbf{G}_u\mathbf{S}_{\nu\nu}\mathbf{G}_u^{\mathrm{H}} + \mathbf{G}_w\mathbf{S}_{ww}\mathbf{G}_w^{\mathrm{H}} + \mathbf{S}_{nn}\right]^{-1}. \tag{3.22}$$

The following theorem ensures under mild conditions that the resulting iteration is stable.

Theorem 1. *If $\mathbf{\Phi} = \mathbf{G}_w\mathbf{S}_{ww}\mathbf{G}_w^{\mathrm{H}} + \mathbf{S}_{nn}$ and the chosen input error PSD $\mathbf{S}_{\nu\nu}$ are positive definite and the system transfer matrix $\mathbf{G}_u(s)$ does not exhibit transmission zeros on the imaginary axis $s = i\omega$, i.e. if $\mathbf{G}_u(i\omega)\mathbf{u} \neq \mathbf{0}$ for any $\mathbf{u} \neq \mathbf{0}$ and all frequencies ω, the learning operator (3.22) yields a stable learning iteration that converges to an asymptotic ouput error PSD $\mathbf{S}_{\eta\eta}^\infty$ given by the solution of*

$$(\mathbf{I}-\mathbf{G}_u\mathbf{L})\,\mathbf{S}_{\eta\eta}^\infty\,(\mathbf{I}-\mathbf{G}_u\mathbf{L})^{\mathrm{H}} - \mathbf{S}_{\eta\eta}^\infty + \mathbf{G}_u\mathbf{L}\mathbf{\Phi} + \mathbf{\Phi}\mathbf{L}^{\mathrm{H}}\mathbf{G}_u^{\mathrm{H}} = \mathbf{0}. \tag{3.23}$$

Proof. Using the definition of the sub-optimal learning operator (3.22) yields

$$\mathbf{I} - \mathbf{G}_u\mathbf{L} = \mathbf{I} - \mathbf{G}_u\mathbf{S}_{\nu\nu}\mathbf{G}_u^{\mathrm{H}}\left[\mathbf{G}_u\mathbf{S}_{\nu\nu}\mathbf{G}_u^{\mathrm{H}} + \mathbf{\Phi}\right]^{-1} = \mathbf{\Phi}\left[\mathbf{G}_u\mathbf{S}_{\nu\nu}\mathbf{G}_u^{\mathrm{H}} + \mathbf{\Phi}\right]^{-1}. \tag{3.24}$$

Since $\mathbf{\Phi}$ is positive definite by assumption, there exists a square root $\mathbf{\Phi}^{1/2}$ that is positive definite and therefore

$$\mathbf{I} - \mathbf{G}_u\mathbf{L} = \mathbf{\Phi}^{1/2}\left[\mathbf{\Psi} + \mathbf{I}\right]^{-1}\mathbf{\Phi}^{-1/2}, \tag{3.25}$$

Die approbierte Originalversion dieser Dissertation ist in der TU Wien Bibliothek verfügbar.
The approved original version of this doctoral thesis is available at the TU Wien Bibliothek.
TU Bibliothek Your knowledge hub WIEN

with $\mathbf{\Psi} = \mathbf{\Phi}^{-1/2}\mathbf{G}_u\mathbf{S}_{\nu\nu}\mathbf{G}_u^{\mathrm{H}}\mathbf{\Phi}^{-1/2}$. As $\mathbf{G}_u$ does not exhibit transmission zeros, $\mathbf{\Psi}$ is positive definite and it follows that

$$\sup_{\omega} \bar{\rho}\left(\mathbf{I} - \mathbf{G}_u\mathbf{L}\right) = \sup_{\omega} \bar{\rho}\left(\left(\mathbf{\Psi} + \mathbf{I}\right)^{-1}\right) = \sup_{\omega} \left(\underline{\rho}\left(\mathbf{\Psi} + \mathbf{I}\right)\right)^{-1} < 1, \tag{3.26}$$

where $\underline{\rho}$ denotes the smallest eigenvalue. Thus, the sub-optimal learning law satisfies the deterministic stability condition (3.17). Additionally, the iteration of the output error PSD (cf. (3.8))

$$\mathbf{S}_{\eta\eta}^{k+1} = \left(\mathbf{I} - \mathbf{G}_u\mathbf{L}\right)\mathbf{S}_{\eta\eta}^{k}\left(\mathbf{I} - \mathbf{G}_u\mathbf{L}\right)^{\mathrm{H}} + \mathbf{G}_u\mathbf{L}\mathbf{\Phi} + \mathbf{\Phi}\mathbf{L}^{\mathrm{H}}\mathbf{G}_u^{\mathrm{H}} \tag{3.27}$$

converges to a unique asymptotic output error PSD $\mathbf{S}_{\eta\eta}^{\infty}$ given by the discrete Lyapunov-type equation (3.23).

□

Remark 9. *The limitation of transmission zeros is always violated at $\omega \to \infty$ for strictly proper systems. This is a necessary consequence of the optimality principle of the Wiener-filter, since for systems with low-pass characteristics it should be avoided to learn high frequencies. This is hardly a problem in practice as one is typically interested in a limited frequency range, as considered in [71]. Alternatively, the feedback operator can be modified such that it includes a small feedthrough term as suggested in [82].*

The learning operator (3.22) is structurally similar to feedforward norm-optimal ILC. Contrary to the presented approach, norm-optimal schemes are typically set up in a finite-horizon framework. Applying a limit argument as used in [83, 84] for comparison, one obtains a frequency-domain representation of feedforward norm-optimal learning laws in the form

$$\mathbf{L}(s) = \left[\mathbf{R} + \mathbf{G}_u^{\mathrm{H}}(s)\mathbf{Q}\mathbf{G}_u(s)\right]^{-1}\mathbf{G}_u^{\mathrm{H}}(s)\mathbf{Q}, \tag{3.28}$$

where $\mathbf{Q}$ is the weighting matrix of the output error and $\mathbf{R}$ is the weighting matrix of the input difference $\mathbf{u}^{k+1}(t) - \mathbf{u}^{k}(t)$ (see, e.g., [85, 86]). For the special case $\mathbf{S}_{\nu\nu}(s) = \sigma_\nu\mathbf{I}$ and $\mathbf{\Phi}(s) = \mathbf{G}_w(s)\mathbf{S}_{ww}(s)\mathbf{G}_w^{\mathrm{H}}(s) + \mathbf{S}_{nn}(s) = \sigma_\Phi\mathbf{I}$, one can easily show that (3.22) is equivalent to (3.28) for $\mathbf{R} = \sigma_R\mathbf{I}$ and $\mathbf{Q} = \sigma_Q\mathbf{I}$ with[1] $\sigma_\nu\sigma_R = \sigma_\Phi\sigma_Q$. In other words: if all components of the stochastic perturbations at iteration k are uncorrelated and of equal noise power and if no information about the input signal is available, Wiener-filter-based learning laws and norm-optimal learning laws are equivalent. Both implement a kind of (Tikhonov-) regularized inversion of the system operator $\mathbf{G}_u$. This idea is directly addressed in [82] by using a pseudo-inverse learning law that can be written as

$$\mathbf{L}(s) = \left[\alpha\mathbf{I} + \mathbf{G}_u^{\mathrm{H}}(s)\mathbf{G}_u(s)\right]^{-1}\mathbf{G}_u^{\mathrm{H}}(s), \tag{3.29}$$

[1] Note the different dimensions of the matrices $\mathbf{R}$, $\mathbf{S}_{\nu\nu}(s) \in \mathbb{R}^{l\times l}$ and $\mathbf{Q}$, $\mathbf{\Phi}(s) \in \mathbb{R}^{m\times m}$.

Die approbierte Originalversion dieser Dissertation ist in der TU Wien Bibliothek verfügbar.
The approved original version of this doctoral thesis is available at the TU Wien Bibliothek.
TU Bibliothek WIEN Your knowledge hub

which is again equivalent to (3.22) and (3.28) for $\alpha = {}^{\sigma_\Phi}/_{\sigma_\nu} = {}^{\sigma_R}/_{\sigma_Q}$.

As one can see from (3.29) and (3.28), norm-optimal schemes introduce regularization by penalizing variations of the input and thus reduce the effective speed of learning - which is somewhat artificial. In contrast, the Wiener-filter-based learning operator (3.22) is regularizing according to the expected output PSD of the perturbations, i.e. $\mathbf{\Phi} = \mathbf{G}_w \mathbf{S}_{ww} \mathbf{G}_w^{\mathrm{H}} + \mathbf{S}_{nn}$. This is exactly what one would expect: learning is avoided when the stochastic perturbations are strong compared to the expected signal components $\mathbf{G}_u \mathbf{S}_{\nu\nu} \mathbf{G}_u^{\mathrm{H}}$.

From a practical point of view, the Wiener-filtering-based approach has two significant benefits: first, one is not bothered with tuning unphysical weighting matrices but rather guided by experimentally accessible quantities. Second, the spectral shaping due to the choice of $\mathbf{S}_{\nu\nu}$ is often appreciated to easily restrict learning to certain frequency ranges or to systematically account for a varying accuracy of the process model $\mathbf{G}_u$ in different frequency ranges.

3.3.2 An optimal iteration-varying learning law

As the measured output error $\boldsymbol{\eta}^k(t)$ decreases due to the action of the learning operator, it is increasingly dominated by stochastic disturbances. Therefore, a stochastically optimal learning law will reduce its learning behavior with increasing iterations (see [75]). Such a behavior is intrinsic to the general solution (3.18) due to the decreasing input error PSD $\mathbf{S}_{\nu\nu}^k$. Because of

$$\boldsymbol{\nu}^{k+1}(t) = \left(\boldsymbol{\mathcal{I}} - \boldsymbol{\mathcal{L}}^k \boldsymbol{\mathcal{G}}_u\right) \boldsymbol{\nu}^k(t) - \boldsymbol{\mathcal{L}}^k \boldsymbol{\mathcal{G}}_w \mathbf{w}^k(t) - \boldsymbol{\mathcal{L}}^k \mathbf{n}^k(t) \tag{3.30}$$

cf. (3.6) and (3.7), one can calculate the evolution of the expected input error PSD in the form

$$\mathbf{S}_{\nu\nu}^{k+1} = \left(\mathbf{I} - \mathbf{L}^k \mathbf{G}_u\right) \mathbf{S}_{\nu\nu}^k \left(\mathbf{I} - \mathbf{L}^k \mathbf{G}_u\right)^{\mathrm{H}} + \mathbf{L}^k \left(\mathbf{G}_w \mathbf{S}_{ww} \mathbf{G}_w^{\mathrm{H}} + \mathbf{S}_{nn}\right) (\mathbf{L}^k)^{\mathrm{H}}. \tag{3.31}$$

Thus, only an initial PSD $\mathbf{S}_{\nu\nu}^0$ is required and the following PSDs can be updated according to the equation above. Using the proposed learning operator (3.18) under the assumption of iteration-independent stochastic properties of $\mathbf{w}^k$ and $\mathbf{n}^k$, i.e.

$$\mathbf{L}^k = \mathbf{S}_{\nu\nu}^k \mathbf{G}_u^{\mathrm{H}} \left[\mathbf{G}_u \mathbf{S}_{\nu\nu}^k \mathbf{G}_u^{\mathrm{H}} + \mathbf{G}_w \mathbf{S}_{ww} \mathbf{G}_w^{\mathrm{H}} + \mathbf{S}_{nn}\right]^{-1}, \tag{3.32a}$$

and plugging it into the forward iteration (3.31) results in

$$\begin{aligned}
\mathbf{S}_{\nu\nu}^{k+1} &= \mathbf{S}_{\nu\nu}^k - 2\mathbf{S}_{\nu\nu}^k \mathbf{G}_u^{\mathrm{H}} (\mathbf{G}_u \mathbf{S}_{\nu\nu}^k \mathbf{G}_u^{\mathrm{H}} + \mathbf{\Phi})^{-1} \mathbf{G}_u \mathbf{S}_{\nu\nu}^k \\
&\quad + \mathbf{S}_{\nu\nu}^k \mathbf{G}_u^{\mathrm{H}} (\mathbf{G}_u \mathbf{S}_{\nu\nu}^k \mathbf{G}_u^{\mathrm{H}} + \mathbf{\Phi})^{-1} \mathbf{G}_u \mathbf{S}_{\nu\nu}^k \mathbf{G}_u^{\mathrm{H}} (\mathbf{G}_u \mathbf{S}_{\nu\nu}^k \mathbf{G}_u^{\mathrm{H}} + \mathbf{\Phi})^{-1} \mathbf{G}_u \mathbf{S}_{\nu\nu}^k \\
&\quad + \mathbf{S}_{\nu\nu}^k \mathbf{G}_u^{\mathrm{H}} (\mathbf{G}_u \mathbf{S}_{\nu\nu}^k \mathbf{G}_u^{\mathrm{H}} + \mathbf{\Phi})^{-1} \mathbf{\Phi} (\mathbf{G}_u \mathbf{S}_{\nu\nu}^k \mathbf{G}_u^{\mathrm{H}} + \mathbf{\Phi})^{-1} \mathbf{G}_u \mathbf{S}_{\nu\nu}^k \\
&= \left(\mathbf{I} - \mathbf{L}^k \mathbf{G}_u\right) \mathbf{S}_{\nu\nu}^k,
\end{aligned} \tag{3.32b}$$

Die approbierte Originalversion dieser Dissertation ist in der TU Wien Bibliothek verfügbar.
The approved original version of this doctoral thesis is available at the TU Wien Bibliothek.
TU WIEN Bibliothek Your knowledge hub

with $\mathbf{\Phi} = \mathbf{G}_w \mathbf{S}_{ww} \mathbf{G}_w^{\mathrm{H}} + \mathbf{S}_{nn}$. Due to the dependence of the learning operator on $\mathbf{S}_{\nu\nu}^k$, (3.32b) is a nonlinear iteration. The following theorem shows that the learning operator (3.32a) with (3.32b) is stable and additionally that $\mathbf{u}^k(t) \to \mathbf{u}^d(t)$ in a stochastic sense, i.e. $\lim_{k\to\infty} \mathbf{S}_{\nu\nu}^k = \mathbf{0}$.

Theorem 2. *If $\mathbf{\Phi} = \mathbf{G}_w \mathbf{S}_{ww} \mathbf{G}_w^{\mathrm{H}} + \mathbf{S}_{nn}$ and the initial input error PSD $\mathbf{S}_{\nu\nu}^0$ are positive definite and the system's transfer matrix $\mathbf{G}_u$ does not exhibit transmission zeros on the imaginary axis (see Theorem 1), the learning operator (3.32a) together with (3.32b) yields a stable learning law that ensures convergence to the optimal error PSDs*

$$\mathbf{S}_{\nu\nu}^{\infty} = \mathbf{0}, \quad \mathbf{S}_{\eta\eta}^{\infty} = \mathbf{G}_w \mathbf{S}_{ww} \mathbf{G}_w^{\mathrm{H}} + \mathbf{S}_{nn}. \tag{3.33}$$

Proof. First, we show by induction that $\mathbf{S}_{\nu\nu}^k$ is positive definite and that

$$\sup_{\omega} \bar{\rho}\left(\mathbf{I} - \mathbf{L}^k \mathbf{G}_u\right) < 1 \tag{3.34}$$

for all $k \in \mathbb{N}$. Assume that $\mathbf{S}_{\nu\nu}^k$ is positive definite. Due to the structure of (3.31), $\mathbf{S}_{\nu\nu}^{k+1}$ is necessarily positive semi-definite. To analyze the eigenvalues of $\mathbf{I} - \mathbf{L}^k \mathbf{G}_u$, we use the identity (see Appendix D)

$$\mathbf{I} - \mathbf{L}^k \mathbf{G}_u = \left[\mathbf{I} + \mathbf{S}_{\nu\nu}^k \mathbf{G}_u^{\mathrm{H}} \left(\mathbf{G}_w \mathbf{S}_{ww} \mathbf{G}_w^{\mathrm{H}} + \mathbf{S}_{nn}\right)^{-1} \mathbf{G}_u\right]^{-1}. \tag{3.35}$$

The matrix $\mathbf{G}_u^{\mathrm{H}} \left(\mathbf{G}_w \mathbf{S}_{ww} \mathbf{G}_w^{\mathrm{H}} + \mathbf{S}_{nn}\right)^{-1} \mathbf{G}_u$ is positive definite due to the assumptions made. Although the product of positive definite matrices is not necessarily positive definite again, it is still true that the eigenvalues of the product are greater than zero, i.e. $\underline{\rho}\left(\mathbf{S}_{\nu\nu}^k \mathbf{G}_u^{\mathrm{H}} (\mathbf{G}_w \mathbf{S}_{ww} \mathbf{G}_w^{\mathrm{H}} + \mathbf{S}_{nn})^{-1} \mathbf{G}_u\right) > 0$. Thus $\mathbf{I} - \mathbf{L}^k \mathbf{G}_u$ has full rank and (3.34) holds true by the same line of reasoning as in Theorem 1. The full-rank property of $\mathbf{I} - \mathbf{L}^k \mathbf{G}_u$ implies that $\mathbf{S}_{\nu\nu}^{k+1}$ is indeed positive definite again which - since $\mathbf{S}_{\nu\nu}^0$ is positive definite - finishes the induction.

While all eigenvalues of $\mathbf{I} - \mathbf{L}^k \mathbf{G}_u$ are necessarily less than one, they approach one as $\mathbf{L}^k$ tends to zero for $k \to \infty$. Thus, the limit of $\mathbf{S}_{\nu\nu}^k$ has to be analyzed more carefully. Since all eigenvalues are inside the unit circle for all k, there exists a norm such that $\left\|\mathbf{I} - \mathbf{L}^k \mathbf{G}_u\right\| < 1$ and thus we know that

$$\left\|\mathbf{S}_{\nu\nu}^{k+1}\right\| < \left\|\mathbf{S}_{\nu\nu}^k\right\|. \tag{3.36}$$

Together with the lower bound $\|\mathbf{S}_{\nu\nu}^k\| > 0$ it is clear that there exists a limit $\|\mathbf{S}_{\nu\nu}^{\infty}\|$, and in the following we want to show that this limit equals zero by contradiction. Assuming that $\mathbf{S}_{\nu\nu}^{\infty} \neq \mathbf{0}$ implies that all eigenvalues of $\mathbf{I} - \mathbf{L}^k \mathbf{G}_u$ are inside the unit circle in the limit. In this case

$$\lim_{k\to\infty} \sup_{\omega} \frac{\|\mathbf{S}_{\nu\nu}^{k+1}\|}{\|\mathbf{S}_{\nu\nu}^k\|} < 1 \tag{3.37}$$

Die approbierte Originalversion dieser Dissertation ist in der TU Wien Bibliothek verfügbar.
The approved original version of this doctoral thesis is available at the TU Wien Bibliothek.
TU WIEN Bibliothek Your knowledge hub

and thus $\|\mathbf{S}_{\nu\nu}^{\infty}\| = 0$, which contradicts the assumption. Thus, it follows that $\mathbf{S}_{\nu\nu}^{k}$ converges indeed to zero for $k \to \infty$ and that the input error converges to zero in mean. As a consequence, the learning kernel $\mathbf{L}^k$ also converges to zero. In view of (3.12), the output error PSD then converges to the minimal asymptotic error

$$\lim_{k\to\infty} \mathbf{S}_{\eta\eta}^{k} = \mathbf{S}_{\eta\eta}^{\infty} = \mathbf{G}_w \mathbf{S}_{ww} \mathbf{G}_w^{\mathrm{H}} + \mathbf{S}_{nn}. \tag{3.38}$$

□

Remark 10. *Sharing the common MMSE framework, the proof in Theorem 2 proceeds along the lines of the convergence proof presented in [75] for a stochastic discrete-time D-type law although the quantities involved have considerably different meaning. Due to the stochastically optimal nature, both learning laws show the same behavior of reducing the learning rate as the estimated error decreases.*

Remark 11. *It is noted occasionally (e.g., [87]) that there exists a stochastic trade-off for ILC concepts: one has to choose between high convergence rate on the one hand and low asymptotic errors on the other hand. We want to stress that this is only true for iteration-invariant learning operators as presented in Section 3.3.1, where the asymptotic output error is only sub-optimal as given in (3.23). For iteration-varying learning laws, this restriction does not apply and a minimal asymptotic output error can be achieved. Even more impressive, the asymptotic input error PSD vanishes (see (3.33)) due to the iterative nature of the learning process.*

3.4 Numerical implementation of the learning law

Solutions of the non-causal Wiener-Hopf equation (3.19) can be obtained with standard methods for integral equations like straightforward discretization or using a finite number of basis functions. In the linear time-invariant case, however, both the learning operator and the plant have comparatively simple descriptions in the Laplace domain compared to the time domain. In the following, we want to use this fact to find numerical solutions of the learning kernel $\mathbf{L}(t)$.

Based on the assumption that the system (3.2) is L_2-stable, there exists some $\varepsilon > 0$ such that the region of convergence (ROC) of $\mathbf{G}_u(s)$ and $\mathbf{G}_w(s)$ includes all s with $\mathrm{Re}\{s\} > -\varepsilon$ (cf. [88]). Conversely, for the adjoint systems $\mathbf{G}_u^{\mathrm{H}}(s)$ and $\mathbf{G}_w^{\mathrm{H}}(s)$, it holds that the stable ROC (cf. backward integration) includes all s with $\mathrm{Re}\{s\} < \varepsilon$. Hence, the imaginary axis $i\omega$ is included in the ROC associated with the learning operator $\mathbf{L}(s)$. As a result, the learning kernel $\mathbf{L}(t)$ can be obtained by the inverse Fourier transform

$$\mathbf{L}(t) = \mathcal{F}^{-1}\left\{\mathbf{L}(i\omega)\right\}, \tag{3.39}$$

Die approbierte Originalversion dieser Dissertation ist in der TU Wien Bibliothek verfügbar.
The approved original version of this doctoral thesis is available at the TU Wien Bibliothek.
TU Bibliothek WIEN Your knowledge hub

which is equivalent to forward integration of the stable part and backward integration of the unstable part (see [89, 90]).

The continuous Fourier transform is often approximately computed using the discrete Fourier transform (DFT) on a discrete grid. Since a discretization of t or ω determines a discretization of the other quantity, a spectrally broad operator $\mathbf{L}(i\omega)$ usually requires a high number of sampling points although $\mathbf{L}(t)$ is (almost) zero at most sampling points.

A simple solution to this problem building on a so-called "fractional Fourier transform" is given in [91]. Assuming that $\mathbf{L}(i\omega)$ is zero outside the finite interval $[-\omega_S/2, \omega_S/2]$, the relation (3.39) can be approximately solved for $t \in [-t_S/2, t_S/2]$ on the discrete grid $t_n = (n - N/2)\beta$ and $\omega_m = (m - N/2)\gamma$ with $0 \leq m, n < N$ by

$$\begin{aligned}\mathbf{L}(t_n) &= \frac{1}{2\pi}\int_{-\omega_S/2}^{\omega_S/2} \mathbf{L}(i\omega)\mathrm{e}^{i\omega t_n}\mathrm{d}\omega \\ &\approx \frac{\gamma}{2\pi}\mathrm{e}^{-i\pi(n-N/2)N\delta}\sum_{m=0}^{N-1}\mathbf{L}(i\omega_m)\mathrm{e}^{-i2\pi\delta m(n-N/2)} \\ &= \frac{\gamma}{2\pi}\mathrm{e}^{-i\pi(n-N/2)N\delta}G_n\left\{\mathbf{L}(i\omega_m)\mathrm{e}^{-i\pi mN\delta}, -\delta\right\}\end{aligned} \tag{3.40}$$

where $\beta = t_S/N$, $\gamma = \omega_S/N$ and $\delta = \beta\gamma/(2\pi)$. The operator G_n denotes the n-th element of the "fractional Fourier transform" evaluated by means of the DFT as given in[2] [91, eq. (14)-(18)]. Using fast Fourier transform (FFT) algorithms, this procedure can be computed very efficiently.

Remark 12. *For infinite-dimensional systems, such as systems with delays, the learning kernel may not be centered around $t = 0$. In this case, the above scheme can be modified as described in [91] to further decrease the computational effort.*

This approach is particularly interesting for distributed-parameter systems, where inversion- or model-based ILC schemes have been discarded in many contributions (e.g., [51, 69]) due to their potential complexity. Using (3.40), one can compute the desired learning kernel $\mathbf{L}(t)$ with arbitrary precision regardless of the distributed nature. This is due to the chosen input-output description of the system (3.2) and (3.3) that is independent of the dimension of the state space, whether it is finite- or infinite-dimensional. Thus, one avoids the computational tasks which typically arise in established state-space approaches [92, 93], such as the solution of (operator) Riccati equations and state-prediction equations that become quite delicate and computationally very expensive for infinite-dimensional systems. Many ILC approaches require the implementation of non-causal learning operators, as e.g. (3.18). To implement such laws, the causal and anti-causal part of the learning operator are usually separated using spectral factorization techniques. Both parts are then solved by forward- and backward integration of

[2] The term "fractional Fourier transform" in [91] is denoting a special case of the Z-transform and has fallen out of use.

Die approbierte Originalversion dieser Dissertation ist in der TU Wien Bibliothek verfügbar.
The approved original version of this doctoral thesis is available at the TU Wien Bibliothek.
TU Bibliothek WIEN Your knowledge hub

the corresponding state-space representation, respectively (e.g., [90, 94]). This procedure is closely related to the existing non-causal stable inversion methods in [82, 89, 90]. Unfortunately, spectral factorization techniques for DPSs are quite demanding (cf. [95]). Using the solution (3.40), one is effectively avoiding the spectral factorization by directly computing the learning kernel $\mathbf{L}(t)$ of the learning operator (3.5b) rather than finding a representation of the learning operator in form of two systems of (partial) differential equations.

3.5 Simulation examples

We want to illustrate the proposed method and apply both learning laws - optimal and sub-optimal - to benchmark problems of finite- and infinite-dimensional nature. Therefore, we first illustrate the application of the numerical algorithm presented in Section 3.4 to an infinite-dimensional example of a 2×2 coupled diffusion-reaction system. The stochastic properties of the fully optimal solution are finally detailed on a finite-dimensional non-minimum-phase multi-input-multi-output (MIMO) example.

3.5.1 A sub-optimal ILC for a system of parabolic PDEs

Building on the solution procedure presented in Section 3.4, we now apply it to the coupled system of parabolic PDEs

$$\frac{\partial \mathbf{x}}{\partial t}(z,t) = \underbrace{\begin{bmatrix} \lambda_1 & 0 \\ 0 & \lambda_2 \end{bmatrix}}_{=\mathbf{\Lambda}} \frac{\partial^2}{\partial z^2}\mathbf{x}(z,t) + \underbrace{\begin{bmatrix} 0 & \sigma_{12} \\ \sigma_{21} & 0 \end{bmatrix}}_{=\mathbf{\Sigma}} \mathbf{x}(z,t) \tag{3.41a}$$

defined on the spatial domain $z \in [0,1]$, with the initial condition $\mathbf{x}(z,0) = \mathbf{0}$, the boundary conditions

$$\mathbf{x}(0,t) = \mathbf{u}(t) \qquad \frac{\partial \mathbf{x}}{\partial z}(1,t) = \underbrace{\begin{bmatrix} \Gamma_{11} & \Gamma_{12} \\ \Gamma_{21} & \Gamma_{22} \end{bmatrix}}_{\mathbf{\Gamma}} \mathbf{x}(1,t), \tag{3.41b}$$

and the output equation

$$\mathbf{y}(t) = \mathbf{x}(1,t). \tag{3.41c}$$

To highlight the regularized inversion performed by the learning law (3.22) and its application to distributed-parameter systems, we present this example in the absence of stochastic disturbances or noise.

To obtain a transfer function description of the system (3.41), we apply the bilateral Laplace transform to (3.41a). This gives the spatial ODE

$$\frac{\partial^2}{\partial z^2}\mathbf{x}(z,s) = \underbrace{\mathbf{\Lambda}^{-1}\left(s\mathbf{I} - \mathbf{\Sigma}\right)}_{=\mathbf{Q}(s)} \mathbf{x}(z,s). \tag{3.42}$$

Die approbierte Originalversion dieser Dissertation ist in der TU Wien Bibliothek verfügbar.
The approved original version of this doctoral thesis is available at the TU Wien Bibliothek.
TU Bibliothek WIEN Your knowledge hub

The dependence of $\mathbf{Q}(s)$ on the Laplace variable s will be omitted for the following calculations. The matrix $\mathbf{Q}$ can be diagonalized by using the state transform $\mathbf{x}(z,s) = \mathbf{P}\boldsymbol{\chi}(z,s)$, which yields

$$\frac{\partial^2}{\partial z^2}\boldsymbol{\chi}(z,s) = \tilde{\mathbf{Q}}^2\boldsymbol{\chi}(z,s), \tag{3.43}$$

with the diagonal matrix $\tilde{\mathbf{Q}} = \sqrt{\mathbf{P}^{-1}\mathbf{Q}\mathbf{P}}$ and the corresponding boundary conditions

$$\boldsymbol{\chi}(0,s) = \mathbf{P}^{-1}\mathbf{u}(s), \qquad \frac{\partial \boldsymbol{\chi}}{\partial z}(1,s) = \tilde{\boldsymbol{\Gamma}}\boldsymbol{\chi}(1,s) \tag{3.44}$$

with $\tilde{\boldsymbol{\Gamma}} = \mathbf{P}^{-1}\boldsymbol{\Gamma}\mathbf{P}$. Applying the ansatz

$$\boldsymbol{\chi}(z,s) = \cosh\left(\tilde{\mathbf{Q}}z\right)\begin{bmatrix} c_{11} \\ c_{21} \end{bmatrix} + \sinh\left(\tilde{\mathbf{Q}}z\right)\begin{bmatrix} c_{12} \\ c_{22} \end{bmatrix} \tag{3.45}$$

to (3.43), (3.44) yields the solution

$$\mathbf{x}(z,s) = \mathbf{P}\left[\cosh\left(\tilde{\mathbf{Q}}z\right) - \sinh\left(\tilde{\mathbf{Q}}z\right)\boldsymbol{\Xi}\right]\mathbf{P}^{-1}\mathbf{u}(s), \tag{3.46}$$

with

$$\boldsymbol{\Xi} = \left[\tilde{\mathbf{Q}}\cosh\left(\tilde{\mathbf{Q}}\right) - \tilde{\boldsymbol{\Gamma}}\sinh\left(\tilde{\mathbf{Q}}\right)\right]^{-1}\left[\tilde{\mathbf{Q}}\sinh\left(\tilde{\mathbf{Q}}\right) - \tilde{\boldsymbol{\Gamma}}\cosh\left(\tilde{\mathbf{Q}}\right)\right]. \tag{3.47}$$

Finally, with (3.41c) the transfer matrix is given by

$$\mathbf{G}_u = \mathbf{P}\left[\cosh\left(\tilde{\mathbf{Q}}\right) - \sinh\left(\tilde{\mathbf{Q}}\right)\boldsymbol{\Xi}\right]\mathbf{P}^{-1}. \tag{3.48}$$

Following the sub-optimal approach presented in Section 3.3.1 and assuming no a priori knowledge of the input error PSD, we choose $\mathbf{S}_{\nu\nu}(s) = \mathbf{I}$. In the absence of any stochastic perturbations, we introduce some regularization by choosing $\mathbf{S}_{nn}(s) = \sigma\mathbf{I}$ with $\sigma = 10^{-3}$. The spectral solution of the learning kernel is given by (3.22). With the parameter values $\lambda_1 = \lambda_2 = 1$, $\sigma_{12} = 1/2$, $\sigma_{21} = -1$, $\Gamma_{11} = 0$, $\Gamma_{12} = 1/2$, $\Gamma_{21} = 1$, and $\Gamma_{22} = 1/10$, one obtains a numerical solution of the learning kernel $\mathbf{L}(t)$ by (3.40) as shown in Figure 3.1.

Using the calculated learning kernel to track a desired output trajectory $\mathbf{y}^d(t) = [y_1^d(t), y_2^d(t)]^{\mathrm{T}}$, $t \in [0,10]$ given by

$$y_1^d(t) = \Theta_5(t-2.5), \quad y_2^d(t) = 3\frac{\mathrm{d}}{\mathrm{d}t}\left(\Theta_5(t) + \Theta_5(t-5)\right) \tag{3.49}$$

with the smoothed step function

$$\Theta_T(t) = \begin{cases} 0 & t \leq 0 \\ 1 & t \geq T \\ \frac{\int_0^t \theta_T(\tau)\mathrm{d}\tau}{\int_0^T \theta_T(\tau)\mathrm{d}\tau} & t \in (0,T), \end{cases} \tag{3.50}$$

Die approbierte Originalversion dieser Dissertation ist in der TU Wien Bibliothek verfügbar.
The approved original version of this doctoral thesis is available at the TU Wien Bibliothek.
TU Bibliothek WIEN Your knowledge hub

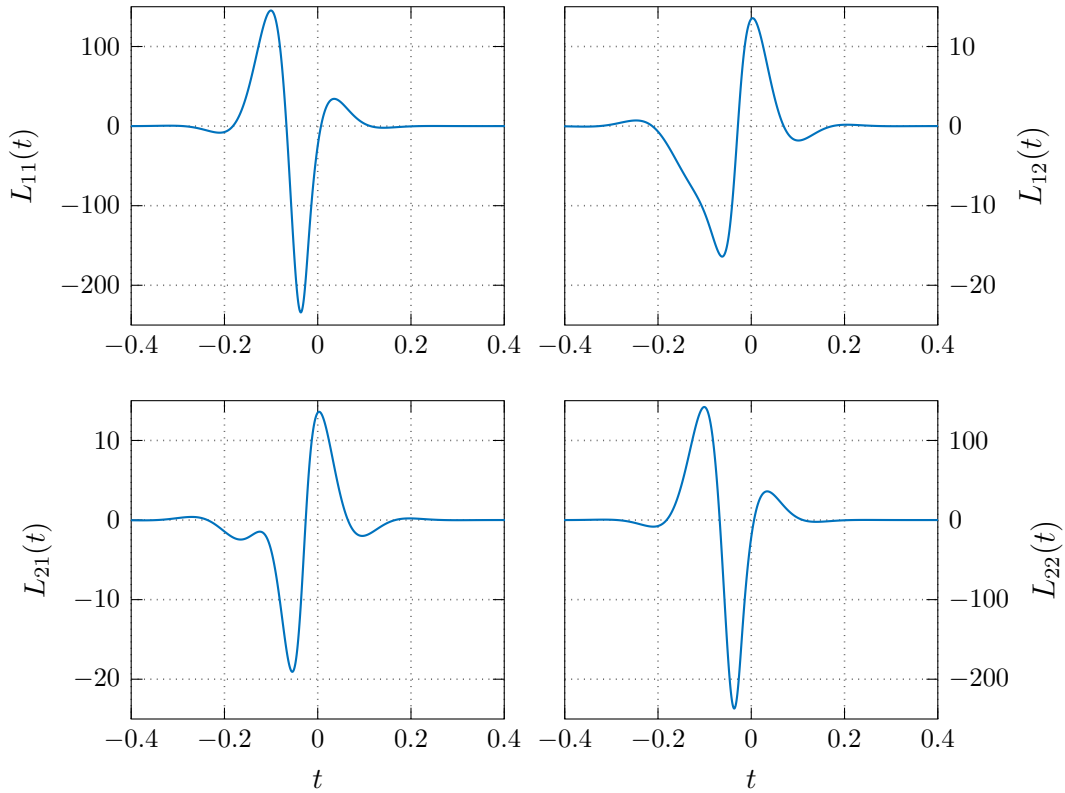

Figure 3.1: Entries of the (non-causal) learning kernel $\mathbf{L}(t)$ for $\mathbf{S}_{nn}(s) = 10^{-3}\mathbf{I}$ and $\mathbf{S}_{\nu\nu}(s) = \mathbf{I}$ obtained by (3.40) using $N = 256$, $t_S = 0.8$, and $\omega_S = 1000$.

Die approbierte Originalversion dieser Dissertation ist in der TU Wien Bibliothek verfügbar.
The approved original version of this doctoral thesis is available at the TU Wien Bibliothek.
TU WIEN Bibliothek Your knowledge hub

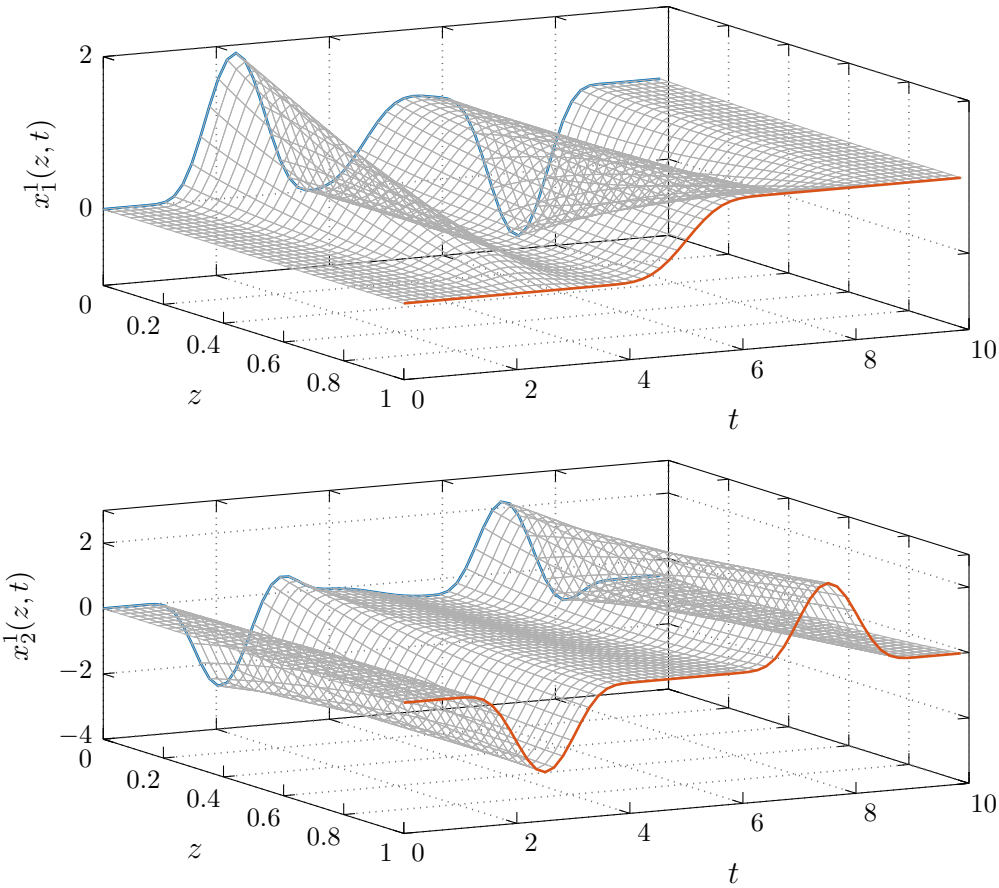

Figure 3.2: State $\mathbf{x}^1(z,t)$ of the PDE system (3.41) with the input $\mathbf{u}^1(t) = \mathbf{x}^1(0,t)$ (blue) that yields $\mathbf{y}(t) = \mathbf{x}^1(1,t) \approx \mathbf{y}^d(t)$ (red) after the first iteration.

whereby

$$\theta_T(t) = \begin{cases} 0 & t \notin (0,T) \\ \exp\left[-\left((1-{}^t\!/_T){}^t\!/_T\right)^{-1.5}\right] & t \in (0,T), \end{cases} \tag{3.51}$$

the system (3.41) converges up to numeric precision of the solver after the first iteration with the resulting state profile $\mathbf{x}^1(z,t)$ shown in Figure 3.2. Using higher values for σ and thus assuming a lower signal-to-noise ratio, one is effectively reducing the learning rate as shown in Figure 3.3 and discussed in Section 3.3.1.

Remark 13. *This example highlights the regularized inversion performed by the learning law (3.22). Standard inversion techniques for infinite-dimensional systems usually apply a flatness-based approach, whereby the set of possible input functions to the ill-posed inverse operator is restricted to smooth functions of some Gevrey class such that the output function is again well-defined (see, e.g., [96–98]). However, unlike for feedforward purposes, one cannot demand such high levels of regularity of the learning operator's input signal due to the presence of*

Die approbierte Originalversion dieser Dissertation ist in der TU Wien Bibliothek verfügbar.
The approved original version of this doctoral thesis is available at the TU Wien Bibliothek.
TU Bibliothek WIEN Your knowledge hub

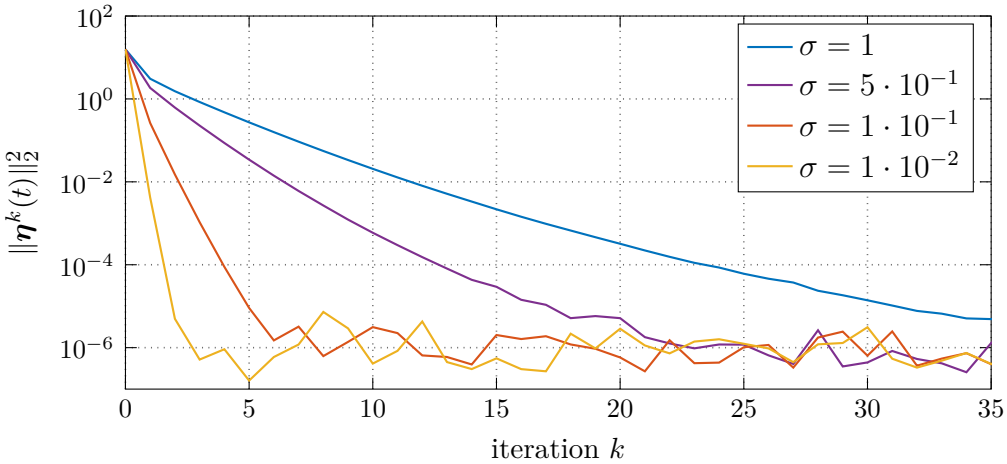

Figure 3.3: Reduced learning behavior according to the expected signal-to-noise ratio with $\mathbf{S}_{nn}(s) = \sigma\mathbf{I}$ and $\mathbf{S}_{\nu\nu}(s) = \mathbf{I}$.

stochastic disturbances and measurement noise. Thus, the only remaining option for ILC purposes is to regularize the learning operator itself as suggested in this chapter. Using such a regularized inversion might be an interesting option also for feedforward applications in case of linear distributed-parameter systems, since flatness-based techniques are significantly more involved using so-called Weierstraß canonical products [99] and may ultimately require resummation techniques [100] dealing with diverging series.

3.5.2 Comparing the sub-optimal with the optimal ILC scheme

While the previous example illustrates the basic procedures and their application to distributed-parameter systems, we will now focus on the stochastic properties of the ILC law (3.5) for sub-optimal (3.22) and optimal learning (3.32) operators and compare it to existing solutions. Therefore, we consider a finite-dimensional MIMO system of the form (3.2) given by

$$\mathbf{G}_u(s) = \begin{bmatrix} \frac{s}{s^2+s+1} & \frac{1}{s^2+s+1} \\ \frac{s+10}{s^2+2s+4} & \frac{1}{s+1} \end{bmatrix}, \quad \mathbf{G}_w(s) = \begin{bmatrix} \frac{s}{s^2+s+1} \\ \frac{3s^2+15/2s+6}{s^3+3s^2+6s+4} \end{bmatrix}. \tag{3.52}$$

This system exhibits zeros in the right half-plane, which can be seen by transforming $\mathbf{G}_u(s)$ into Smith-McMillan form. The noise process is assumed to be band-limited white noise with power σ_n^2 and bandwidth ω_n, i.e., its PSD is given by

$$\mathbf{S}_{nn}(s) = \begin{cases} \sigma_n^2 \frac{\pi}{\omega_n}\mathbf{I} & |\mathrm{Im}\{s\}| \leq \omega_n \\ \mathbf{0} & \text{else}, \end{cases} \tag{3.53}$$

Die approbierte Originalversion dieser Dissertation ist in der TU Wien Bibliothek verfügbar.
The approved original version of this doctoral thesis is available at the TU Wien Bibliothek.
TU Bibliothek WIEN Your knowledge hub

where $\sigma_n^2 = 1/100$ and $\omega_n = 321.7$ is chosen to be at the Nyquist frequency of the simulation. Similarly, the disturbance is given by

$$\mathbf{S}_{ww}(s) = \begin{cases} 1/10 & |\mathrm{Im}\,\{s\}\,| \in [\pi, 2\pi] \\ 0 & \text{else.} \end{cases} \tag{3.54}$$

The control task is to track a desired output $\mathbf{y}^d(t) = [y_1^d(t), y_2^d(t)]^{\mathrm{T}}$, $t \in [0, 20]$ with

$$y_1^d(t) = 5\,\Theta_{10}(t-5), \qquad y_2^d(t) = 10\,\frac{\mathrm{d}}{\mathrm{d}t}\Theta_{10}(t-5). \tag{3.55}$$

To specify the learning operators, we have to choose the initial input error PSD $\mathbf{S}_{\nu\nu}^0(s)$ for the optimal case (3.32) and the fixed input error PSD $\mathbf{S}_{\nu\nu}(s)$ for the sub-optimal case (3.22), respectively. Because these PSDs are usually unknown, they are effectively tuning parameters that have to be chosen as part of the design process. Since we expect the input to consist of predominantly lower frequencies, we choose both to be

$$\mathbf{S}_{\nu\nu}^0(s) = \mathbf{S}_{\nu\nu}(s) = \frac{0.01}{|1+s|^2}\mathbf{I}. \tag{3.56}$$

Finally, the two Wiener-filter-based approaches are compared to existing norm-optimal approaches. By choosing $\mathbf{R} = \sigma_R\mathbf{I}$ and $\mathbf{Q} = \sigma_Q\mathbf{I}$ as in Section 3.3.1, the resulting norm-optimal learning law is equivalent to the pseudo-inverse solution [82] given by the frequency-domain representation (3.29) with a single remaining tuning parameter $\alpha = \sigma_R/\sigma_Q$.

In Figure 3.4, the evolution of the L^2-norms of the input and output errors are shown for all three learning operators. As expected, the optimal learning operator (3.32) settles around the expected steady-state level given by the optimal asymptotic output error PSD $\mathbf{S}_{\eta\eta}^\infty$ in (3.33) indicated by the dashed line in Figure 3.4. Since the asymptotic error PSD of the sub-optimal ILC (3.23) is quite close to the optimal value, both Wiener-filter-based learning operators perform roughly equal while the pseudo-inverse operator (using $\alpha = 1/10$) is not able to achieve a similarly low output error on average.

The reason for this can be seen in the bottom plot of Figure 3.4: lacking stochastic information, the pseudo-inverse operator is hardly able to separate stochastic perturbations from signal information and thus settles at a significantly higher steady-state level of the input error compared to the Wiener-filter-based operators that avoid learning stochastic perturbations (cf. Figure 3.5). Lowering the regularization parameter (i.e. increasing $\mathbf{Q}$ w.r.t. $\mathbf{R}$) to $\alpha = 1/100$ deteriorates the performance, while increasing it to $\alpha = 2$ reduces the asymptotic input error at the cost of slower convergence (cf. Remark 11). Comparing the sub-optimal learning operator with the optimal learning operator shows that the input error of the sub-optimal approach reaches a steady-state level, while the optimal learning operator asymptotically approaches zero as predicted by the theory. However, the convergence rate is usually quite slow. Depending on the exact application

Die approbierte Originalversion dieser Dissertation ist in der TU Wien Bibliothek verfügbar.
The approved original version of this doctoral thesis is available at the TU Wien Bibliothek.
TU Bibliothek WIEN Your knowledge hub

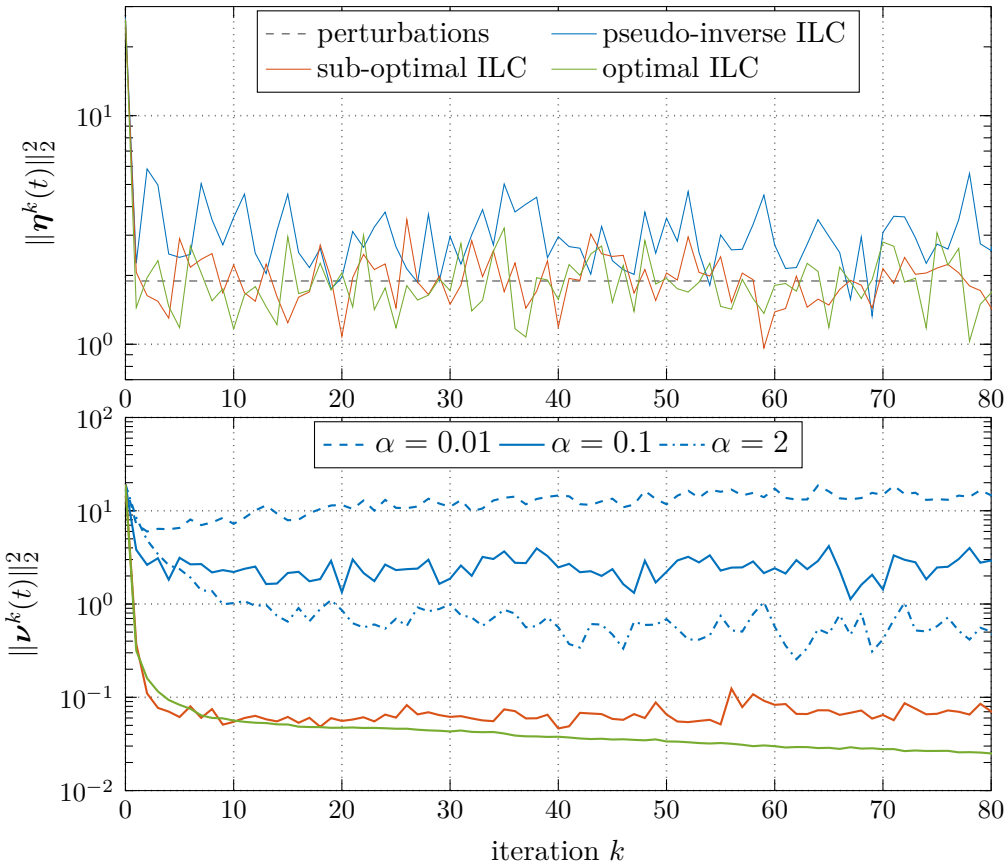

Figure 3.4: Evolution of the input and output error's L^2-norms for three different learning operators: pseudo-inverse (blue), sub-optimal (red) and optimal (green). For clarity, the evolution of the output error is only depicted for the case $\alpha = 1/10$.

scenario, one may choose to avoid the extra computational effort of implementing an iteration-varying learning law as its impact on the output error is quite limited, at least in this example.

Die approbierte Originalversion dieser Dissertation ist in der TU Wien Bibliothek verfügbar.
The approved original version of this doctoral thesis is available at the TU Wien Bibliothek.
TU Bibliothek WIEN Your knowledge hub

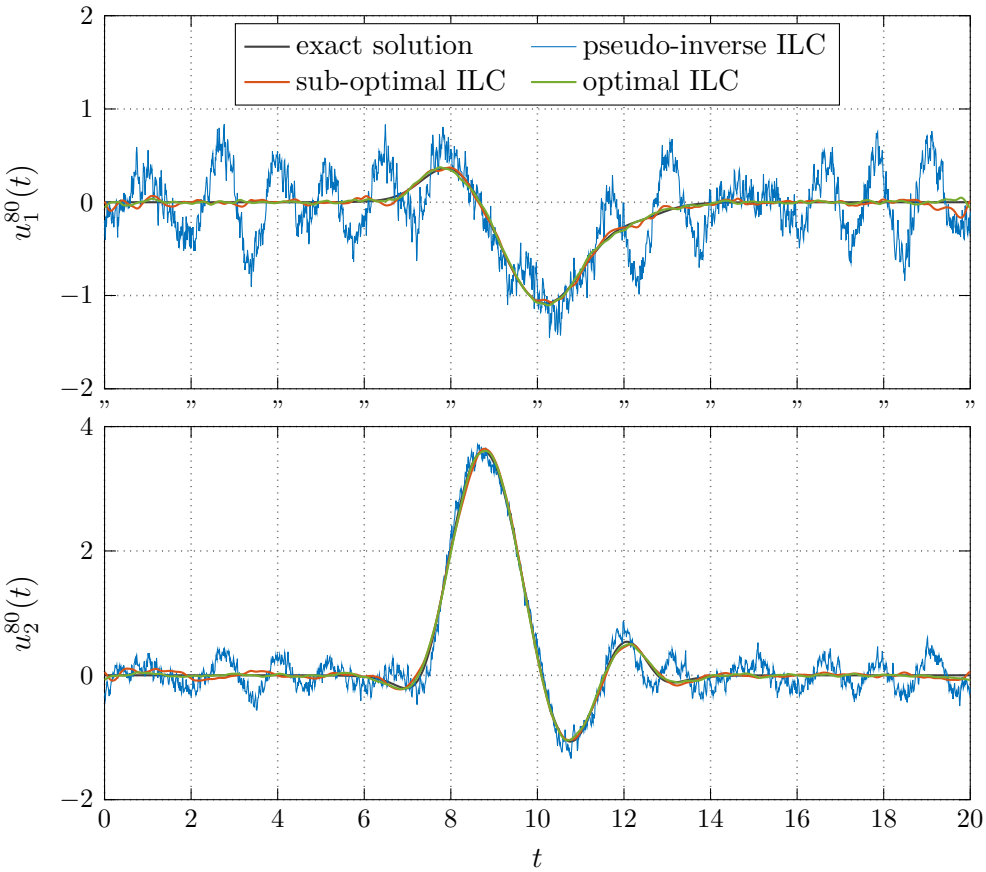

Figure 3.5: The learned input signals after 80 iterations $\mathbf{u}^{80}(t)$ using a pseudo-inverse (blue), a sub-optimal (red) or an optimal (green) learning operator compared to the exact inverse solution (black) for the desired output $\mathbf{y}^d(t)$.

Die approbierte Originalversion dieser Dissertation ist in der TU Wien Bibliothek verfügbar.
The approved original version of this doctoral thesis is available at the TU Wien Bibliothek.

CHAPTER 4

Iterative Pulse-Shape Control for Ultra-Short Laser Pulses

Based on the mathematical model developed in Chapter 2 and exploiting the ILC concepts presented in the previous chapter, we can now start with the actual controller design for the CPA system. To restate the control objective, we want to adapt the adjustable input filter $G_{\mathrm{F}}^{n}(\omega)$ such that a desired output pulse $E_{\mathrm{out}}^{d}(t) \in L^2 \cap L^\infty$ is achieved, see also Figure 2.1. While regenerative amplifiers are able to produce quite extreme pulses dynamically, the achievable output pulses in steady-state operation are limited by either the available gain at a certain frequency or the population of excited states of the individual resonant transitions sustainable by the pumping process. Optical filters such as acousto-opptic modulators (AOMs) are usually placed behind the stretcher to protect its components from damage due to high energy densities of the incoming laser pulses. Since both stretcher and filter are linear devices, their position can be interchanged for the control design, which allows to reformulate the control problem of adaptively adjusting the filter as a problem of iteratively adjusting the virtual input pulse $E_{\mathrm{v,in}}^{n}(t)$, see also Figure 4.1. Assuming that the seed pulse $E_{\mathrm{seed}}(t)$ is spectrally broad enough, a suitable transfer function of the filter is given by

$$G_{\mathrm{F}}^{n}(\omega) = \frac{\hat{E}_{\mathrm{v,in}}^{n}(\omega)}{\hat{E}_{\mathrm{seed}}(\omega)}. \tag{4.1}$$

The constraint of the spectral filter (2.11) thus results in an admissible set of virtual input pulses given by

$$\left|\hat{E}_{\mathrm{v,in}}^{n}(\omega)\right| \leq \left|\hat{E}_{\mathrm{seed}}(\omega)\right| \tag{4.2}$$

for all $\omega \in \mathbb{R}$.

Die approbierte Originalversion dieser Dissertation ist in der TU Wien Bibliothek verfügbar.
The approved original version of this doctoral thesis is available at the TU Wien Bibliothek.
TU WIEN Bibliothek Your knowledge hub

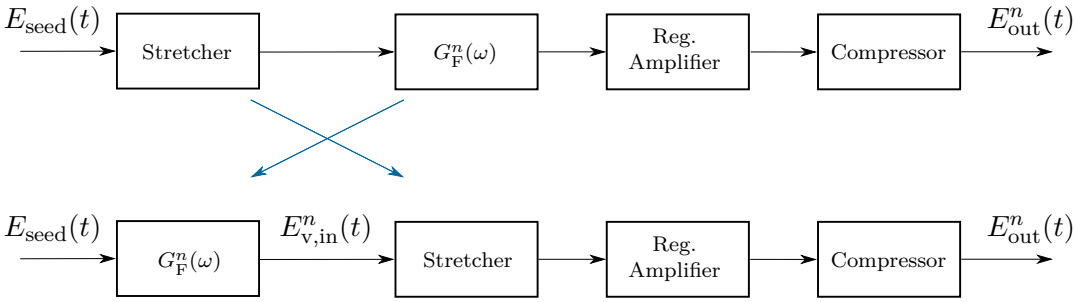

Figure 4.1: Separation of the CPA system with spectral filter into an uncontrolled amplifier with adjustable virtual input pulse $E_{\text{v,in}}^n(t)$.

Using ILC to determine suitable pulses $E_{\text{v,in}}^n(t)$ seems natural in this reformulated setting. In [51], a PD-type ILC law was used to apply pulse-shape control for a single-pass laser amplifier described by a simple Frantz-Nodvik model with uniform gain. Additionally, the initial population inversion is completely restored for each pulse, i.e., different pulses are not coupled and the system behaves identical for each iteration. Even in this simplified scenario, PD-type ILC laws show a rather slow convergence. Given the extremely high and variable amounts of gain exhibited by the more general CPA system considered in this thesis, one could expect painfully slow rates of convergence or even instability. In fact, the dispersive effects of the linear Schrödinger equation alone causes PD-type (or P-type) ILC laws to diverge eventually. This becomes quite clear when one considers that PD-type laws can be seen as an inversion of a first-order low-pass behavior while the linear Schrödinger equation effectively introduces an all-pass behavior with an additional phase proportional to ω^2, see (4.15). More formally, this can be verified using the stability criterion (3.17).

A model-based scheme seems more suitable for this particular task, but the complex nonlinear and infinite-dimensional character of the system limits the usability as well as availability of such methods. However, the main nonlinearity affecting the input-output behavior is due to the depletion of the population distributions, see (2.25) and (2.27). Such saturation effects are typically handled quite well by ILC schemes, wherefore a learning approach based on a reduced, linear model seems will be pursued.

Remark 14. *By applying ILC methods, we are tacitly neglecting the coupling of subsequent pulses and limit our focus solely on the pulse-shaping task while treating the coupling as a minor variation of the system behavior. As we will show in Section 4.5, this is fine for weakly coupled pulses where the CPA is operated in a stable regime. In general, however, this analysis falls short of capturing the full picture and one has to specifically address these dynamics as in Chapter 5.*

Die approbierte Originalversion dieser Dissertation ist in der TU Wien Bibliothek verfügbar.
The approved original version of this doctoral thesis is available at the TU Wien Bibliothek.
TU Bibliothek Your knowledge hub WIEN

4.1 Reduced linear input-output behavior

The main idea to obtain a simplified input-output behavior is to neglect the complex population dynamics and calculate the pulse evolution by an approximate linear model. Henceforth, we make the following assumptions:

Assumption 1. *The influence of the nonlinear polarization due to the Kerr effect can be neglected in (2.23).*

This assumption is typically fulfilled since CPA systems use the stretcher/compressor arrangement to avoid the intensity regime where strong Kerr effects emerge.

Assumption 2. *The population densities remain at the stationary, unsaturated level $N_j^0(z)$ for all N_{RT} cycles and all pulses.*

Remark 15. *Note the difference between stationary (unsaturated) populations $N_j^0(z)$ as stationary solutions to (2.31) and (2.32), i.e. when there is no depletion due to amplified pulses, and steady-state populations $N_j^s(z)$, i.e. the depleted population density for a fixed input pulse $E_{v,in}(t)$, where the population loss due to the amplification process (i.e., the sequence of pulse models in Figure 2.5) is exactly canceled by the regeneration process (i.e., the sequence of pump models in Figure 2.5) due to the complete model's alternating chain of pulse and pump models given in Section 2.2.3.*

As long as the overall pulse energy inside the cavity remains comparatively low (below 100 µJ for the given system), the amplifier is not saturating and the steady state population remains close to its stationary level, i.e. $N_j^s(z) \approx N_j^0(z)$. This is clearly not the case for operating scenarios with high energy pulses close to the capabilities of the CPA system. As a consequence, Assumption 2 will be relaxed in Section 4.3 using an adaptive design.

Utilizing both assumptions, (2.23) and (2.25) can be rewritten as with a simplified linear pulse model

$$i\frac{\partial E}{\partial z} = -\frac{k_2}{2}\frac{\partial^2 E}{\partial t^2} + \frac{\omega_0^2}{2c_0^2\varepsilon_0 k_0}(P_1 + P_2 + P_3 + P_4) \tag{4.3a}$$

$$\frac{\partial P_j}{\partial t} = -\frac{\omega_j^2 + i\omega_0\Delta\omega_j - \omega_0^2}{\Delta\omega_j + i2\omega_0}P_j - \frac{\kappa_j}{\Delta\omega_j + i2\omega_0}\Delta N_{5j}^0 E, \tag{4.3b}$$

where $\Delta N_{5j}^0 = N_5^0 - N_j^0$ is the stationary solution of (2.31), (2.32) and (2.26). In vector notation, the stationary solution results from

$$\mathbf{0} = \mathbf{\Gamma}_1(I_\mathrm{P}(z))\mathbf{N}^0(z) + \mathbf{\Gamma}_2(I_\mathrm{P}(z))N_\mathrm{dop} \tag{4.4a}$$

$$\frac{\partial I_\mathrm{P}(z)}{\partial z} = \sigma_\mathrm{P}\left(\begin{bmatrix}1 & 1 & 1 & 1 & 2\end{bmatrix}\mathbf{N}^0(z) - N_\mathrm{dop}\right)I_\mathrm{P}(z), \tag{4.4b}$$

Die approbierte Originalversion dieser Dissertation ist in der TU Wien Bibliothek verfügbar.
The approved original version of this doctoral thesis is available at the TU Wien Bibliothek.
TU Bibliothek Your knowledge hub WIEN

with $\mathbf{N}^0(z) = [N_1^0(z), \ldots, N_5^0(z)]^{\mathrm{T}}$, $I_{\mathrm{P}}(0) = I_0$ and

$$\mathbf{\Gamma}_1(I_{\mathrm{P}}(z)) = \begin{bmatrix} -\tilde{\gamma}_1 & \gamma_{21}-\gamma_{01} & -\gamma_{01} & -\gamma_{01} & \gamma_{51}-\gamma_{01} \\ \gamma_{12}-\gamma_{02} & -\tilde{\gamma}_2 & \gamma_{32}-\gamma_{02} & -\gamma_{02} & \gamma_{52}-\gamma_{02} \\ -\gamma_{03} & \gamma_{23}-\gamma_{03} & -\tilde{\gamma}_3 & \gamma_{43}-\gamma_{03} & \gamma_{53}-\gamma_{03} \\ -\gamma_{04} & -\gamma_{04} & \gamma_{34}-\gamma_{04} & -\tilde{\gamma}_4 & \gamma_{54}-\gamma_{04} \\ -\frac{\sigma_{\mathrm{P}} I_{\mathrm{P}}(z)}{\hbar\omega_{\mathrm{P}}} & -\frac{\sigma_{\mathrm{P}} I_{\mathrm{P}}(z)}{\hbar\omega_{\mathrm{P}}} & -\frac{\sigma_{\mathrm{P}} I_{\mathrm{P}}(z)}{\hbar\omega_{\mathrm{P}}} & -\frac{\sigma_{\mathrm{P}} I_{\mathrm{P}}(z)}{\hbar\omega_{\mathrm{P}}} & -\tilde{\gamma}_5((z)) \end{bmatrix} \tag{4.5}$$

$$\mathbf{\Gamma}_2(I_{\mathrm{P}}(z))^T = \begin{bmatrix} \gamma_{01} & \gamma_{02} & \gamma_{03} & \gamma_{04} & \frac{\sigma_{\mathrm{P}} I_{\mathrm{P}}(z)}{\hbar\omega_{\mathrm{P}}} \end{bmatrix}, \tag{4.6}$$

using the abbreviations

$$\tilde{\gamma}_1 = \gamma_{10}+\gamma_{12}+\gamma_{01} \tag{4.7}$$

$$\tilde{\gamma}_2 = \gamma_{20}+\gamma_{21}+\gamma_{23}+\gamma_{02} \tag{4.8}$$

$$\tilde{\gamma}_3 = \gamma_{30}+\gamma_{32}+\gamma_{34}+\gamma_{03} \tag{4.9}$$

$$\tilde{\gamma}_4 = \gamma_{40}+\gamma_{43}+\gamma_{04} \tag{4.10}$$

$$\tilde{\gamma}_5(z) = \gamma_{50}+\gamma_{51}+\gamma_{52}+\gamma_{53}+\gamma_{54}+2\frac{\sigma_{\mathrm{P}} I_{\mathrm{P}}(z)}{\hbar\omega_{\mathrm{P}}}. \tag{4.11}$$

Remark 16. *The scalar ODE (4.4b) can be solved analytically as*

$$I_P(z) = I_0 \exp\left[\sigma_P \int_0^z \left(\begin{bmatrix}1 & 1 & 1 & 1 & 2\end{bmatrix} \mathbf{N}^0(z) - N_{dop}\right) \mathrm{d}z\right]. \tag{4.12}$$

Inserting this result into (4.4a) yields a system of implicit integral equations whose solution at a position $\bar{z}$ only depends on values $\mathbf{N}^0(z)$ for $z \leq \bar{z}$. By progressively solving it from the left boundary $z = 0$ to the right boundary $z = L$, one can obtain numerically efficient solutions of (4.4).

Applying the Fourier transform to (4.3b) yields the spectral description of the susceptibility of the j-th transition

$$\begin{aligned} \hat{P}_j(z,\omega) &= \frac{-\kappa_j(N_5^0(z) - N_j^0(z))}{i\omega(\Delta\omega_j + 2i\omega_0) + \omega_j^2 + i\omega_0\Delta\omega_j - \omega_0^2}\hat{E}(z,\omega) \\ &= \chi_j(\omega; \Delta N_{5j}^0(z))\, \hat{E}(z,\omega). \end{aligned} \tag{4.13}$$

With (4.13), the remaining equation (4.3a) can be solved analytically using (2.28) and (2.29) which gives the transfer function of a single pass

$$\hat{E}_{\mathrm{out,RA}}^{n,k}(\omega) = G_{\mathrm{sp}}\left(\omega; \overline{\Delta\mathbf{N}^0}\right) \hat{E}_{\mathrm{in,RA}}^{n,k}(\omega) \tag{4.14}$$

where

$$G_{\mathrm{sp}}\left(\omega; \overline{\Delta\mathbf{N}^0}\right) = \exp\left[-i\int_0^L \frac{k_2}{2}\omega^2 + \frac{\omega_0^2}{2c_0^2\varepsilon_0 k_0}\sum_{j=1}^4 \chi_j\left(\omega; \Delta N_{5j}^0(z)\right) \mathrm{d}z\right]$$

Die approbierte Originalversion dieser Dissertation ist in der TU Wien Bibliothek verfügbar.
The approved original version of this doctoral thesis is available at the TU Wien Bibliothek.
TU Bibliothek WIEN Your knowledge hub

$$= \exp\left[-\frac{iL}{2}\left(k_2\omega^2 + \frac{\omega_0^2}{c_0^2\varepsilon_0 k_0}\sum_{j=1}^{4}\chi_j\left(\omega;\overline{\Delta N_{5j}^0}\right)\right)\right] \tag{4.15}$$

with $\overline{\Delta\mathbf{N}^0} = \left[\overline{\Delta N_{51}^0},\ldots,\overline{\Delta N_{54}^0}\right]^{\mathrm{T}}$. Using the amplified output pulse of the RA $E_{\mathrm{out,RA}}^n(t)$ given in (2.38) and the description of a single pass by (4.14) and (4.15) together with the round-trip losses due to (2.35b), one obtains the simplified input-output description of the RA

$$\hat{E}_{\mathrm{out,RA}}^n(\omega) = \eta_{\mathrm{RC}}^{N_{\mathrm{RT}}-1} G_{\mathrm{sp}}\left(\omega;\overline{\Delta\mathbf{N}^0}\right)^{N_{\mathrm{RT}}}\hat{E}_{\mathrm{in,RA}}^n(\omega). \tag{4.16}$$

Since the phase introduced by the stretcher (2.10), (2.9) and the compressor (2.12) compensates each other perfectly due to (2.13), the overall reduced linear model with the virtual control input due to (4.1) is given by

$$\hat{E}_{\mathrm{out}}^n(\omega) = \eta_{\mathrm{S}}\eta_{\mathrm{C}}\eta_{\mathrm{RC}}^{N_{\mathrm{RT}}-1} G_{\mathrm{sp}}\left(\omega;\overline{\Delta\mathbf{N}^0}\right)^{N_{\mathrm{RT}}}\hat{E}_{\mathrm{v,in}}^n(\omega) = G\left(\omega;\overline{\Delta\mathbf{N}^0}\right)\hat{E}_{\mathrm{v,in}}^n(\omega), \tag{4.17}$$

where the mean steady state population inversion $\overline{\Delta\mathbf{N}^0}$ is a finite-dimensional parameter vector defining the overall gain of the CPA system - a fact that will be used later on.

4.2 Wiener-Filter-based ILC

We now want to track a desired output pulse $E_{\mathrm{out}}^{\mathrm{d}}(t) \in L^2(-\infty,\infty)\cap L^\infty(-\infty,\infty)$ by means of the virtual control input $E_{\mathrm{v,in}}^n(t)$, using the reduced input-output behavior derived in the previous section, subject to the input constraints (4.2). The handling of input constraints can be done easily by projecting onto the set of feasible input signals (see, e.g., [101]). Thus, we consider a general learning law in the frequency domain

$$\hat{E}_{\mathrm{v,in}}^{n+1}(\omega) = \mathcal{T}\left[\hat{E}_{\mathrm{v,in}}^n(\omega) + L(\omega)\left(\hat{E}_{\mathrm{out}}^{\mathrm{d}}(\omega) - \hat{E}_{\mathrm{out}}^n(\omega)\right)\right], \tag{4.18}$$

with the linear learning operator L and the nonlinear truncation operator $\mathcal{T}$ given by

$$\mathcal{T}\left(\hat{E}(\omega)\right) = \begin{cases}\hat{E}(\omega) & \text{if } |\hat{E}| \le |\hat{E}_{\mathrm{seed}}| \\ |\hat{E}_{\mathrm{seed}}(\omega)|\exp\left(i\arg\hat{E}(\omega)\right) & \text{else.}\end{cases} \tag{4.19}$$

Thus, a suitable ILC method to obtain the learning operator L is required. Since the ILC law (4.18) is already formulated in the frequency domain due to the nature of the constraints (4.2), it seems natural to resort to frequency domain approaches. Additionally, by employing the numerical scheme presented in Section 3.4, the infinite-dimensional character of the reduced system does not cause any problems.

Applying (regularized) inversion-based learning laws on infinite time horizons such as in [82], the spectrally narrow high-gain nature of the system (see Figure 2.6)

Die approbierte Originalversion dieser Dissertation ist in der TU Wien Bibliothek verfügbar.
The approved original version of this doctoral thesis is available at the TU Wien Bibliothek.
TU Bibliothek WIEN Your knowledge hub

yields particularly high learning gains in spectral regions where no signal is present and where learning should be avoided. In view of the unmodeled dynamics and in particular the neglected influence of the Kerr effect due to Assumption 1, it is inevitable to limit learning to those spectral regions where the input signal is expected to be strong. At this point, the Wiener-filter-based ILC law developed in the previous chapter proves to be very useful since it adjusts its learning action to the expected signal-to-disturbance ratio.

While the iteration-varying learning law given in Section 3.3.2 has some nice theoretical properties, the estimation of the input error's PSD $\mathbf{S}_{\nu\nu}^{n}$ in (3.32b) renders it quite susceptible to any model-plant mismatch. In light of the strongly nonlinear behavior of CPAs and the simplified linear input-output description (4.17) which shall be used for the ILC design, using the iteration-invariant law of Section 3.3.1 seems clearly advantageous.

Assuming no additional process disturbances $\mathbf{S}_{ww} = \mathbf{0}$ and choosing a spectrally uniform noise PSD $S_{nn} = \gamma_{\mathrm{ILC}} > 0$ as a simple regularization parameter in the absence of any further a-priori knowledge, the learning operator (3.22) is given by

$$L(\omega) = \frac{S_{\mathrm{in}}(\omega)G^{*}(\omega)}{\gamma_{\mathrm{ILC}} + G(\omega)S_{\mathrm{in}}(\omega)G^{*}(\omega)} \tag{4.20}$$

using $S_{\nu\nu}(i\omega) = S_{\mathrm{in}}(\omega)$ to shape the learning behavior. Note that the Hermitian conjugate $(\cdot)^{\mathrm{H}}$ reduces to the complex conjugate $(\cdot)^{*}$ in the scalar case.

Proposition 1. *For $S_{\mathrm{in}}(\omega)$ bounded away from zero, the sequence of input pulses $\hat{E}_{\mathrm{v,in}}^{n}(\omega)$ generated by the ILC law (4.18), with (4.19) and (4.20) applied to the reduced linear model (4.17) stays bounded for any arbitrary desired pulse $\hat{E}_{\mathrm{out}}^{d}(\omega)$. For all ω where the input constraints (4.2) are not violated, the output pulse converges to the desired pulse $\hat{E}_{\mathrm{out}}^{n}(\omega) \to \hat{E}_{\mathrm{out}}^{d}(\omega)$.*

Proof. The evolution of the input error $\hat{e}^{n}(\omega) = \hat{E}_{\mathrm{v,in}}^{\mathrm{d}}(\omega) - \hat{E}_{\mathrm{v,in}}^{n}(\omega)$ with a desired input pulse fulfilling $\hat{E}_{\mathrm{out}}^{\mathrm{d}}(\omega) = G(\omega)\hat{E}_{\mathrm{v,in}}^{\mathrm{d}}(\omega)$ is given by

$$\hat{e}^{n+1}(\omega) = \hat{E}_{\mathrm{v,in}}^{\mathrm{d}}(\omega) - \mathcal{T}\left[\hat{E}_{\mathrm{v,in}}^{\mathrm{d}}(\omega) - (1 - L(\omega)G(\omega))\,\hat{e}^{n}(\omega)\right]. \tag{4.21}$$

Notice that the evolution of the input error and the evolution of the output error are equivalent as long as the input constraints are not violated, i.e., $\mathcal{T} = \mathcal{I}$. For all ω where this is the case, it follows from Theorem 1 that

$$\hat{e}^{\infty}(\omega) = 0. \tag{4.22}$$

If the constraints are violated, however, it can be deduced from (4.19) that $|\mathcal{T}[\hat{a}(\omega)]| \leq |\hat{a}(\omega)|$ and thus (4.21) yields

$$\left|\hat{e}^{n+1}(\omega)\right| \leq 2\left|\hat{E}_{\mathrm{v,in}}^{\mathrm{d}}(\omega)\right| + |1 - L(\omega)G(\omega)|\,|\hat{e}^{n}(\omega)|. \tag{4.23}$$

Die approbierte Originalversion dieser Dissertation ist in der TU Wien Bibliothek verfügbar.
The approved original version of this doctoral thesis is available at the TU Wien Bibliothek.
TU Bibliothek WIEN Your knowledge hub

Thus, for some arbitrary initial error $\hat{e}^0(\omega)$ it follows that

$$|\hat{e}^n(\omega)| \leq |1 - L(\omega)G(\omega)|^n \left|\hat{e}^0(\omega)\right| + 2\left|\hat{E}^{\mathrm{d}}_{\mathrm{v,in}}(\omega)\right| \sum_{k=0}^{n-1} |1 - L(\omega)G(\omega)|^k . \tag{4.24}$$

For $S_{\mathrm{in}}(\omega)$ bounded away from zero, it follows that $|1 - L(\omega)G(\omega)| \leq \beta < 1$ for all ω and, as a result, the input error stays bounded since

$$|\hat{e}^\infty(\omega)| = \lim_{n\to\infty} |\hat{e}^n(\omega)| \leq \frac{2}{1-\beta}\left|\hat{E}^{\mathrm{d}}_{\mathrm{v,in}}(\omega)\right| \tag{4.25}$$

and we assumed $\left|\hat{E}^{\mathrm{d}}_{\mathrm{v,in}}(\omega)\right|$ to be bounded. □

Since programmable spectral filters are usually specified in the frequency domain, the ILC law can be implemented directly as given in (4.18) together with (4.1). When choosing $S_{\mathrm{in}}(\omega)$, one may use any information on the expected input signal available. The value of γ_{ILC} is then serving as a threshold separating spectral ranges where learning occurs (i.e., $|G(\omega)S_{\mathrm{in}}(\omega)G^*(\omega)| \gg \gamma_{\mathrm{ILC}}$) from spectral ranges where learning is avoided (i.e., $|G(\omega)S_{\mathrm{in}}(\omega)G^*(\omega)| \ll \gamma_{\mathrm{ILC}}$).

4.3 Adaptive ILC

The Wiener-Filter-based learning operator presented above suffers from two distinct problems: First, it uses the stationary mean population inversion $\overline{\Delta\mathbf{N}^0}$ due to Assumption 2 and therefore considerably overestimates the gain exhibited by the CPA system for high energy pulses. While this reduces the speed of convergence significantly, it can also impair the stability assertions of Proposition 1, although simulation studies suggest that this is only the case for heavily saturating scenarios. Second, it requires an accurate model of the CPA system, in particular of the gain medium, in order to obtain a good learning gain. However, we do know corresponding input and output measurements, which can be used to adaptively estimate the CPAs current state. Therefore, we relax Assumption 2 by replacing it with

Assumption 3. *The drop of the population densities during a single pass of the laser pulse can be neglected for the pulse propagation.*

Using this assumption, one is still able to describe the pulse evolution by the single pass gain function given in (4.15) with some initial mean population inversion denoted by $\overline{\Delta\mathbf{N}^1}$. For the following pass, the same relation will hold true, but with some unknown depleted mean population inversion $\overline{\Delta\mathbf{N}^2}$. Proceeding in this way, one ends up with a total gain similar to (4.17) given by

$$\tilde{G}\left(\omega; \overline{\Delta\mathbf{N}^1}, \ldots, \overline{\Delta\mathbf{N}^{N_{\mathrm{RT}}}}\right) = \eta_{\mathrm{S}}\eta_{\mathrm{C}}\eta_{\mathrm{RC}}^{N_{\mathrm{RT}}-1} \prod_{k=1}^{N_{\mathrm{RT}}} G_{\mathrm{sp}}\left(\omega; \overline{\Delta\mathbf{N}^k}\right) \tag{4.26}$$

Die approbierte Originalversion dieser Dissertation ist in der TU Wien Bibliothek verfügbar.
The approved original version of this doctoral thesis is available at the TU Wien Bibliothek.
TU Bibliothek Your knowledge hub WIEN

with the unknown mean population inversions $\overline{\Delta\mathbf{N}^k}$, $k = 1, \ldots, N_{\mathrm{RT}}$. Using the definition of χ_j in (4.13) one can rewrite the equation above as

$$\tilde{G}\left(\omega; \overline{\Delta\mathbf{N}^1}, \ldots, \overline{\Delta\mathbf{N}^{N_{\mathrm{RT}}}}\right) = G\left(\omega; \overline{\Delta\mathbf{N}}\right), \tag{4.27}$$

where

$$\overline{\Delta\mathbf{N}} = \frac{1}{N_{\mathrm{RT}}} \sum_{k=1}^{N_{\mathrm{RT}}} \overline{\Delta\mathbf{N}^k} \tag{4.28}$$

denotes the averaged mean population inversions over the number of round trips N_{RT}. This shows that the reduced linear model derived in Section 4.1 can still be used if Assumption 2 is violated by replacing the stationary, unsaturated population inversions $\overline{\boldsymbol{\Delta}\mathbf{N}^0}$ with averaged mean population inversions $\overline{\boldsymbol{\Delta}\mathbf{N}}$ as long as Assumption 3 remains valid. This way, one effectively parametrizes the total transfer function of the reduced model by a finite set of parameters $\overline{\Delta\mathbf{N}} = \left[\overline{\Delta N_{51}}, \ldots, \overline{\Delta N_{54}}\right]^{\mathrm{T}}$ equal to the number of resonant (lasing) transitions of the gain medium, i.e. in the case of Ho:YAG by four parameters. Thus, the CPA's transfer function for the n-th pulse can be estimated using the optimization problem

$$\Delta\mathbf{N}^n_{\mathrm{opt}} = \underset{\overline{\Delta\mathbf{N}}}{\operatorname{argmin}}\ J^n(\overline{\Delta\mathbf{N}}), \tag{4.29}$$

with the objective function

$$J^n(\overline{\Delta\mathbf{N}}) = \left\| \hat{E}^n_{\mathrm{out}}(\cdot) - G(\,\cdot\,; \overline{\Delta\mathbf{N}})\hat{E}^n_{\mathrm{v,in}}(\cdot) \right\|_2 \tag{4.30}$$

to find a suitable averaged mean population inversion $\Delta\mathbf{N}^n_{\mathrm{opt}}$ such that $G(\omega; \Delta\mathbf{N}^n_{\mathrm{opt}})$ optimally reproduces the measured input-output behavior. The adaptive ILC law is then given by (see (4.18)-(4.20))

$$\hat{E}^{n+1}_{\mathrm{v,in}}(\omega) = \mathcal{T}\left[\hat{E}^n_{\mathrm{v,in}}(\omega) + L^n(\omega)\left(\hat{E}^{\mathrm{d}}_{\mathrm{out}}(\omega) - \hat{E}^n_{\mathrm{out}}(\omega)\right)\right], \tag{4.31}$$

with the adaptive learning operator

$$L^n(\omega) = \frac{S^n_{\mathrm{in}}(\omega) G^*(\omega; \Delta\mathbf{N}^n_{\mathrm{opt}})}{\gamma_{\mathrm{ILC}} + G(\omega; \Delta\mathbf{N}^n_{\mathrm{opt}}) S^n_{\mathrm{in}}(\omega) G^*(\omega; \Delta\mathbf{N}^n_{\mathrm{opt}})}\ . \tag{4.32}$$

Since the transfer function is changing from iteration to iteration, $S^n_{\mathrm{in}}(\omega)$ is also allowed to vary with iterations for the sake of completeness.

Since the pulse energy is equivalent with the squared L^2-norm, it is convenient to use the output error energy analogous to (2.6)

$$W^n_{\mathrm{err}} = \frac{A_{\mathrm{B}}}{2Z_0} \left\| E^{\mathrm{d}}_{\mathrm{out}} - E^n_{\mathrm{out}} \right\|_2^2 \tag{4.33}$$

to illustrate the convergence behavior. In Figure 4.2, the difference in the convergence speed is shown for laser pulses with a total energy of 100 µJ, 1 mJ and

Die approbierte Originalversion dieser Dissertation ist in der TU Wien Bibliothek verfügbar.
The approved original version of this doctoral thesis is available at the TU Wien Bibliothek.
TU Bibliothek WIEN Your knowledge hub

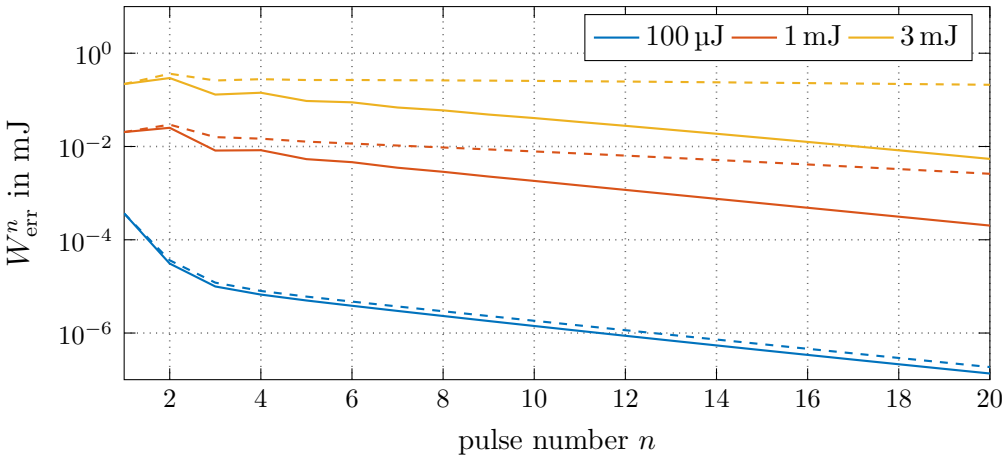

Figure 4.2: Evolution of the error energy W^n_{err} according to (4.33)for adaptive (solid line) and non-adaptive (dashed line) ILC strategies for a laser pulse with 100 µJ, 1 mJ and 3 mJ, respectively. For the 3 mJ pulse, the non-adaptive ILC strategy is not able to generate the desired output pulse and tends to diverge.

3 mJ, respectively. The initial population is chosen as a solution to (4.4), i.e. the CPA is fully pumped. The 100 µJ pulse is too weak to significantly deplete the population levels, which is why the adaptive and the non-adaptive ILC strategy converge at roughly the same rate. The 1 mJ pulse produces some saturation effects but still both ILC strategies converge to the desired pulse, although with a significant difference in convergence speed. For the heavily saturating 3 mJ pulse, the non-adaptive ILC strategy accumulates phase errors due to the increasingly erroneous reduced model and tends to diverge. In contrast, the adaptive ILC strategy is generating the desired pulse perfectly.

The presented approach is a fast and simple way to consistently estimate the observed transfer function based on unknown population densities. Since the values of κ_j in (2.25) are rarely known, this approach is able to estimate the combined quantity $\kappa_j \Delta N_{5j}$. Moreover, it is easy to extend the optimization problem (4.29) such that it includes the unknown quantities ω_j and $\Delta\omega_j$ and possibly an overall scaling factor $\eta = \eta_{\mathrm{S}} \eta_{\mathrm{C}} \eta_{\mathrm{RC}}^{N_{\mathrm{RT}}-1}$. Thus, the proposed algorithm is able to handle arbitrary gain media without the burden of identifying the complex system dynamics. Only a given number of resonant lasing transitions is required, which can be easily obtained by suitable measurements.

Die approbierte Originalversion dieser Dissertation ist in der TU Wien Bibliothek verfügbar.
The approved original version of this doctoral thesis is available at the TU Wien Bibliothek.
TU Bibliothek WIEN Your knowledge hub

4.4 Simulation results for the experimentally validated model

To demonstrate the algorithm presented in the previous section in more detail, we apply the adaptive ILC scheme consisting of the optimization problem (4.29) and the ILC law (4.31) with (4.19) and (4.32) to the mathematical model derived in Chapter 2. This model was parametrized by experimental data using the method given in Appendix B. Although the presented approach is able to handle arbitrary shaped pulses, let us consider a simple and common Gaussian pulse profile as desired pulse shape at first. Thus, for a pulse with the desired energy $W_{\text{out}}^{\text{d}}$ the desired pulse is given by

$$\hat{E}_{\text{out}}^{\text{d}}(\omega) = \sqrt{\frac{4\sqrt{\pi}Z_0 W_{\text{out}}^{\text{d}}}{A_{\text{B}}\Delta\omega^{\text{d}}}} \exp\left[-\left(\frac{\omega-\omega_0^{\text{d}}}{\sqrt{2}\Delta\omega^{\text{d}}}\right)^2\right], \tag{4.34}$$

with the desired central frequency ω_0^{d} and the desired spectral width $\Delta\omega^{\text{d}}$. For the following simulation examples, a desired central frequency of $\omega_0^{\text{d}} = 8.9998 \cdot 10^{14}\,\text{rad/s}$ and a spectral width of $\Delta\omega^{\text{d}} = 8.2116 \cdot 10^{11}\,\text{rad/s}$ are chosen. The initial population densities before the first pulse enters the CPA system are assumed to be fully pumped and thus can be obtained by solving (4.4). Finally, the CPA system is fed by (measured) 29.4 nJ seed pulses at a repetition rate of $f_{\text{rep}} = 1\,\text{kHz}$ and the pulse stays inside the resonator for $N_{\text{RT}} = 23$ round-trips. All further parameters are listed in Table E.1.

Concerning the adaptive ILC law, one has to choose a suitable function $S_{\text{in}}^n(\omega)$ and the regularization parameter γ_{ILC}. In the absence of any more reliable information, we set $S_{\text{in}}^n(\omega) = \left(|\hat{E}_{\text{out}}^{\text{d}}(\omega)|/|G(\omega)|\right)^2$ for simplicity. Thus, the learning operator (4.32) is reduced to

$$L^n(\omega) = \frac{1}{G(\omega;\Delta\mathbf{N}_{\text{opt}}^n)} \frac{|\hat{E}_{\text{out}}^{\text{d}}(\omega)|^2}{\gamma_{\text{ILC}} + |\hat{E}_{\text{out}}^{\text{d}}(\omega)|^2}, \tag{4.35}$$

which corresponds to the inverse plant with a frequency-dependent weighting factor determined by the desired output pulse. As mentioned in Section 4.2, the regularization parameter γ_{ILC} is separating spectral ranges where learning is desirable from those where learning should be avoided relative to $|\hat{E}_{\text{out}}^{\text{d}}(\omega)|^2$.

Remark 17. *Strictly speaking, this choice is violating Proposition 1 since $S_{in}^n(\omega)$ is not bounded away from zero for $\omega \to \infty$. Thus, the rate of convergence is becoming arbitrary small for high frequencies. However, this does not pose a problem as the considered frequency range is finite in all applications.*

Remark 18. *As explained in Section 2.1, stretcher and compressor were chosen such that they compensate each other perfectly. As a result, the spectral filter*

Die approbierte Originalversion dieser Dissertation ist in der TU Wien Bibliothek verfügbar.
The approved original version of this doctoral thesis is available at the TU Wien Bibliothek.
TU Bibliothek Your knowledge hub WIEN

$G_F^n(\omega)$ has to compensate the quadratic phase which results from the dispersion introduced by the nonlinear Schrödinger equation (2.23). In practice, quadratic and cubic phase components are usually handled by adjusting the stretcher's phase coefficients $\varphi_{S,2}$ and $\varphi_{S,3}$ instead of using the spectral filter $G_F^n(\omega)$. To visualize the details of the input filter's phase shift, quadratic and cubic phase components have been eliminated in the following plots for illustration purposes.

4.4.1 Mildly saturating pulses (1 mJ)

The first simulation example considers a desired 1 mJ pulse using a pumping source with an optical power of 35 W (i.e., a pumping intensity of $I_0 = {}^{P_{\text{pump}}}/_{A_{\text{B}}} = 6.96 \cdot 10^7\,\text{W/m}^2$) as shown in Figure 4.3. The first plot shows the evolution of the mean population inversion $\overline{\Delta N_{5j}^n}$ before and after the regeneration period, i.e., $\overline{N_{5,\text{out}}^n(z) - N_{j,\text{out}}^n(z)}$ and $\overline{N_{5,\text{pulse}}^{n+1,1}(z) - N_{j,\text{pulse}}^{n+1,1}(z)}$ in Figure 2.5, respectively. The corresponding output, input and error energy levels are shown in the second plot. The two lower plots depict the output pulse E_{out}^n and the input filter G_{F}^n at the last iteration $n = 40$. As one can see, the mean population inversions $\overline{\Delta N_{5j}^n}$ are slowly depleting due to the energy extracted by the amplified pulses. However, the final steady-state level where the pumping process is fully compensating those energy losses is not too far away from the initial unsaturated level. The output pulse's error energy W_{err}^n according to (4.33) is converging fast and after 40 pulses it is already a factor of 10^5 smaller than the desired energy W_{out}^d. The population-induced coupling of sequential pulses produces some zig zagging, see Figure 4.3, which is vanishing as the population inversion approaches its steady-state level. This effect can be reduced by increasing γ_{ILC} and thus reducing the learning gain at the expense of a reduced rate of convergence as shown in Figure 4.4. The output pulse after 40 iterations as shown in the third plot of Figure 4.3 is practically matching the desired pulse shape. Since the absolute value of the spectral filter $G_{\text{F}}^{40}(\omega)$ to achive this pulse is below one and the gain medium is not saturated, one can further increase the energy extracted from the CPA.

4.4.2 Limiting input constraints (3 mJ)

Increasing the desired energy to 3 mJ while still operating with the same pumping intensity, one can see in Figure 4.5 that now the input filter is limited by the constraints (2.11). This yields a distorted output pulse as shown in the third plot of Figure 4.5. While the extracted energy is lower than 3 mJ due to the input constraints, the mean population inversions have dropped significantly. One can observe that the increased pulse energy not only increases the difference of the population inversion before and after the regeneration period but also causes the steady-state inversions to deplete further, i.e., the equilibrium of energy extraction and regeneration settles at a lower level. Due to the active input constraints, the

Die approbierte Originalversion dieser Dissertation ist in der TU Wien Bibliothek verfügbar.
The approved original version of this doctoral thesis is available at the TU Wien Bibliothek.
TU Bibliothek WIEN Your knowledge hub

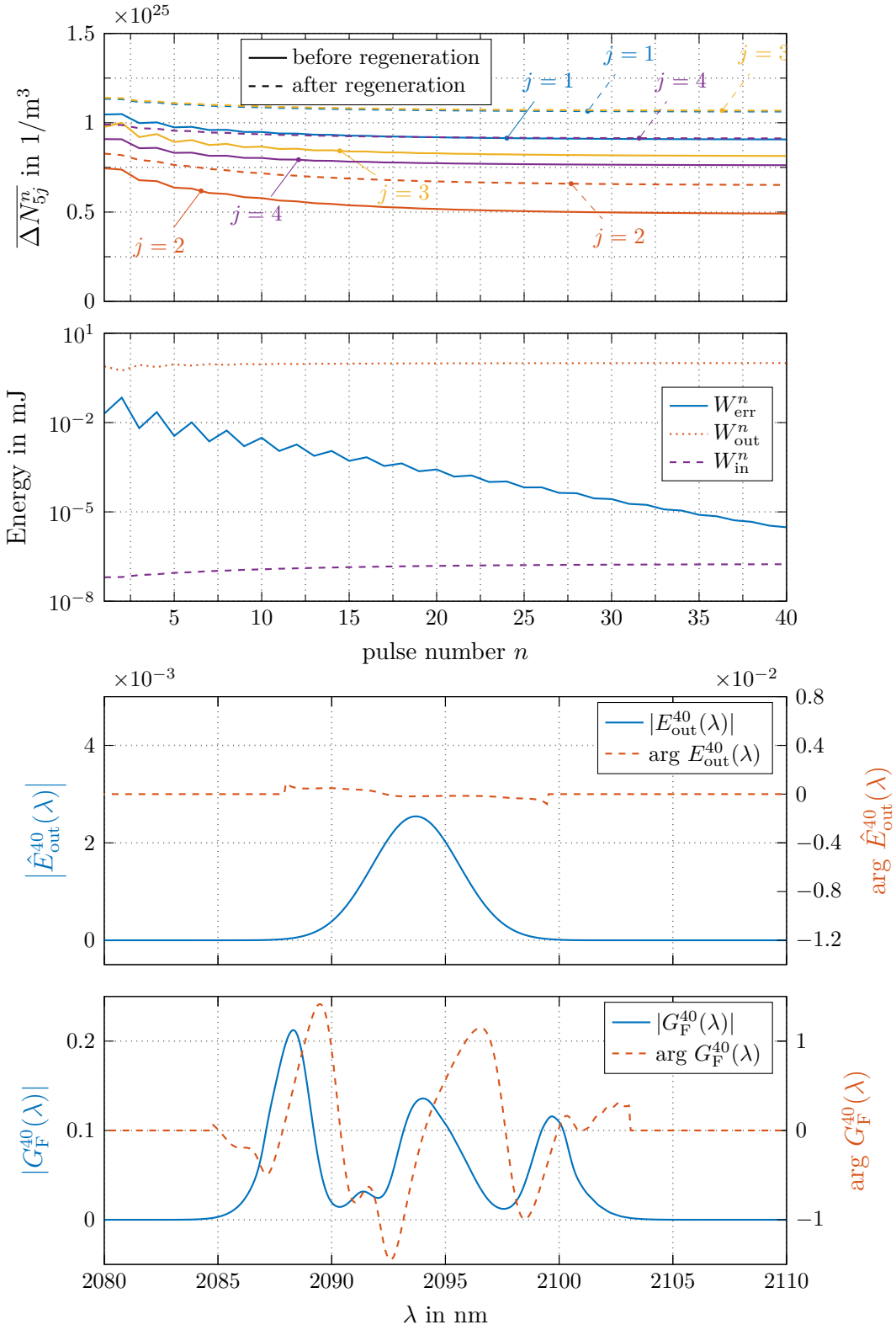

Figure 4.3: Convergence behavior of a 1 mJ pulse at 35 W pumping power using $\gamma_{\mathrm{ILC}} = 10^{-9}$.

Die approbierte Originalversion dieser Dissertation ist in der TU Wien Bibliothek verfügbar.
The approved original version of this doctoral thesis is available at the TU Wien Bibliothek.
TU Bibliothek Your knowledge hub WIEN

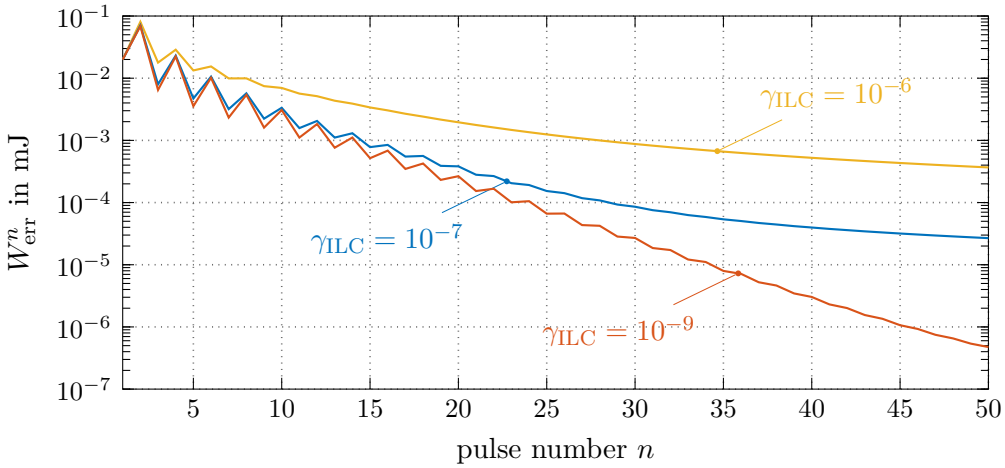

Figure 4.4: Evolution of the error energy for different values of the regularization parameter: $\gamma_{\mathrm{ILC}} = 10^{-6}$ (yellow), $\gamma_{\mathrm{ILC}} = 10^{-7}$ (blue), and $\gamma_{\mathrm{ILC}} = 10^{-9}$ (red).

output error is settling at a finite level. Notice that the error is decreasing for the first pulses and then rises slightly to its steady state as the population inversion increasingly depletes and the input constraints become active. The amplifier still has a small amount of energy stored after the amplification phase at steady state since all mean population inversions are positive. However, further analysis shows that the amplifier is operated close to its maximum power since the remaining gains of the laser medium are already canceled by the resonator losses.

4.4.3 Fully saturating pulses (3 mJ)

By increasing the power of the pumping source to 60 W (i.e., increasing the pumping intensity to $1.1937 \cdot 10^8\,\mathrm{W/m^2}$) one is able to generate the desired 3 mJ pulse, as shown in Figure 4.6. Due to the higher pumping intensity, the population inversion after the regeneration phase is raised. Since this also reduces the coupling of consecutive pulses, the zig zagging almost vanishes. The difference in the time domain between the constrained pulse according to Figure 4.5 and the output pulse according to Figure 4.6 is shown in Figure 4.7. For pulses much stronger than 3 mJ, the proposed learning law is struggling to cope with the effects of the neglected Kerr nonlinearity (see Assumption 1) and one would have to investigate methods that systematically take the pulse's acquired nonlinear phase components into account or circumvent the issue completely by increasing the stretching ratio of the CPA.

Die approbierte Originalversion dieser Dissertation ist in der TU Wien Bibliothek verfügbar.
The approved original version of this doctoral thesis is available at the TU Wien Bibliothek.
TU Bibliothek WIEN Your knowledge hub

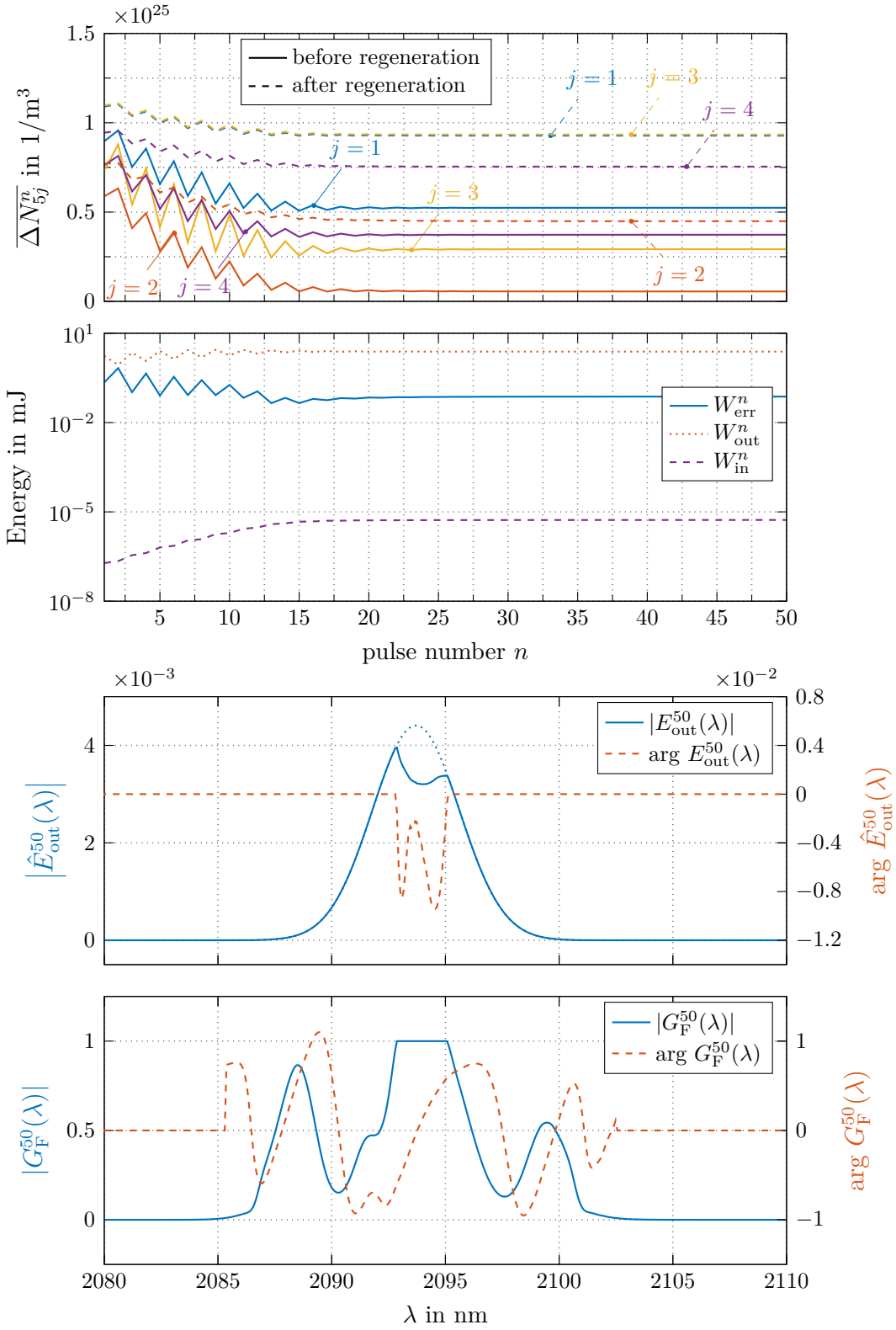

Figure 4.5: Convergence behavior of a 3 mJ pulse at 35 W pumping power using $\gamma_{\mathrm{ILC}} = 10^{-9}$. The desired values of $|\hat{E}_{\mathrm{out}}|$ are indicated by a dotted line for reference.

Die approbierte Originalversion dieser Dissertation ist in der TU Wien Bibliothek verfügbar.
The approved original version of this doctoral thesis is available at the TU Wien Bibliothek.
TU Bibliothek WIEN Your knowledge hub

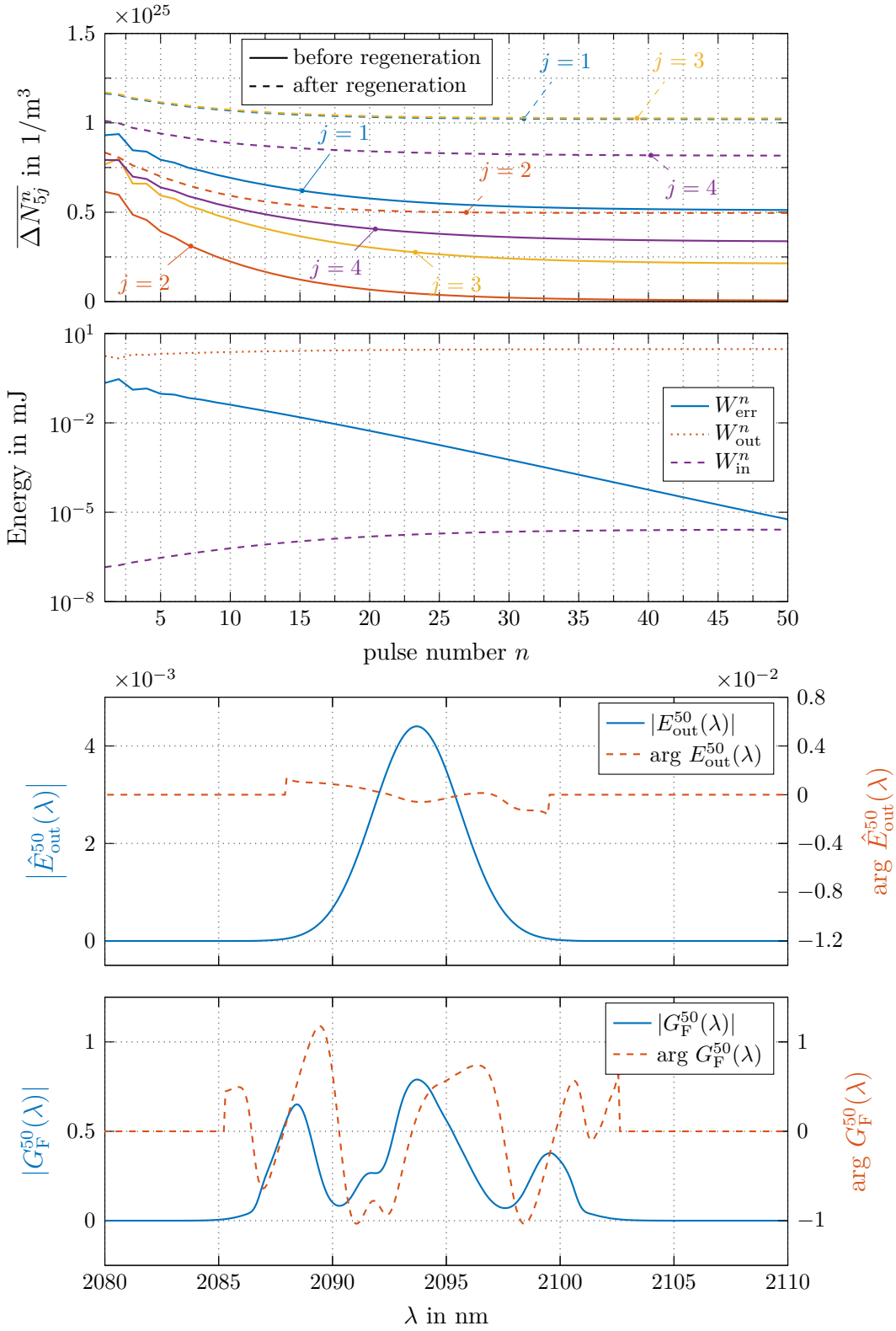

Figure 4.6: Convergence behavior of a 3 mJ pulse at 60 W pumping power using $\gamma_{\mathrm{ILC}} = 10^{-9}$.

Die approbierte Originalversion dieser Dissertation ist in der TU Wien Bibliothek verfügbar.
The approved original version of this doctoral thesis is available at the TU Wien Bibliothek.
TU Bibliothek Your knowledge hub WIEN

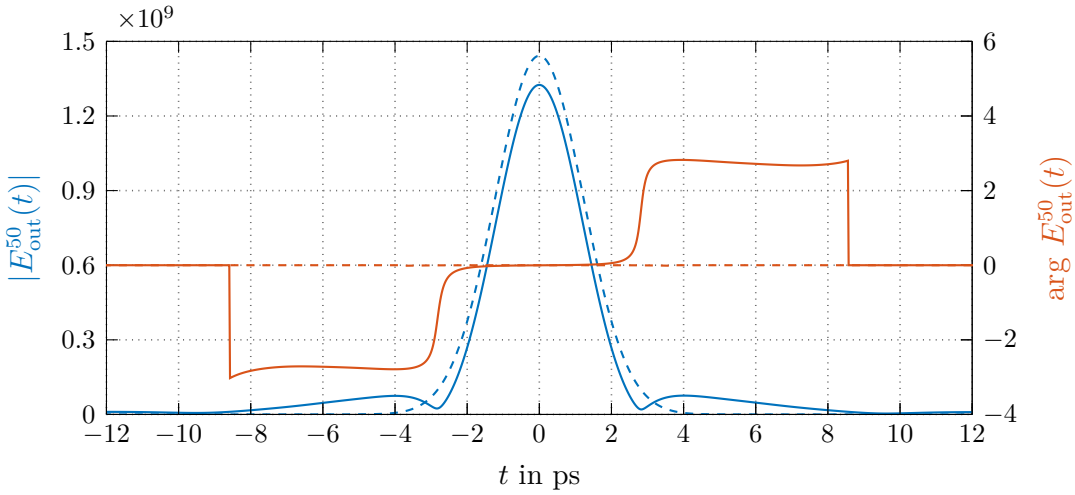

Figure 4.7: A comparison of the constrained (solid line) and unconstrained (dashed line) temporal output pulse $E^{50}_{\text{out}}(t)$ corresponding to Figure 4.5 and Figure 4.6, respectively.

4.4.4 Triple pulse

As mentioned above, the presented method is able to generate arbitrarily shaped pulses as long as the desired pulse is within the capabilities of both the amplifier and the input filter. Figure 4.8 shows the learned input filter to obtain a superposition of three pulses by setting

$$\hat{E}^{\text{d}}_{\text{out}}(\omega) = A_0 \cos\left(\frac{5\,\omega}{2\,\Delta\omega^{\text{d}}}\right) \exp\left[-\left(\frac{\omega-\omega_0^{\text{d}}}{\sqrt{2}\Delta\omega^{\text{d}}}\right)^2\right], \tag{4.36}$$

with A_0 chosen such that the total pulse energy is 1.5 mJ.

Remark 19. *Since the desired pulse $\hat{E}^{d}_{out}(\omega)$ is zero for $5\omega/\pi\Delta\omega^{d} = \pm 1, 3, 5, \ldots$, it follows that the chosen $S_{in}(\omega)$ in (4.35) is not bounded away from zero. Similar to Remark 9, this does not cause any practical problems as illustrated in this example. Notice that the artifacts visible at the phase of the resulting input filter G_F in Figure 4.8 are due to the ill-posedness of the amplitude-phase representation for vanishing amplitudes only.*

4.5 Pulse-to-pulse dynamics

The previous section clearly shows that the presented ILC law is able to track a desired output pulse E^{d}_{out} as long as it is within the range of admissible output pulses given by the energy supply due to the pumping process and the input

Die approbierte Originalversion dieser Dissertation ist in der TU Wien Bibliothek verfügbar.
The approved original version of this doctoral thesis is available at the TU Wien Bibliothek.
TU Bibliothek WIEN Your knowledge hub

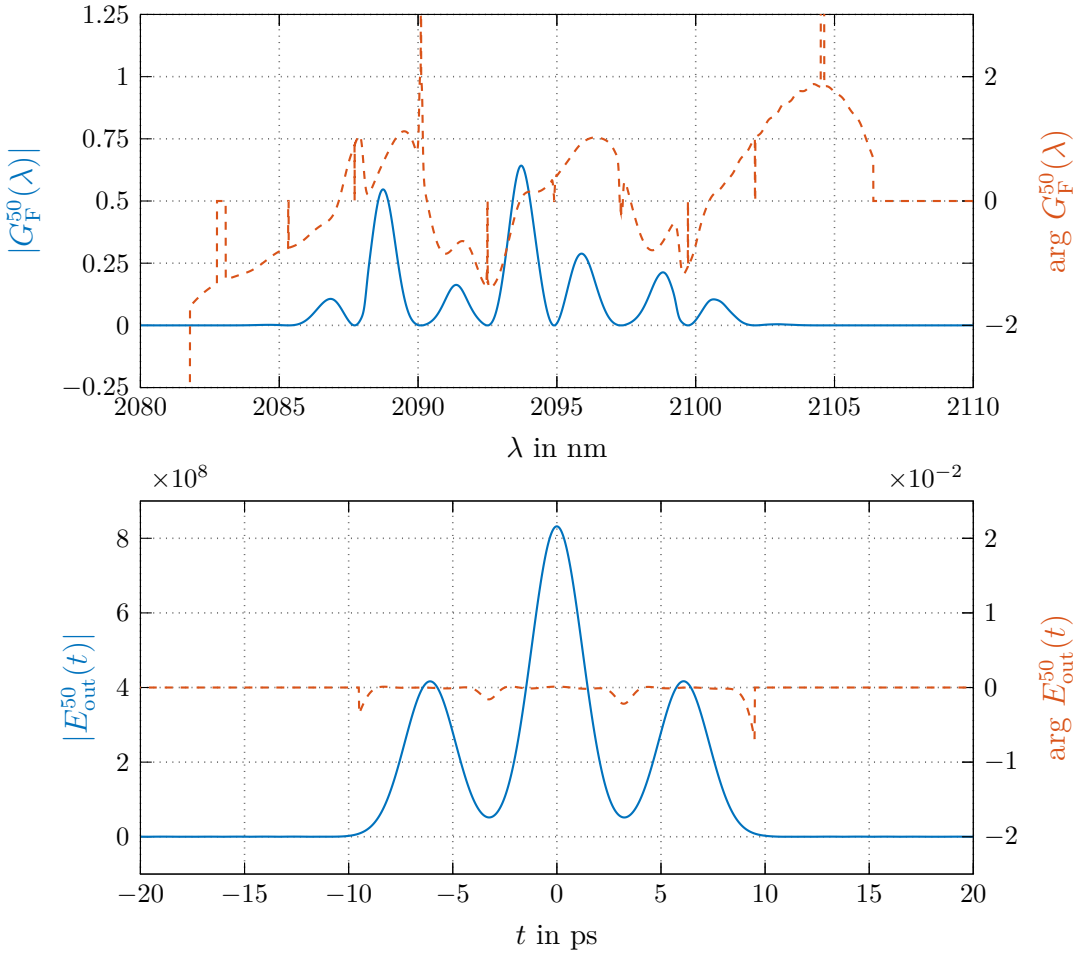

Figure 4.8: Input filter $G_{\mathrm{F}}^{50}(\lambda)$ and the resulting output pulse $E_{\mathrm{out}}^{50}(t)$ for the desired pulse (4.36) using $\gamma_{\mathrm{ILC}} = 1 \cdot 10^{-8}$. Notice that the artifacts visible at the input filter are only due to the phase representation and not caused by the ILC law.

Die approbierte Originalversion dieser Dissertation ist in der TU Wien Bibliothek verfügbar.
The approved original version of this doctoral thesis is available at the TU Wien Bibliothek.
TU Bibliothek Your knowledge hub WIEN

constraints. Additionally, the coupling of subsequent pulses due to the population dynamics is interacting with the learning law, as illustrated in Figure 4.4. To get hold of this pulse-to-pulse dynamics, we introduce the state variable

$$\mathbf{x}^n = \begin{bmatrix} N^{n,1}_{1,\text{pulse}}(\cdot) \\ \vdots \\ N^{n,1}_{5,\text{pulse}}(\cdot) \end{bmatrix} \in \mathcal{X} = L^1\left([0,L];\mathbb{R}^5\right) \tag{4.37a}$$

and the input and output variables

$$\mathbf{u}^n = E^n_{\text{v,in}}(\cdot) \in \mathcal{P} = L^2(S;\mathbb{C}) \cap L^\infty(S;\mathbb{C}) \tag{4.37b}$$

$$\mathbf{y}^n = E^n_{\text{out}}(\cdot) \in \mathcal{P}, \tag{4.37c}$$

with the compact subset $S \subset \mathbb{R}_{\geq 0}$. Without going into details, the complete description of the pulse amplification process as shown in Figure 2.5 can be written as

$$\mathbf{x}^{n+1} = f(\mathbf{x}^n, \mathbf{u}^n) \tag{4.38a}$$

$$\mathbf{y}^n = h(\mathbf{x}^n, \mathbf{u}^n) \tag{4.38b}$$

using the dynamic and output maps $f : \mathcal{X} \times \mathcal{P} \to \mathcal{X}$ and $g : \mathcal{X} \times \mathcal{P} \to \mathcal{P}$, respectively. Thus, the CPA can be considered a discrete-time dynamical system on an infinite-dimensional state-space $\mathcal{X}$ with inputs and outputs belonging to $\mathcal{P}$. In the same way, the ILC laws (4.18) and (4.31) can be written as

$$\mathbf{u}^{n+1} = g_{\text{ILC}}(\mathbf{y}^n, \mathbf{u}^n) \tag{4.39}$$

where $g_{\text{ILC}} : \mathcal{P} \times \mathcal{P} \to \mathcal{P}$ is an affine map for the non-adaptive ILC law (4.18) and a general nonlinear map for the adaptive ILC law (4.31). As a result, when designing ILC laws to iteratively shape the output pulse one is introducing feedback to the pulse-to-pulse dynamics of the CPA as already indicated by Figure 4.4. The effects of this feedback can be quite severe and can even destabilize an otherwise stable CPA as illustrated in Figure 4.9 and Figure 4.10 unless the learning action is dramatically reduced by increasing γ_{ILC}.

Up to now, we have assumed that each single output pulse is measureable. While such single-shot measurements are possible in theory and advanced schemes have been proposed recently in [102], they are experimentally quite demanding and the required phase retrieval algorithms are computationally complex and quite difficult to apply on a pulse-to-pulse basis. Thus, one is usually limited to steady-state measurements in most experimental setups, which are typically available after a certain number of output pulses. Under these limitations, applying the ILC law only for each N_{M}-th pulse effectively evades the feedback issues discussed above at the price of a slower convergence rate (see Figure 4.9 with $N_{\text{M}} = 5$). Such an approach is particularly in line with the proposed adaptive ILC law (4.31),

Die approbierte Originalversion dieser Dissertation ist in der TU Wien Bibliothek verfügbar.
The approved original version of this doctoral thesis is available at the TU Wien Bibliothek.
TU Bibliothek WIEN Your knowledge hub

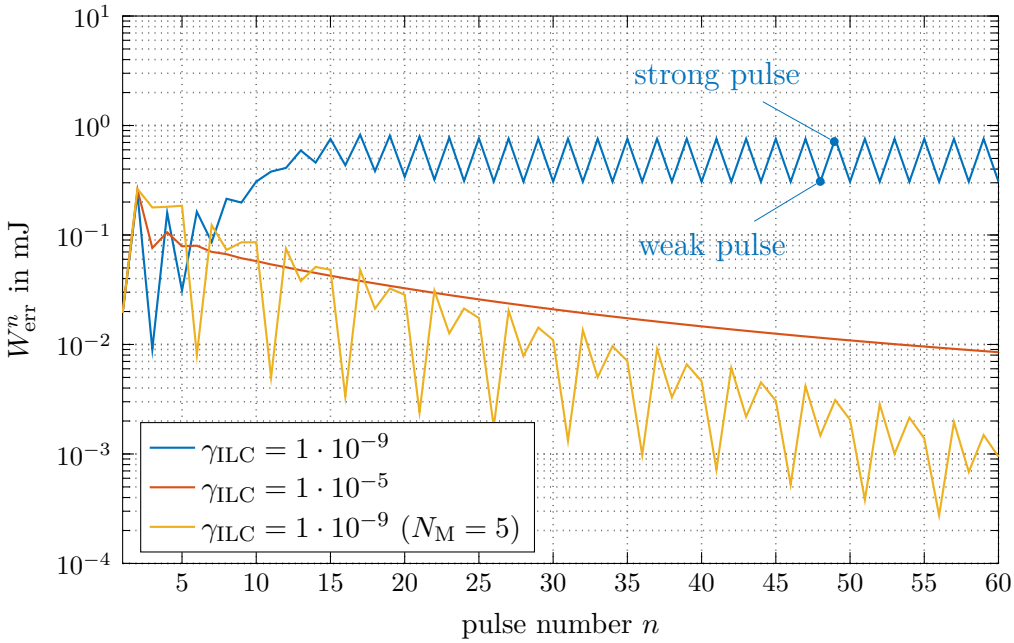

Figure 4.9: Example for the instability introduced by the (adaptive) ILC law (4.31) at 20 W pumping power due to its implicit modification of the the pulse-to-pulse dynamics (4.38a) for $\gamma_{\mathrm{ILC}} = 1 \cdot 10^{-9}$. Increasing the regularization parameter to $\gamma_{\mathrm{ILC}} = 1 \cdot 10^{-5}$ can eliminate such instabilities at the cost of a very slow convergence behavior. Applying the learning law each fifth pulse (i.e., $N_{\mathrm{M}} = 5$) already avoids this parasitic feedback. However, each learning step still significantly excites the amplifier's pulse-to-pulse dynamics. In the unstable scenario, the coupling between the ILC law and the pulse-to-pulse dynamics eventually converges to a limit cycle comprising a weak and a strong pulse. The corresponding output pulses and input filters are depicted in Figure 4.10.

as it estimates the *current* averaged mean population inversion $\Delta\mathbf{N}^n_{\mathrm{opt}}$ by given input and output measurements and uses this estimate to adapt the *next* virtual input pulse. This procedure implicitly assumes that the current state is a good approximation of the next state, i.e., $\mathbf{x}^n \approx \mathbf{x}^{n+1}$, which is only true in the vicinity of a steady state. As a result, applying the ILC law to each fifth pulse with $\gamma_{\mathrm{ILC}} = 1 \cdot 10^{-9}$ offers a superior effective convergence speed compared to applying the ILC law to each pulse with $\gamma_{\mathrm{ILC}} = 1 \cdot 10^{-5}$ to ensure stability (see Figure 4.9).

All the considerations above require a pulse-to-pulse dynamic (4.38a) that is inherently stable. However, it is known from the literature [31] that regenerative amplifiers can eventually become unstable. In light of this discussion, a more detailed analysis of methods to influence the pulse-to-pulse dynamics by feedback seems interesting. To this end, one will have to rethink potential measurements for feedback controllers as well as ways to reduce the model complexity.

Die approbierte Originalversion dieser Dissertation ist in der TU Wien Bibliothek verfügbar.
The approved original version of this doctoral thesis is available at the TU Wien Bibliothek.
TU WIEN Bibliothek Your knowledge hub

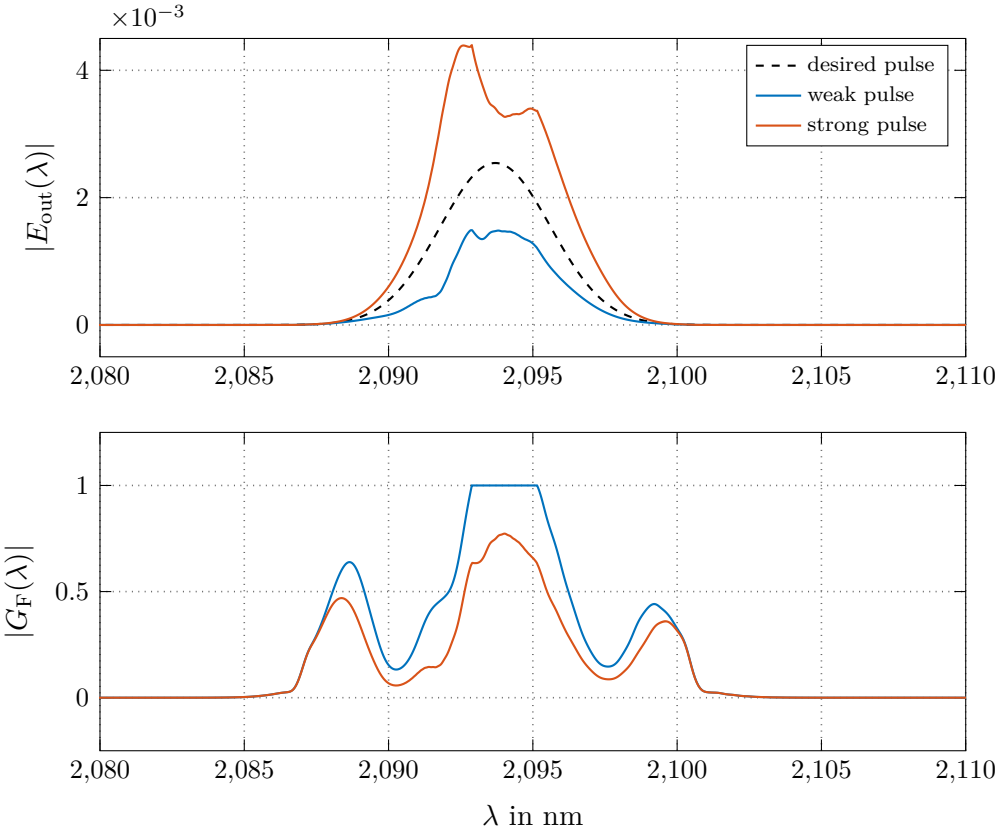

Figure 4.10: Limit cycle of the destabilized CPA shown in Figure 4.9 (for the case $\gamma_{\mathrm{ILC}} = 1 \cdot 10^{-9}$) due to the feedback introduced by the adaptive ILC law (4.31). The output pulse E_{out} is iterating between a strong (i.e., stronger than desired) and a weak (i.e., weaker than desired) pulse. However, due to the dynamics of the CPA, the strong pulse corresponds to a weak virtual input pulse $E_{\mathrm{v,in}}$ and thus a lower input filter G_{F} and vice versa.

Die approbierte Originalversion dieser Dissertation ist in der TU Wien Bibliothek verfügbar.
The approved original version of this doctoral thesis is available at the TU Wien Bibliothek.
TU Bibliothek Your knowledge hub WIEN

CHAPTER 5

Active Feedback Stabilization of Regenerative Amplifiers

Based on the detailed mathematical model presented in Chapter 2, an iterative pulse-shape control was presented in the previous chapter. The focus on controlling the shape of the laser pulse required to model the distribution of energy over the spectrum of the pulse in detail, while the coupling of subsequent pulses was neglected for the task at hand. In Section 4.5, we have shown that these simplifications can be problematic in specific cases where the learning law starts to excite the pulse-to-pulse dynamics. As pointed out, this is not very restrictive for practical applications, as spectral measurement techniques such as FROG [38] typically (but not necessarily) require a significant number of output pulses to complete a single measurement. Thus, the regenerative amplifier is usually given enough time to settle at a steady state after each modification of the spectral filter due to the learning law.

However, as noted in Chapter 2, the coupling of subsequent pulses can be quite significant. Due to the highly nonlinear characteristics of the laser dynamics, this can lead to an inherently unstable and even chaotic behavior depending on the exact parameters of the regenerative amplifier. While the general field of nonlinear laser dynamics has received significant attention from the scientific community, there are only few papers dedicated to regenerative amplifiers. One of the first reports of instabilities and chaotic behavior in [103] was followed by a more detailed mathematical analysis of the dynamics in [31] by using a simple energy model. As it turns out, the dynamics of a regenerative amplifier are mainly influenced by the available pumping power, the number of round-trips, the energy of the seed pulse and the desired pulse repetition rate.

In the following, let us briefly illustrate the effects of this instability for different optical pumping powers P_{pump} while keeping all other parameters constant. For pumping powers below a certain threshold power, the gain of the laser medium

Die approbierte Originalversion dieser Dissertation ist in der TU Wien Bibliothek verfügbar.
The approved original version of this doctoral thesis is available at the TU Wien Bibliothek.
TU WIEN Bibliothek Your knowledge hub

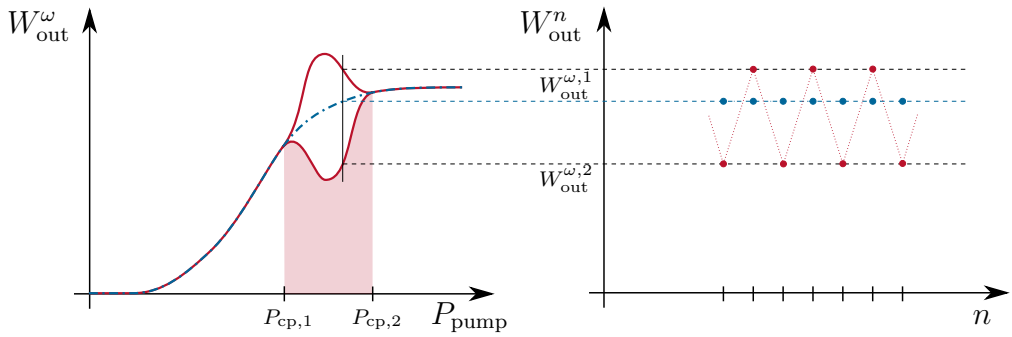

Figure 5.1: Illustration of the destabilizing effect of the pulse-to-pulse dynamics for two different sets of parameters with varying levels of optical pumping powers P_{pump}. The first parameter set (blue) yields a stable amplifier for all pumping powers. The second set (red) exhibits a period-doubling bifurcation between the two critical pumping powers $P_{cp,1}$ and $P_{cp,2}$ with the ω-limit set containing two points $W^{\omega,1}_{\text{out}}$ and $W^{\omega,2}_{\text{out}}$.

does not exceed the losses during one round-trip and thus the output pulse energy W^{s}_{out} is close to zero. Above the threshold, higher pumping powers yield stronger output pulses until the laser medium starts to saturate, see Figure 5.1. Depending on the values of the other parameters of the regenerative amplifier, it can happen that the system dynamics exhibits period-doubling bifurcations above a critical pumping power $P_{cp,1}$. In this case, the ω-limit set contains two or more points and the sequence of output pulses converges to a periodic orbit for $n \to \infty$. For specific parameter combinations, the dynamic behavior can even show chaotic properties resulting in a completely aperiodic orbit (see [31]). Above a pumping power $P_{cp,2}$, the system dynamics become stable again.

From a design perspective, the existence of unstable operational regions is highly unsatisfying. First of all, the unstable parameter regions are located in the vicinity of the region with the highest possible output energy [33]. Additionally, the operation regime above $P_{cp,2}$ is avoided because passing through the instability region may produce pulse energies beyond the destruction threshold of the laser medium. Since the repetition rate is usually given by the desired application, the remaining approach to suppress instabilities by design is to increase the available energy of the seed pulses [32, 33]. This, however, requires additional amplification stages as typical pulse sources like mode-locked lasers are only able to deliver pulses with a few nano joule. With the availability of automatically adjustable input filters, the question of feedback stabilization by modulating the input pulse energy arises naturally.

In this chapter, we present feedback stabilization methods for regenerative amplifiers. To this end, an opposite perspective to the previous chapter is taken by only considering the inter-pulse coupling while neglecting its spectral properties.

Die approbierte Originalversion dieser Dissertation ist in der TU Wien Bibliothek verfügbar.
The approved original version of this doctoral thesis is available at the TU Wien Bibliothek.
TU Bibliothek WIEN Your knowledge hub

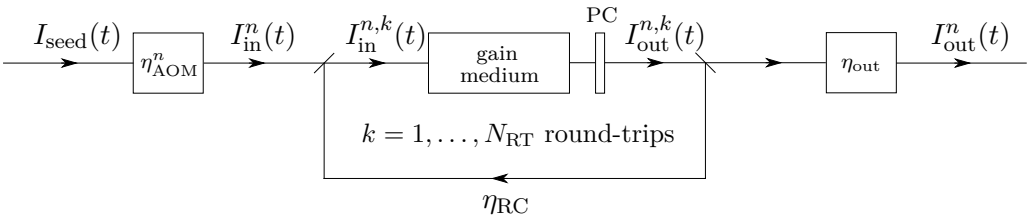

Figure 5.2: Schematic overview of a controlled regenerative amplifier.

The regenerative amplifier can thus be described by a simpler Frantz-Nodvik-based model [41, 66] which will be presented in Section 5.1. The resulting nonlinear discrete-time dynamical system can be considered a simplified energy-based description of the amplifier's pulse-to-pulse dynamics given in Section 4.5 and generalizes the energy-based model derived in [31]. The dynamics are analyzed in Section 5.2 and suitable feedback strategies are devised in Section 5.3 to stabilize the system in the vicinity of a given operating point. Building on these results, Section 5.4 develops a gain-scheduling solution to deal with adjustable pumping intensities that allows to safely steer the system into arbitrary operating points, both in the stable and unstable operating regime. Finally, some experimental results are presented in Section 5.5. All simulation scenarios presented in this chapter are performed using the parameters given in Table E.3.

5.1 Dynamical Frantz-Nodvik model of regenerative amplifiers

In cases the spectral properties of the pulse amplification process can be neglected, instead of using the rather complex Maxwell-Bloch equations as in Chapter 2, the laser light can be treated as a transport process of monochromatic photons conveying no additional phase information [66]. This is equivalent to describing the laser light merely by its intensity I (see [30, Chapter 10]) that can be connected to the Maxwell-Bloch equations by using the electric field E and its relationship to the intensity via $I = \frac{1}{2Z_0} EE^*$ as used in Chapter 2 to describe the effects of the pumping process (see Section 2.2.2). Such models, or more precisely their analytic solutions, are known as Frantz-Nodvik models [66]. By analogy with the model presented in Chapter 2, we will focus on the simplest case of a regenerative amplifier using a ring cavity as shown in Figure 5.2. Thus, seed pulses $I_{\text{seed}}(t)$ from a source with repetition rate f_{rep} pass some kind of modulation device[1] that is assumed to be an acousto-optic modulator (AOM). While AOMs can be

[1]This more neutral term was preferred compared to filter in the previous chapters since all spectral information has been removed from the model.

Die approbierte Originalversion dieser Dissertation ist in der TU Wien Bibliothek verfügbar.
The approved original version of this doctoral thesis is available at the TU Wien Bibliothek.

actuated quite fast, we only require a level of additional damping that can be adjusted for each individual seed pulse in this application. Thus, the resulting input pulse $I_{\text{in}}^n(t)$ is given by

$$I_{\text{in}}^n(t) = \eta_{\text{AOM}}^n I_{\text{seed}}(t), \tag{5.1}$$

with the AOM's adjustable loss factor η_{AOM}^n. It is assumed that further injection losses are already included in $I_{\text{seed}}(t)$ and thus $\eta_{\text{AOM}}^n \in [0, 1]$. The resulting pulse $I_{\text{in}}^n(t)$ is then injected into the resonator cavity with concentrated losses η_{RC}. Similar to Chapter 2, we will use $I_{\text{in}}^{n,k}(t)$ and $I_{\text{out}}^{n,k}(t)$ to denote the k-th round-trip of the n-th input and output pulse, respectively. The final amplified pulse after N_{RT} round-trips is then released by switching the Pockel's cell (PC) and all losses due to the pulse extraction are again subsumed in η_{out}, i.e.,

$$I_{\text{out}}^n(t) = \eta_{\text{out}} I_{\text{out}}^{n,N_{\text{RT}}}(t). \tag{5.2}$$

To obtain a dynamical model of the regenerative amplifier, we will proceed in some way as in Chapter 2 and split the complete amplification process in a pulse model and a pump model. However, this requires some knowledge of the structure of the gain medium first.

5.1.1 Four-level and Quasi-three-level laser materials

When neglecting the spectral properties of the pulse amplification process, there is no need to consider the fine structure of the material as in Chapter 2, but the fundamental structure - whether it behaves as a three-level, four-level or quasi-three-level material - is still important. Due to the high pumping powers required to achieve lasing gains (i.e., to achieve population inversion on the lasing transition) for three-level laser materials, four-level or quasi-three-level laser materials such as neodymium-doped or ytterbium- and erbium-doped media, respectively, are quite popular for laser amplifiers. In particular for applications where a high power efficiency is required, the low quantum defect of quasi-three-level materials is advantageous.

Without loss of generality we therefore want to consider a model for quasi-three-level materials in the remainder of this chapter. This also includes four-level materials as a special case. To model the atomic population dynamics, we assume an energy level diagram as depicted in Figure 5.3. The energy difference between the ground level E_0 and the first excited state E_1 is small enough so that the excited state E_1 is populated at thermal equilibrium for non-cryogenic temperatures. Thus, there exist upward and downward relaxation processes with the relaxation rates γ_{01} and γ_{10}. The same situation applies to the upper pair of energy levels E_2 and E_3 and their associated relaxation rates γ_{23} and γ_{32}, respectively. The pumping process excites particles from the ground state to the uppermost state and the population difference between the energy levels E_2 and

Die approbierte Originalversion dieser Dissertation ist in der TU Wien Bibliothek verfügbar.
The approved original version of this doctoral thesis is available at the TU Wien Bibliothek.
TU Bibliothek WIEN Your knowledge hub

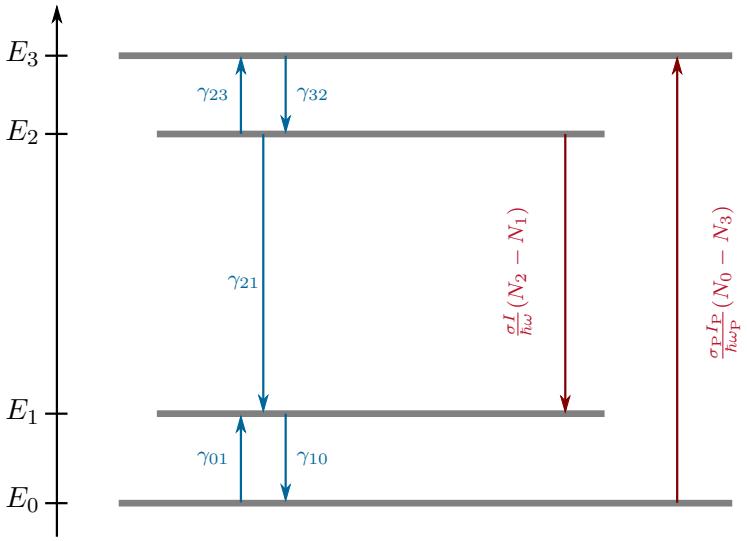

Figure 5.3: Energy level diagram of a quasi-three-level laser material.

E_1 can be used for lasing. Additionally, there is a single downward relaxation transition between E_2 and E_1 to model the natural decay of excited states.

Using the energy level scheme Figure 5.3, one readily obtains the corresponding set of atomic rate equations

$$\frac{\partial N_3}{\partial t} = -\gamma_{32}N_3 + \gamma_{23}N_2 + \frac{\sigma_P I_P}{\hbar\omega_P}(N_0 - N_3) \tag{5.3a}$$

$$\frac{\partial N_2}{\partial t} = -\gamma_{21}N_2 + \gamma_{32}N_3 - \gamma_{23}N_2 - \frac{\sigma I}{\hbar\omega}(N_2 - N_1) \tag{5.3b}$$

$$\frac{\partial N_1}{\partial t} = -\gamma_{10}N_1 + \gamma_{21}N_2 + \gamma_{01}N_0 + \frac{\sigma I}{\hbar\omega}(N_2 - N_1) \tag{5.3c}$$

$$\frac{\partial N_0}{\partial t} = -\gamma_{01}N_0 + \gamma_{10}N_1 - \frac{\sigma_P I_P}{\hbar\omega_P}(N_0 - N_3) \tag{5.3d}$$

to describe the evolution of the population densities $N_i, i = 0, \ldots, 3$. As in Chapter 2, the sum of the population densities is determined by the density of the dopant, i.e. $\sum_{i=0}^{3} N_i = N_{\text{dop}}$.

For the case that the radiative and nonradiative surroundings of the doped atoms are at the same equilibrium temperature, the populations ultimately thermalize towards a Boltzmann distribution[2]. Therefore, the upward and downward directed relaxation rates have to satisfy the relationship [30, p. 202]

$$\frac{\gamma_{ij}}{\gamma_{ji}} = \exp\left(-\frac{E_j - E_i}{kT}\right) = B_{ij}, \tag{5.4}$$

[2]This fact is very intuitive but seemed to lack mathematical rigor for quite some time. A detailed discussion of the properties of rate equations can be found in [104].

Die approbierte Originalversion dieser Dissertation ist in der TU Wien Bibliothek verfügbar.
The approved original version of this doctoral thesis is available at the TU Wien Bibliothek.
TU Bibliothek WIEN Your knowledge hub

with the Boltzmann constant k and the temperature of the surroundings T. Apart from satisfying relation (5.4), the upward and downward relaxation processes within the closely spaced lower or upper levels are usually much faster than the downward relaxation between the two pairs, i.e., $\gamma_{10}, \gamma_{01}, \gamma_{32}, \gamma_{23} \gg \gamma_{21}$. Additionally, we assume that these processes are faster than the duration of the laser pulses t_{pulse}, i.e. $1 \ll \gamma_{32} t_{\text{pulse}}$ and $1 \ll \gamma_{10} t_{\text{pulse}}$. As a result, the lower and upper pair of levels effectively act as one and any deviation from a Boltzmann distribution within the pair is decaying fast. This can be shown in a more rigorous way by applying the linear state transform

$$\begin{bmatrix} N_0 \\ N_1 \\ N_2 \\ N_3 \end{bmatrix} \mapsto \begin{bmatrix} N_{\text{L,s}} \\ N_{\text{L,f}} \\ N_{\text{U,s}} \\ N_{\text{U,f}} \end{bmatrix} = \begin{bmatrix} N_0 + N_1 \\ N_1 - B_{01} N_0 \\ N_2 + N_3 \\ N_3 - B_{23} N_2 \end{bmatrix} \tag{5.5}$$

to the rate equations (5.3). One can then use singular perturbation methods [105] to eliminate the fast redistribution dynamics of $N_{\text{L,f}}$ and $N_{\text{U,f}}$. For the limit $\gamma_{10}, \gamma_{32} \to \infty$, it follows that

$$N_{\text{L,f}} = 0 \qquad \text{and} \qquad N_{\text{U,f}} = 0 \tag{5.6}$$

while the remaining slow dynamics of $N_{\text{L,s}}$ and $N_{\text{U,s}}$ are given by the reduced rate equations

$$\frac{\partial N_{\text{U,s}}}{\partial t} = -\gamma_{21} f_2 N_{\text{U,s}} + \frac{\sigma_{\text{P}} I_{\text{P}}}{\hbar \omega_{\text{P}}} (f_0 N_{\text{L,s}} - f_3 N_{\text{U,s}}) - \frac{\sigma I}{\hbar \omega} (f_2 N_{\text{U,s}} - f_1 N_{\text{L,s}}) \tag{5.7a}$$

$$\frac{\partial N_{\text{L,s}}}{\partial t} = +\gamma_{21} f_2 N_{\text{U,s}} - \frac{\sigma_{\text{P}} I_{\text{P}}}{\hbar \omega_{\text{P}}} (f_0 N_{\text{L,s}} - f_3 N_{\text{U,s}}) + \frac{\sigma I}{\hbar \omega} (f_2 N_{\text{U,s}} - f_1 N_{\text{L,s}}), \tag{5.7b}$$

with the relative occupancy factors f_i of the i-th energy level

$$f_0 = \frac{1}{1 + B_{01}} \qquad f_1 = \frac{B_{01}}{1 + B_{01}} \tag{5.8a}$$

$$f_2 = \frac{1}{1 + B_{23}} \qquad f_3 = \frac{B_{23}}{1 + B_{23}}. \tag{5.8b}$$

From their definition it is clear that $f_0 + f_1 = f_2 + f_3 = 1$. Evaluating the inverse state transform of (5.5) with (5.6) leads to

$$N_0 = f_0 N_{\text{L,s}} \qquad N_1 = f_1 N_{\text{L,s}} \tag{5.9a}$$

$$N_2 = f_2 N_{\text{U,s}} \qquad N_3 = f_3 N_{\text{U,s}}, \tag{5.9b}$$

Die approbierte Originalversion dieser Dissertation ist in der TU Wien Bibliothek verfügbar.
The approved original version of this doctoral thesis is available at the TU Wien Bibliothek.
TU Bibliothek WIEN Your knowledge hub

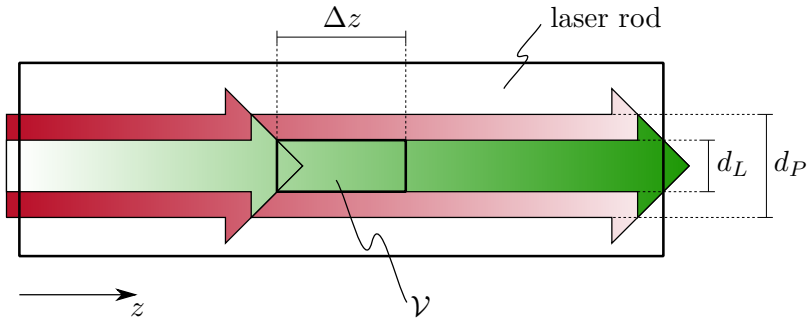

Figure 5.4: Illustration of the amplification of a laser beam (green) overlapping with the aligned continous pumping beam (red) in an endpumped configuration. While the pumping beam is gradually absorbed in z direction, the pulses of the laser beam are amplified.

i.e., the total population of the lower and upper pair $N_{\mathrm{L,s}}$ and $N_{\mathrm{U,s}}$, respectively, is distributed within the associated two levels in a static ratio given by the occupancy factors f_j, $j = 0, \ldots, 3$. With the usual definition of the population inversion $\Delta N = N_2 - N_1 = f_2 N_{\mathrm{U,s}} - f_1 N_{\mathrm{L,s}}$ and $N_{\mathrm{L,s}} + N_{\mathrm{U,s}} = N_{\mathrm{dop}}$, one obtains the simplified dynamics

$$\begin{aligned}\frac{\partial \Delta N}{\partial t} = &- \gamma_{21} f_2 (f_1 N_{\mathrm{dop}} + \Delta N) - \frac{\sigma I}{\hbar\omega}(f_1 + f_2)\Delta N \\ &+ \frac{\sigma_{\mathrm{P}} I_{\mathrm{P}}}{\hbar\omega_{\mathrm{P}}}\left((f_0 f_2 - f_3 f_1) N_{\mathrm{dop}} - (f_0 + f_3)\Delta N\right).\end{aligned} \tag{5.10}$$

The known results for the case of a four-level laser material can be retrieved by setting $f_0 = f_2 = 1$ and $f_1 = f_3 = 0$.

5.1.2 Full description of the amplification and pumping process

With the dynamics of the population inversion (5.10), the only missing component is the description of the intensity distribution of the laser and the pump beam. In the following, we assume that the laser medium is operated in a so-called end-pumpend configuration, i.e. that the continuous pumping beam is fed through the crystal axially aligned with the laser beam and in the same direction of propagation as shown in Figure 5.4. Thereby, the pumping beam is gradually absorbed by the medium due to the energy loss for exciting atoms from E_0 to E_3. Conversely, the laser pulses are amplified while propagating through the medium.

As in Chapter 2, we assume that the transversal intensity profile of the pulses and the pumping beam is homogeneous over a diameter d_L and d_P, respectively, and zero outside, whereby $d_L \leq d_P$.

Die approbierte Originalversion dieser Dissertation ist in der TU Wien Bibliothek verfügbar.
The approved original version of this doctoral thesis is available at the TU Wien Bibliothek.
TU Bibliothek WIEN Your knowledge hub

Aligning the propagation direction with the z-axis and using an energy conservation argument for a volume $\mathcal{V}$ (e.g., see [30, Cha. 10]) yields the equations describing the intensity of the pulse I and of the pumping beam I_P according to

$$\frac{\partial I}{\partial t} + v\frac{\partial I}{\partial z} = \sigma v(N_2 - N_1)I \tag{5.11a}$$

$$\frac{\partial I_\mathrm{P}}{\partial t} + v_\mathrm{P}\frac{\partial I_\mathrm{P}}{\partial z} = -\sigma_\mathrm{P} v_\mathrm{P}(N_0 - N_3)I_\mathrm{P}, \tag{5.11b}$$

with the velocities v and v_P corresponding to the transition frequencies[3] ω and ω_P, respectively. Combining these equations with the population dynamics (5.10) and using the relations (5.9), one obtains the complete model

$$\frac{\partial I}{\partial t} + v\frac{\partial I}{\partial z} = \sigma v(f_1 + f_2)\Delta N\, I \tag{5.12a}$$

$$\frac{\partial I_\mathrm{P}}{\partial t} + v_\mathrm{P}\frac{\partial I_\mathrm{P}}{\partial z} = -\sigma_\mathrm{P} v_\mathrm{P}\frac{(f_0 f_2 - f_3 f_1)N_\mathrm{dop} - (f_0 + f_3)\Delta N}{f_1 + f_2} I_\mathrm{P} \tag{5.12b}$$

$$\begin{aligned}\frac{\partial \Delta N}{\partial t} &= -\gamma_{21} f_2(f_1 N_\mathrm{dop} + \Delta N) - \frac{\sigma I}{\hbar\omega}(f_1 + f_2)\Delta N \\ &\quad + \frac{\sigma_\mathrm{P} I_\mathrm{P}}{\hbar\omega_\mathrm{P}}\left((f_0 f_2 - f_3 f_1)N_\mathrm{dop} - (f_0 + f_3)\Delta N\right).\end{aligned} \tag{5.12c}$$

The mathematical model above is valid for all points in time and has to be accompanied with suitable initial and boundary conditions. Due to the cyclic structure of the amplification process using N_{RT} round-trips in the resonator cavity, each round-trip can be described by a single instance of the above model coupled by their initial and boundary conditions as presented in Chapter 2. Such an approach is quite common for detailed descriptions of optical cavities [106] or frequency-comb generation in micro-resonators [107].

In the following, we will proceed as in Chapter 2 and split the description of the regenerative amplifier into two temporal phases: one that describes the interaction of the pulse field with the laser material and one that covers the remaining times where only the continuous pumping beam interacts with the laser material.

5.1.3 Amplification during a single passage (pulse model)

For a single passage of the laser pulse through the laser material, we neglect the influence of the comparatively weak pumping beam and the relaxation of the excited populations via γ_{21} due to the extremely short time scales, as done in Chapter 2. Applying these assumptions to (5.12) and transforming the equations

[3] This merely states that the group velocities are given by the dispersion relation $k(\omega)$ at the corresponding transition frequency.

Die approbierte Originalversion dieser Dissertation ist in der TU Wien Bibliothek verfügbar.
The approved original version of this doctoral thesis is available at the TU Wien Bibliothek.
TU Bibliothek WIEN Your knowledge hub

onto a time frame $t \mapsto t - z/v$ travelling with the pulse, one obtains

$$\frac{\partial I}{\partial z} = \sigma(f_1 + f_2)\Delta N\, I \tag{5.13a}$$

$$\frac{\partial \Delta N}{\partial t} = -\frac{\sigma I}{\hbar\omega}(f_1 + f_2)\Delta N, \tag{5.13b}$$

with a generic input pulse at the left boundary $I(0,t) = I_{\text{in}}(t)$ and the initial densitiy of the population inversion $\Delta N(z,0) = \Delta N_{\text{in}}(z)$. The desired output pulse at the opposite boundary $z = L$ is given by $I_{\text{out}}(t) = I(L,t)$ where L denotes the length of the laser medium. Again, the remaining population inversion is given by $\Delta N_{\text{out}}(z) = \Delta N(z, t_{\text{end}})$ with t_{end} large enough such that the pulse has completely passed through the laser medium.

Equation (5.13) can be solved analytically, see, e.g., [30, 66]. Solving the intensity equation (5.13a) by separation of variables yields

$$I_{\text{out}}(t) = \exp\left(\sigma(f_1 + f_2)\int_0^L \Delta N(z,t)\mathrm{d}z\right) I_{\text{in}}(t). \tag{5.14}$$

Defining the total available population inversion according to

$$N_{\text{tot}}(t) = \int_0^L \Delta N(z,t)\mathrm{d}z, \tag{5.15}$$

the input and output pulses are connected by a simple time-varying gain $G(t)$ in the form

$$I_{\text{out}}(t) = \exp\left(\sigma(f_1 + f_2)N_{\text{tot}}(t)\right) I_{\text{in}}(t) = G(t)I_{\text{in}}(t). \tag{5.16}$$

The temporal evolution of the gain $G(t)$ can be described by (5.13b). Taking the time derivative of (5.15) together with (5.13b) and (5.14) results in

$$\frac{\mathrm{d}}{\mathrm{d}t}N_{\text{tot}}(t) = -\frac{1}{\hbar\omega}\left(I_{\text{out}}(t) - I_{\text{in}}(t)\right) = -\frac{1}{\hbar\omega}\left[\exp\left(\sigma(f_1 + f_2)N_{\text{tot}}(t)\right) - 1\right] I_{\text{in}}(t), \tag{5.17}$$

which can be solved analytically to

$$\ln\left(\frac{1 - \exp(-\sigma(f_1 + f_2)N_{\text{tot}}(0))}{1 - \exp(-\sigma(f_1 + f_2)N_{\text{tot}}(t))}\right) = \frac{\sigma(f_1 + f_2)}{\hbar\omega}\int_0^t I_{\text{in}}(\xi)\mathrm{d}\xi. \tag{5.18}$$

This result relates the remaining population inversion $N_{\text{tot}}(t)$ at time t with the cummulated energy or fluence $U_{\text{in}}(t) = \int_0^t I_{\text{in}}(\xi)\mathrm{d}\xi$ relative to the so-called saturation fluence $U_{\text{sat}} = \frac{\hbar\omega}{\sigma(f_1+f_2)}$. Analogously, the result

$$\ln\left(\frac{\exp(\sigma(f_1 + f_2)N_{\text{tot}}(0)) - 1}{\exp(\sigma(f_1 + f_2)N_{\text{tot}}(t)) - 1}\right) = \frac{\sigma(f_1 + f_2)}{\hbar\omega}\int_0^t I_{\text{out}}(\xi)\mathrm{d}\xi \tag{5.19}$$

Die approbierte Originalversion dieser Dissertation ist in der TU Wien Bibliothek verfügbar.
The approved original version of this doctoral thesis is available at the TU Wien Bibliothek.
TU Bibliothek Your knowledge hub WIEN

can be obtained by eliminating $I_{\text{in}}(t)$ instead of $I_{\text{out}}(t)$ in (5.17) using (5.14). Defining an initial gain $G_{\text{in}} = G(0) = \exp(\sigma(f_1 + f_2)\int_0^L \Delta N_{\text{in}}(z)\mathrm{d}z)$, the time-varying gain $G(t)$ can be calculated from (5.18) as

$$G(t) = \frac{G_{\text{in}}}{G_{\text{in}} - (G_{\text{in}} - 1)\exp\left(-\frac{\sigma(f_1+f_2)}{\hbar\omega}\int_0^t I_{\text{in}}(t)\mathrm{d}t\right)}. \tag{5.20}$$

While the gain at each point in time is depending on the exact pulse shape $I_{\text{in}}(t)$, the limit $t \to \infty$ in (5.18) shows that the total population inversion extracted from the laser material is only depending on the pulse energy. In turn, combining (5.18) and (5.19), one easily sees that the output pulse energy can be calculated from the initial gain and the energy of the input pulse. Introducing the normalized total fluence

$$H_{\text{in/out}} = \lim_{t\to\infty} \frac{1}{U_{\text{sat}}} U_{\text{in/out}}(t) = \frac{\sigma(f_1 + f_2)}{\hbar\omega}\int_0^\infty I_{\text{in/out}}(\xi)\mathrm{d}\xi \tag{5.21}$$

and the remaining gain after amplification $G_{\text{out}} = \lim_{t\to\infty} G(t)$, these relations can be written as

$$G_{\text{out}} = f_{\text{dep}}(G_{\text{in}}, H_{\text{in}}) = \frac{G_{\text{in}}}{G_{\text{in}} - (G_{\text{in}} - 1)\exp(-H_{\text{in}})} \tag{5.22a}$$

$$H_{\text{out}} = f_{\text{gain}}(G_{\text{in}}, H_{\text{in}}) = \ln\left[G_{\text{in}}\exp(H_{\text{in}}) - G_{\text{in}} + 1\right] \tag{5.22b}$$

linking the initial gain G_{in} and the fluence H_{in} with the remaining gain G_{out} and the corresponding fluence H_{out} of the amplified pulse.

5.1.4 Gain regeneration due to pumping (pump model)

Now that a simple expression for the pulse amplification and the resulting saturation of the available gain has been found, a compatible description of the gain regeneration due to the pumping process shall be derived. Since no laser pulse is present during the regeneration periods (i.e., $I(z,t) = 0$), the full set of equations (5.12) can be rewritten as

$$\frac{1}{v_{\text{P}}}\frac{\partial I_{\text{P}}}{\partial t} = -\frac{\partial I_{\text{P}}}{\partial z} - \sigma_{\text{P}}\frac{(f_0 f_2 - f_3 f_1)N_{\text{dop}} - (f_0 + f_3)\Delta N}{f_1 + f_2} I_{\text{P}} \tag{5.23a}$$

$$\frac{\partial \Delta N}{\partial t} = -\gamma_{21} f_2 (f_1 N_{\text{dop}} + \Delta N) + \frac{\sigma_{\text{P}} I_{\text{P}}}{\hbar\omega_{\text{P}}}\left((f_0 f_2 - f_3 f_1)N_{\text{dop}} - (f_0 + f_3)\Delta N\right), \tag{5.23b}$$

with the initial condition $\Delta N(z,0) = \Delta N_{\text{in}}(z)$ using some arbitrary initial population inversion $\Delta N_{\text{in}}(z)$ and the boundary condition $I_{\text{P}}(0,t) = I_0$. Here, I_0 denotes the intensity of the pumping beam that is assumed to stay constant within a single regeneration cycle of duration t_{pump}.

Die approbierte Originalversion dieser Dissertation ist in der TU Wien Bibliothek verfügbar.
The approved original version of this doctoral thesis is available at the TU Wien Bibliothek.
TU Bibliothek Your knowledge hub WIEN

Additionally, the transport-like equation (5.23a) would require an initial condition for the intensity distribution $I_\mathrm{P}(z,0)$. However, for typical values of $t_\mathrm{pump} \gg {}^{L}/_{v_\mathrm{P}}$ used in regenerative amplifiers, the transport-like equation (5.23a) with the constant boundary condition can be considered stationary as any perturbation to its steady state propagates through the laser rod extremely fast. Thus, applying singular perturbation theory (i.e., $v_\mathrm{P} \to \infty$), one obtains

$$\frac{\partial I_\mathrm{P}}{\partial z} = -\sigma_\mathrm{P} \frac{(f_0 f_2 - f_3 f_1) N_\mathrm{dop} - (f_0 + f_3)\Delta N}{f_1 + f_2} I_\mathrm{P} \tag{5.24a}$$

$$\frac{\partial \Delta N}{\partial t} = -\gamma_{21} f_2 (f_1 N_\mathrm{dop} + \Delta N) + \frac{\sigma_\mathrm{P} I_\mathrm{P}}{\hbar\omega_\mathrm{P}} \left((f_0 f_2 - f_3 f_1) N_\mathrm{dop} - (f_0 + f_3)\Delta N\right). \tag{5.24b}$$

Proceeding as in the previous section by solving (5.24a) and reformulating (5.24b) in terms of the total population inversion (5.15) yields

$$\begin{aligned}\frac{\mathrm{d}}{\mathrm{d}t} N_\mathrm{tot}(t) = &- \gamma_{21} f_2 (f_1 N_\mathrm{dop} L + N_\mathrm{tot}(t)) \\ &+ I_0 \frac{f_1 + f_2}{\hbar\omega_\mathrm{P}} \left[1 - \exp\left(-\sigma_\mathrm{P}(\kappa_1 N_\mathrm{dop} L - \kappa_2 N_\mathrm{tot}(t))\right)\right]\end{aligned} \tag{5.25}$$

with $\kappa_1 = \frac{f_0 f_2 - f_1 f_3}{f_1 + f_2}$ and $\kappa_2 = \frac{f_0 + f_3}{f_1 + f_2}$. For the general case, this equation is not solvable analytically. Since the equation is solvable for the limit scenarios of a vanishing pumping beam ($I_0 = 0$) and a vanishing relaxation rate γ_{21}, one can apply operator-splitting techniques to obtain approximate solutions of the full problem (5.25). However, it can be observed that the resulting approximation is not accurate enough to capture the dynamic behavior for repetition rates $f_\mathrm{rep} \approx {}^{1}/_{\gamma_{21}}$. Therefore, (5.25) has to be solved numerically. Using (5.16), this differential equation can be reformulated directly in terms of $G(t)$ as

$$\begin{aligned}\frac{\mathrm{d}}{\mathrm{d}t} G(t) = &- \gamma_{21} f_2 \left[\sigma f_1 (f_1 + f_2) N_\mathrm{dop} L + \ln(G(t))\right] G(t) \\ &+ I_0 \sigma \frac{(f_1 + f_2)^2}{\hbar\omega_\mathrm{P}} \left[1 - \exp\left(-\sigma_\mathrm{P}(\kappa_1 N_\mathrm{dop} L)\right) G(t)^{\frac{\kappa_2 \sigma_\mathrm{P}}{(f_1+f_2)\sigma}}\right] G(t)\end{aligned} \tag{5.26}$$

with the initial condition $G(0) = \exp\left(\sigma(f_1 + f_2) \int_0^L \Delta N_\mathrm{in}(z)\mathrm{d}z\right) = G_\mathrm{in}$. Thus, the gain after the regeneration period is given by $G_\mathrm{out} = G(t_\mathrm{pump})$. For convenience, we introduce the nomenclature

$$G_\mathrm{out} = f_\mathrm{pump}(G_\mathrm{in}) \tag{5.27}$$

analogous to the previous section to describe the connection between G_in and G_out as a solution to (5.26).

Die approbierte Originalversion dieser Dissertation ist in der TU Wien Bibliothek verfügbar.
The approved original version of this doctoral thesis is available at the TU Wien Bibliothek.
TU Bibliothek WIEN Your knowledge hub

5.1.5 Discrete-time dynamical model

With the pulse and pump model available, one is finally able to describe the complete dynamics of the regenerative amplifier. The coupling of the pulse and pump model to obtain a description of a single round-trip can be approached analogous to Chapter 2 and in particular to Section 4.5 and Figure 2.5. When considering the more complex spectral description, the pump model includes the redistribution of populations between various energy levels, e.g., the closely spaced intermediate levels that where necessary to account for the spectral properties of the amplification process in Chapter 2. Since we have neglected the spectral properties in this chapter, the pump model only accounts for the relaxation and pumping process, both of which are significantly slower and hardly provide any contribution during the small duration it takes the pulse to complete one round-trip. Thus, we will neglect the effects of the pump model during the N_{RT} consecutive round-trips of one amplification phase. Using the solution of a single passage through the laser medium according to (5.22) and considering the losses due to the resonator cavity, one can write the effect of a single round-trip according to Figure 5.2 as

$$\begin{bmatrix} G^{n,k+1} \\ H_{\mathrm{in}}^{n,k+1} \end{bmatrix} = \begin{bmatrix} f_{\mathrm{dep}}(G^{n,k}, H_{\mathrm{in}}^{n,k}) \\ \eta_{\mathrm{RC}} f_{\mathrm{gain}}(G^{n,k}, H_{\mathrm{in}}^{n,k}) \end{bmatrix} = \mathbf{f}_{\mathrm{SP}} \left(\begin{bmatrix} G^{n,k} \\ H_{\mathrm{in}}^{n,k} \end{bmatrix} \right), \tag{5.28}$$

whereby $G^{n,k}$ denotes the gain before the n-th pulse passes the laser medium for the k-th time. Therefore, using the iterated function

$$\mathbf{f}_{\mathrm{MP}} = \mathbf{f}_{\mathrm{SP}}^{(N_{\mathrm{RT}})} = \underbrace{\mathbf{f}_{\mathrm{SP}} \circ \ldots \circ \mathbf{f}_{\mathrm{SP}}}_{N_{\mathrm{RT}} \text{ times}} \tag{5.29}$$

to describe N_{RT} successive round-trips, the pulse-to-pulse dynamics of the regenerative amplifier's gain are given by

$$G^{n+1,1} = f_{\mathrm{pump}} \left(\begin{bmatrix} 1 & 0 \end{bmatrix} \mathbf{f}_{\mathrm{MP}} \left(\begin{bmatrix} G^{n,1} \\ H_{\mathrm{in}}^{n} \end{bmatrix} \right) \right). \tag{5.30}$$

Choosing the input variable $u^n = H_{\mathrm{in}}^n$, the output variable $y^n = H_{\mathrm{out}}^n$ and the state variable $x^n = G^{n,1}$, the nonlinear discrete-time dynamic model of the regenerative amplifier reads as, see also (4.38a),

$$x^{n+1} = f_{\mathrm{pump}} \left(\begin{bmatrix} 1 & 0 \end{bmatrix} \mathbf{f}_{\mathrm{MP}} \left(\begin{bmatrix} x^n \\ u^n \end{bmatrix} \right) \right) = f(x^n, u^n) \tag{5.31a}$$

$$y^n = \frac{\eta_{\mathrm{out}}}{\eta_{\mathrm{RC}}} \begin{bmatrix} 0 & 1 \end{bmatrix} \mathbf{f}_{\mathrm{MP}} \left(\begin{bmatrix} x^n \\ u^n \end{bmatrix} \right) = h(x^n, u^n), \tag{5.31b}$$

with the initial condition x^0 given by the initial population inversion $\Delta N^0(z)$ according to (5.16) and (5.15)

$$x^0 = G^0 = \exp \left(\sigma(f_1 + f_2) \int_0^L \Delta N^0(z) \mathrm{d}z \right). \tag{5.32}$$

Die approbierte Originalversion dieser Dissertation ist in der TU Wien Bibliothek verfügbar.
The approved original version of this doctoral thesis is available at the TU Wien Bibliothek.
TU WIEN Bibliothek Your knowledge hub

By integration of (5.1), the input variable can be expressed as a function of the adjustable loss of the AOM as $u^n = \eta^n_{\mathrm{AOM}} H_{\mathrm{seed}}$. Since $\eta^n_{\mathrm{AOM}} \in [0, 1]$, it follows that the system is subject to the input constraints

$$0 \leq u^n \leq \bar{u}, \tag{5.33}$$

with $\bar{u} = H_{\mathrm{seed}}$. The one-dimensional dynamic system (5.31) can be considered a generalization of the model presented in [31], where an idealized four-level medium with linearized dynamics in conjunction with a space-independent description of the laser medium is used. Thus, the presented model is much better suited to describe the dynamics observed in realistic regenerative amplifiers over a large range of different pumping powers and pulse intensities. The derivation presented above is not limited to ring cavities or the simple pumping scheme used in this section. For extensions to multi-pass pumping configurations and linear cavities, the reader is referred to Appendix C.

5.2 Stability analysis of the uncontrolled amplifier

Apart from short transient operations during start-up or when switching to a different operating point, regenerative amplifiers are mainly run in steady-state operation. For a given constant input u^s, the resulting steady state x^s is given by the nonlinear equation, see (5.31)

$$x^s = f(x^s, u^s) \tag{5.34}$$

with the corresponding steady-state output

$$y^s = h(x^s, u^s). \tag{5.35}$$

The Jacobian of $\mathbf{f}_{\mathrm{SP}}$ with respect to x and u reads as

$$\nabla \mathbf{f}_{\mathrm{SP}}\left(\begin{bmatrix} x \\ u \end{bmatrix}\right) = \begin{bmatrix} \frac{\partial \mathbf{f}_{\mathrm{SP}}}{\partial x} & \frac{\partial \mathbf{f}_{\mathrm{SP}}}{\partial u} \end{bmatrix} = \begin{bmatrix} \frac{\mathrm{e}^{-u}}{((x-1)\mathrm{e}^{-u}-x)^2} & \frac{x(x-1)\mathrm{e}^{-u}}{((x-1)\mathrm{e}^{-u}-x)^2} \\ \eta_{\mathrm{RC}} \frac{e^u-1}{x(\mathrm{e}^u-1)+1} & \eta_{\mathrm{RC}} \frac{xe^u}{x(\mathrm{e}^u-1)+1} \end{bmatrix} \tag{5.36}$$

and thus the Jacobian of the iterated function $\mathbf{f}_{\mathrm{MP}}$ results in

$$\begin{aligned} \nabla \mathbf{f}_{\mathrm{MP}}\left(\begin{bmatrix} x \\ u \end{bmatrix}\right) =& \nabla \mathbf{f}_{\mathrm{SP}}\left(\mathbf{f}_{\mathrm{SP}}^{(N_{\mathrm{RT}}-1)}\left(\begin{bmatrix} x \\ u \end{bmatrix}\right)\right) \times \nabla \mathbf{f}_{\mathrm{SP}}\left(\mathbf{f}_{\mathrm{SP}}^{(N_{\mathrm{RT}}-2)}\left(\begin{bmatrix} x \\ u \end{bmatrix}\right)\right) \times \ldots \\ & \times \nabla \mathbf{f}_{\mathrm{SP}}\left(\mathbf{f}_{\mathrm{SP}}\left(\begin{bmatrix} x \\ u \end{bmatrix}\right)\right) \times \nabla \mathbf{f}_{\mathrm{SP}}\left(\begin{bmatrix} x \\ u \end{bmatrix}\right). \end{aligned} \tag{5.37}$$

Introducing small deviations from the steady state $\Delta x^n = x^n - x^s$, $\Delta u^n = u^n - u^s$ and $\Delta y^n = y^n - y^s$, the behavior of the nonlinear system (5.31) can

Die approbierte Originalversion dieser Dissertation ist in der TU Wien Bibliothek verfügbar.
The approved original version of this doctoral thesis is available at the TU Wien Bibliothek.
TU Bibliothek WIEN Your knowledge hub

be approximated in the vicinity of the operating point (x^s, u^s) by the linearized system

$$\Delta x^{n+1} = \Phi\,\Delta x^n + \Gamma\,\Delta u^n \tag{5.38a}$$
$$\Delta y^n = \mathrm{C}\,\Delta x^n + \mathrm{D}\,\Delta u^n, \tag{5.38b}$$

with

$$\begin{aligned}
\Phi &= \frac{\partial f}{\partial x}(x^s, u^s) = \frac{\mathrm{d}f_{\mathrm{pump}}}{\mathrm{d}G_{\mathrm{in}}}\left(\begin{bmatrix}1 & 0\end{bmatrix}\mathbf{f}_{\mathrm{MP}}\left(\begin{bmatrix}x^s\\u^s\end{bmatrix}\right)\right)\begin{bmatrix}1 & 0\end{bmatrix}\nabla\mathbf{f}_{\mathrm{MP}}\left(\begin{bmatrix}x^s\\u^s\end{bmatrix}\right)\begin{bmatrix}1\\0\end{bmatrix}\\
\Gamma &= \frac{\partial f}{\partial u}(x^s, u^s) = \frac{\mathrm{d}f_{\mathrm{pump}}}{\mathrm{d}G_{\mathrm{in}}}\left(\begin{bmatrix}1 & 0\end{bmatrix}\mathbf{f}_{\mathrm{MP}}\left(\begin{bmatrix}x^s\\u^s\end{bmatrix}\right)\right)\begin{bmatrix}1 & 0\end{bmatrix}\nabla\mathbf{f}_{\mathrm{MP}}\left(\begin{bmatrix}x^s\\u^s\end{bmatrix}\right)\begin{bmatrix}0\\1\end{bmatrix}\\
\mathrm{C} &= \frac{\partial h}{\partial x}(x^s, u^s) = \frac{\eta_{\mathrm{out}}}{\eta_{\mathrm{RC}}}\begin{bmatrix}0 & 1\end{bmatrix}\nabla\mathbf{f}_{\mathrm{MP}}\left(\begin{bmatrix}x^s\\u^s\end{bmatrix}\right)\begin{bmatrix}1\\0\end{bmatrix}\\
\mathrm{D} &= \frac{\partial h}{\partial u}(x^s, u^s) = \frac{\eta_{\mathrm{out}}}{\eta_{\mathrm{RC}}}\begin{bmatrix}0 & 1\end{bmatrix}\nabla\mathbf{f}_{\mathrm{MP}}\left(\begin{bmatrix}x^s\\u^s\end{bmatrix}\right)\begin{bmatrix}0\\1\end{bmatrix}.
\end{aligned} \tag{5.39}$$

Remark 20. *Note that $f_{pump}(G_{in})$ is used to denote a solution of (5.26) with the initial condition $G(0) = G_{in}$. Since (5.26) is solved numerically, the derivative $\frac{\mathrm{d}f_{pump}}{\mathrm{d}G_{in}}$ required in (5.39) has to be approximated by some kind of difference quotient, which in turn requires the solution of (5.26) for two (or more) initial values.*

Rigorous results on the stability of nonlinear discrete-time systems are rather sparse in the literature compared to the continuous-time case. This is not too surprising, as discrete-time descriptions usually stem from sampled-data systems with an underlying plant that is continuous in time. Since the exact treatment of nonlinear sampled data systems is hardly possible in practice due to the required analytical solution of the nonlinear dynamics, a quasi-continuous design approach is usually pursued. The plant in this chapter is inherently discrete in time due to its pulsed nature. The use of Lyapunov-based stability analysis for discrete-time systems dates back to Hahn [108] with additional material presented in [109]. Results for time-varying systems are presented in [110] and modern concepts such as input-to-state stability were analyzed in [111, 112]. A very recent compilation [113] tried to summarize existing discrete-time results analogous to the classic results presented by Khalil [114] for the continuous-time case. According to Lyapunov's indirect method [113, Theorem 3.3] for discrete-time systems, in the case of (5.38) the condition

$$|\Phi| < 1 \tag{5.40}$$

is sufficient for local asymptotic stability of (5.31), which is equivalent to the classic results concerning the attraction of fixed points.

Due to the one-dimensional state space, the solution of (5.34) can be solved graphically as in [31], which is very instructive to give a rough understanding of the involved parameters. As mentioned at the beginning of this chapter, the

Die approbierte Originalversion dieser Dissertation ist in der TU Wien Bibliothek verfügbar.
The approved original version of this doctoral thesis is available at the TU Wien Bibliothek.
TU Bibliothek Your knowledge hub WIEN

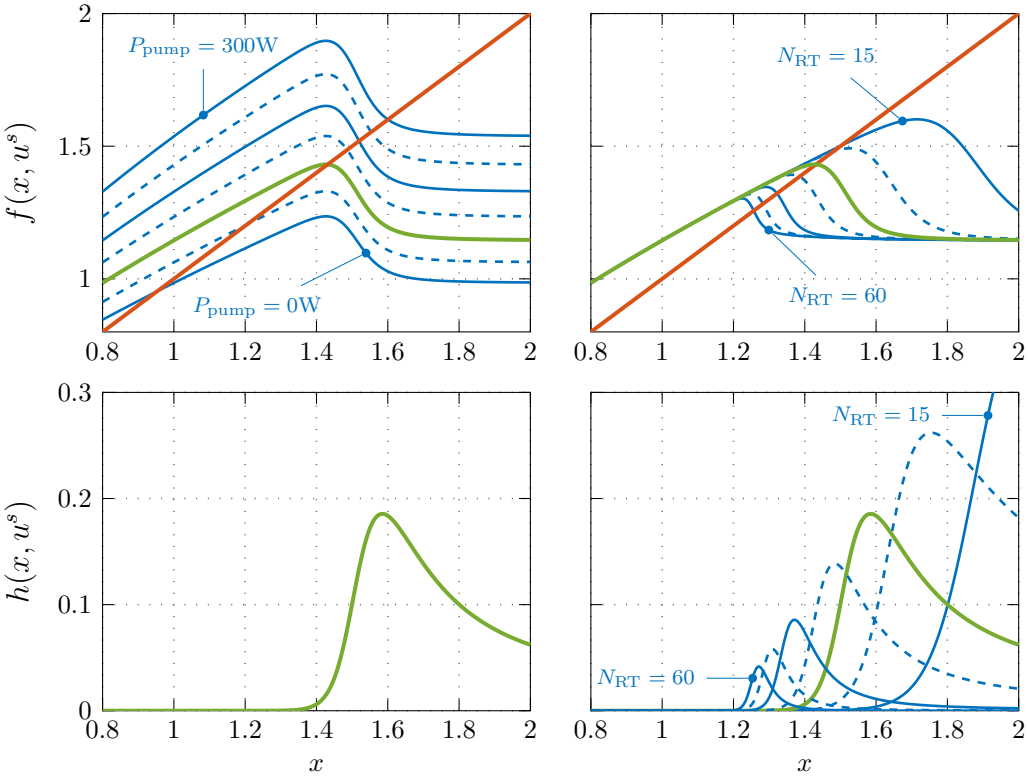

Figure 5.5: Graphical illustration of the fixed-point equation (5.34) to obtain the steady state x^s (top) and the corresponding output equation for a given steady-state input u^s (bottom) for different pumping powers P_{pump} and numbers of round-trips N_{RT}. On the left: Variable pumping power $P_{\text{pump}} \in \{0\,\text{W}, 50\,\text{W}, 100\,\text{W} \ldots, 300\,\text{W}\}$ and $N_{\text{RT}} = 25$. On the right: Variable round-trips $N_{\text{RT}} \in \{15, 20, 25, 30, 40, 50, 60\}$ and $P_{\text{pump}} = 100\,\text{W}$. The common case $N_{\text{RT}} = 25$ and $P_{\text{pump}} = 100\,\text{W}$ is highlighted in green.

main design parameters influencing the regenerative amplifier's dynamics are the available pumping power P_{pump} (and thus the resulting intensity $I_0 = {}^{4P_{\text{pump}}}/d_{\text{P}}^2\pi$ in (5.26)), the number of round-trips N_{RT}, the energy of the seed pulses H_{seed} and the repetition rate f_{rep}. From a control perspective, the repetition rate is often given by the desired application scenario and the energy of the seed pulses is limited by the given pulse source. Thus, we only consider the influence of P_{pump} and N_{RT} in this chapter.

A numerical example for a regenerative amplifier operated at $f_{\text{rep}} = 1\,\text{kHz}$ with $H_{\text{seed}} = 10\,\text{nJ}$ is shown in Figure 5.5 for different values of P_{pump} and N_{RT}. The system dynamics can be separated into three regimes: First, an unsaturated regime for low values of x where $f(x, u^s)$ is rising approximately linear. For $N_{\text{RT}} = 25$ as shown in Figure 5.5 on the left, this corresponds to roughly $x \leq 1.4$. Steady-state solutions in this regime are stable and the system behavior is approximately linear.

Die approbierte Originalversion dieser Dissertation ist in der TU Wien Bibliothek verfügbar.
The approved original version of this doctoral thesis is available at the TU Wien Bibliothek.
TU WIEN Bibliothek Your knowledge hub

In this region, only parts of the available energy is extracted by the pulse. Second, the fully saturated regime for very large values of x (e.g., $x > 1.6$ for $N_{\mathrm{RT}} = 25$ in Figure 5.5) where almost all stored energy is extracted by the pulse. However, this regime does usually not yield the strongest output pulses as indicated by the corresponding output function $h(x, u^s)$ at the bottom of Figure 5.5. This is caused by the round-trip losses outgrowing the remaining gain of the laser material during the last round-trips. The most interesting regime sits right between the unsaturated and the fully saturated regime and is characterized by a potentially unstable and strongly nonlinear behavior. Moreover, the operating point with the highest steady-state output pulses y^s is usually located in the vicinity of this regime.

As expected, increasing the available pumping power yields higher restored states for the following pulses. Due to the quasi-three-level nature of the laser material, some amount of pumping is required to achieve a transparent steady state (i.e., a unit gain steady state $x^s = 1$) while $P_{\mathrm{pump}} = 0$ yields $x^s < 1$ (see Figure 5.5 on the left). Since the output function $h(x, u^s)$ does not contain f_{pump}, it is clear there is no impact due to variations of the pumping power. The higher the number of round-trips, the more rapidly the system transitions from an unsaturated to a fully saturated regime and thus the higher is its potential for instabilities to emerge. Additionally, the shape of the output function $h(x, u^s)$ stongly depends on the number of round-trips. While it seems that a lower number of round-trips is beneficial for achieving high output pulses (due to the low losses), this is somewhat misleading as they would require tremendous levels of pumping power to achieve the necessary steady-states x^s.

Remark 21. *Intuitively, one would expect that the steady-state equation (5.34) always has a single unique solution. Without rigorous mathematical analysis it shall be illustrated that one can indeed assume this to be true: For $x = 1$ it follows from (5.22) and (5.27) that $f(1, u^s) = f_{pump}(1)$. Conversely, for $x \gg 1$ it is immediately clear that the circulating pulse will deplete the energy stored in the gain medium completely for a significant number of round-trips. By inspecting (5.22), it is clear that $\lim_{x\to\infty} f(x, u^s) = f_{pump}(1)$. Additionally, the contribution of the pumping process reduces with increasing levels of population inversion, i.e., $\frac{\partial f(x,u^s)}{\partial x} \leq 1$. Since $f(x, u)$ is continuous in both arguments, it is clear that for amplifying operation, i.e., $f(1, u^s) = f_{pump}(1) \geq 1$, there always exists a unique solution x^s of (5.34).*

Finally, to illustrate the dynamical behavior of regenerative amplifiers, a set of simulation scenarios is shown in Figure 5.6 with the corresponding visualization of the steady-state equation (5.34) for reference. The output pulses $y^n = H^n_{\mathrm{out}}$ are converted from normalized total fluence to pulse energies $W^n_{\mathrm{out}} = \frac{d_{\mathrm{L}}^2 \pi}{4} U_{\mathrm{sat}} H^n_{\mathrm{out}}$ for convenience. To obtain a initial condition (5.32), a stationary solution of (5.25) for a given $I_0 = {}^{4W_{\mathrm{pump}}}/_{d_{\mathrm{P}}^2 \pi}$ was chosen for illustration purposes, i.e. the laser

Die approbierte Originalversion dieser Dissertation ist in der TU Wien Bibliothek verfügbar.
The approved original version of this doctoral thesis is available at the TU Wien Bibliothek.
TU WIEN Bibliothek Your knowledge hub

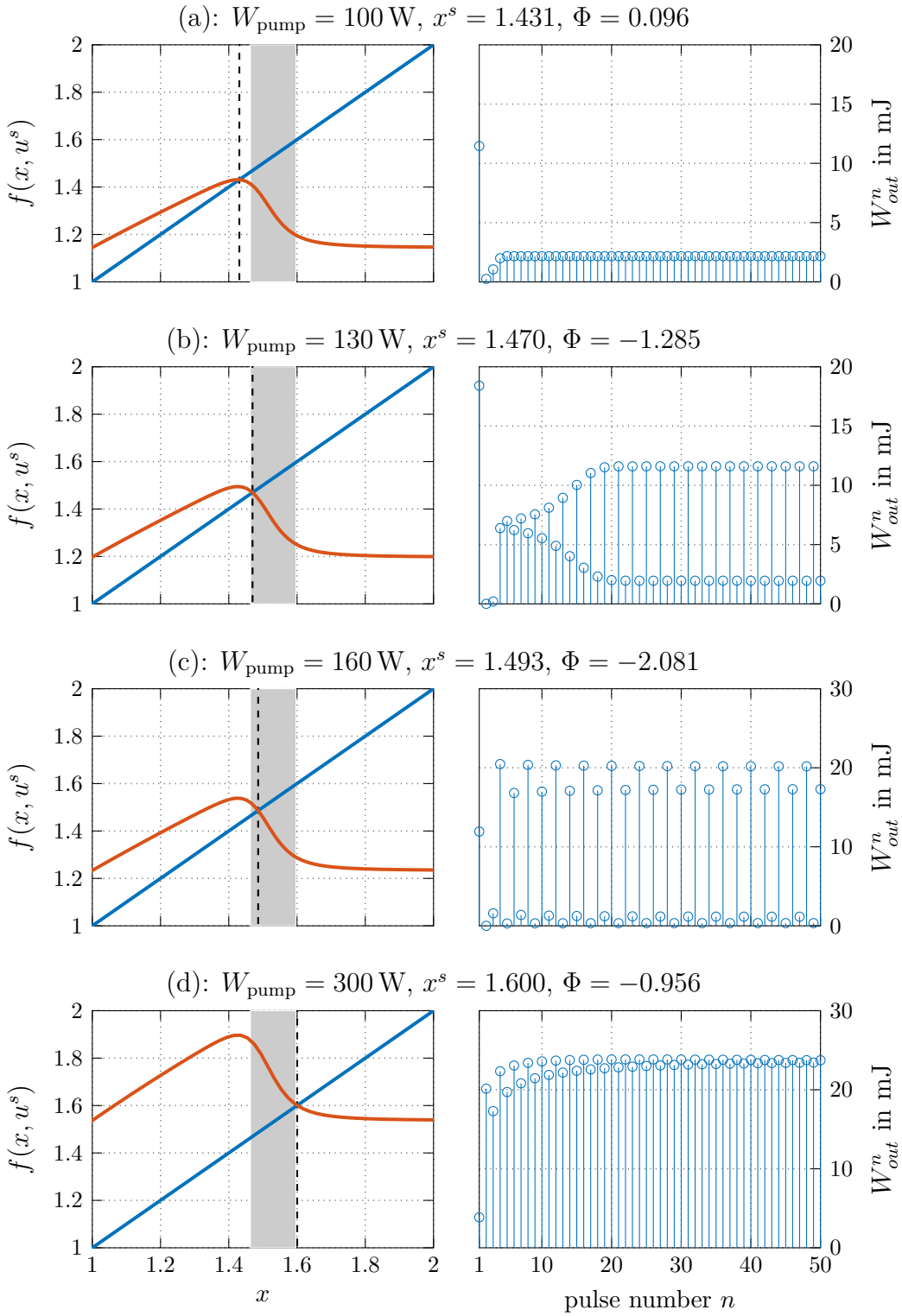

Figure 5.6: Dynamical behavior of a regenerative amplifier for different pumping powers. The shaded area indicates unstable regions where $\left|\frac{\partial f}{\partial x}(x, u^s)\right| \geq 1$.

Die approbierte Originalversion dieser Dissertation ist in der TU Wien Bibliothek verfügbar.
The approved original version of this doctoral thesis is available at the TU Wien Bibliothek.
TU Bibliothek Your knowledge hub WIEN

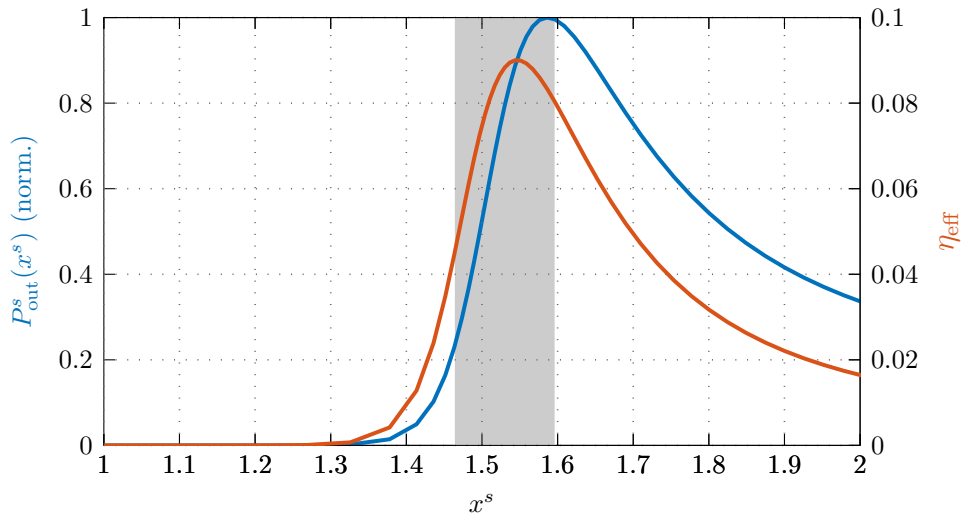

Figure 5.7: Normalized steady-state output power $P^s_{\text{out}} = W^s_{\text{out}} f_{\text{rep}}$ and steady-state efficiency $\eta_{\text{eff}} = {}^{P^s_{\text{out}}}/_{P_{\text{pump}}}$ as a function of x^s for the same scenario as in Figure 5.6. The shaded area indicates unstable operating points.

medium is initially fully pumped. The first simulation scenario in Figure 5.6 (a) coincides with the common case in Figure 5.5, i.e. $N_{\text{RT}} = 25$ and $P_{\text{pump}} = 100\,\text{W}$, where the amplifier starts to saturate but is still operated at a stable point. The fully pumped initial condition results in a strong first pulse that eliminates the accumulated population inversion. After that, the amplifier is returning to the steady-state output y^s. Increasing the pumping power to $P_{\text{pump}} = 130\,\text{W}$, one enters the unstable regime and the output pulses converge to a limit cycle with two energies (see Figure 5.6 (b)). Further increasing the pumping power to $P_{\text{pump}} = 160\,\text{W}$, the period doubles again and a limit cycle with four energies emerges (see Figure 5.6 (c)). Notice that the energy of the first pulse decreased compared to $P_{\text{pump}} = 130\,\text{W}$ although the resulting steady state x^s increased. Analyzing the evolution of the pulse energy over the number of round-trips, one can see that the circulating pulse extracts the available energy stored in the gain medium quite fast and suffers significant losses over the final round-trips. For $P_{\text{pump}} = 300\,\text{W}$, the amplifier becomes stable again (see Figure 5.6 (d)). According to Figure 5.5, the resulting steady state $x^s = 1.600$ is close to the maximum of $h(x, u^s)$, i.e. the amplifier is operated close to its maximum output power given the number of round-trips chosen in this example. However, operating points with maximum output power do not yield the highest efficiency $\eta_{\text{eff}} = \frac{P^s_{\text{out}}}{P_{\text{pump}}}$ for steady-state operation due to the high losses. Operating at maximum efficiency usually requires to go deeper into the unstable operational regimes (see Figure 5.7).

Die approbierte Originalversion dieser Dissertation ist in der TU Wien Bibliothek verfügbar.
The approved original version of this doctoral thesis is available at the TU Wien Bibliothek.
TU Bibliothek WIEN Your knowledge hub

5.3 Feedback stabilization of unstable operating points

Building on the derived model and its analysis above, we now want to proceed to influence the dynamics by applying feedback control methods. Using measurements of the output pulses y^n is probably the most obvious point to start investigating feedback schemes. For ultra-short pulses in the femto- or pico-seconds range, however, providing measurements of the energy of a single pulse can become a quite challenging task, as the pulses only contribute a tiny fraction to the time intervals given by the repetition rate. In particular, standard methods rely on optical power measurements and thus only provide mean pulse energies.

Therefore, we start by proposing an alternative way of using the transmitted pump light instead before we get back to using measured pulse energies.

5.3.1 Feedback stabilization using pump light measurements

Like incoming laser pulses are amplified due to the population inversion in the laser medium, so is the light of the pumping beam absorbed. As a result, one can see fluctuations in the transmitted pump light due to the extraction and regeneration of the population inversion as shown in Figure 5.8. Solving (5.24) by separation of variables, one can see that the quotient of transmitted and incident intensities of the pump light is given by

$$\frac{I_\mathrm{P}(L,t)}{I_0} = \exp\left(-\sigma_\mathrm{P}\kappa_1 L N_\mathrm{dop} + \sigma_\mathrm{P}\kappa_2 \int_0^L \Delta N(z,t)\mathrm{d}z\right). \tag{5.41}$$

Using the definition of $G(t)$ in (5.16) together with (5.15), this can be reformulated as

$$\frac{I_\mathrm{P}(L,t)}{I_0} = \left[\frac{G(t)}{G_\mathrm{max}}\right]^{\frac{\sigma_\mathrm{P}(f_0+f_3)}{\sigma(f_1+f_2)^2}}, \tag{5.42}$$

where $G_\mathrm{max} = \exp\left(\sigma(f_1+f_2)\frac{\kappa_1}{\kappa_2} L N_\mathrm{dop}\right)$ denotes the gain at which the medium is transparent to the pumping beam (cf. the population necessary to achieve $\frac{\partial I_\mathrm{P}}{\partial z} = 0$ in (5.24a)), i.e. the pumping process becomes ineffective. Since the state x^n is defined as the gain at time t^n just before the first round-trip of a pulse, one obtains

$$x^n = G_\mathrm{max}\left[\frac{I_\mathrm{P}(L,t^n)}{I_0}\right]^{\frac{\sigma(f_1+f_2)^2}{\sigma_\mathrm{P}(f_0+f_3)}}. \tag{5.43}$$

Thus, by measuring the transmitted light $I_\mathrm{P}(L,t^n)$ we can directly infer the value of the system's state x^n which in turn shall be used in the following to

Die approbierte Originalversion dieser Dissertation ist in der TU Wien Bibliothek verfügbar.
The approved original version of this doctoral thesis is available at the TU Wien Bibliothek.
TU Bibliothek WIEN Your knowledge hub

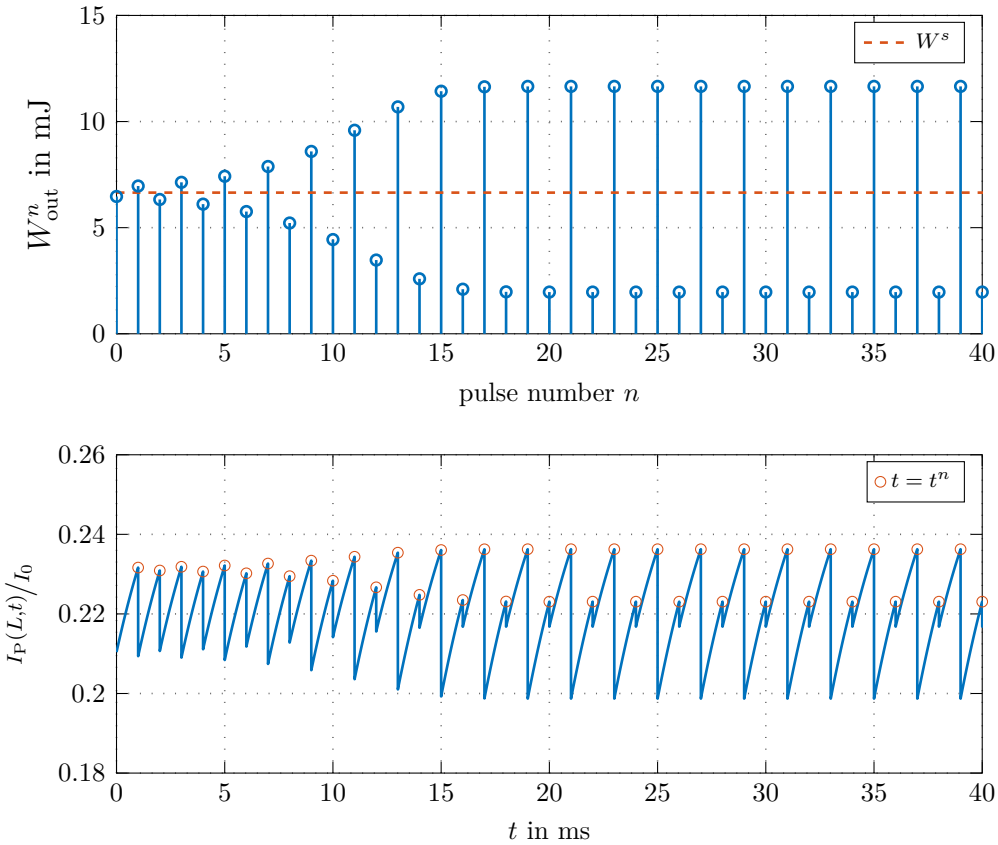

Figure 5.8: Pulse build-up of a regenerative amplifer operated with $P_{\text{pump}} = 130\,\text{W}$ and the corresponding transmitted pump light $I_{\text{P}}(L,t)$. The markers indicate the desired values at $t = t^n$.

Die approbierte Originalversion dieser Dissertation ist in der TU Wien Bibliothek verfügbar.
The approved original version of this doctoral thesis is available at the TU Wien Bibliothek.
TU Bibliothek Your knowledge hub WIEN

stabilize the desired operating point (x^s, u^s). Since we are mainly interested in a local stabilization of the system, the simple state feedback law

$$u^n = u^s + \varsigma\left(k_{\mathrm{FB}}(x^n - x^s)\right), \tag{5.44}$$

with the feedback gain k_{FB} and a strictly monotonous sigmoid-like function $\varsigma : \mathbb{R} \to \mathbb{R}$ with $\varsigma(0) = 0$ and $\frac{\mathrm{d}\varsigma}{\mathrm{d}u}(0) = 1$, is used. To ensure that the input constraints (5.33) are met, we additionally demand that $\lim_{\xi\to-\infty} \varsigma(\xi) \geq -u^s$ and $\lim_{\xi\to\infty} \varsigma(\xi) \leq \bar{u} - u^s$. From physical reasoning it is quite intuitive that $f(x, u_2) < f(x, u_1)$ for $x > 1$ and $u_2 > u_1$, i.e., driving the regenerative amplifier with a stronger pulse results in a diminished gain for the following pulse, and a numerical analysis of (5.31) strongly supports this claim. Thus, it follows that Γ according to (5.39) is always negative and the system is locally controlable at all operating points (x^s, u^s) for $x^s > 1$ which includes all operational regimes of practical interest. Choosing the feedback gain as

$$k_{\mathrm{FB}} = \frac{\Phi_{\mathrm{des}} - \Phi}{\Gamma}, \tag{5.45}$$

the resulting linearized dynamics of the closed-loop system, i.e., (5.31) together with (5.38) and (5.44), yields $\Delta x^{n+1} = \Phi_{\mathrm{des}} \Delta x^n$. Thus, the system under control is locally asymptotically stable if $|\Phi_{\mathrm{des}}|$ is chosen smaller than one. The region of attraction of the closed-loop dynamics is determined by the exact shape of ς. As mentioned above, we are mostly interested in operating the regenerative amplifier close to a steady state and thus achieving global asymptotic stability (GAS) is not of the utmost importance.

For the following demonstration purposes, we choose $u^s = \bar{u}/2$. Additionally, we want to avoid very small input values, as the system becomes increasingly sensitive. Thus, we obtain a smooth feedback law (5.44) using

$$\varsigma(\xi) = (1 - \varepsilon) u^s \tanh\left(\frac{\xi}{(1 - \varepsilon) u^s}\right), \tag{5.46}$$

where ε serves as a tuning parameter to adjust the (relative) clearance towards both input constraints.

Simulation results for different pumping levels (see also Figure 5.6) are shown in Figure 5.9 for three different pumping powers: a) $P_{\mathrm{pump}} = 130\,\mathrm{W}$, b) $P_{\mathrm{pump}} = 160\,\mathrm{W}$, and c) $P_{\mathrm{pump}} = 230\,\mathrm{W}$. On the left-hand side of each scenario, one can see the closed-loop dynamics given by $f_{\mathrm{CL}}(x) = f(x, u^s + \varsigma(k_{\mathrm{FB}}(x^n - x^s)))$ (solid line) and their derivative $f'_{\mathrm{CL}}(x) = \frac{\mathrm{d}f_{\mathrm{CL}}}{\mathrm{d}x}(x)$ (dashed line). The resulting behavior of the output pulses $W^n_{\mathrm{out}} = \frac{d_{\mathrm{L}}^2 \pi}{4} y^n$ with the initial state close to the steady state $x^0 \approx x^s$ is illustrated on the right-hand side. The corresponding open-loop behavior is included in blue for perspective. In all three cases, the feedback law (5.44) with (5.46) using $\varepsilon = 0.02$ successfully stabilizes the closed-loop dynamics given by

Die approbierte Originalversion dieser Dissertation ist in der TU Wien Bibliothek verfügbar.
The approved original version of this doctoral thesis is available at the TU Wien Bibliothek.
TU Bibliothek WIEN Your knowledge hub

$f_{\mathrm{CL}}(x) = f(x, u^s + \varsigma(k_{\mathrm{FB}}(x^n - x^s)))$. Additionally, in Figure 5.9 (a), the absolute value of the derivative $f'_{\mathrm{CL}}(x) = \frac{\mathrm{d}f_{\mathrm{CL}}}{\mathrm{d}x}(x)$ is less than 1, which is why $f_{\mathrm{CL}}(x)$ is Lipschitz continuous with a Lipschitz constant less than 1. Therefore, the closed-loop dynamics are in fact GAS due to the contraction mapping theorem. While such an analysis is not possible for the remaining scenarios, extensive simulation studies still suggest that the resulting closed-loop dynamics are indeed GAS, too.

Remark 22. *Without going into details, an analysis based on the contraction mapping theorem can be extended to the case (b) by separating the domain of the state variable into two sets: one that yields again a contraction mapping while being a positive invariant set of the system dynamics and another one that maps into the first set within one step.*

Notice that the mean value of the output pulses in Figure 5.9 of the unstable system is *not* the same as for the stabilized system, i.e. the expected steady-state solution of (5.35). In fact, the pumping power of the case presented in Figure 5.9 (c) corresponds to a scenario with maximum steady-state efficiency according to Figure 5.7. However, the unstable operation results in over-proportional losses that deteriorate the efficiency significantly compared to the steady-state solution.

Measuring $I_{\mathrm{P}}(L, t^n)$ directly is somewhat problematic in practice since it requires to reliably detect the peak value under sampling in a noisy environment. Additionally, the control law (5.44) calculates the current input u^n based on x^n, both of which are defined at time t^n. Thus, it is necessary to obtain an estimate $\hat{x}^n$ due to measurements of the transmitted pump light for times $t \in [t^{n-1}, t^n - t_{\mathrm{ac}}]$, where t_{ac} is the total time necessary to adjust the AOM at the input, to process the measurements, and to calculate the control law (5.44). A simple and robust way to achieve this is by measuring $I_{\mathrm{P}}(L, t)$ at k times $\tilde{t}_k \in [t^{n-1}, t^n - t_{\mathrm{ac}}]$ and use polynomial or exponential approximations in the least-squares sense to extrapolate $I_{\mathrm{P}}(L, t)$ at $t = t^n$ as illustrated in Figure 5.10. The resulting $\hat{I}_{\mathrm{P}}(L, t^n)$ can then be used to calculate $\hat{x}^n$ according to (5.43).

5.3.2 Feedback stabilization using pulse energy measurements

While approaching the stabilization task by measuring the transmitted pump light is a simple and elegant method, such measurements are not always available as for broadband pumping sources such as flash lamps or arc lamps, which are not considered in this thesis. Additionally, if the energy of the amplified pulses are significantly below the capabilities of the gain medium, the fluctuation in the transmitted pumping beam may be to small to be measured reliably as it is the case in Section 5.5. In such cases, one can still follow the straight forward way to stabilize the regenerative amplifier using measurements of the pulse energy. Doing so will ultimately require to somehow infer the current state from measurements,

Die approbierte Originalversion dieser Dissertation ist in der TU Wien Bibliothek verfügbar.
The approved original version of this doctoral thesis is available at the TU Wien Bibliothek.
TU Bibliothek WIEN Your knowledge hub

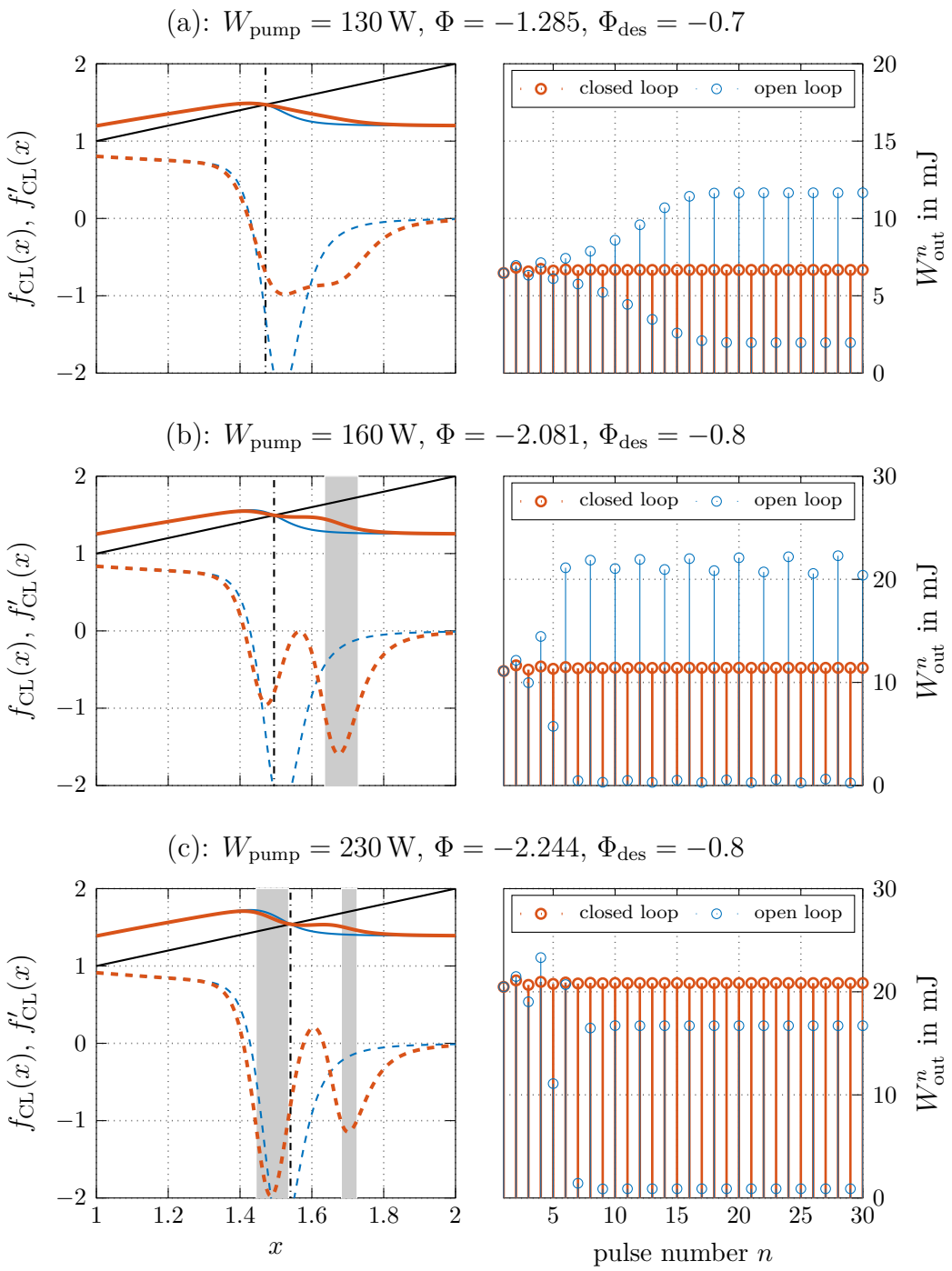

Figure 5.9: Feedback stabilization of a RA for three scenarios. On the left: the closed-loop dynamics $f_{\text{CL}}(x)$ (solid) and its derivative $f'_{\text{CL}}(x)$ (dashed). On the right: the resulting sequence of output pulses W^n_{out} for $x^0 \approx x^s$. The shaded areas indicate regions where $|f'_{\text{CL}}(x)| \geq 1$ and the corresponding open-loop behavior is illustrated in blue.

Die approbierte Originalversion dieser Dissertation ist in der TU Wien Bibliothek verfügbar.
The approved original version of this doctoral thesis is available at the TU Wien Bibliothek.
TU Bibliothek Your knowledge hub WIEN

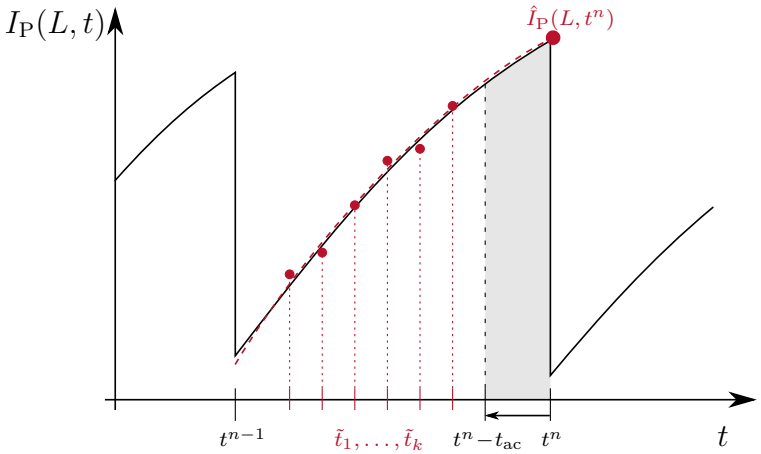

Figure 5.10: Estimation of $I_{\mathrm{P}}(L,t^n)$ by extrapolating measurements at times $\tilde{t}_k$ using polynomial or exponential least-squares approximations.

whether explicitly by using state observers or implicitly by using some kind of output feedback. In the following, we will proceed along the latter path as it comes up with an easily implementable and computationally inexpensive control law by transforming the system in so-called sensor coordinates.

In the vicinity of any x with $\frac{\partial h}{\partial x}(x,u) \neq 0$ there exists an inverse map $h^{-1}(y,u)$ such that $h(h^{-1}(y,u),u) = y$ for all u. Using this inverse map, (5.31) can be written as

$$y^{n+1} = h\left(f\left(h^{-1}(y^n,u^n),u^n\right),u^{n+1}\right) = f_1(y^n,u^n,u^{n+1}). \tag{5.47}$$

Notice the appearance of two different time instances of u due to the system model's direct feed-through. Introducing the new state $\mathbf{z}^n = [y^n,u^n]^T$ and the new input $\nu^n = u^{n+1}$ yields the dynamically extended system model

$$\mathbf{z}^{n+1} = \begin{bmatrix} f_1(z_1^n,z_2^n,\nu^n) \\ \nu^n \end{bmatrix} = \mathbf{f}(\mathbf{z}^n,\nu^n), \tag{5.48}$$

with the initial condition $\mathbf{z}^0 = [y^0,u^0]^T$, where u^0 can be chosen arbitrarily and $y^0 = h(x^0,u^0)$. It is easy to see that any operating point (x^s,u^s) of the original system with the corresponding steady-state output $y^s = h(x^s,u^s)$ yields a steady-state $\mathbf{z}^s = [y^s,u^s]^T$ of the extended system (5.48) with $\nu^s = u^s$. Using $\Delta\mathbf{z}^n = [\Delta y^n,\Delta u^n]^T$ and $\Delta\nu^n = \nu^n - \nu^s$, one can linearize the extended system model at the steady state $\mathbf{z}^s$, see (5.38), which yields

$$\Delta\mathbf{z}^{n+1} = \underbrace{\begin{bmatrix} \Phi & C\Gamma - \Phi D \\ 0 & 0 \end{bmatrix}}_{\boldsymbol{\Phi}} \mathbf{z}^n + \underbrace{\begin{bmatrix} D \\ 1 \end{bmatrix}}_{\boldsymbol{\Gamma}} \Delta\nu^n. \tag{5.49}$$

Die approbierte Originalversion dieser Dissertation ist in der TU Wien Bibliothek verfügbar.
The approved original version of this doctoral thesis is available at the TU Wien Bibliothek.
TU Bibliothek WIEN Your knowledge hub

Note that the definition of the inverse map h^{-1} in (5.47) entails that $\frac{\partial h^{-1}}{\partial u} = -\left(\frac{\partial h}{\partial x}\right)^{-1} \frac{\partial h}{\partial u}$. We can therefore stabilize the original system (5.31) in the vicinity of the operating point (x^s, u^s) by stabilizing the linear system (5.49), which is always possible as long as the controllability matrix

$$\mathcal{R}(\mathbf{\Phi}, \mathbf{\Gamma}) = \begin{bmatrix} \mathbf{\Gamma} & \mathbf{\Gamma\Phi} \end{bmatrix} = \begin{bmatrix} D & C\Gamma \\ 1 & 0 \end{bmatrix} \tag{5.50}$$

has full rank. As one would have expected, this is not the case if the assumption of $\frac{\partial h}{\partial x}(x, u) \neq 0$ is violated (notice that $\Gamma = \frac{\partial f}{\partial u} < 0$ as stated in Section 5.3.1) and therefore no inverse map h^{-1} exists. As illustrated in Figure 5.5, the point with maximum output energy (but not with maximum efficiency, see Figure 5.7) is the only point where this happens. For all other points, a control law of the form

$$\nu^n = \nu^s + \varsigma\left(\mathbf{k}_{\mathrm{FB}}^T \Delta \mathbf{z}^n\right) \tag{5.51}$$

can be used to stabilize the plant. To determine the feedback gain $\mathbf{k}_{\mathrm{FB}}$, one can use standard methods for the linearized system like pole placement or solving a discrete-time algebraic Riccati equation (DARE) as part of a linear quadratic regulator (LQR) problem. Writing the control law with original variables, the output feedback law reads as

$$u^{n+1} = u^s + \varsigma\left(\mathbf{k}_{\mathrm{FB}}^T \begin{bmatrix} \Delta y^n \\ \Delta u^n \end{bmatrix}\right). \tag{5.52}$$

Apart from output measurements, the output feedback law (5.52) requires a corresponding input value to determine the following input pulse. With $\Delta u^n = u^n - u^s$ in mind, one can see that the resulting feedback law (5.52) is in fact a dynamic system itself.

Due to the strongly nonlinear behavior of the output function h it is quite clear that an output feedback law based on a linear approximation of the plant will not achieve GAS but is rather sensitive to significant deviations from the designed operating point. For simplicity, we thus choose $\varsigma(u) = u^s \operatorname{sat}(u/u^s)$ with the saturation function

$$\operatorname{sat}(u) = \begin{cases} -(1-\varepsilon) & \text{if } u \leq -(1-\varepsilon) \\ (1-\varepsilon) & \text{if } u \geq (1-\varepsilon) \\ u & \text{otherwise,} \end{cases} \tag{5.53}$$

as simulation studies indicate that other sigmoid functions do not increase the region of attraction in contrast to the state feedback law proposed in Section 5.3.1. While the proposed output feedback law (5.52) works as expected in the vicinity of the designed operating point (x^s, u^s), it is hard to give estimates of the associated region of attraction. Moreover, the significance of the simulation results strongly

Die approbierte Originalversion dieser Dissertation ist in der TU Wien Bibliothek verfügbar.
The approved original version of this doctoral thesis is available at the TU Wien Bibliothek.
TU Bibliothek WIEN Your knowledge hub

depends on the chosen operating points, initial errors or other disturbances. Since we will revisit the presented output feedback law (5.52) for variable pumping powers in Section 5.4, which gives a clearer picture of its performance, it was refrained from presenting dedicated simulation scenarios in this section.

5.4 Variable pumping power

Most crucial design parameters cannot be (easily) changed during operation, e.g., the number of round-trips usually involves precise timing and may require adaptions of the pulse stretcher and compressor for CPA systems or increasing the seed energy requires additional amplification stages beyond a certain level. The available optical pumping power, however, can be varied comparatively easily. For example, when taking the regenerative amplifier into operation, the pumping power is usually increased slowly up to the desired (stable) operating point to avoid strong transient pulses. In this section, we want to finally use the developed control laws to systematically and safely steer a regenerative amplifier to a desired operating point by considering the pumping power as a second input variable that can be adjusted slowly compared to the repetition rate of the amplifier.

Using the general description of the pumping process (5.23) with the incident pumping intensity $I_0(t) = {}^{4P_{\text{pump}}(t)}/_{d_{\text{P}}^2\pi}$ and assuming that $I_0(t)$ changes very slowly compared to the time it takes for the pumping beam to propagate through the gain medium, one can proceed analogously to (5.26) to obtain the regeneration dynamics

$$\begin{aligned}\frac{\mathrm{d}}{\mathrm{d}t}G(t) = &-\gamma_{21} f_2 \left[\sigma f_1 (f_1+f_2) N_{\text{dop}} L + \ln(G(t))\right] G(t) \\ &+ \sigma \frac{4P_{\text{pump}}(t)}{d_{\text{P}}^2 \pi} \frac{(f_1+f_2)^2}{\hbar\omega_{\text{P}}} \left[1 - \exp\left(-\sigma_{\text{P}}(\kappa_1 N_{\text{dop}} L)\right) G(t)^{\frac{\kappa_2 \sigma_{\text{P}}}{(f_1+f_2)\sigma}}\right] G(t).\end{aligned} \tag{5.54}$$

Assuming that the pumping power remains constant for the time between two consecutive pulses, i.e., $P_{\text{pump}}(t) \approx p^n$ for $t \in [t^n, t^{n+1})$, its solution can again be written formally as

$$G_{\text{out}} = f_{\text{pump}}(G_{\text{in}}; p^n). \tag{5.55}$$

Thus, for slowly changing pumping intensities, the dynamics of the resulting discrete-time model according to (5.31) can be written as

$$x^{n+1} = f_{\text{pump}}\left(\begin{bmatrix}1 & 0\end{bmatrix} \mathbf{f}_{\text{MP}}\left(\begin{bmatrix}x^n \\ u^n\end{bmatrix}\right); p^n\right) = f(x^n, u^n; p^n) \tag{5.56a}$$

$$y^n = \frac{\eta_{\text{out}}}{\eta_{\text{RC}}} \begin{bmatrix}0 & 1\end{bmatrix} \mathbf{f}_{\text{MP}}\left(\begin{bmatrix}x^n \\ u^n\end{bmatrix}\right) = h(x^n, u^n). \tag{5.56b}$$

Clearly, the pumping power determines the regenerative amplifier's steady state x^s and thus its open-loop dynamics as shown in Figure 5.6. While its

Die approbierte Originalversion dieser Dissertation ist in der TU Wien Bibliothek verfügbar.
The approved original version of this doctoral thesis is available at the TU Wien Bibliothek.
TU Bibliothek WIEN Your knowledge hub

influence is highly nonlinear, the previous sections demonstrated that local (i.e., linearly designed) feedback laws can stabilize the amplifier (at least) within a certain region of attraction around each operating point (x^s, u^s). It is thus quite intuitive to develop several control laws for different operating points and combine them within a gain-scheduling approach [115]. We therefore express the steady state x^s as a function of the scheduling parameter[4] p, i.e., a parametrized solution of the fixed-point equation

$$x^s(p) = f(x^s(p), u^s; p), \tag{5.57}$$

to obtain a family of linear systems, see (5.38)

$$\Delta x^{n+1} = \Phi(p)\,\Delta x^n + \Gamma(p)\,\Delta u^n \tag{5.58a}$$
$$\Delta y^n = \mathrm{C}(p)\,\Delta x^n + \mathrm{D}(p)\,\Delta u^n, \tag{5.58b}$$

with $\Delta u^n = u^n - u^s$, $\Delta x^n = x^n - x^s(p)$, and $\Delta y^n = y^n - y^s(p)$ as well as Φ, Γ, C, and D analogous to (5.39). Using the feedback stabilization approaches from the previous section, we shall now construct a family of control laws that stabilize the system in the vicinity of each $x^s(p)$.

Gain scheduling using pump light measurements

Since $\Gamma(p) < 0$ for all p, we can proceed as in Section 5.3.1. For a current pumping power p^n, one obtains the control law

$$u^n = u^s + \varsigma\left(k_{\mathrm{FB}}(p^n)(x^n - x^s(p^n))\right), \tag{5.59}$$

where

$$k_{\mathrm{FB}}(p) = \frac{\Phi_{\mathrm{des}}(p) - \Phi(p)}{\Gamma(p)} \tag{5.60}$$

with the desired dynamics $\Phi_{\mathrm{des}}(p)$ of the closed-loop system. Since the primary objective is to stabilize the regenerative amplifier, one may only interfere with its natural dynamics when necessary, i.e., if $|\Phi(p)| \geq 1$. Since $\Phi(p) < 1$ (see Figure 5.5) and including some safety margin, we choose

$$\Phi_{\mathrm{des}}(p) = \begin{cases} \Phi(p) & \text{if } \Phi(p) > -0.9 \\ -0.9 & \text{otherwise.} \end{cases} \tag{5.61}$$

The resulting feedback gain $k_{\mathrm{FB}}(p)$ is illustrated in Figure 5.11.

[4]The choice of a scheduling parameter is not unique. For example, one could use y^s for operational regions where p and y^s map one-to-one. Both choices are equivalent as long as the design model matches the experimentally observed dynamics perfectly. If this is not the case, each choice has their particular advantages.

Die approbierte Originalversion dieser Dissertation ist in der TU Wien Bibliothek verfügbar.
The approved original version of this doctoral thesis is available at the TU Wien Bibliothek.
TU Bibliothek WIEN Your knowledge hub

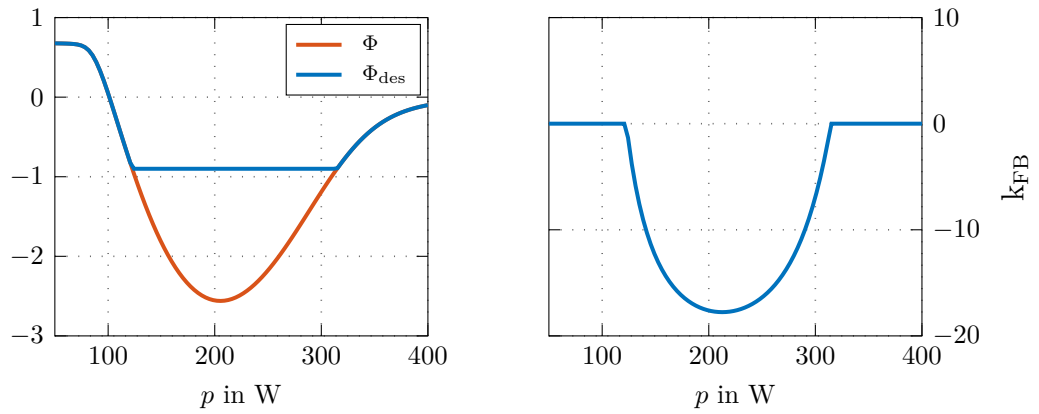

Figure 5.11: The plant's open-loop dynamics Φ and the desired closed-loop dynamics Φ_{des} with the resulting feedback gain k_{FB} according to (5.60).

Gain scheduling using pulse energy measurements

Analogous to the previous section, we can transfer the output feedback law given by (5.52) into a gain-scheduling scenario, which yields

$$u^{n+1} = u^s + \varsigma\left(\mathbf{k}_{\text{FB}}^T(p^n)\begin{bmatrix} y^n - y^s(p^n) \\ u^n - u^s \end{bmatrix}\right), \tag{5.62}$$

with the feedback gain $\mathbf{k}_{\text{FB}}^T(p)$. In contrast to the previous section, however, we are not able to find a suitable feedback gain for all p, since there exists values $\tilde{p}$ where the controllability matrix $\mathcal{R}(\mathbf{\Phi}, \mathbf{\Gamma})$ becomes singular as shown in Figure 5.12. While the singular points for $p = 0$ and $p \to \infty$ are irrelevant from a practical perspective, the singularity at the operating point with maximal output energies is more troublesome. Additionally, while a stabilizing solution exists in the vicinity of such singular points, the required feedback gains are usually very high which can be problematic to implement in the presence of measurement uncertainties and noise. A standard procedure to deal with such singular points is to limit the resulting feedback gains in its vicinity by selecting a region around $\tilde{p}$ within which one interpolates between the values at the boundary in some sense. Assigning the nearest boundary values and using an LQR formulation, one obtains a feedback gain $\mathbf{k}_{\text{FB}}^T(p)$ as illustrated in Figure 5.12. As noted in Section 5.3.2, the feedback law (5.62) is a dynamic system itself, whereby its linearized dynamics are determined by $k_{\text{FB},2}$. With this in mind, we can see that the LQR-based solution in Figure 5.12 yields control laws that are unstable on their own for p approximately between 250 W and 300 W but successfully stabilize the closed-loop dynamics as shown in Figure 5.15.

Die approbierte Originalversion dieser Dissertation ist in der TU Wien Bibliothek verfügbar.
The approved original version of this doctoral thesis is available at the TU Wien Bibliothek.
TU Bibliothek WIEN Your knowledge hub

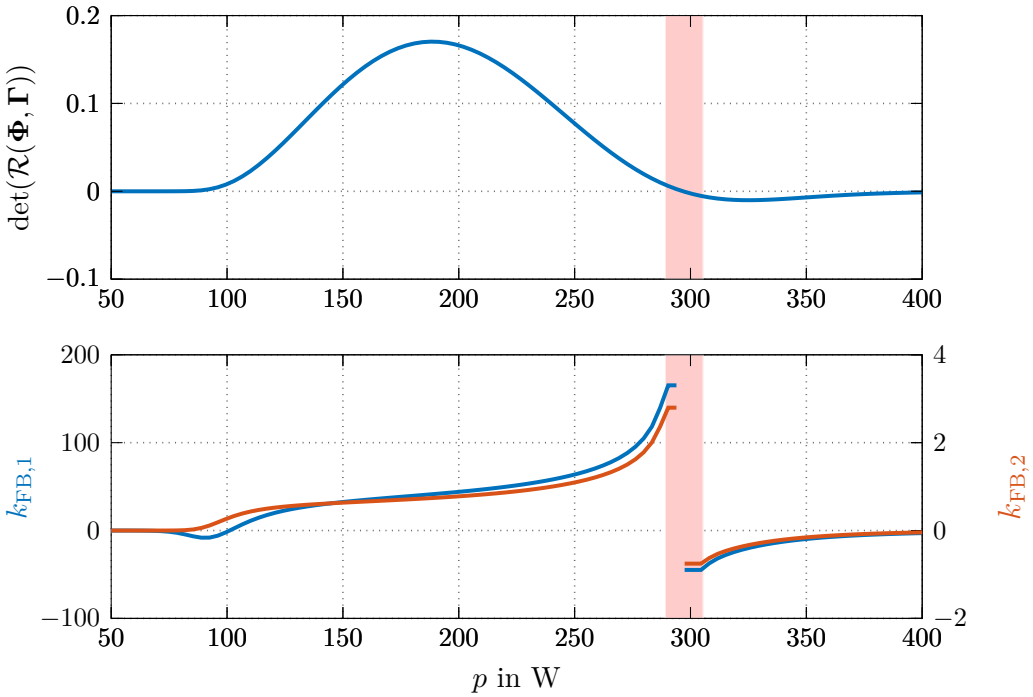

Figure 5.12: A possible feedback gain $\mathbf{k}_{\mathrm{FB}}^T(p)$ using an LQR formulation and a local interpolation around the singular point $\tilde{p} \approx 297\,\mathrm{W}$.

Comparison

The performance of the two gain scheduling designs presented above shall be illustrated with a simulation scenario that covers most of the interesting operational regimes of a regenerative amplifier. Therefore, the optical pumping power $P_{\mathrm{pump}}(t)$ (and thus p^n) is chosen to start from a weakly pumped state at 50 W. Afterwards, the power is linearly increased such that the amplifier passes the unstable regime and remains at a stable operating point at 350 W for 40 ms. Afterwards, the power is decreased quickly to 130 W which is still unstable without feedback and held there for the remaining time. This second slope is chosen fast enough to demonstrate the limits of the gain scheduling approach and illustrate the differences between the feedback laws (5.59) and (5.62). In view of the following controlled scenarios, the input is chosen to be constant at half the seed energy $u^n = \bar{u}/2$, i.e., $\eta_{\mathrm{AOM}}^n = 1/2$ to leave some headroom for the control. Notice that the reduced input energy results in a slightly larger unstable region of the regenerative amplifier compared to Figure 5.6, where the input pulse was equal to the seed pulse, i.e., $\eta_{\mathrm{AOM}}^n = 1$.

For reference, an open-loop scenario is illustrated in Figure 5.13. At first, the pumping intensity is too low to yield significant output pulses. Increasing the power beyond 80 W, the energy of the output pulses rises linearly with the supplied pumping power until the amplifier becomes unstable. Notice that the

Die approbierte Originalversion dieser Dissertation ist in der TU Wien Bibliothek verfügbar.
The approved original version of this doctoral thesis is available at the TU Wien Bibliothek.
TU Bibliothek WIEN Your knowledge hub

amplifier entered the unstable regime earlier but the oscillations require some time to build up (compare with 130 W of pumping power at the end). While the steady-state output energy W_{out}^n should increase further, both output pulses are often significantly below that value due to the overly increased losses of the stronger pulses. After the amplifier leaves the unstable regime, its output pulses converge back to their steady-state values. Going back the opposite direction repeats the same behavior. Since the final value of the pumping power is still within the unstable regime, the amplifier settles at the corresponding limit cycle consisting of a strong and a weak output pulse. Applying state feedback due to the transmitted pump light according to the feedback law (5.59), the amplifier is able to follow the desired steady-state behavior very well as shown in Figure 5.14. Notice that the required input corrections are fairly low. Even when decreasing the pumping power rapidly at the end, the desired steady-state values are held remarkably well. Afterwards, one can observe that the rapid transition caused some minor deviations that are damped by the feedback law with the desired dynamics (cp. Figure 5.11). In comparison, the output feedback law (5.62) performs quite well too when varying the pumping power at a sufficiently slow rate as shown in Figure 5.15. However, the required modulations of the input are significantly larger compared to Figure 5.14. This is partially due to the small deviations between the calculated output pulses at steady state $y^s(p^n)$ and the steady-state output pulses produced by the numerical solution of the full system model (5.12). In particular, the gain of each passage through the gain medium is systematically over- or underestimated depending on the chosen numerical scheme applied to solve (5.12). When passing through the singular point $\tilde{p}$ at approximately $t = 66\,\text{ms}$, one can see a small step in η_{AOM}^n due to the discontinuous feedback gain (see Figure 5.12) with only a minor effect on the amplifier's dynamics. A similar effect can be seen when the time evolution of the pumping power changes rapidly (i.e., at $t = 80\,\text{ms}$ and $t = 120\,\text{ms}$) due to the added dynamics introduced by the integrator state in the extended system model (5.48). Combining such disturbances with the rapidly decreasing pumping power of the second slope, the feedback law struggles to keep the amplifier stable and some small oscillations start to appear (see Figure 5.15 for $t \geq 120\,\text{ms}$). The feedback law (5.59) still manages to damp those oscillations even while the pumping power continues to decrease rapidly and keeps the amplifier stable at the end. However, the prescribed trajectory of the pumping power clearly operates the gain-scheduling approach at its limits.

As indicated in Section 5.3, the output feedback law lacks the robustness of the state feedback law in stabilizing a steady state due to the nonlinearity of the output function $h(x, u)$. Comparing Figure 5.15 with Figure 5.14, this also applies to the case of variable pumping powers and their related gain-scheduling controllers. While the state feedback seems to compare favorably, not least due to its simplicity, one will be bound to the availability as well as reliability and precision of certain measurements in practice. For example, the variations in

Die approbierte Originalversion dieser Dissertation ist in der TU Wien Bibliothek verfügbar.
The approved original version of this doctoral thesis is available at the TU Wien Bibliothek.
TU Bibliothek WIEN Your knowledge hub

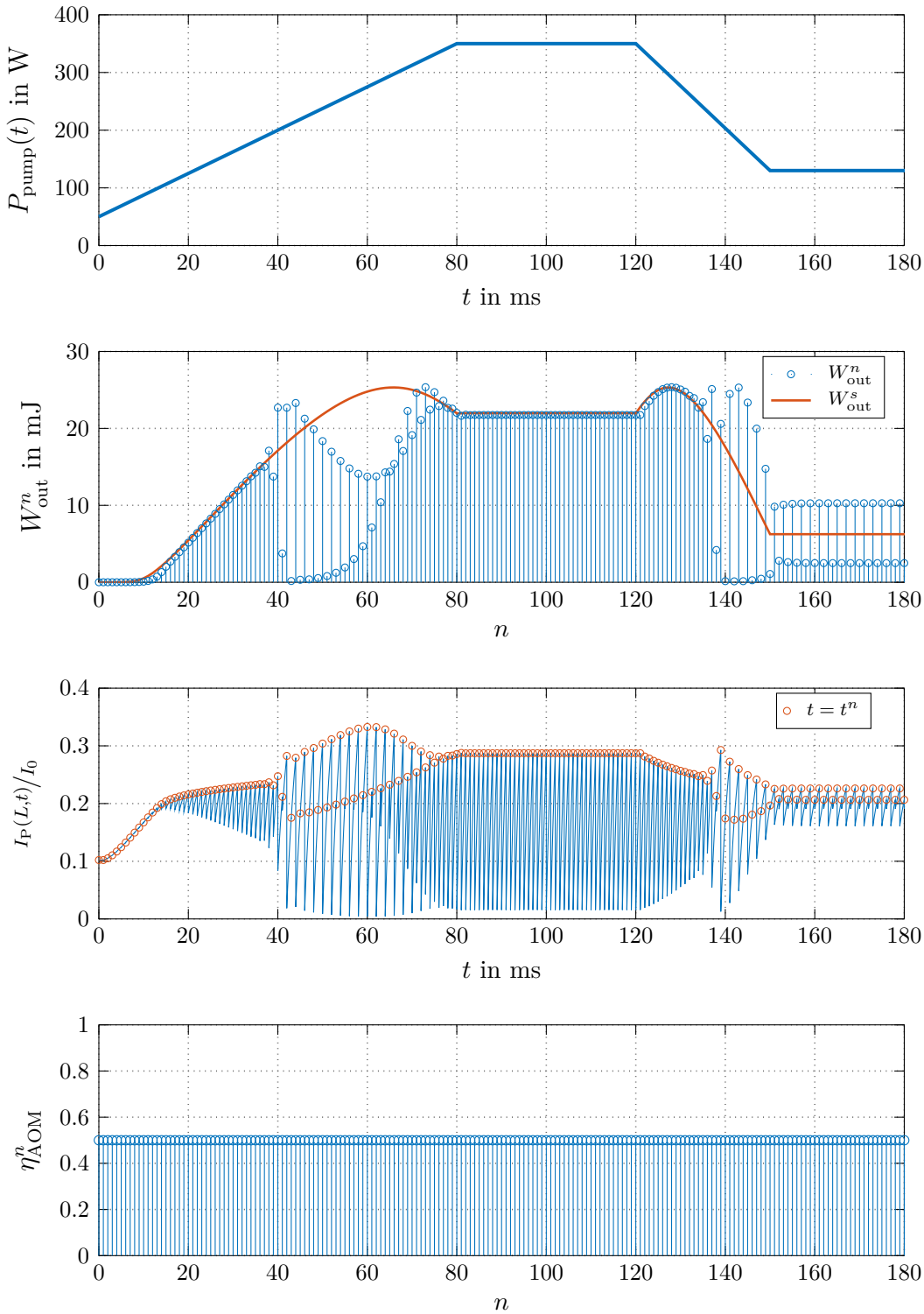

Figure 5.13: Open-loop behavior of a regenerative amplifier for the given trajectory of the optical pumping power $P_{\text{pump}}(t)$ passing through the unstable operational regime.

Die approbierte Originalversion dieser Dissertation ist in der TU Wien Bibliothek verfügbar.
The approved original version of this doctoral thesis is available at the TU Wien Bibliothek.
TU WIEN Bibliothek Your knowledge hub

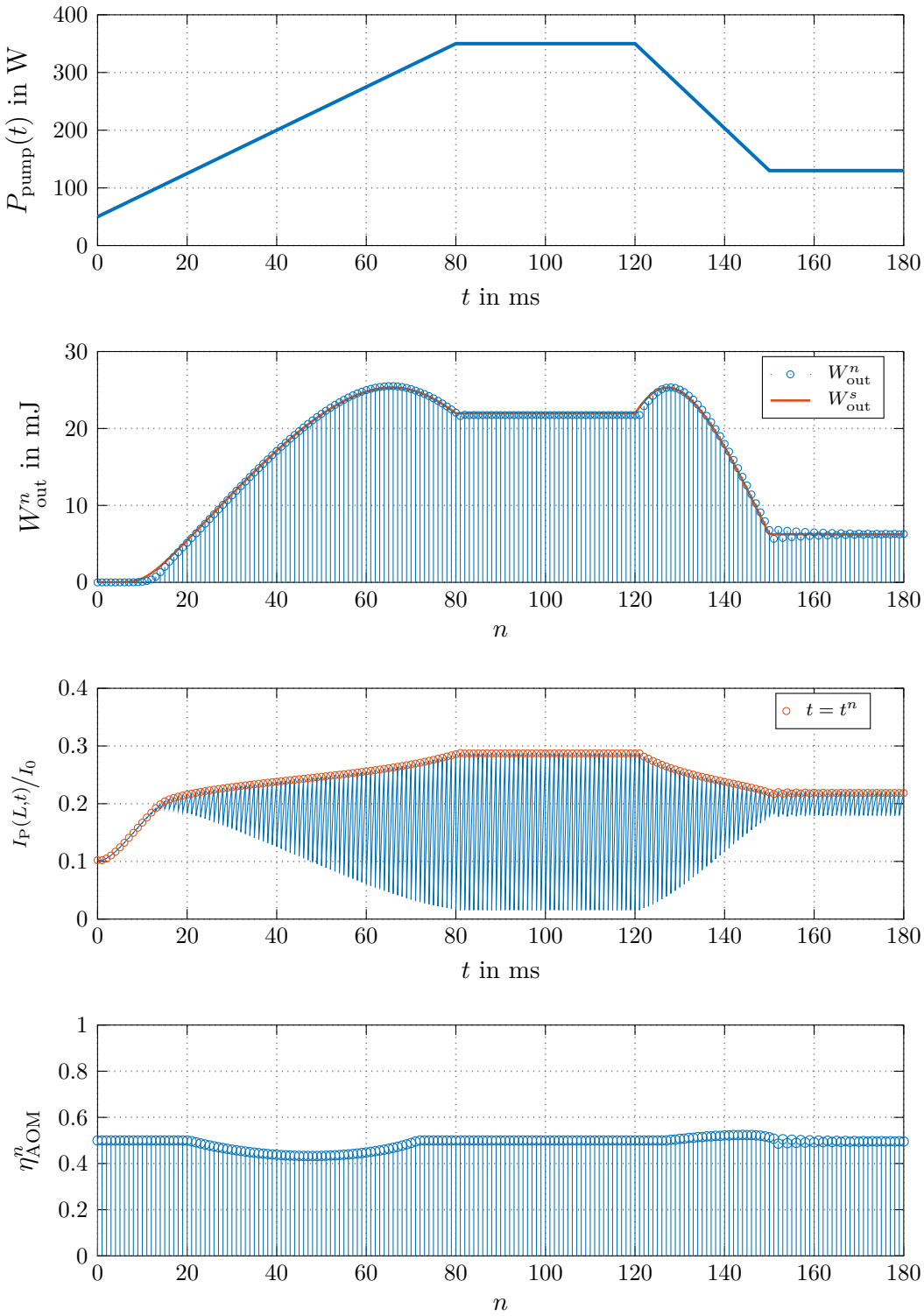

Figure 5.14: Behavior of a stabilized regenerative amplifier using the state feedback law (5.59) for the given trajectory of the optical pumping power $P_{\text{pump}}(t)$ passing through the unstable operational regime.

Die approbierte Originalversion dieser Dissertation ist in der TU Wien Bibliothek verfügbar.
The approved original version of this doctoral thesis is available at the TU Wien Bibliothek.
TU WIEN Bibliothek Your knowledge hub

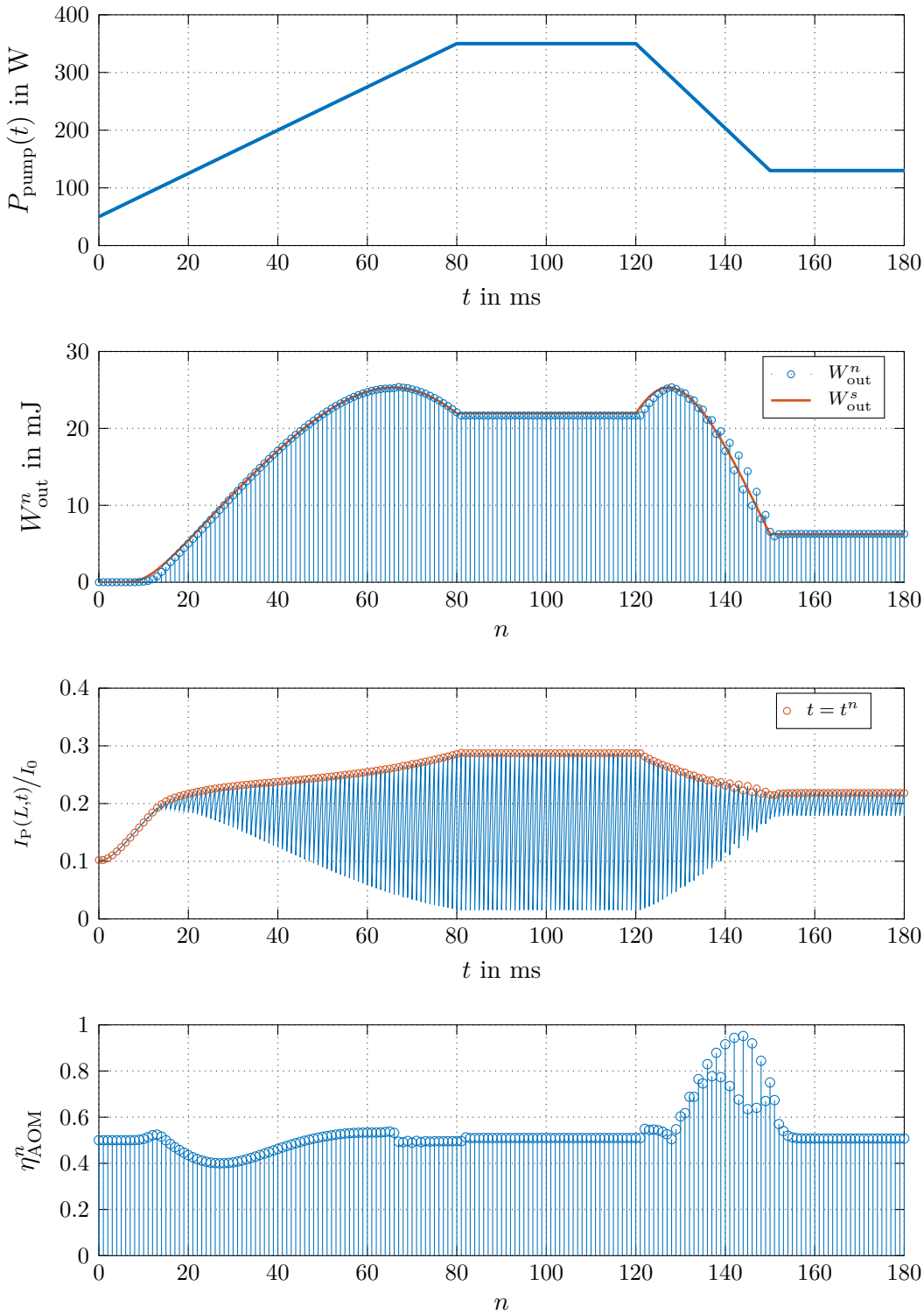

Figure 5.15: Behavior of a stabilized regenerative amplifier using the output feedback law (5.62) for a given trajectory of the optical pumping power $P_{\text{pump}}(t)$ passing through the unstable operational regime.

Die approbierte Originalversion dieser Dissertation ist in der TU Wien Bibliothek verfügbar.
The approved original version of this doctoral thesis is available at the TU Wien Bibliothek.
TU WIEN Bibliothek Your knowledge hub

the transmitted pump light can become too small to be measured reliably in the presence of measurement noise.

5.5 Experimental results

To demonstrate the effectiveness of the proposed feedback in practice, it is applied to a regenerative amplifier from our partners at the Photonics Institute at TU Wien. The amplifier utilizes a linear cavity design with a double-pass pumping scheme (see Appendix C) and is seeded by 2 nJ pulses at $f_{\text{rep}} = 1\,\text{kHz}$. By choosing $N_{\text{RT}} = 184$ (i.e., each pulse passes the gain medium 368 times due to the linear cavity), one obtains an amplifier that allows sustained unstable operation at low power outputs without damaging the gain material. However, due to the low energy extraction at such operating points, the fluctuations of the transmitted pump light are too small to be measured reliably. As a result, the feedback stabilization using pulse energy measurements presented in Section 5.3.2 is the only possible option.

Measuring the energy of the output pulses is usually done by measuring the averaged optical power of the output beam and therefore only provides mean values of the output pulse's energy. A simple method to obtain the energy of one individual pulse is to feed the output current of a photo diode (that is proportional to the pulse intensity I) into a small capacitor as shown in Figure 5.16. While the resulting voltage v_{ph} is slowly decaying due to parasitic resistances, the jump height is directly proportional to the energy of the incident laser pulse. To obtain robust estimates of the jump height, one can again use polynomial or exponential least-squares approximations as in Section 5.3.1 depending on the time constant of the measured decay. As Figure 5.17 shows, the mean estimated jump height of v_{ph} is indeed in very good agreement with the mean energy of the output pulses as measured through optical power measurements. As a result, we are able to measure W_{out}^{n} with sufficient accuracy.

Remark 23. *To increase the signal-to-noise ratio, measurements of the pulse build-up*[5] *were used instead of measuring the final output pulse. As long as the amplifier is hardly saturating and the gain during each round-trip remains at roughly the same level, which is the case for the comparatively low power outputs in this example, both measurements are approximately the same.*

A comparison of the average output energy $\overline{W_{\text{out}}^{n}}$ and measurements of the limit set of the output energy W_{out}^{ω} (due to Figure 5.16) with simulation results using the parameters given in Table E.4 is illustrated in Figure 5.18. Notice that

[5]The term pulse build-up is used to describe the transmitted light behind a mirror of the resonator cavity, i.e. a densely packed pulse burst consisting of all $k = 1, \ldots, N_{\text{RT}}$ pulses $I_{\text{out}}^{n,k}(t)$ separated by the round-trip time inside the cavity.

Die approbierte Originalversion dieser Dissertation ist in der TU Wien Bibliothek verfügbar.
The approved original version of this doctoral thesis is available at the TU Wien Bibliothek.
TU Bibliothek Your knowledge hub WIEN

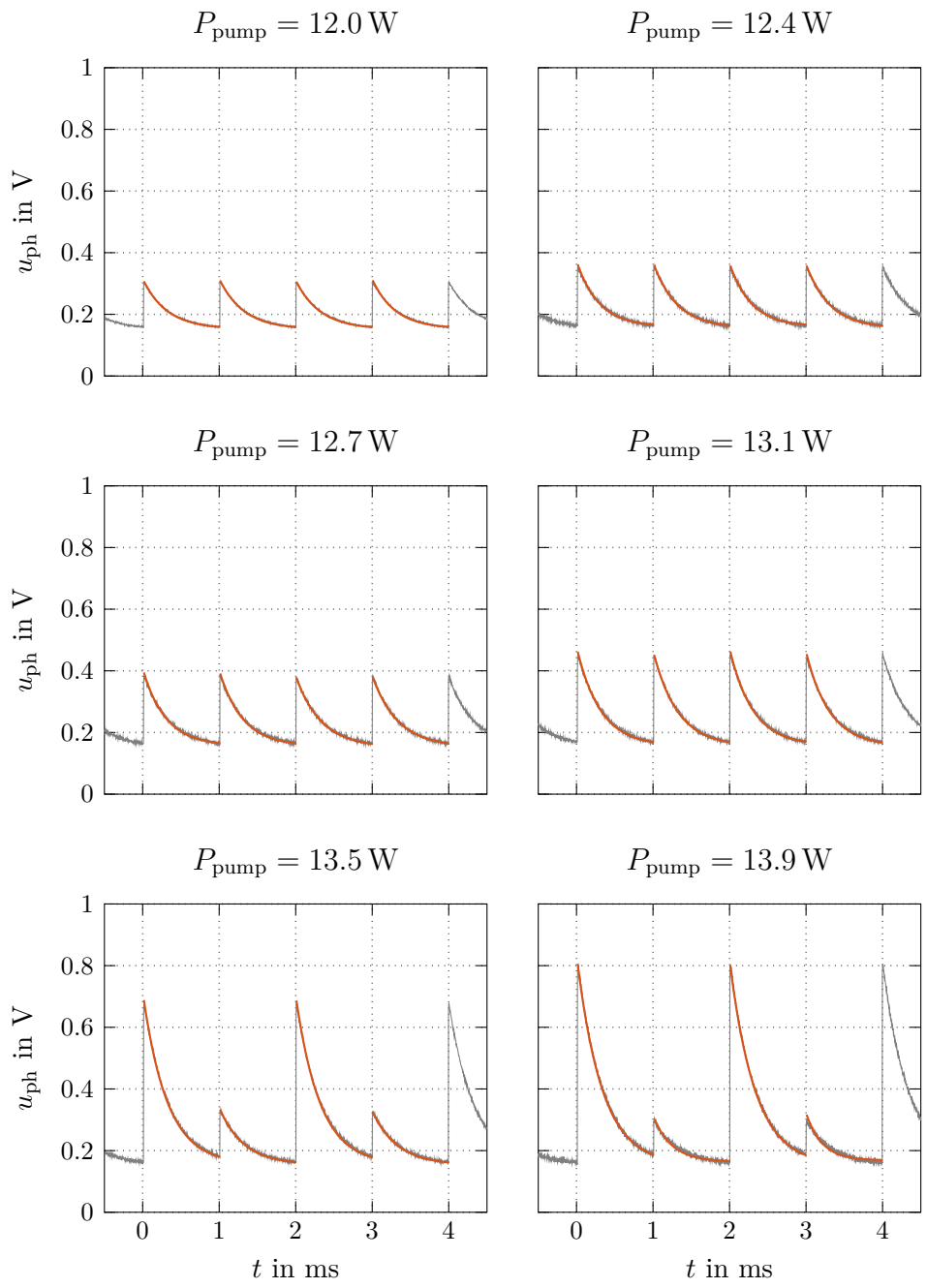

Figure 5.16: Measurement of the voltage at the photo diode v_{ph} (gray) for different optical pumping powers P_{pump}. To reliably estimate the jump height of v_{ph}, exponential least-squares approximations are applied to each segment (red).

Die approbierte Originalversion dieser Dissertation ist in der TU Wien Bibliothek verfügbar.
The approved original version of this doctoral thesis is available at the TU Wien Bibliothek.
TU Bibliothek Your knowledge hub WIEN

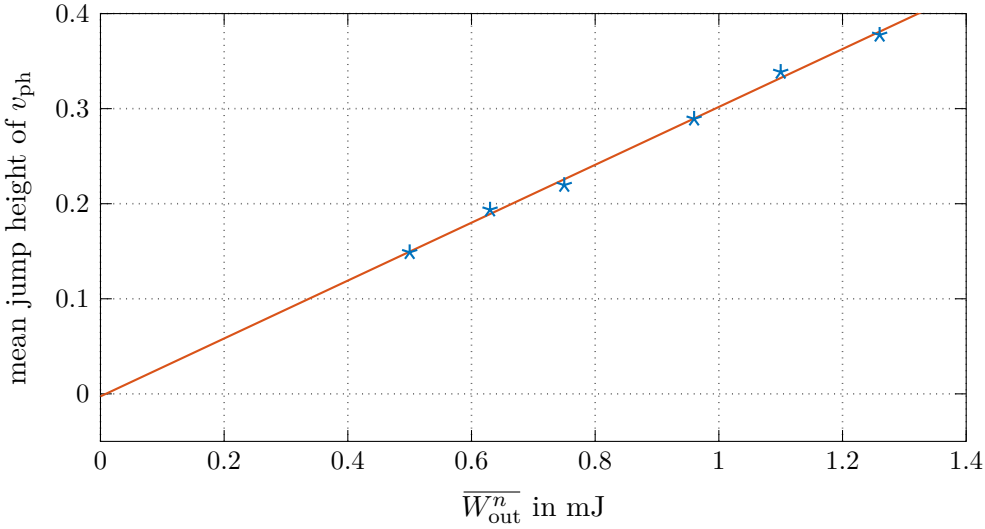

Figure 5.17: Comparison of the mean jump height of v_{ph} in Figure 5.16 with the mean energy of the output pulses $\overline{W^n_{\mathrm{out}}}$ obtained by measuring the averaged optical output power.

the parameters were chosen such that the amplifier is starting to become unstable at $P_{\mathrm{pump}} = 13.1\,\mathrm{W}$ as indicated by the measurements.

Choosing $u^s = 0.7\bar{u}$ and applying the gain-scheduled feedback law (5.62) to the experimental setup, one is able to stabilize the regenerative amplifier and steer it into otherwise unstable operational regions. When deactivating the feedback law by setting $u^n = u^s$ (i.e., $\eta^n_{\mathrm{AOM}} = 0.7$), small perturbations build up and the amplifier approaches the limit cycle again, as shown in Figure 5.19. The corresponding measured voltage $v_{\mathrm{ph}}(t)$ and the driving voltage of the AOM $v_{\mathrm{AOM}}(t)$ are shown in Figure 5.20 for small time segments with activated and deactivated feedback, respectively. Here, $v_{\mathrm{AOM}}(t)$ is linked to η^n_{AOM} by linear interpolation between a lower threshold voltage $\underline{v}_{\mathrm{AOM,th}}$ corresponding to $\eta^n_{\mathrm{AOM}} = \underline{\eta}_{\mathrm{AOM}}$ and an upper threshold voltage $\overline{v}_{\mathrm{AOM,th}}$ corresponding to $\eta^n_{\mathrm{AOM}} = 1$, respectively. Accounting for the actuation time of the AOM (compare Figure 5.10), $v_{\mathrm{AOM}}(t)$ for $t \in [t^n - t_{\mathrm{ac}}, t^{n+1} - t_{\mathrm{ac}}]$ is given by

$$v_{\mathrm{AOM}}(t) = \begin{cases} \underline{v}_{\mathrm{AOM,th}} & \text{if } \eta^n_{\mathrm{AOM}} < \underline{\eta}_{\mathrm{AOM}} \\ \underline{v}_{\mathrm{AOM,th}} + k_{\mathrm{AOM}} \left(\eta^n_{\mathrm{AOM}} - \underline{\eta}_{\mathrm{AOM}}\right) & \text{if } \eta^n_{\mathrm{AOM}} \in [\underline{\eta}_{\mathrm{AOM}}, 1] \\ \overline{v}_{\mathrm{AOM,th}} & \text{otherwise,} \end{cases} \tag{5.63}$$

where $k_{\mathrm{AOM}} = {}^{(\overline{v}_{\mathrm{AOM,th}} - \underline{v}_{\mathrm{AOM,th}})}/_{(1-\underline{\eta}_{\mathrm{AOM}})}$. For the presented experimental results, the values $\underline{\eta}_{\mathrm{AOM}} = 0.1$, $\underline{v}_{\mathrm{AOM,th}} = 0.5\,\mathrm{V}$, $\overline{v}_{\mathrm{AOM,th}} = 1\,\mathrm{V}$, and $t_{\mathrm{ac}} = 150\,\mu\mathrm{s}$ were chosen.

Remark 24. *Since the amplifier is used in other research activities at the Photonics Institute, it is subject to regular modifications to adapt to the specific needs*

Die approbierte Originalversion dieser Dissertation ist in der TU Wien Bibliothek verfügbar.
The approved original version of this doctoral thesis is available at the TU Wien Bibliothek.
TU Bibliothek Your knowledge hub WIEN

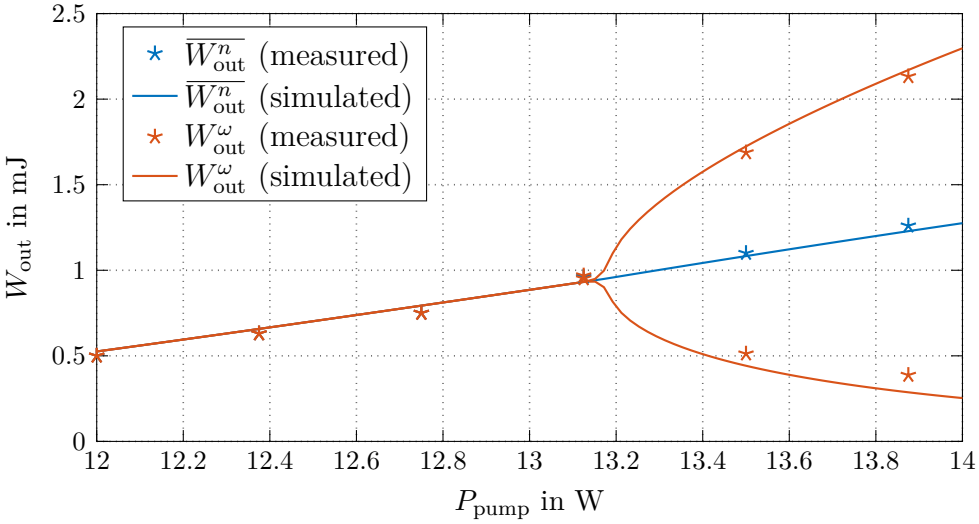

Figure 5.18: Comparison of measured and simulated pulse energies using the parameters given in Table E.4. Blue indicates mean values while red indicates values of the ω-limit set.

of each experiment. As a result, it seems that η_{RC} has decreased somewhat between the first set of measurements used to calibrate the model (i.e., data illustrated in Figure 5.16, Figure 5.17 and Figure 5.18) and the second set of measurements with the implemented feedback control (i.e., data illustrated in Figure 5.19 and Figure 5.20). As a result, the experimental setup used to implement the feedback control is unstable at lower pumping powers (compare Figure 5.19 operated at $P_{pump} = 13.1\,\text{W}$ and Figure 5.18). By only adapting the expected steady-state output $y^s(p)$, the feedback law (5.62) was able to stabilize the amplifier successfully, which highlights the robustness of the proposed approach.

Remark 25. *Apart from stabilizing the amplifier, the feedback reduced the fluctuations of the measured output pulses (i.e., the standard deviation of the output energy) from approximately 5.2% to 3.3% relative to the average pulse energy, which could be useful for applications that require precise pulse energies.*

Die approbierte Originalversion dieser Dissertation ist in der TU Wien Bibliothek verfügbar.
The approved original version of this doctoral thesis is available at the TU Wien Bibliothek.
TU Bibliothek WIEN Your knowledge hub

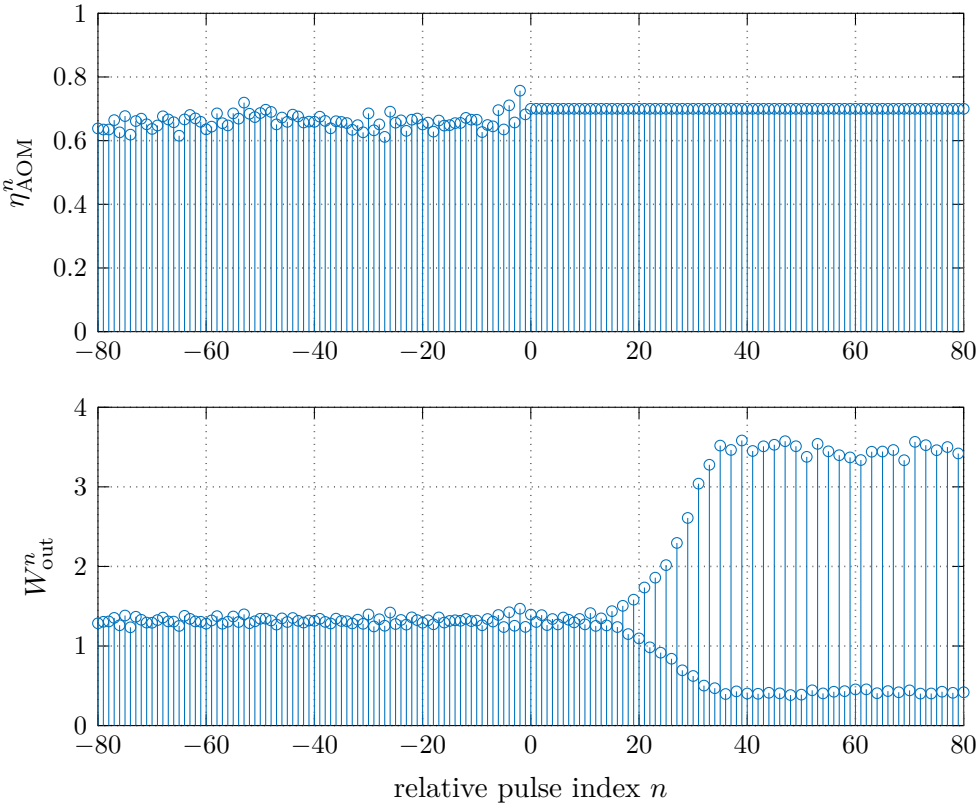

Figure 5.19: Feedback-stabilized regenerative amplifier operated at $P_{\mathrm{pump}} = 13.1\,\mathrm{W}$ using the feedback law (5.62). For $n \geq 0$, the feedback is deactivated by setting $u^n = u^s$. As a result, small perturbations build up and the output pulse energy W^n_{out} approaches the limit cycle again.

Die approbierte Originalversion dieser Dissertation ist in der TU Wien Bibliothek verfügbar.
The approved original version of this doctoral thesis is available at the TU Wien Bibliothek.
TU Bibliothek WIEN Your knowledge hub

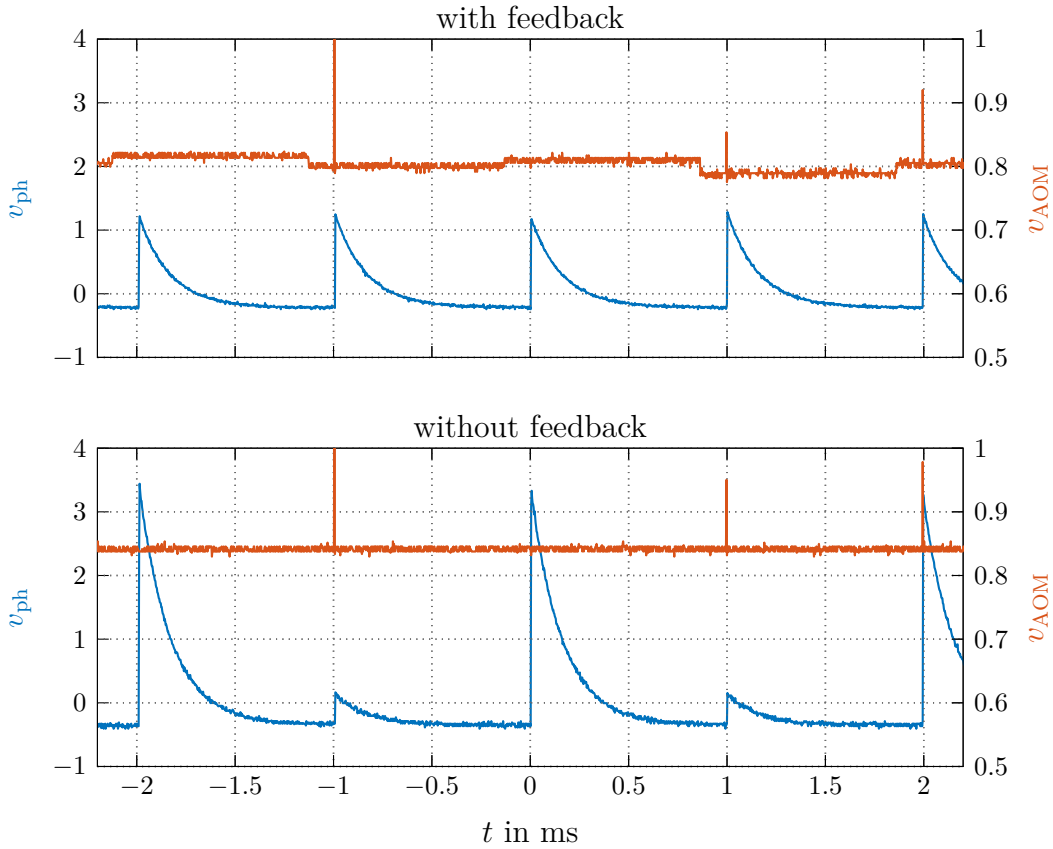

Figure 5.20: Measured voltage v_{ph} (blue) and the driving voltage of the AOM v_{AOM} (red) corresponding to small time segments with activated and deactivated feedback in Figure 5.19, respectively.

Die approbierte Originalversion dieser Dissertation ist in der TU Wien Bibliothek verfügbar.
The approved original version of this doctoral thesis is available at the TU Wien Bibliothek.
TU WIEN Bibliothek Your knowledge hub

Die approbierte Originalversion dieser Dissertation ist in der TU Wien Bibliothek verfügbar.
The approved original version of this doctoral thesis is available at the TU Wien Bibliothek.

CHAPTER 6

Control of the Formation and Amplification of Pulse Bursts in Regenerative Amplifiers using the Vernier Effect

The generation of pulse bursts of high intensity laser light has many important applications, such as ablation-cooled material processing [116] that reduces the damage from heat accumulation or the seeding of free electron lasers [16] as used in the European XFEL to investigate the dynamics of chemical reactions or the atomic structure of molecules, viruses and cells. Another application particular in line with the general theme of this thesis is the amplification of pulses by coherent pulse stacking [34]. Using a Gires-Tournois interferometer, an adequately spaced pulse burst can be "stacked" together into a single pulse and consequently the pulse energy of the individual pulses can be reduced while still obtaining the desired output energy. Thus, rather than amplifying a single pulse, the energy is spread temporally into a tightly spaced sequence of pulses which are recombined after amplification analogous to chirped pulse amplification methods. This method usually implements some kind of pulse splitting scheme such as birefringent materials [117] that require polarization-insensitive amplifiers or rather complicated piezo-actuated pulse splitters [118]. Recently, an alternative was proposed in [35] that relies on the Vernier effect, whereby the round-trip time of the resonator cavity is slightly detuned with respect to the repetition rate of the seed source. Keeping the cavity open therefore successively appends new seed pulses to the circulating pulse burst. When the desired number of pulses is reached, the cavity is closed and the inserted pulse burst is circulated for the desired number of round-trips.

Analogous to the CPA case, the pulse stacking requires precise phase and pulse energy control to efficiently compress the spread energy back into one single pulse. While the required phase can be controlled easily, the individual pulses

Die approbierte Originalversion dieser Dissertation ist in der TU Wien Bibliothek verfügbar.
The approved original version of this doctoral thesis is available at the TU Wien Bibliothek.
TU WIEN Bibliothek Your knowledge hub

comprising a pulse burst see different gains due to the nonlinear nature of the amplification process and the resulting saturation effects. Thus, one needs to carefully adjust the energy of the injected seed pulses such that the resulting output pulse burst exhibits a desired signature, i.e., a desired energy distribution of the total burst energy into the individual pulses. This can be done easily by using adjustable input filters such as AOMs, but finding suitable settings can be quite tedious. Analogous to Chapter 4, the application of automatic control methods seems highly desirable.

The aim of this chapter is to develop suitable control methods for such Vernier-effect-based regenerative amplifiers (RAs) to produce pulse bursts with a desired signature. Therefore, Section 6.1 extends the dynamical model of RAs from Section 5.1 to describe the formation of pulse bursts. Section 6.2 applies optimization-based methods to the developed model to obtain suitable settings for the input filter. Since the quality of these feedforward solutions strongly depends on the fidelity of the underlying model, an ILC scheme is proposed in Section 6.3 for increased robustness. Finally, feedback stabilization methods known from Chapter 5 are extended to Vernier-based RAs and combined with the developed tracking control methods in Section 6.4. As in the previous chapter, all simulation scenarios are performed using the parameters given in Table E.3.

6.1 A dynamical model of pulse burst formation and amplification

In the following, we want to describe the dynamical behavior of a regenerative amplifier with a detuned resonator cavity to create pulse bursts analogous to Section 5.1. For such an energy-based description, all the timing details relevant for building such an amplifier can be neglected and the only remaining quantity due to the detuned cavity is the temporal distance between two consecutive pulses $\Delta t = {}^{1}/_{f_{\mathrm{rep}}} - t_{\mathrm{RT}}$. Here, f_{rep} again represents the repetition rate of the seed pulses and t_{RT} is the time a pulse needs to complete a cavity round-trip. Additionally, $|\Delta t|$ is assumed to be large enough such that consecutive pulses do not overlap. Such a pulse burst of $N_{\mathrm{P}} \ll N_{\mathrm{RT}}$ pulses is illustrated in Figure 6.1, whereby the numbering of the pulses is according to the order they pass the gain medium. Using the normalized fluence as introduced in (5.21), the energy distribution of a pulse burst can thus be described by a vector $\mathbf{H} \in \mathbb{R}^{N_{\mathrm{P}}}$, where each component H_i represents the normalized fluence of the corresponding time slot, i.e.

$$H_i = \frac{1}{U_{sat}} \int_{(i-1)\Delta t}^{i\Delta t} I(t)\mathrm{d}t. \tag{6.1}$$

Finally, the pulse injection procedure due to the switching Pockel's cell (PC) can be simply described by a cycle-dependent cavity efficiency coefficient η_{RC}^{k}. This is

Die approbierte Originalversion dieser Dissertation ist in der TU Wien Bibliothek verfügbar.
The approved original version of this doctoral thesis is available at the TU Wien Bibliothek.
TU WIEN Bibliothek Your knowledge hub

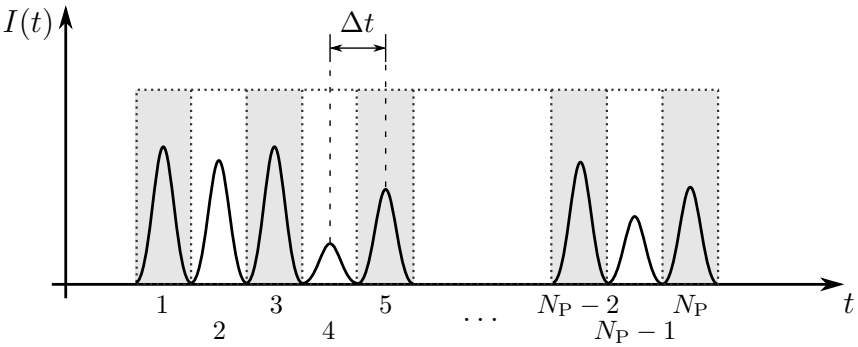

Figure 6.1: A pulse burst comprised of N_P non-overlapping pulses with a maximum pulse-width of Δt. The numbering of the pulses is according to the order they pass the gain medium.

possible since the PC is operated in three distinct states. Initially, the cavity is kept open. During the formation phase, the PC is operated in a partially switched state that allows pulses to further enter the cavity but drastically increases the cavity losses as well as the losses for injecting a pulse into the cavity[1]. Finally, when the desired number of pulses N_P is reached, the PC is fully switched and the pulse burst is locked inside the cavity for the remaining amplification phase. While the injection losses are significantly higher compared to the conventional operation in the previous chapter, their value remains constant for all injected pulses. Therefore, the effect of the increased injection losses can be accounted for by reducing the available seed energy analogous to the previous chapter. However, the cavity efficiency coefficient η_{RC}^k varies over the round-trips of a pulse burst according to

$$\eta_{RC}^k = \begin{cases} \eta_{RC,F} & \text{for } k \leq N_P \\ \eta_{RC,A} & \text{otherwise,} \end{cases} \tag{6.2}$$

where $\eta_{RC,A}$ and $\eta_{RC,F}$ denote the coefficients during the amplification and formation phase, respectively. Since the partially switched PC adds additional losses to the formation phase, it is clear that $\eta_{RC,F} > \eta_{RC,A}$.

A schematic overview of the resulting setup is given in Figure 6.2. The (compensated) seed pulse H_{seed} is fed through the AOM, which can be adjusted freely for all k input pulses of the n-th pulse burst. Accordingly, the k-th input pulse of the n-th pulse burst is given by

$$H_{in}^{n,k} = \eta_{AOM}^{n,k} H_{seed}, \tag{6.3}$$

[1]Without going into details, Pockel's cells can be used as switches by combining their ability to rotate the polarization of the light pulse with suitable polarization-sensitive optics. A partially switched PC thus potentially adds losses to the input pulse as it only injects a part of the pulse into the cavity. Conversely, a partially switched PC allows parts of the trapped pulses to leave the cavity which can be seen as increased cavity losses.

Die approbierte Originalversion dieser Dissertation ist in der TU Wien Bibliothek verfügbar.
The approved original version of this doctoral thesis is available at the TU Wien Bibliothek.
TU Bibliothek WIEN Your knowledge hub

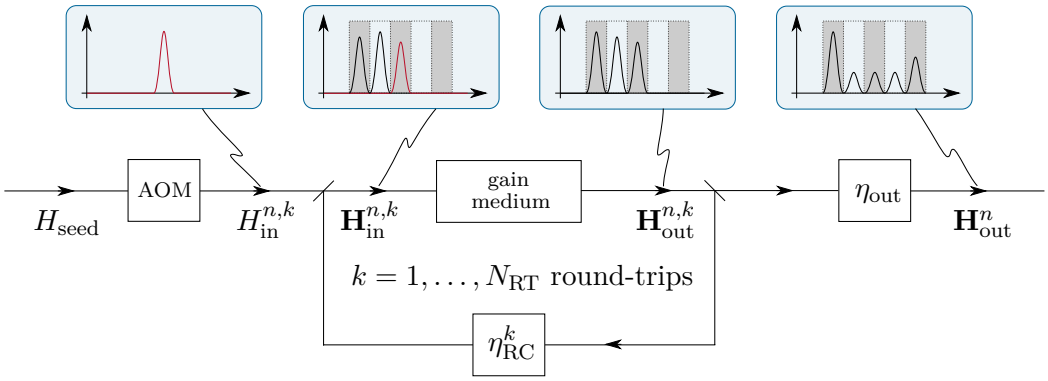

Figure 6.2: Schematic overview of the setup to create pulse bursts with a RA using the Vernier effect. In the illustrated case, the round-trip time of the cavity is lower than the time between incoming seed pulses, i.e., $\Delta t > 0$. Therefore, the individual pulses are appended to the back of the pulse burst, see also Figure 6.1.

for $k = 1, \ldots, N_{\text{P}}$ with the known limitations $0 \leq \eta_{\text{AOM}}^{n,k} \leq 1$. These input pulses are then successively appended to the circulating pulse burst. Whether the individual pulses are appended to the front or the back of the pulse burst is determined by the sign of Δt. For $\Delta t > 0$, the pulse burst finishes a round-trip before the next seed pulse is injected to the cavity and pulses are appended to the back as illustrated in Figure 6.2. Conversely, the pulses are appended to the front for $\Delta t < 0$. Thus, the assignment of $H_{\text{in}}^{n,k}$ to the "time slots" of the circulating pulse bursts $\mathbf{H}_{\text{in}}^{n,k}$ depends on the chosen detuning.

To incorporate both cases easily, we derive a more general description of the formation and amplification process. Consider an arbitrary pulse burst $\mathbf{H}$ already inside the resonator and assume one would be able to add some normalized fluence $\delta\mathbf{H}$ to all pulses, i.e., the pulse burst approaching the laser medium with an initial gain G is given by $\mathbf{H}_{\text{in}} = \mathbf{H} + \delta\mathbf{H}$. Using the functions f_{dep} and f_{gain} according to (5.22), the amplification of the first pulse is given by

$$H_{\text{out},1} = f_{\text{gain}}\left(G, H_1 + \delta H_1\right). \tag{6.4}$$

Taking the depletion due to the first pulse into account, the amplification of the second pulse is described by

$$H_{\text{out},2} = f_{\text{gain}}\left(f_{\text{dep}}\left(G, H_1 + \delta H_1\right), H_2 + \delta H_2\right). \tag{6.5}$$

Proceeding in this manner, one obtains the amplified pulse burst after the laser medium as

$$\mathbf{H}_{\text{out}} = \begin{bmatrix} f_{\text{gain}}\left(G, H_1 + \delta H_1\right) \\ f_{\text{gain}}\left(f_{\text{dep}}\left(G, H_1 + \delta H_1\right), H_2 + \delta H_2\right) \\ f_{\text{gain}}\left(f_{\text{dep}}\left(G, \sum_{i=1}^{2} H_i + \delta H_i\right), H_3 + \delta H_3\right) \\ \vdots \\ f_{\text{gain}}\left(f_{\text{dep}}\left(G, \sum_{i=1}^{N_{\text{P}}-1} H_i + \delta H_i\right), H_{N_{\text{P}}} + \delta H_{N_{\text{P}}}\right) \end{bmatrix}. \tag{6.6}$$

Die approbierte Originalversion dieser Dissertation ist in der TU Wien Bibliothek verfügbar.
The approved original version of this doctoral thesis is available at the TU Wien Bibliothek.
TU Bibliothek Your knowledge hub WIEN

Using this description and taking into account the resonator losses η_{RC}^k, the k-th round-trip of the pulse burst $\mathbf{H}^{n,k}$ in the resonator cavity with a laser medium of gain $G^{n,k}$ can be described analogously to (5.28) by

$$\begin{bmatrix} G^{n,k+1} \\ \mathbf{H}^{n,k+1} \end{bmatrix} = \mathbf{f}_{\mathrm{SP}}^k \left(\begin{bmatrix} G^{n,k} \\ \mathbf{H}^{n,k} \end{bmatrix}, \delta\mathbf{H}^{n,k} \right), \tag{6.7}$$

with

$$\mathbf{f}_{\mathrm{SP}}^k \left(\begin{bmatrix} G \\ \mathbf{H} \end{bmatrix}, \delta\mathbf{H} \right) = \begin{bmatrix} f_{\mathrm{dep}} \left(G, \sum_{i=1}^{N_{\mathrm{P}}} H_i + \delta H_i \right) \\ \eta_{\mathrm{RC}}^k f_{\mathrm{gain}} \left(G, H_1 + \delta H_1 \right) \\ \eta_{\mathrm{RC}}^k f_{\mathrm{gain}} \left(f_{\mathrm{dep}} \left(G, H_1 + \delta H_1 \right), H_2 + \delta H_2 \right) \\ \eta_{\mathrm{RC}}^k f_{\mathrm{gain}} \left(f_{\mathrm{dep}} \left(G, \sum_{i=1}^{2} H_i + \delta H_i \right), H_3 + \delta H_3 \right) \\ \vdots \\ \eta_{\mathrm{RC}}^k f_{\mathrm{gain}} \left(f_{\mathrm{dep}} \left(G, \sum_{i=1}^{N_{\mathrm{P}}-1} H_i + \delta H_i \right), H_{N_{\mathrm{P}}} + \delta H_{N_{\mathrm{P}}} \right) \end{bmatrix}. \tag{6.8}$$

Notice that $\mathbf{f}_{\mathrm{SP}}^k$ varies with the round-trip index k due to the variable losses (6.2) only. It is clear that $\delta\mathbf{H}^{n,k} = \mathbf{0}$ for $k \geq N_{\mathrm{P}}$, i.e., the cavity is closed during the amplification phase. During the formation phase $k \leq N_{\mathrm{P}}$, however, the time slots are filled in a consecutive manner starting either from the front or from the back. For the case $\Delta t > 0$, one can easily see that the pulse assignment is given by

$$\delta\mathbf{H}^{n,k} = \begin{cases} H_{\mathrm{in}}^{n,k} \mathbf{e}_k & \text{for } k \in [1, \ldots, N_{\mathrm{P}}] \\ \mathbf{0} & \text{otherwise,} \end{cases} \tag{6.9a}$$

with the standard unit vectors $\mathbf{e}_k$. Conversely, the case $\Delta t < 0$ yields

$$\delta\mathbf{H}^{n,k} = \begin{cases} H_{\mathrm{in}}^{n,k} \mathbf{e}_{N_{\mathrm{P}}+1-k} & \text{for } k \in [1, \ldots, N_{\mathrm{P}}] \\ \mathbf{0} & \text{otherwise.} \end{cases} \tag{6.9b}$$

Using $\mathbf{H}^{n,1} = \mathbf{0}$, i.e., the cavity is empty at the beginning of each pulse burst formation, and collecting all input pulses in $(\mathbf{H}_{\mathrm{in}}^n)^T = \left[H_{\mathrm{in}}^{n,1}, \ldots, H_{\mathrm{in}}^{n,N_{\mathrm{P}}} \right]$, an iterated function similar to (5.29) can be defined as

$$\begin{aligned} &\mathbf{f}_{\mathrm{MP}}^{(k)} \left(G^n, \mathbf{H}_{\mathrm{in}}^n \right) = \\ &\quad \mathbf{f}_{\mathrm{SP}}^k \left(\mathbf{f}_{\mathrm{SP}}^{k-1} \left(\ldots \mathbf{f}_{\mathrm{SP}}^1 \left(\begin{bmatrix} G^n \\ \mathbf{0} \end{bmatrix}, \delta\mathbf{H}^{n,1} \right) \ldots, \delta\mathbf{H}^{n,k-1} \right), \delta\mathbf{H}^{n,k} \right) \end{aligned} \tag{6.10}$$

with $\delta\mathbf{H}^{n,k}$ according to (6.9a) for $\Delta t > 0$ or (6.9b) for $\Delta t < 0$, respectively. Using the definitions $\mathbf{u}^n = \mathbf{H}_{\mathrm{in}}^n$, $\mathbf{y}^n = \mathbf{H}_{\mathrm{out}}^n = \eta_{\mathrm{out}} \mathbf{H}_{\mathrm{out}}^{n,N_{\mathrm{RT}}}$, and $x^n = G^n$ together with $\mathbf{f}_{\mathrm{MP}} = \mathbf{f}_{\mathrm{MP}}^{(N_{\mathrm{RT}})}$, one obtains the desired nonlinear discrete-time dynamic model

$$x^{n+1} = f_{\mathrm{pump}} \left(\begin{bmatrix} 1 & \mathbf{0}^T \end{bmatrix} \mathbf{f}_{\mathrm{MP}} \left(x^n, \mathbf{u}^n \right) \right) = f(x^n, \mathbf{u}^n) \tag{6.11a}$$

Die approbierte Originalversion dieser Dissertation ist in der TU Wien Bibliothek verfügbar.
The approved original version of this doctoral thesis is available at the TU Wien Bibliothek.
TU Bibliothek WIEN Your knowledge hub

$$\mathbf{y}^n = \frac{\eta_{\text{out}}}{\eta_{\text{RC,A}}} \begin{bmatrix} \mathbf{0} & \mathbf{I} \end{bmatrix} \mathbf{f}_{\text{MP}}\left(x^n, \mathbf{u}^n\right) = \mathbf{h}(x^n, \mathbf{u}^n), \tag{6.11b}$$

with the zero column vector $\mathbf{0} \in \mathbb{R}^{N_\text{P}}$ and the identity matrix $\mathbf{I} \in \mathbb{R}^{N_\text{P} \times N_\text{P}}$. Thus, the formation and amplification of pulse bursts is again described by a nonlinear discrete-time dynamic model with a scalar state variable but with N_P input and output variables. The input variables again inherit the AOM's limitations, i.e.,

$$0 \leq u_k^n \leq \bar{u}, \tag{6.12}$$

for $k = 1, \ldots, N_\text{P}$ with $\bar{u} = H_{\text{seed}}$.

6.2 Optimization-based input shaping

Building on the mathematical model derived in the previous section, we now want to find a suitable input subject to the constraints (6.12) such that the amplifier delivers output pulse bursts with the desired burst signature, i.e., the desired distribution of the total energy into the individual pulses, when operated at steady state.

A simple and powerful tool for such tasks in the presence of constraints is to use optimization-based methods, i.e., we want to find a suitable input $\mathbf{u}^\text{s}$ by solving the opimization problem

$$\begin{aligned} \mathbf{u}^\text{s} = \underset{\mathbf{u} \in \mathbb{R}^{N_\text{P}}}{\operatorname{argmin}} \quad & J(x^s, \mathbf{u}) \\ \text{subject to} \quad & x^s = f(x^s, \mathbf{u}) \\ & u_k \leq \bar{u}, \quad k = 1, \ldots, N_\text{P} \\ & u_k \geq 0 \end{aligned} \tag{6.13}$$

with some cost function $J(x, \mathbf{u})$.

A straight forward idea is to decompose the pulse burst $\mathbf{y} \in \mathbb{R}^{N_\text{P}}$ into desired and undesired components and maximize the first while minimizing the latter. To formulate this in a mathematically precise way, we denote a desired burst signature by the vector $\mathbf{s} \in \mathbb{R}^{N_\text{P}}$ with purely positive components $s_k \geq 0$ and $\|\mathbf{s}\|_2 = 1$. The space of desired pulse burst is then given by $\operatorname{span}(\mathbf{s})$ and the content of an output pulse burst into the direction of the desired burst signature is given by the inner product $y_\parallel = \mathbf{s}^T\mathbf{y}$. Conversely, all deviations from the desired signature can be combined in $\mathbf{y}_\perp = \mathbf{V}_\perp^T\mathbf{y} \in \mathbb{R}^{N_\text{P}-1}$ such that we obtain an orthogonal decomposition $\mathbb{R}^{N_\text{P}} = \operatorname{span}(\mathbf{s}) \oplus \operatorname{span}(\mathbf{V}_\perp)$, i.e., $\mathbf{V}_\perp^T\mathbf{s} = \mathbf{0}$. For convenience, the subspace of undesired burst signatures is equipped with an orthogonal basis $\mathbf{V}_\perp^T\mathbf{V}_\perp = \mathbf{I}$, too. As a result, each pulse burst can be decomposed into its desired and undesired components in the form

$$\mathbf{y} = \mathbf{P}_\parallel\mathbf{y} + \mathbf{P}_\perp\mathbf{y} \tag{6.14}$$

Die approbierte Originalversion dieser Dissertation ist in der TU Wien Bibliothek verfügbar.
The approved original version of this doctoral thesis is available at the TU Wien Bibliothek.
TU Bibliothek WIEN Your knowledge hub

using the orthogonal projection matrices $\mathbf{P}_{\parallel} = \mathbf{s}\mathbf{s}^T$ and $\mathbf{P}_{\perp} = \mathbf{V}_{\perp}\mathbf{V}_{\perp}^T$.

It is easy to see that we can achieve both tasks - maximizing the desired components while minimizing the undesired components of a pulse burst - within a single cost function by weighting the desired energy content $\mathbf{y}^T\mathbf{P}_{\parallel}\mathbf{y}$ negative and the energy of all deviations $\mathbf{y}^T\mathbf{P}_{\perp}\mathbf{y}$ positive. Thus, we can search for a suitable input $\mathbf{u}^{\mathrm{s}}$ by solving the optimization problem (6.13) using the cost function

$$J(x^s, \mathbf{u}) = \mathbf{h}^T(x^s, \mathbf{u}) \left(-\mathbf{P}_{\parallel} + \alpha_1 \mathbf{P}_{\perp}\right) \mathbf{h}(x^s, \mathbf{u}), \tag{6.15}$$

with the weighting parameter $\alpha_1 > 0$. For a given solution $\mathbf{u}^s$, the desired steady-state settings for the AOM during the k-th pulse are given by

$$\eta^s_{\mathrm{AOM},k} = \frac{u^s_k}{\bar{u}} \tag{6.16}$$

according to (6.3). To quantify the fidelity of the burst signature, a normalized signature error

$$e_{\mathrm{s}} = \frac{\|\mathbf{P}_{\perp}\mathbf{y}\|_2}{\|\mathbf{y}\|_2} \tag{6.17}$$

is used.

While this approach works reasonably well in general, it is quite sensitive due to the large range of possible output energies depending on the available level of pumping. Thus, the obtained numerical solutions of the optimization problem (6.13) strongly depend on the chosen initial solution and the weighting parameter α_1. To illustrate these effects, the optimization problem (6.13) is solved numerically for a desired burst signature

$$\mathbf{s}^T = {}^1\!/\!\sqrt{10} \begin{bmatrix} 2 & 2 & 1 & 1 \end{bmatrix} \tag{6.18}$$

using an SQP algorithm[2] and a weighting parameter $\alpha_1 = 10$. The resulting solution in terms of the desired steady-state settings of the AOM $\boldsymbol{\eta}^s_{\mathrm{AOM}}$ and the output energy $\mathbf{W}^s_{\mathrm{out}} = \frac{d_{\mathrm{L}}^2 \pi}{4} U_{\mathrm{sat}} \mathbf{y}^s$ with the corresponding normalized signature error e_{s} is shown in Figure 6.3 for different pumping powers P_{pump}. As one can see from e_{s}, the SQP algorithms fails do produce usable solutions for very low pumping power levels $P_{\mathrm{pump}} \leq 70\,\mathrm{W}$. For intermediate pumping powers, a decent solution is obtained although the resulting signature error e_{s} is quite high due to the relatively low value of α_1 necessary to keep the solution robust against local minima of the cost function (6.15). For very high pumping powers, the heavily saturating amplifier becomes quite insensitive to changes of the input energy as one can see from the strongly varying solutions of $\boldsymbol{\eta}^s_{\mathrm{AOM}}$ for $P_{\mathrm{pump}} > 200\,\mathrm{W}$. Additionally, the optimization algorithm reduces the input energies at high pumping levels

[2]To be more precise, the SQP solver using an active-set method available through the MATLAB 2017b optimization toolbox was used.

Die approbierte Originalversion dieser Dissertation ist in der TU Wien Bibliothek verfügbar.
The approved original version of this doctoral thesis is available at the TU Wien Bibliothek.
TU Bibliothek WIEN Your knowledge hub

to counter the increasing saturation and keep the output energy at a maximum. It is known from the previous chapter that reduced input energies yield a less stable amplifier. Moreover, it reduces the available control reserve to stabilize the system by feedback. Thus, a reduction of the total input energy is not a desirable behavior.

To avoid such issues, one clearly has to normalize the cost function with respect to the total energy while penalizing any reduction of the input pulses. This can be done by using a modified cost function

$$J(x^s, \mathbf{u}) = \frac{\mathbf{h}^T(x^s, \mathbf{u}) \left(-\mathbf{P}_\parallel + \alpha_1 \mathbf{P}_\perp\right) \mathbf{h}(x^s, \mathbf{u})}{\mathbf{h}^T(x^s, \mathbf{u}) \left(\mathbf{P}_\parallel + \alpha_1 \mathbf{P}_\perp\right) \mathbf{h}(x^s, \mathbf{u})} + \alpha_2 \operatorname{trace}\left(\bar{u}^2 \mathbf{I} - \mathbf{u}\mathbf{u}^T\right) \tag{6.19}$$

with the weighting parameters $\alpha_1, \alpha_2 > 0$. The resulting solution of (6.13) with the modified cost function (6.19) and $\alpha_1 = 40$ and $\alpha_2 = 1/20$ is shown in Figure 6.4. In general, the cost function (6.19) yields a much more robust and stable solution. As intended, the steady-state output energy $\mathbf{W}^s_{\text{out}}$ is saturating with higher pumping powers since the input energy is not reduced as it is the case in Figure 6.3. Since the modified cost function (6.19) is less prone to local minima, one can increase the weighting parameter α_1 and therefore significantly improve the fidelity of the resulting output pulse as indicated by a signature error e_{s} below 1 %. The AOM settings of $\eta_{\text{AOM},1}$ and $\eta_{\text{AOM},2}$ approach 1 while $\eta_{\text{AOM},3}$ and $\eta_{\text{AOM},4}$ approach $1/2$ for low pumping powers as one would expect from an unsaturated and thus almost linear amplifier[3] that should yield the desired burst signature (6.18). Below approximately 70 W, the second pulse is injected into the cavity without additional damping due to the AOM while all other pulses are somewhat reduced in energy. With increasing pump power, the discrepancy between the gain experienced by the leading pulses and the gain of the trailing pulses increases. Consequently, the damping of the leading pulses is increased continuously while only the last pulse is injected into the cavity without additional damping.

6.3 Tracking of desired pulse bursts using ILC

The quality of the optimization-based solution obtain in Section 6.2 strongly depends on the fidelity of the underlying model. While one can counter model and parameter uncertainties with ever increasing depth of modelling and extensive identification procedures, a residual mismatch between the mathematical model and the measured physical reality is inevitable. Additionally, the efforts linked to establishing models of such high fidelity are often daunting to practitioners and simply too expensive for commercial applications. If suitable output measurements

[3] Strictly speaking, one has to neglect the different number of round-trips of the individual pulses, too.

Die approbierte Originalversion dieser Dissertation ist in der TU Wien Bibliothek verfügbar.
The approved original version of this doctoral thesis is available at the TU Wien Bibliothek.
TU Bibliothek WIEN Your knowledge hub

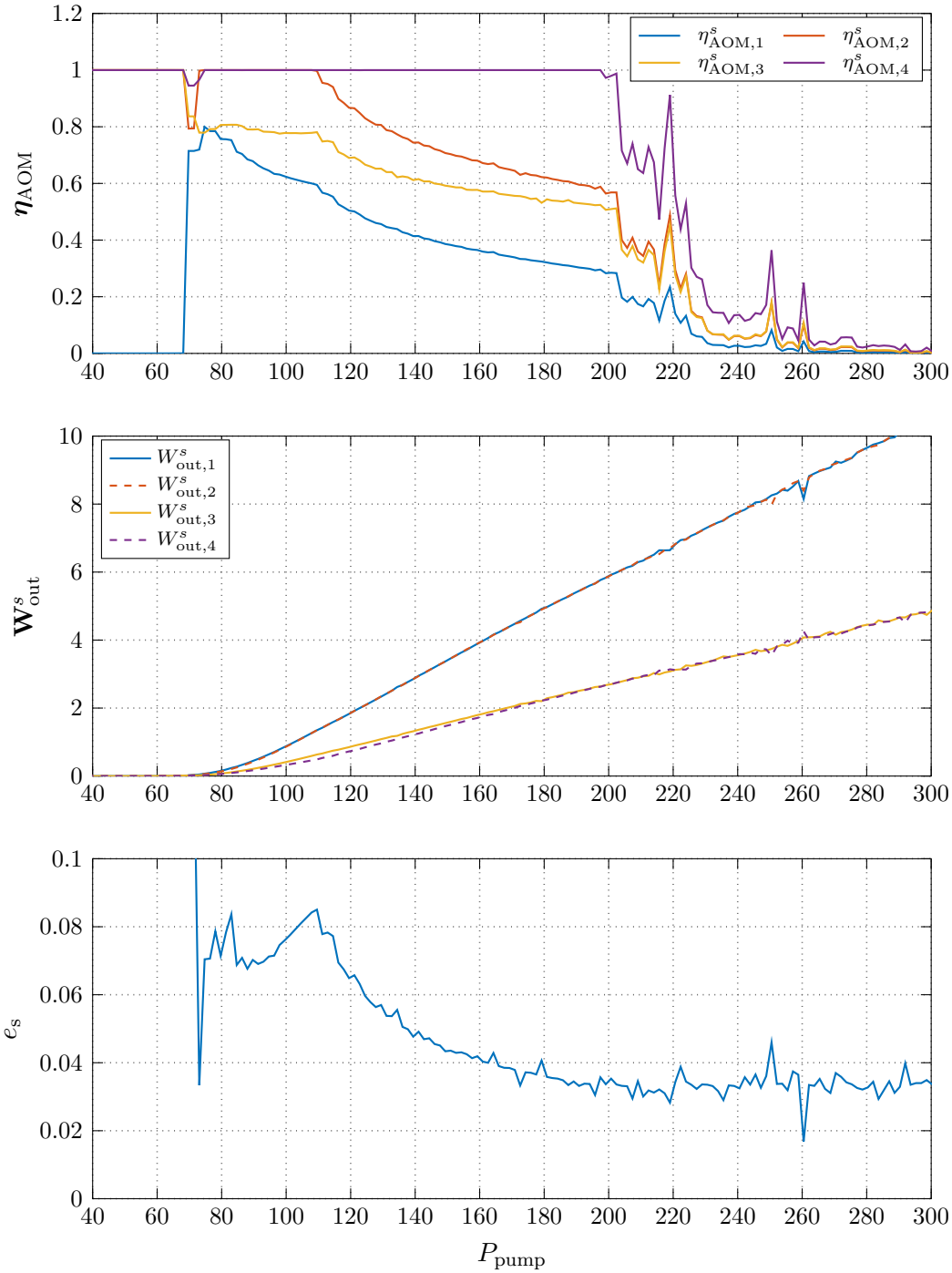

Figure 6.3: Solution of the optimization problem (6.13) using the cost function (6.15) and the desired burst signature (6.18) for different pumping powers with the weighting parameter $\alpha_1 = 10$.

Die approbierte Originalversion dieser Dissertation ist in der TU Wien Bibliothek verfügbar.
The approved original version of this doctoral thesis is available at the TU Wien Bibliothek.
TU Bibliothek Your knowledge hub WIEN

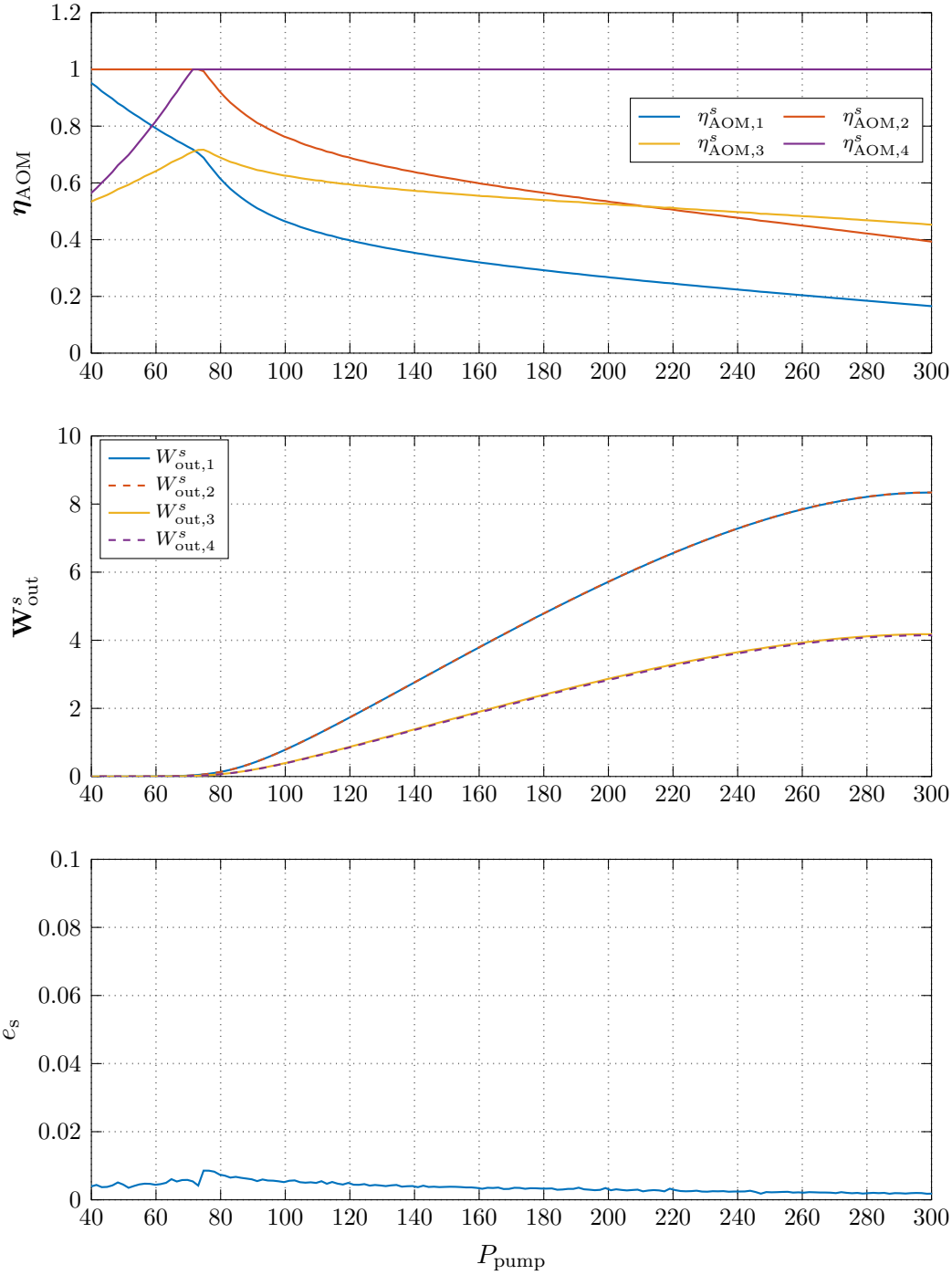

Figure 6.4: Solution of the optimization problem (6.13) using the modified cost function (6.19) and the desired burst signature (6.18) for different pumping powers with the weighting parameters $\alpha_1 = 40$ and $\alpha_2 = 1/20$.

Die approbierte Originalversion dieser Dissertation ist in der TU Wien Bibliothek verfügbar.
The approved original version of this doctoral thesis is available at the TU Wien Bibliothek.
TU Bibliothek Your knowledge hub WIEN

are available, it evidently makes sense to apply learning methods such that any residual errors are corrected in an iterative fashion similar to Chapter 4.

We thus want to learn in the vicinity of a steady-state

$$x^s = f(x^s, \mathbf{u}^s) \tag{6.20}$$

where the steady-state input $\mathbf{u}^s$ is obtained by solving the optimization problem (6.13). The corresponding desired steady-state output is given by

$$\mathbf{y}^s = \mathbf{h}(x^s, \mathbf{u}^s). \tag{6.21}$$

Proceeding as in Section 5.2 by introducing the small deviations of the steady state $\Delta x^n = x^n - x^s$, $\mathbf{\Delta u}^n = \mathbf{u}^n - \mathbf{u}^s$ and $\mathbf{\Delta y}^n = \mathbf{y}^n - \mathbf{y}^s$, the behavior of the nonlinear system (6.11) can be approximated by the linearized system

$$\Delta x^{n+1} = \Phi\, \Delta x^n + \mathbf{\Gamma}\, \mathbf{\Delta u}^n \tag{6.22a}$$
$$\mathbf{\Delta y}^n = \mathbf{C}\, \Delta x^n + \mathbf{D}\, \mathbf{\Delta u}^n, \tag{6.22b}$$

with the matrices

$$\begin{aligned}
\Phi &= \frac{\partial f}{\partial x}(x^s, \mathbf{u}^s) = \frac{\mathrm{d}f_{\mathrm{pump}}}{\mathrm{d}G_{\mathrm{in}}}\left(\begin{bmatrix}1 & \mathbf{0}^T\end{bmatrix}\mathbf{f}_{\mathrm{MP}}\left(x^s, \mathbf{u}^s\right)\right)\begin{bmatrix}1 & \mathbf{0}^T\end{bmatrix}\frac{\partial \mathbf{f}_{\mathrm{MP}}}{\partial x}\left(x^s, \mathbf{u}^s\right)\\
\mathbf{\Gamma} &= \frac{\partial f}{\partial \mathbf{u}}(x^s, \mathbf{u}^s) = \frac{\mathrm{d}f_{\mathrm{pump}}}{\mathrm{d}G_{\mathrm{in}}}\left(\begin{bmatrix}1 & \mathbf{0}^T\end{bmatrix}\mathbf{f}_{\mathrm{MP}}\left(x^s, \mathbf{u}^s\right)\right)\begin{bmatrix}1 & \mathbf{0}^T\end{bmatrix}\frac{\partial \mathbf{f}_{\mathrm{MP}}}{\partial \mathbf{u}}\left(x^s, \mathbf{u}^s\right)\\
\mathbf{C} &= \frac{\partial \mathbf{h}}{\partial x}(x^s, \mathbf{u}^s) = \frac{\eta_{\mathrm{out}}}{\eta_{\mathrm{RC,A}}}\begin{bmatrix}\mathbf{0} & \mathbf{I}\end{bmatrix}\frac{\partial \mathbf{f}_{\mathrm{MP}}}{\partial x}\left(x^s, \mathbf{u}^s\right)\\
\mathbf{D} &= \frac{\partial \mathbf{h}}{\partial \mathbf{u}}(x^s, \mathbf{u}^s) = \frac{\eta_{\mathrm{out}}}{\eta_{\mathrm{RC,A}}}\begin{bmatrix}\mathbf{0} & \mathbf{I}\end{bmatrix}\frac{\partial \mathbf{f}_{\mathrm{MP}}}{\partial \mathbf{u}}\left(x^s, \mathbf{u}^s\right).
\end{aligned} \tag{6.23}$$

The required derivatives of $\mathbf{f}_{\mathrm{MP}}$ are somewhat technical and rely on the derivative of $\mathbf{f}_{\mathrm{SP}}^k$ given in (6.8) with respect to the first argument, i.e. $\mathbf{z}^T = \left[G, \mathbf{H}^T\right]$, evaluated at the iterated function $\mathbf{f}_{\mathrm{MP}}^{(k-1)}$. We therefore define

$$\nabla \mathbf{f}_{\mathrm{SP}}^k\left(x, \mathbf{u}\right) = \frac{\partial \mathbf{f}_{\mathrm{SP}}^k}{\partial \mathbf{z}}\left(\mathbf{f}_{\mathrm{MP}}^{(k-1)}\left(x, \mathbf{u}\right), \delta\mathbf{H}^k(\mathbf{u})\right). \tag{6.24}$$

Notice the slight abuse of notation: the definition of $\mathbf{f}_{\mathrm{SP}}^k(\mathbf{z}, \delta\mathbf{H})$ given in (6.8) only depends on a single input pulse according to the mappings of $\delta\mathbf{H}$ due to (6.9a) or (6.9b), respectively. However, the evaluation at the iterated function $\mathbf{f}_{\mathrm{MP}}^{(k-1)}$ given in (6.10) potentially depends on all input values gathered in $\mathbf{u} = \mathbf{H}_{\mathrm{in}}$. With this convenient notation, the required derivatives are given by

$$\frac{\partial \mathbf{f}_{\mathrm{MP}}}{\partial x}\left(x, \mathbf{u}\right) = \nabla \mathbf{f}_{\mathrm{SP}}^{N_{\mathrm{RT}}}\left(x, \mathbf{u}\right) \times \nabla \mathbf{f}_{\mathrm{SP}}^{N_{\mathrm{RT}}-1}\left(x, \mathbf{u}\right) \times \ldots \times \nabla \mathbf{f}_{\mathrm{SP}}^{1}\left(x, \mathbf{u}\right)\begin{bmatrix}1\\ \mathbf{0}\end{bmatrix}$$

Die approbierte Originalversion dieser Dissertation ist in der TU Wien Bibliothek verfügbar.
The approved original version of this doctoral thesis is available at the TU Wien Bibliothek.
TU Bibliothek WIEN Your knowledge hub

$$= \left(\prod_{k=1}^{N_{\mathrm{RT}}} \nabla \mathbf{f}_{\mathrm{SP}}^{k} \left(x, \mathbf{u} \right) \right) \begin{bmatrix} 1 \\ \mathbf{0} \end{bmatrix} \tag{6.25a}$$

and

$$\frac{\partial \mathbf{f}_{\mathrm{MP}}}{\partial u_i} \left(x, \mathbf{u} \right) = \left(\prod_{k=i+1}^{N_{\mathrm{RT}}} \nabla \mathbf{f}_{\mathrm{SP}}^{k} \left(x, \mathbf{u} \right) \right) \frac{\partial \mathbf{f}_{\mathrm{SP}}^{i}}{\partial \delta \mathbf{H}} \left(\mathbf{f}_{\mathrm{MP}}^{(i-1)} \left(x, \mathbf{u} \right) \right) \mathbf{e}_i \tag{6.25b}$$

for positive detuning or

$$\frac{\partial \mathbf{f}_{\mathrm{MP}}}{\partial u_i} \left(x, \mathbf{u} \right) = \left(\prod_{k=N_{\mathrm{P}}-i+1}^{N_{\mathrm{RT}}} \nabla \mathbf{f}_{\mathrm{SP}}^{k} \left(x, \mathbf{u} \right) \right) \frac{\partial \mathbf{f}_{\mathrm{SP}}^{N_{\mathrm{P}}-i}}{\partial \delta \mathbf{H}} \left(\mathbf{f}_{\mathrm{MP}}^{(N_{\mathrm{P}}-i-1)} \left(x, \mathbf{u} \right) \right) \mathbf{e}_{N_{\mathrm{P}}-i} \tag{6.25c}$$

for negative detuning, respectively. Note that the matrix product is not commutative and thus the order of the products is fixed according to (6.25a).

Similar to FROG measurements used in Chapter 4, measurements of a pulse burst's signature usually require several bursts to resolve the different pulse energies adequately. Thus, one is essentially bound to steady-state measurements and as a result to amplifiers that are either inherently stable or stabilized without relying on measurements of the pulse signature. While the latter will be treated in the upcoming section, the following will focus on inherently stable amplifiers. For simplicity, we assume that the signature of every N_{M}-th pulse is available, i.e. the obtained measurements are not some kind of average over the last pulses. This is a reasonable assumption if N_{M} is large enough such that an eventual excitation from the steady state has already decayed. As a result, a description of the amplifier's steady-state response to small input perturbations is sufficient, which is readily given by

$$\Delta \mathbf{y}^n = \left(\frac{1}{1-\Phi} \mathbf{C} \boldsymbol{\Gamma} + \mathbf{D} \right) \Delta \mathbf{u}^n = \mathbf{G}_{\mathrm{S}} \Delta \mathbf{u}^n, \tag{6.26}$$

with the stationary input-output gain $\mathbf{G}_{\mathrm{S}}$. Since we assumed that the amplifier is inherently stable it follows that $|\Phi| < 1$. Using this local input-output description, an iterative input correction can be obtained by the ILC law

$$\mathbf{u}^{n+1} = \begin{cases} \mathrm{sat}\left(\mathbf{u}^n + \mathbf{L} \Delta \mathbf{y}^n \right) & \text{if } n \equiv 0 \pmod{N_{\mathrm{M}}} \\ \mathbf{u}^n & \text{otherwise,} \end{cases} \tag{6.27}$$

with the stationary learning gain $\mathbf{L}$. The saturation function reads as

$$\mathrm{sat}(u) = \begin{cases} \varepsilon \bar{u} & \text{if } u \leq \varepsilon \bar{u} \\ \bar{u} & \text{if } u \geq \bar{u} \\ u & \text{otherwise,} \end{cases} \tag{6.28}$$

Die approbierte Originalversion dieser Dissertation ist in der TU Wien Bibliothek verfügbar.
The approved original version of this doctoral thesis is available at the TU Wien Bibliothek.
TU Bibliothek WIEN Your knowledge hub

with $0 < \varepsilon \ll 1$ to avoid vanishing input pulses. The initial correction is set to zero, i.e., $\Delta\mathbf{u}^0 = \mathbf{0}$, and thus $\mathbf{u}^0 = \mathbf{u}^s$. To obtain a suitable learning gain $\mathbf{L}$, the Wiener-filtering-based approach presented in Chapter 3 can be used. For the given stationary scenario, however, the resulting learning gain is equivalent to simple (regularized-) inversion-based schemes (recall the analysis in Section 3.3.1). Analogous to (3.29), we choose

$$\mathbf{L} = \left(\alpha\mathbf{I} + \mathbf{G}_\mathrm{S}^T\mathbf{G}_\mathrm{S}\right)^{-1}\mathbf{G}_\mathrm{S}^T, \tag{6.29}$$

with the regularization parameter $\alpha > 0$.

The learning law (6.27) together with (6.29) is able to correct minor disturbances of the underlying model easily and produce desired pulse bursts $\mathbf{y}^s$. While this is exactly what we initially wanted to do, it brings along some issues. To illustrate this, consider the optimization-based input shaping in Section 6.2. There we have seen that influencing the burst signature is easy but influencing the total energy is only possible to some extent. Trying to adjust the input $\mathbf{u}^n$ to produce a desired $\mathbf{y}^s$ necessarily leads to input values close to or at the input constraints. It is thus often more desirable to restrict learning to the undesired signature components while leaving the desired components unchanged according to (6.14). This can be easily integrated into the learning law (6.27) by using the projection matrix $\mathbf{P}_\perp$ to obtain the projected learning gain

$$\mathbf{L}_\perp = \left(\alpha\mathbf{I} + \mathbf{G}_\mathrm{S}^T\mathbf{P}_\perp\mathbf{G}_\mathrm{S}\right)^{-1}\mathbf{G}_\mathrm{S}^T\mathbf{P}_\perp. \tag{6.30}$$

A exemplary comparison between the standard learning gain (6.29) and the projected learning gain (6.30) is given in Figure 6.5 for a desired pulse signature $\mathbf{s}^T = 1/2\begin{bmatrix}1 & 1 & 1 & 1\end{bmatrix}$ and $N_\mathrm{M} = 10$. The regularization parameter is chosen as $\alpha = 1 \cdot 10^8$, which is roughly one order of magnitude smaller than the smallest eigenvalue of $\mathbf{G}_\mathrm{S}^T\mathbf{G}_\mathrm{S}$. To see some significant model mismatch, a 5 % reduction in the pumping power compared to the nominal case $P_\mathrm{pump} = 100\,\mathrm{W}$ was used[4]. Clearly, the learning gain (6.29) is trying to compensate the reduced pumping power by increasing the input energy until it reaches the upper input constraint, i.e., $\eta_\mathrm{AOM,i}^n = 1$. At this point, the desired signature cannot be held anymore. Conversely, the projected learning law (6.30) is ignoring the reduced total output energy and corrects the burst signature only. Hence, the norm of the error's desired component, i.e., $\|\mathbf{P}_\parallel\Delta\mathbf{y}^n\|_2$, remains unchanged by the learning law while the norm of the error's orthogonal components, i.e., $\|\mathbf{P}_\perp\Delta\mathbf{y}^n\|_2$, is reduced with each application of the learning law.

It is quite interesting to notice that the full learning law (6.29) causes significantly stronger dynamic excitations compared to the projected learning law (see the second and third row in Figure 6.5). This can be attributed to the desired

[4]Notice that this not only varies the total gain but also the relative gain levels due to different levels of saturation.

Die approbierte Originalversion dieser Dissertation ist in der TU Wien Bibliothek verfügbar.
The approved original version of this doctoral thesis is available at the TU Wien Bibliothek.
TU Bibliothek WIEN Your knowledge hub

pulse signature $\mathbf{s}$, as the uniform pulse signature combined with the projected learning law suppresses any "common mode" action of the learning process and thus excites the system dynamics to a lesser extent.

In summary, the presented ILC-based tracking scheme is able to adapt to changes in the desired burst signature, which is clearly limited to a certain range of possible variations. In particular, shifting energy from the front of the pulse burst to the back or vice verse is difficult for highly saturated amplifiers as it alters the linearized system behavior (6.26) quite significantly.

6.4 Combined tracking control and feedback stabilization

We are now able to calculate input pulses which, after being injected into the cavity and amplified thereafter, form a desired pulse burst or are at least adapted to match the desired burst signature. Since we inject several seed pulses into the cavity during one amplification period, the Vernier-effect-based burst formation results in more stable amplifier dynamics compared to a single pulse operation. Additionally, the formation and amplification of pulse bursts is typically done in a dedicated pre-amplifier where energy efficiency plays only a minor role. Nevertheless, one can ask how to include some kind of feedback for safe operation of the amplifier at inherently unstable operating points. This requires measurements that capture the pulse-to-pulse (or rather burst-to-burst) dynamics. We therefore have to deal with two separate kinds of measurements that are available on different time scales and for different purposes: one that is available for each pulse burst and that can be used for feedback stabilization and one occasional measurement resolving the energy of the individual pulses comprising the pulse burst. The aim of this section is to systematically integrate such measurements and the corresponding feedback stabilization approaches from Chapter 5 with the tracking schemes presented in the previous sections.

6.4.1 Combined tracking and state-feedback control

In Section 5.3.1, the availability of measurements of the transmitted pumping light was used to obtain simple estimates of the amplifier's state. This is still possible for the burst amplifiers considered in this chapter as the time scales between two pulse bursts is several orders of magnitude larger than the duration of a single pulse burst. Using the estimation scheme presented in Section 5.3.1 we can simply assume knowledge of the current state x^n for the following derivations.

As stated above, the feedback control and the learning control laws operate on quite different time scales. Since we have direct access to the current state, it is intuitive to consider a kind of "separation of time scales" approach and design both control laws independent of each other. As a result, the learning action

Die approbierte Originalversion dieser Dissertation ist in der TU Wien Bibliothek verfügbar.
The approved original version of this doctoral thesis is available at the TU Wien Bibliothek.
TU Bibliothek WIEN Your knowledge hub

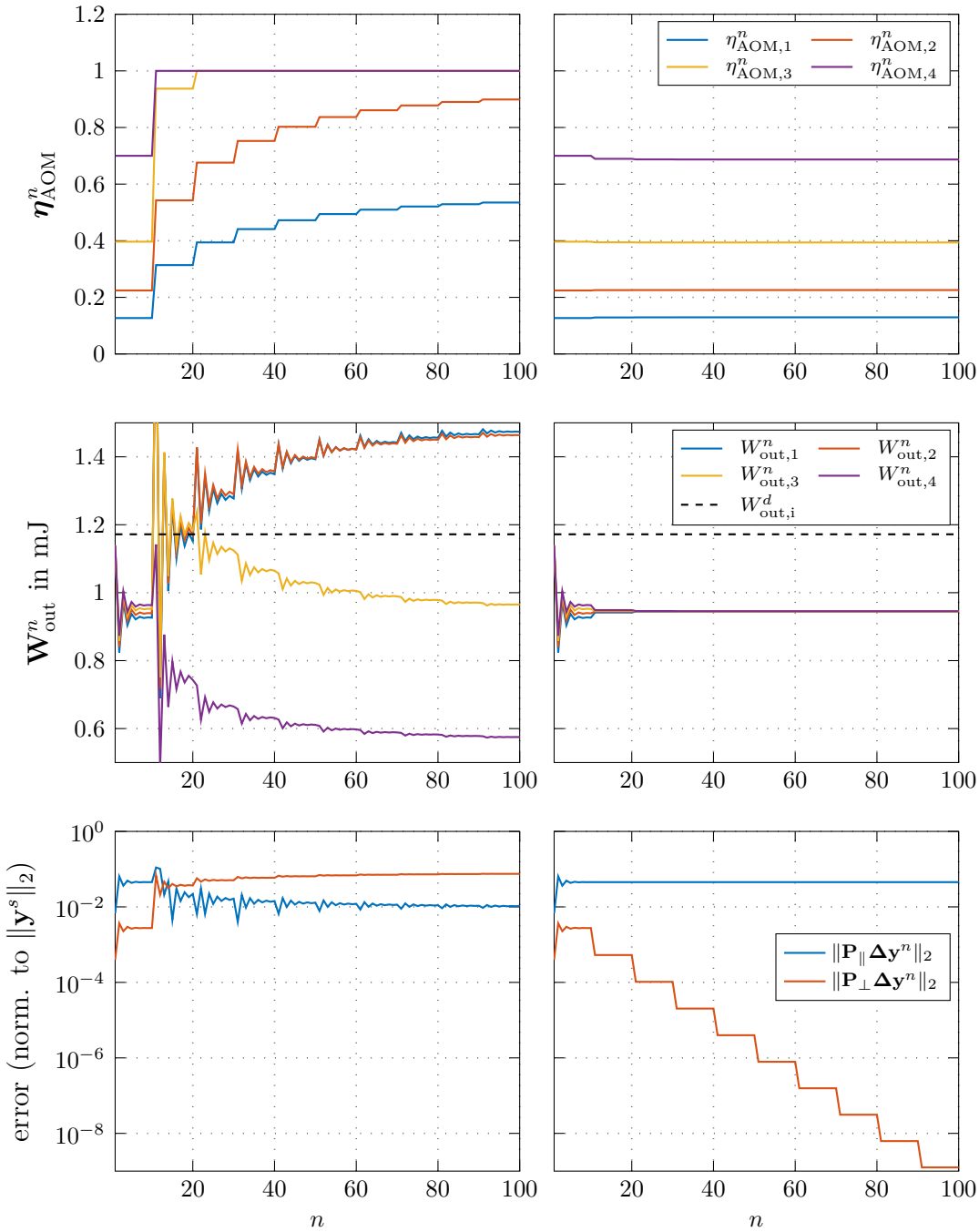

Figure 6.5: Comparison between the standard learning gain (6.29) on the left and the projected learning gain (6.30) on the right, with $\alpha = 1 \cdot 10^8$ and $N_{\mathrm{M}} = 10$ and a 5 % reduced pumping power compared to the nominal case $P_{\mathrm{pump}} = 100\,\mathrm{W}$. The steady-state input $\mathbf{u}^s$ is obtained via the optimization problem (6.13) for an upper bound $\bar{u} = {}^7\!/_{10} H_{\mathrm{seed}}$ to allow for corrections due to the ILC law (6.27).

Die approbierte Originalversion dieser Dissertation ist in der TU Wien Bibliothek verfügbar.
The approved original version of this doctoral thesis is available at the TU Wien Bibliothek.
TU Bibliothek Your knowledge hub WIEN

will necessarily excite the amplifier's dynamics, which is usually a behavior one wants to avoid in favor of a design where the system dynamics are decoupled from the learning law. Additionally, we want to avoid a control scheme where the ILC law drives the amplifier away from the desired operating point, which is particularly critical for unstable amplifiers. To formulate such a control law, we parametrize the linearized input $\Delta\mathbf{u}^n$ by two independent components, a feedback input $\Delta u^n_{\mathrm{FB}} \in \mathbb{R}$ and the remaining inputs for the learning law $\mathbf{\Delta u}^n_{\mathrm{ILC}} \in \mathbb{R}^{N_{\mathrm{P}}-1}$ using

$$\Delta\mathbf{u}^n = \mathbf{s}_{\mathrm{FB}}\Delta u^n_{\mathrm{FB}} + \mathbf{V}_{\mathrm{ILC}}\mathbf{\Delta u}^n_{\mathrm{ILC}} \tag{6.31}$$

with some signature of the feedback action $\mathbf{s}_{\mathrm{FB}}$ and its orthogonal complement in $\mathbf{V}_{\mathrm{ILC}}$, i.e., $\operatorname{span}(\mathbf{s}_{\mathrm{FB}}) \oplus \operatorname{span}(\mathbf{V}_{\mathrm{ILC}}) = \mathbb{R}^{N_{\mathrm{P}}}$. Additionally, we again choose $\mathbf{V}_{\mathrm{ILC}}$ such that $\mathbf{V}^T_{\mathrm{ILC}}\mathbf{V}_{\mathrm{ILC}} = \mathbf{I}$. Using the state-feedback law

$$\Delta u^n_{\mathrm{FB}} = k_{\mathrm{FB}}\Delta x^n \tag{6.32}$$

together with the system's linearized behavior (6.22) in the vicinity of the operating point $(x^s, \mathbf{u}^s)$ due to the optimization problem (6.13), one obtains the closed-loop dynamics

$$\Delta x^{n+1} = (\Phi + k_{\mathrm{FB}}\mathbf{\Gamma}\mathbf{s}_{\mathrm{FB}})\,\Delta x^n + \mathbf{\Gamma}\mathbf{V}_{\mathrm{ILC}}\,\mathbf{\Delta u}^n_{\mathrm{ILC}} \tag{6.33a}$$

$$\mathbf{\Delta y}^n = (\mathbf{C} + k_{\mathrm{FB}}\mathbf{D}\mathbf{s}_{\mathrm{FB}})\,\Delta x^n + \mathbf{D}\mathbf{V}_{\mathrm{ILC}}\,\mathbf{\Delta u}^n_{\mathrm{ILC}}. \tag{6.33b}$$

Using the feedback gain

$$k_{\mathrm{FB}} = \frac{\Phi_{\mathrm{des}} - \Phi}{\mathbf{\Gamma}\mathbf{s}_{\mathrm{FB}}} \tag{6.34}$$

with $|\Phi_{\mathrm{des}}| < 1$ renders the system (6.33) locally asymptotically stable and the residual stationary input-output behavior is given by

$$\mathbf{\Delta y}^\infty = \underbrace{\left[\frac{1}{1-\Phi_{\mathrm{des}}}\left(\mathbf{C} + k_{\mathrm{FB}}\mathbf{D}\mathbf{s}_{\mathrm{FB}}\right)\mathbf{\Gamma} + \mathbf{D}\right]}_{=\mathbf{G}_{\mathrm{S}}}\mathbf{V}_{\mathrm{ILC}}\,\mathbf{\Delta u}^\infty_{\mathrm{ILC}}. \tag{6.35}$$

Clearly, we will not be able to use the $N_{\mathrm{P}} - 1$ inputs in $\mathbf{\Delta u}^\infty_{\mathrm{ILC}}$ to fully adjust $\mathbf{\Delta y}^\infty \in \mathbb{R}^{N_{\mathrm{P}}}$ and due to the analysis of the previous section we probably should not even try. Splitting (6.35) into desired components $\Delta y^\infty_{\parallel} = \mathbf{s}^T\mathbf{\Delta y}^\infty$ and undesired components $\mathbf{\Delta y}_{\perp}{}^\infty = \mathbf{V}^T_{\perp}\mathbf{\Delta y}^\infty$ analogous to Section 6.2, i.e.,

$$\Delta y^\infty_{\parallel} = \mathbf{s}^T\mathbf{G}_{\mathrm{S}}\mathbf{V}_{\mathrm{ILC}}\,\mathbf{\Delta u}^\infty_{\mathrm{ILC}} \tag{6.36a}$$

$$\mathbf{\Delta y}_{\perp}{}^\infty = \mathbf{V}^T_{\perp}\mathbf{G}_{\mathrm{S}}\mathbf{V}_{\mathrm{ILC}}\,\mathbf{\Delta u}^\infty_{\mathrm{ILC}}, \tag{6.36b}$$

we can use (6.36b) to correct deviations from the desired burst signature. Assuming again that a measurement of the burst signature is available every N_{M}-th burst, one obtains the combined control law

$$\mathbf{u}^n = \begin{cases} \operatorname{sat}\left(\mathbf{u}^s + \mathbf{s}_{\mathrm{FB}}k_{\mathrm{FB}}\Delta x^n + \mathbf{L}_{\perp}\Delta\mathbf{y}^{n-1}\right) & \text{if } n \equiv 0 \pmod{N_{\mathrm{M}}} \\ \operatorname{sat}\left(\mathbf{u}^s + \mathbf{s}_{\mathrm{FB}}k_{\mathrm{FB}}\Delta x^n\right) & \text{otherwise,} \end{cases} \tag{6.37}$$

Die approbierte Originalversion dieser Dissertation ist in der TU Wien Bibliothek verfügbar.
The approved original version of this doctoral thesis is available at the TU Wien Bibliothek.
TU Bibliothek WIEN Your knowledge hub

with the projected learning gain

$$\mathbf{L}_\perp = \mathbf{V}_{\mathrm{ILC}} \left(\alpha \mathbf{I} + \mathbf{V}_{\mathrm{ILC}}^T \mathbf{G}_{\mathrm{S}}^T \mathbf{P}_\perp \mathbf{G}_{\mathrm{S}} \mathbf{V}_{\mathrm{ILC}}\right)^{-1} \mathbf{V}_{\mathrm{ILC}}^T \mathbf{G}_{\mathrm{S}}^T \mathbf{P}_\perp \tag{6.38}$$

due to (6.36b) and (6.31) analogous to (6.30).

The derivations above are independent of any specific choice for $\mathbf{s}_{\mathrm{FB}}$. From (6.33) it is clear that we can decouple the system dynamics from the learning process by ensuring that $\mathbf{\Gamma}\mathbf{V}_{\mathrm{ILC}} = \mathbf{0}$ which is equivalent to $\mathbf{s}_{\mathrm{FB}} = {}^1\!/\!_{\|\mathbf{\Gamma}\|_2}\mathbf{\Gamma}^T$ and yields the simple input-output behavior

$$\mathbf{G}_{\mathrm{S}} = \mathbf{D}. \tag{6.39}$$

A simulation scenario for this choice and using desired burst signature $\mathbf{s}^T = {}^1\!/\!_{10}\begin{bmatrix}2 & 2 & 1 & 1\end{bmatrix}$ at a pumping power $P_{\mathrm{pump}} = 250\,\mathrm{W}$ is shown in Figure 6.6. The desired steady-state output $\mathbf{y}^s$ is again calculated using the optimization-based procedure in Section 6.2 with $\bar{u} = {}^7\!/\!_{10}H_{\mathrm{seed}}$. The learning law's regularization parameter is chosen as $\alpha = 1 \cdot 10^{11}$, which is roughly in the same order of magnitude as the smallest eigenvalue of $\mathbf{V}_{\mathrm{ILC}}^T \mathbf{G}_{\mathrm{S}}^T \mathbf{P}_\perp \mathbf{G}_{\mathrm{S}} \mathbf{V}_{\mathrm{ILC}}$. As one can see, an initial deviation of the state x^n provokes a feedback action that in turn results in an erroneous signature of the output burst. Measurements of the burst signature are available each $N_{\mathrm{M}} = 10$ pulse bursts at which the ILC acts on deviations from the desired signature. Since the system dynamics and the learning process are decoupled, the ILC's input corrections do not excite the state x^n. After three corrections due to the learning process, the norm of the output error's undesired components $\|\mathbf{P}_\perp \mathbf{\Delta}\mathbf{y}^n\|_2$ are already four orders of magnitude below the norm of the desired steady-state pulse burst $\|\mathbf{y}^s\|_2$. The norm of the desired components $\|\mathbf{P}_\parallel \mathbf{\Delta}\mathbf{y}^n\|_2$ is changing slightly as a by-product of the learning process, see (6.36a), but is not corrected by the projected learning law.

While using the degree of freedom introduced by $\mathbf{s}_{\mathrm{FB}}$ to dynamically decouple the stabilization and learning process is a very obvious choice, it is not necessarily always the best as illustrated in Figure 6.7 by comparing it to a homogeneously distributed feedback action $\mathbf{s}_{\mathrm{FB}}^T = {}^1\!/\!_4\begin{bmatrix}1 & 1 & 1 & 1\end{bmatrix}$ and a signature-like distributed feedback action $\mathbf{s}_{\mathrm{FB}}^T = \boldsymbol{\eta}_{\mathrm{AOM}}^s / \|\boldsymbol{\eta}_{\mathrm{AOM}}^s\|_2$, respectively. Both alternatives clearly excite the system dynamics but with only minor effects. Conversely, the signature-like distributed feedback action introduces significantly less distortions of the output burst's signature compared to the other choices as it only scales $\boldsymbol{\eta}_{\mathrm{AOM}}^n$ but keeps its signature unchanged. This is particularly visible at the first few pulses, i.e., $n < 10$, where the action of the feedback law increases the norm of the undesired components $\|\mathbf{P}_\perp \Delta\mathbf{y}^n\|_2$. However, a detailed evaluation of the control performance would need to incorporate different desired pulse bursts and the effects of a plant-model mismatch. The latter is particularly critical for highly unstable plants (as the presented simulation scenario with $\Phi \approx -2.06$) where the performance of the feedback is deteriorated and one may prefer to decouple both control processes as good as possible again.

Die approbierte Originalversion dieser Dissertation ist in der TU Wien Bibliothek verfügbar.
The approved original version of this doctoral thesis is available at the TU Wien Bibliothek.
TU Bibliothek WIEN Your knowledge hub

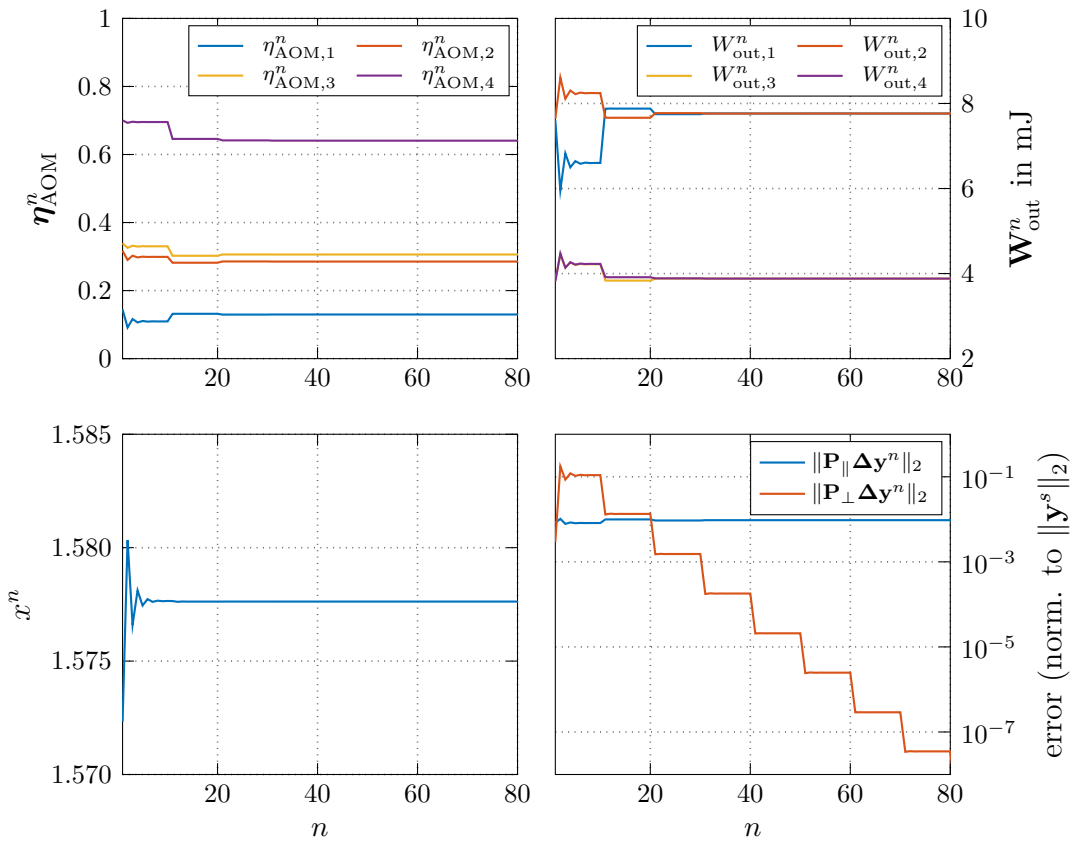

Figure 6.6: Combined stabilization by state feedback and tracking of a desired burst signature $\mathbf{s}^T = {}^1\!/_{10}\begin{bmatrix}2 & 2 & 1 & 1\end{bmatrix}$ by the control law (6.37) with (6.38). The system dynamics is decoupled from the learning process by choosing $\mathbf{s}_{\mathrm{FB}} = {}^{\boldsymbol{\Gamma}}\!/_{\|\boldsymbol{\Gamma}\|_2}$.

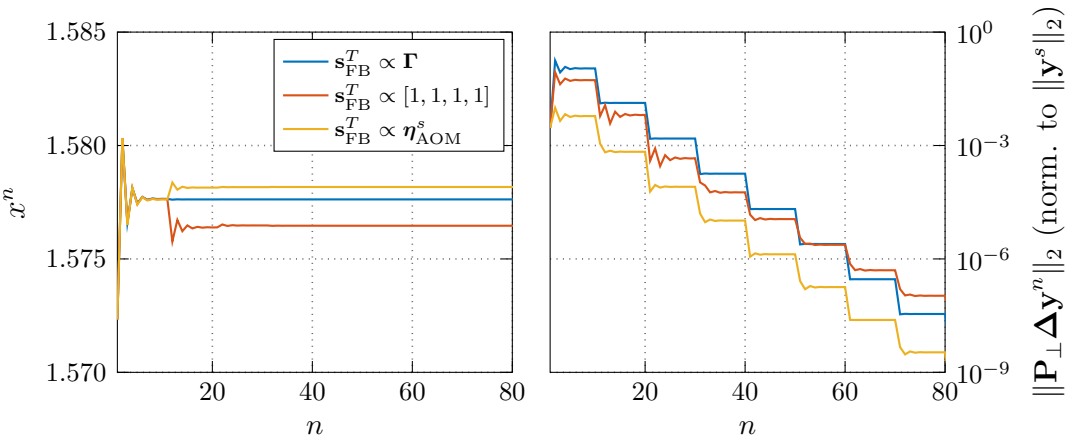

Figure 6.7: Comparison of different choices of $\mathbf{s}^T_{\mathrm{FB}}$: the dynamically decoupled case $\mathbf{s}^T_{\mathrm{FB}} = {}^{\boldsymbol{\Gamma}}\!/_{\|\boldsymbol{\Gamma}\|_2}$ (blue), the case of a homogeneously distributed feedback action $\mathbf{s}^T_{\mathrm{FB}} = {}^1\!/_4\begin{bmatrix}1 & 1 & 1 & 1\end{bmatrix}$ (red), and the case of a signature-like distributed feedback action $\mathbf{s}^T_{\mathrm{FB}} = {}^{\boldsymbol{\eta}^s_{\mathrm{AOM}}}\!/_{\|\boldsymbol{\eta}^s_{\mathrm{AOM}}\|_2}$ (yellow).

Die approbierte Originalversion dieser Dissertation ist in der TU Wien Bibliothek verfügbar.
The approved original version of this doctoral thesis is available at the TU Wien Bibliothek.
TU Bibliothek Your knowledge hub WIEN

6.4.2 Combined tracking and output-feedback control

While "single-shot" measurements of the energies of each individual pulse comprising a pulse burst are quite involved, measuring the total energy of the pulse burst $y_\Sigma^n = \mathbf{1}^T\mathbf{y}^n$ with $\mathbf{1}^T = \begin{bmatrix}1 & 1 & \dots & 1\end{bmatrix} \in \mathbb{R}^{N_\mathrm{P}}$ is again comparatively easy. As a result, one can directly transfer the approach of Section 5.3.2 to the case of pulse bursts by using $y_\Sigma = h_\Sigma(x, \mathbf{u}) = \mathbf{1}^T\mathbf{h}(x, \mathbf{u})$ and its inverse map with respect to the first argument $x = h_\Sigma^{-1}(y_\Sigma, \mathbf{u})$ to obtain, see (6.11)

$$y_\Sigma^{n+1} = h_\Sigma\left(f\left(h_\Sigma^{-1}\left(y_\Sigma^n, \mathbf{u}^n\right), \mathbf{u}^n\right), \mathbf{u}^{n+1}\right) = f_1\left(y_\Sigma^n, \mathbf{u}^n, \mathbf{u}^{n+1}\right). \tag{6.40}$$

Defining the extended state

$$\mathbf{z}^{n+1} = \begin{bmatrix} y_\Sigma^n \\ \mathbf{u}^n \end{bmatrix} = \begin{bmatrix} z_1^n \\ \mathbf{z}_2^n \end{bmatrix} \in \mathbb{R}^{N_\mathrm{P}+1} \tag{6.41}$$

and $\boldsymbol{\nu}^n = \mathbf{u}^{n+1}$ yields the dynamically extended system description in sensor coordinates

$$\mathbf{z}^{n+1} = \begin{bmatrix} f_1(z_1^n, \mathbf{z}_2^n, \boldsymbol{\nu}^n) \\ \boldsymbol{\nu}^n \end{bmatrix} = \mathbf{f}(\mathbf{z}^n, \boldsymbol{\nu}^n) \tag{6.42}$$

analogous to (5.48), with the initial condition $z_1^0 = y_\Sigma^0$ and $\mathbf{z}_2^0 = \mathbf{u}^0$ where $\mathbf{u}^0$ can be chosen freely and y_Σ^0 is linked to x^0 by $y_\Sigma^0 = h_\Sigma(x^0, \mathbf{u}^0)$. Proceeding as in Section 5.3.2, the extended system can be linearized around an operating point given by $(x^s, \mathbf{u}^s)$ with the resulting linear dynamics in its vicinity

$$\boldsymbol{\Delta}\mathbf{z}^{n+1} = \begin{bmatrix} \Phi & \mathbf{1}^T\left(\mathbf{C}\boldsymbol{\Gamma} - \Phi\mathbf{D}\right) \\ \mathbf{0} & \mathbf{0} \end{bmatrix} \boldsymbol{\Delta}\mathbf{z}^n + \begin{bmatrix} \mathbf{1}^T\mathbf{D} \\ \mathbf{E} \end{bmatrix} \boldsymbol{\Delta}\nu^n \tag{6.43a}$$

$$\boldsymbol{\Delta}\mathbf{y}^n = \frac{1}{\mathbf{1}^T\mathbf{C}} \begin{bmatrix} \mathbf{C} & \mathbf{1}^T\mathbf{C}\mathbf{D} - \mathbf{C}\mathbf{1}^T\mathbf{D} \end{bmatrix} \boldsymbol{\Delta}\mathbf{z}^n, \tag{6.43b}$$

where $\boldsymbol{\Delta}\mathbf{z}^n = \mathbf{z}^n - \mathbf{z}^s$, $\boldsymbol{\Delta}\nu^n = \boldsymbol{\nu}^n - \mathbf{u}^s$, and $\boldsymbol{\Delta}\mathbf{y}^n = \mathbf{y}^n - \mathbf{y}^s$. Using a linear feedback control with a residual learning input $\mathbf{u}_\mathrm{ILC}^n \in \mathbb{R}^{N_\mathrm{P}-1}$ in the form

$$\boldsymbol{\Delta}\nu^n = \mathbf{K}_\mathrm{FB}\boldsymbol{\Delta}\mathbf{z}^n + \mathbf{V}_\mathrm{ILC}\mathbf{u}_\mathrm{ILC}^n \tag{6.44}$$

with the control gain $\mathbf{K}_\mathrm{FB} = \begin{bmatrix}\mathbf{k}_\mathrm{FB,y} & \mathbf{K}_\mathrm{FB,u}\end{bmatrix}$ yields the closed-loop dynamics

$$\boldsymbol{\Delta}\mathbf{z}^{n+1} = \underbrace{\begin{bmatrix} \Phi + \mathbf{1}^T\mathbf{D}\mathbf{k}_\mathrm{FB,y} & \mathbf{1}^T\left(\mathbf{C}\boldsymbol{\Gamma} - \Phi\mathbf{D} + \mathbf{D}\mathbf{K}_\mathrm{FB,u}\right) \\ \mathbf{k}_\mathrm{FB,y} & \mathbf{K}_\mathrm{FB,u} \end{bmatrix}}_{\boldsymbol{\Phi}_\mathrm{CL}} \boldsymbol{\Delta}\mathbf{z}^n + \underbrace{\begin{bmatrix} \mathbf{1}^T\mathbf{D} \\ \mathbf{E} \end{bmatrix}}_{\boldsymbol{\Gamma}_\mathrm{ILC}} \mathbf{V}_\mathrm{ILC}\mathbf{u}_\mathrm{ILC}^n, \tag{6.45}$$

with the resulting stationary input-output behavior

$$\boldsymbol{\Delta}\mathbf{y}^\infty = \underbrace{\frac{1}{\mathbf{1}^T\mathbf{C}} \begin{bmatrix} \mathbf{C} & \mathbf{1}^T\mathbf{C}\mathbf{D} - \mathbf{C}\mathbf{1}^T\mathbf{D} \end{bmatrix} \left(\mathbf{E} - \boldsymbol{\Phi}_\mathrm{CL}\right)^{-1} \boldsymbol{\Gamma}_\mathrm{ILC}}_{\mathbf{G}_\mathrm{S}} \mathbf{V}_\mathrm{ILC}\mathbf{u}_\mathrm{ILC}^\infty. \tag{6.46}$$

Die approbierte Originalversion dieser Dissertation ist in der TU Wien Bibliothek verfügbar.
The approved original version of this doctoral thesis is available at the TU Wien Bibliothek.
TU Bibliothek WIEN Your knowledge hub

Contrary to the state feedback in the previous section, we cannot fully decouple the system dynamics from the learning process due to the dynamic extension. However, it is quite intuitive to impose that Δy_Σ^∞ shall not be altered by the learning process, i.e.,

$$\mathbf{1}^T \mathbf{G}_\mathrm{S} \mathbf{V}_\mathrm{ILC} = \mathbf{0}. \tag{6.47}$$

Finally, a combined output feedback and learning law can be given analogously to the previous section as

$$\mathbf{u}^{n+1} = \begin{cases} \mathrm{sat}\left(\mathbf{u}^s + \mathbf{K}_{\mathrm{FB,u}} \Delta \mathbf{u}^n + \mathbf{k}_{\mathrm{FB,y}} \Delta y_\Sigma^n + \mathbf{L}_\perp \Delta \mathbf{y}^n\right) & \text{if } n \equiv 0 \pmod{N_\mathrm{M}} \\ \mathrm{sat}\left(\mathbf{u}^s + \mathbf{K}_{\mathrm{FB,u}} \Delta \mathbf{u}^n + \mathbf{k}_{\mathrm{FB,y}} \Delta y_\Sigma^n\right) & \text{otherwise,} \end{cases} \tag{6.48}$$

with the projected learning gain due to (6.38) using $\mathbf{V}_\mathrm{ILC}$ according to (6.47). The resulting learning law is itself a dynamic system driven by the measured Δy_Σ^n with a linearized dynamic matrix given by $\mathbf{K}_{\mathrm{FB,u}}$.

Remark 26. *In principle, one can reduce the dimensionality of the extended system (6.43) from $N_P - 1$ to only 2 by replacing $\mathbf{z}_2^n = \mathbf{u}^n$ with $z_2^n = \mathbf{1}^T \left(\mathbf{C\Gamma} - \Phi \mathbf{D}\right) \mathbf{u}^n$. Such a description is clearly not able to describe the full range of outputs $\mathbf{\Delta y}^n$ but can explain only a certain subspace. Consequently, one would have to introduce an additional decomposition of the output space, which the author wanted to avoid in this work for clarity.*

A simulation scenario analogous to the previous section but using the combined control law (6.48) is shown in Figure 6.8. The output feedback using measurements of Δy_Σ^n is successfully stabilizing the plant while the projected learning law reduces the undesired components of the output error $\|\mathbf{P}_\perp \mathbf{\Delta y}^n\|_2$ with each iteration. While $\mathbf{V}_\mathrm{ILC}$ was chosen such that it only avoids to influence the stationary value of the dynamic output-feedback's driving quantity Δy_Σ^∞, the simulation scenario shows only very small dynamic excitation due to the learning action.

Die approbierte Originalversion dieser Dissertation ist in der TU Wien Bibliothek verfügbar.
The approved original version of this doctoral thesis is available at the TU Wien Bibliothek.
TU Bibliothek WIEN Your knowledge hub

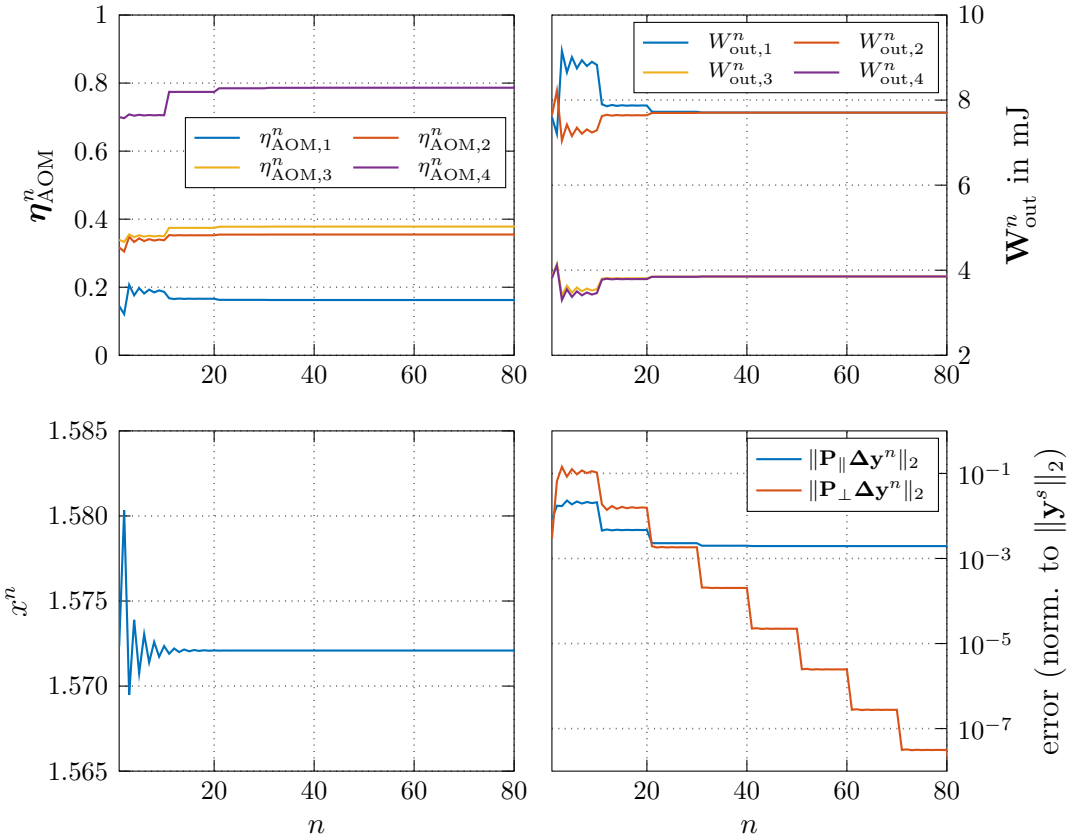

Figure 6.8: Combined stabilization by output feedback and tracking of a desired burst signature $\mathbf{s}^T = {}^1\!/_{10}\begin{bmatrix}2 & 2 & 1 & 1\end{bmatrix}$ using the the control law (6.48). The feedback law is stationary decoupled from the learning process by choosing $\mathbf{V}_{\mathrm{ILC}}$ such that (6.47) is fulfilled.

Die approbierte Originalversion dieser Dissertation ist in der TU Wien Bibliothek verfügbar.
The approved original version of this doctoral thesis is available at the TU Wien Bibliothek.
TU Bibliothek Your knowledge hub WIEN

Die approbierte Originalversion dieser Dissertation ist in der TU Wien Bibliothek verfügbar.
The approved original version of this doctoral thesis is available at the TU Wien Bibliothek.

CHAPTER 7

Conclusions and Outlook

As stated at the beginning of this work, the number of contributions applying control concepts to laser amplifiers for short and ultra-short pulses, in particular those who approach the given tasks from a genuine control background, is rather limited. The main objective of this thesis is thus to take a first look at such systems from the perspective of a control engineer and provide suitable control solutions to selected problems.

7.1 Conclusions

Following this objective necessarily started by describing the considered system by a detailed mathematical model as presented in Chapter 2. While the effects of the pulse stretcher, the spectral filter, and the pulse compressor are described in the frequency domain, the mathematical model of the regenerative amplifier requires a description of the light pulse's propagation as well as its interaction with the doped ions inside the laser medium. By separating the rather slow dynamics of the pumping process (i.e., the pump model) from the fast dynamics of the pulse propagation (i.e., the pulse model), the whole amplification process can be seen as an alternating sequence of simpler models. This repetitive structure combined with the complexity inherent to the pulse model leads to a significant computational effort to obtain numerical solutions of even a single output pulse. Thus, tailored numerical methods are given in Appendix A to keep the computational burden within reasonable bounds.

In Chapter 3, a general linear iterative learning control (ILC) law for continous-time linear systems was developed that is stochastically optimal in a minimum mean squares error (MMSE) sense. The proposed learning operator is a general-

Die approbierte Originalversion dieser Dissertation ist in der TU Wien Bibliothek verfügbar.
The approved original version of this doctoral thesis is available at the TU Wien Bibliothek.
TU WIEN Bibliothek Your knowledge hub

ization of existing MMSE-optimal approaches and represents a systematic dual to existing feedforward norm-optimal concepts by using a kind of Wiener-filter to optimally estimate the input correction of each iteration based on the observed measurement. Thus, the proposed ILC law combines the superior convergence speed of inversion-based or norm-optimal approaches with the stochastic optimality of various stochastic ILC schemes. The kernel function of the learning operator is determined by the non-causal Wiener-Hopf equation. Using the numerically efficient FFT-based algorithm presented in Section 3.4, both spectral factorization techniques and solutions to Riccati equations can be avoided. Therefore, such an approach is applicable to distributed-parameter systems (DPSs) in a late-lumping sense which have not been treated directly with model-based ILC methods so far. In general, Wiener-filter-based approaches require knowledge of the input error's power spectral density (PSD). Starting from an initial value, one can use a forward prediction equation to obtain an optimal but iteration-varying learning operator. Keeping the input error PSD fixed, one obtains a simple iteration-invariant suboptimal solution that performs quite close to the more complex optimal solution depending on the exact setting. Allowing to spectrally shape the learning behavior and being directly applicable to DPSs, such Wiener-filtering-based ILC laws provide an ideal framework for the pulse-shape control of chirped pulse amplifiers (CPAs).

Chapter 4 presents an adaptive strategy to produce desired pulses with CPAs. To this end, the detailed nonlinear and infinite-dimensional model derived and validated in Chapter 2 was reduced such that its input-output behavior can be described by a transfer function that is characterized by the mean population densities of the laser medium. Introducing effective, averaged mean population densities, one is able to consistently estimate the current state of the amplifier by solving an optimization problem. This approach has the advantage that it can easily estimate not only the population densities but also other unknown parameters essential for the input-output behavior. This approximate transfer function estimated by input-output measurements was then used to apply the Wiener-filtering-based ILC scheme. Thus, one obtains an adaptive algorithm to track desired output pulses, which is structurally simple, fast and does not rely on parameters that are hard to identify. Apart from physical constants and measureable quantities, one only needs to specify the number of resonant transitions. As it turned out, applying the (adaptive) ILC law to each consecutive pulse may excite the pulse-to-pulse dynamics and can even destabilize the CPA under certain circumstances. However, this might not be a serious concern for practical applications as phase-resolved output measurements usually require several pulses to complete.

Motivated by these results, Chapter 5 investigates the pulse-to-pulse dynamics in more detail. To this end, a simplified model of the underlying RA was introduced by neglecting the spectral nature of the pulses and only considering monochromatic light carrying no additional phase information. Using existing analytic solutions of

Die approbierte Originalversion dieser Dissertation ist in der TU Wien Bibliothek verfügbar.
The approved original version of this doctoral thesis is available at the TU Wien Bibliothek.
TU WIEN Bibliothek Your knowledge hub

the resulting set of equations after some simplifications resulted in a simple energy-based description of the RA's dynamics in form of a nonlinear time-discrete system, which generalizes existing models from the literature. Based on the linearization of the resulting model it was shown that the RA can be stabilized in the vicinity of a desired operating point using measurements of the transmitted pump light or measurements of the output pulse's energy, respectively. To safely steer the system to a desired operating point using an externally controllable pumping power, both feedback designs can be extended by a gain scheduling approach. Since the proposed approach of feedback stabilization for pulse energy measurements relies on a dynamic system extension to transform it into so-called sensor coordinates, it is ill-posed at a single operating point due to the pulse-to-pulse dynamics becoming locally non-observable. In practice, however, it is still possible to steer the system through this point by traversing its vicinity fast enough while truncating the scheduled feedback gains.

As Chapter 6 shows, the energy-based description nicely extends to the case of pulse burst formation and amplification in RAs using detuned cavities. To obtain steady-state output pulse bursts with a desired signature, the pulse bursts were decomposed into desired and undesired components and an optimization problem was formulated to maximize the total energy while minimizing the deviation from the desired signature subject to input and steady-state constraints. Possible deviations from the desired output pulse burst due to model or parameter uncertainties can be eliminated by using ILC methods similarly to Chapter 4. As it turned out, using a projected learning gain that only corrects deviations from the desired signature but does not try to correct the total energy of the pulse bursts has significant advantages. Finally, the ILC-based tracking schemes can be combined with the feedback control approaches presented in the previous chapter to obtain more advanced control concepts that influence the systems dynamics while correcting deviations from the desired signature whenever such measurements are available.

7.2 Outlook

The relative simplicity of the energy-based model in Chapter 6 compared to the quite complex model presented in Chapter 2 allowed to easily separate desired from undesired components and only remove the latter ones using iterative learning schemes. Basically, the resulting control law is learning the input pulses required to produce a desired *temporal* energy distribution. The complex description of the pulse propagation by the nonlinear Schrödinger equation (NLSE) coupled with the resulting atomic polarizations was necessary to resolve the spectral nature of the light pulse, i.e., the fact that a short light pulse contains components of different frequencies. Thus, the ILC law developed in Chapter 4 is essentially learning to reproduce a desired *spectral* energy distribution. Unlike in the case of pulse

Die approbierte Originalversion dieser Dissertation ist in der TU Wien Bibliothek verfügbar.
The approved original version of this doctoral thesis is available at the TU Wien Bibliothek.
TU Bibliothek WIEN Your knowledge hub

bursts, it is trying to reproduce a desired output pulse and not just the desired pulse shape. As a result, the (adaptive) ILC law presented in Chapter 4 excites the pulse-to-pulse dynamics significantly stronger than necessary and drives the input filter into saturation in case the chosen output pulse is not sustainable at the given pumping power. Transferring the projected learning approach from the temporal case in Chapter 6 back to the spectral case in Chapter 4 is obviously desirable. Ultimately, one could try to separate a energy-based description of the pulse-to-pulse dynamics from the full spectral model and apply feedback control strategies while using ILC methods to learn the spectral energy distribution of some kind of "residual model".

Since the feedback stabilization of RAs was a complete novelty, a primary target was to keep the complexity of the control concept at a reasonable level having in mind the implementation on the experimental system. Clearly, there are several ways how one can improve the presented designs. Just to give a few examples, one could use observer-based feedback schemes that would allow to estimate uncertain or varying parameters to obtain an adaptive feedback design. The briefly outlined proof of global asymptotic stability (GAS) of the state feedback using pump light measurements already included a kind of constructive method to design nonlinear control laws from scratch without using linearized models. It is not fully clear, however, if this is always possible or how to optimally choose the steady-state input in view of the desired reserve for feedback control. Depending on the model calibration, the pulse burst generation and amplification treated in Chapter 6 could clearly benefit from using model-predictive control methods together with an observer-based state estimation scheme that combines continuous (energy or transmitted pump light) measurements and the occasional information on the exact energy distribution. While operating optical amplifiers in steady state is clearly standard, one could use control schemes to create desired pulse sequences or create desired limit cycles.

Applying ILC schemes to nonlinear dispersive systems such as the NLSE in Chapter 4 is a quite delicate matter for several reasons: First, the effects of the nonlinear phase due to the Kerr nonlinearity are not captured by the simple linear models. Second, the system itself is usually not introducing any damping. Since the effects of the nonlinear phase acquired during propagation are rather weak in CPAs due to the reduced power densities, this was not much of an issue in this thesis. If one starts to enter strong Kerr regimes, however, such simple learning laws start to diverge fast. Trying to take corrective measures to improve convergence is indeed possible and was explored in [119]. Additionally, the use of micro-resonators to create frequency combs has generated significant interest in recent years [107, 120]. Their description by Lugiato-Lefever equations [107, 121] or so-called coupled-mode equations [107] is very similar to the NLSE and one might be able to apply similar methods as presented in this thesis.

Many application scenarios of control strategies for DPSs require to handle higher-dimensional domains [122]. The control of steady-state profiles or using

Die approbierte Originalversion dieser Dissertation ist in der TU Wien Bibliothek verfügbar.
The approved original version of this doctoral thesis is available at the TU Wien Bibliothek.
TU Bibliothek WIEN Your knowledge hub

simple dynamic approximations is quite common in adaptive optics (e.g., see [123]) while the dynamic control of DPSs is often solved by resorting to classic early-lumping approaches (e.g., see [124]) as pointed out in Chapter 3. Extending the presented ILC approach to higher-dimensional domains in a late-lumping sense would be quite interesting. In particular, the dynamic control of (nonlinear) hyperbolic PDEs or dispersive systems as mentioned above seems to provide fruitful applications as the model errors introduced by early-lumping approaches may destabilize simple ILC schemes. Additionally, one could use such ILC laws to shape the transversal pulse profile of the laser pulses generated by CPAs. Some first steps in this direction have already been explored with first application examples in [119]. The resulting tools to produce desired spatio-temporally shaped light pulses might be useful for applications such as laser ablation since recent studies [19] indicate that specifically shaped pulses can improve their ability to penetrate materials by considering the electron dynamics of the material's atoms.

Die approbierte Originalversion dieser Dissertation ist in der TU Wien Bibliothek verfügbar.
The approved original version of this doctoral thesis is available at the TU Wien Bibliothek.
TU Bibliothek WIEN Your knowledge hub

Die approbierte Originalversion dieser Dissertation ist in der TU Wien Bibliothek verfügbar.
The approved original version of this doctoral thesis is available at the TU Wien Bibliothek.

APPENDIX A

Efficient numerical solution strategies for CPAs

As presented in Section 2.2, we can describe the amplification of a single pulse entering a regenerative amplifier as an alternating sequence of pulse and pump models. Together with the descriptions of pulse stretchers and pulse compressors given in Section 2.1 this yields a detailed mathematical model of chirped pulse amplifiers based on first principles. Its high complexity calls for tailored numerical simulation methods to keep the computational effort manageable.

In terms of computational burden, the main contributor is clearly the pulse model with its complex pulse propagation and the interaction of the light field with the laser medium. The pump model can be solved in a similar manner but at greatly reduced effort since the spatial dynamics of the pumping beam was removed by singular perturbation methods. Since the descriptions of the pulse stretcher (2.10) and pulse compressor (2.12) together with the adjustable input filter can be efficiently treated numerically in the Fourier domain by using the fast Fourier transform (FFT), the following will solely focus on simulation techniques for the pulse model. To summarize the results of Section 2.2.1, the propagation of light through the laser medium can be described by, see (2.23), (2.25), and (2.27),

$$i\frac{\partial E}{\partial z} = -\frac{k_2}{2}\frac{\partial^2 E}{\partial t^2} + \frac{1}{2}\omega_0\varepsilon_0 n_0 n_2 |E|^2 E + \frac{\omega_0^2}{2c_0^2\varepsilon_0 k_0}\sum_{i=1}^{4} P_j \tag{A.1a}$$

$$\frac{\partial P_j}{\partial t} = -\frac{\omega_j^2 + i\omega_0\Delta\omega_j - \omega_0^2}{\Delta\omega_j + i2\omega_0}P_j + \frac{\kappa_j}{\Delta\omega_j + i2\omega_0}(N_j - N_5)E \tag{A.1b}$$

$$\begin{aligned}\frac{\partial N_j}{\partial t} &= +\frac{1}{2\hbar}\mathrm{Im}\left\{E^* P_j\right\}, \qquad j = 1,\ldots,4\\ \frac{\partial N_5}{\partial t} &= -\frac{1}{2\hbar}\mathrm{Im}\left\{E^*\sum_{i=1}^{4} P_j\right\},\end{aligned} \tag{A.1c}$$

Die approbierte Originalversion dieser Dissertation ist in der TU Wien Bibliothek verfügbar.
The approved original version of this doctoral thesis is available at the TU Wien Bibliothek.
TU WIEN Bibliothek Your knowledge hub

with the initial and boundary conditions, see (2.28),

$$E(0,t) = E^{n,k}_{\text{in,RA}}(t) \tag{A.2a}$$

$$E(z,0) = 0 \tag{A.2b}$$

$$\left.\frac{\partial E(z,t)}{\partial t}\right|_{t=0} = 0 \tag{A.2c}$$

$$P_j(z,0) = 0 \tag{A.2d}$$

$$N_j(z,0) = N^{n,k}_{j,\text{pulse}}(z) \tag{A.2e}$$

and the desired amplified pulse, see (2.29),

$$E^{n,k}_{\text{out,RA}}(t) = E(L,t). \tag{A.3}$$

The remaining population density $N^{n,k}_{j,\text{dep}}(z)$ after the amplification process is given according to (2.30). Thus, the pulse model consists of three physical components, namely the pulse progagation due to the nonlinear Schrödinger equation (A.1a), the atomic polarisations due to the resonant dipole equations (A.1b) of each transition and the corresponding rate equations (A.1c) for the population densities of each atomic energy level.

High fidelity numerical solutions of the one-dimensional nonlinear Schrödinger equation (NLSE) are usually obtained by operator splitting methods (e.g., see [125]) progressing along the spatial coordinate z. For a given temporal solution $E(z_n,t)$ at some point z_n we can solve for corresponding response of the material by integration of the coupled system of ordinary differential equations (ODEs) (A.1b) and (A.1c)[1]. As a result, the complete pulse model can be solved by a two-step procedure as illustrated in Figure A.1: a first step (S1) determines the polarizations $P_j(z_n,t)$ and the population densities $N_j(z_n,t)$ corresponding to an (initial) pulse $E(z_n,t)$ while a second step (S2) propagates the pulse for a small distance Δz by solving (A.1a) under the external drive of the atomic polarizations calculated during (S1).

Step 1: Solution of the atomic response

Using the abbreviations $P_j(t) = P_j(z_n,t)$ and $\Delta N_j(t) = N_5(z_n,t) - N_j(z_n,t)$ as well as $E(t) = E(z_n,t)$ for a generic point z_n, the response of the doped atoms given by (A.1b) and (A.1c) can be written as

$$\frac{\partial P_j(t)}{\partial t} = -a_j P_j(t) - b_j \Delta N_j(t) E(t) \tag{A.4a}$$

$$\frac{\partial N_j(t)}{\partial t} = +\frac{1}{2\hbar}\text{Im}\left\{E^*(t)P_j(t)\right\}, \quad j = 1,\ldots,4 \tag{A.4b}$$

[1] In quantum mechanical terms, we are solving the von-Neumann equation of the density operator.

Die approbierte Originalversion dieser Dissertation ist in der TU Wien Bibliothek verfügbar.
The approved original version of this doctoral thesis is available at the TU Wien Bibliothek.
TU Bibliothek WIEN Your knowledge hub

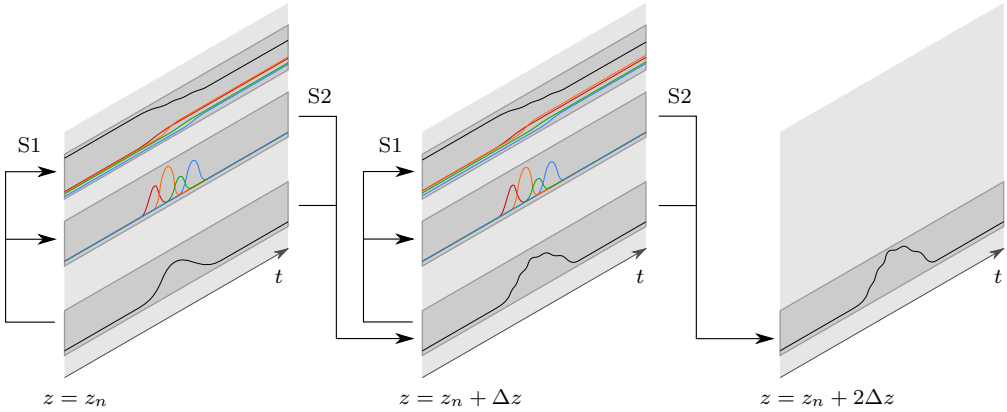

Figure A.1: A two-step procedure to solve (A.1) by progressing over the spatial coordinate z. The first step (S1) calculates the atomic polarizations $P_j(z_n, t)$ and population densities $N_j(z_n, t)$ corresponding to a given temporal pulse profile $E(z_n, t)$. The second step (S2) propagates the pulse according to the nonlinear Schrödinger equation (A.1a) for a small distance Δz under the external drive of the previously calculated atomic polarizations.

$$\frac{\partial N_5(t)}{\partial t} = -\frac{1}{2\hbar}\mathrm{Im}\left\{E^*(t)\sum_{j=1}^{4} P_j(t)\right\}, \tag{A.4c}$$

using the abbreviations $a_j = \frac{\omega_j^2 + i\omega_0\Delta\omega_j - \omega_0^2}{\Delta\omega_j + i2\omega_0}$ and $b_j = \frac{\kappa_j}{\Delta\omega_j + i2\omega_0}$.

Since the polarization dynamics are usually very fast while the population densities evolve significantly slower, the system of ODEs (A.4) is extremely stiff from a numerical point of view. However, we require precise solutions of the polarizations to reproduce the pulse amplification and the resulting extraction of the populations at sufficient accuracy[2]. Additionally, the driving electric field $E(t)$ is usually very complex and heavily chirped, which requires a high number of sampling points. It is therefore reasonable to exploit the linear structure of (A.4a) by calculating the formal solution of (A.4) at a time $t + h$, which yields the implicit integral equation

$$P_j(t+h) = \mathrm{e}^{-a_j h}P_j(t) - b_j\int_t^{t+h} \mathrm{e}^{-a_j(h+t-\tau)}\Delta N_j(\tau)E(\tau)\mathrm{d}\tau$$
$$N_j(t+h) = N_j(t) + \frac{1}{2\hbar}\int_t^{t+h} \mathrm{Im}\left\{E^*(\tau)P_j(\tau)\right\}\mathrm{d}\tau, \quad j = 1, \ldots, 4$$

[2]This is easy to see as the pulse amplitude tends to grow exponentially for linear amplifiers, i.e., in the absence of gain saturation as well as nonlinear and dispersive propagation effects, and small errors build up very fast.

Die approbierte Originalversion dieser Dissertation ist in der TU Wien Bibliothek verfügbar.
The approved original version of this doctoral thesis is available at the TU Wien Bibliothek.
TU Bibliothek WIEN Your knowledge hub

$$N_5(t+h) = N_5(t) - \frac{1}{2\hbar}\int_t^{t+h} \mathrm{Im}\left\{E^*(\tau)\sum_{j=1}^{4} P_j(\tau)\right\}\mathrm{d}\tau.$$

Using an equally spaced temporal grid with a step width $h = \Delta t$ and applying the trapezoidal rule, one obtains the system of equations

$$P_{j,m+1} = \mathrm{e}^{-a_j\Delta t}P_{j,m} - \frac{b_j\Delta t}{2}\Delta N_{j,m}\left(\mathrm{e}^{-a_j\Delta t}E_m + E_{m+1}\right) \tag{A.5a}$$

$$\begin{aligned} N_{j,m+1} &= N_{j,m} + \frac{\Delta t}{4\hbar}\mathrm{Im}\left\{E_m^* P_{j,m} + E_{m+1}^* P_{j,m+1}\right\}, \quad j = 1,\dots,4 \\ N_{5,m+1} &= N_{5,m} - \frac{\Delta t}{4\hbar}\sum_{j=1}^{4}\mathrm{Im}\left\{E_m^* P_{j,m} + E_{m+1}^* P_{j,m+1}\right\}, \end{aligned} \tag{A.5b}$$

with the abbreviations $P_{j,m} = P_j(t_m)$, $N_{j,m} = N_j(t_m)$ and $E_m = E(t_m)$. Additionally, we assumed that $N_j(t_{m+1}) \approx N_j(t_m)$ due to the comparatively slow population dynamics at the considered field intensities. This assumption renders (A.5a) independent of $N_{j,m+1}$, wherefore the system of equations (A.5) can be solved explicitly by inserting (A.5a) into (A.5b). The resulting explicit numerical scheme is fast and simple to calculate while providing a sufficient level of accuracy by utilizing the linear structure.

Step 2: Pulse propagation

Now that the dopant's local atomic response to the pulse $E(z_n, t)$ is known, one can use the obtained polarizations $P_j(z_n, t)$ to determine how the electric field is deformed during propagation by a spatial length Δz according to (A.1a). For one-dimensional spatial domains, operator-splitting methods can be considered the standard tools to solve NLSEs [125]. Thus, we rewrite (A.1a) in the form

$$i\frac{\partial E}{\partial z} = \mathcal{D}(E) + \mathcal{N}(E) + \mathcal{X}, \tag{A.6}$$

with the operators

$$\mathcal{D}(E) = -\frac{k_2}{2}\frac{\partial^2 E}{\partial t^2} \tag{A.7a}$$

$$\mathcal{N}(E) = \frac{1}{2}\omega_0\varepsilon_0 n_0 n_2 |E|^2 E \tag{A.7b}$$

$$\mathcal{X} = \frac{\omega_0^2}{2c_0\varepsilon_0 k_0}\sum_{j=1}^{4} P_j. \tag{A.7c}$$

Using sequential Strang- and Lie-Trotter-Splitting [126], the desired solution of the full problem (A.6) can be approximately decomposed into five simple subproblems: First, the effect of the exogenous drive and the Kerr nonlinearity, i.e.,

Die approbierte Originalversion dieser Dissertation ist in der TU Wien Bibliothek verfügbar.
The approved original version of this doctoral thesis is available at the TU Wien Bibliothek.
TU Bibliothek WIEN Your knowledge hub

$i\frac{\partial E}{\partial z} = \mathcal{X}$ and $i\frac{\partial E}{\partial z} = \mathcal{N}(E)$, are successively solved for half the spatial step width. The dispersion is considered afterwards by a full step using the free Schrödinger equation $i\frac{\partial E}{\partial z} = \mathcal{D}(E)$. Finally, the approximate solution is obtained by applying two half steps of the exogenous drive and the Kerr nonlinearity again. Assuming that the polarizations remain unchanged over the considered spatial interval, all sub-problems can be solved analytically and the approximate solution of the full problem (A.6) at $z_{n+1} = z_n + \Delta z$ is given by

$$
\begin{aligned}
E^{(1)}(t) &= E(z_n, t) - i\frac{\Delta z}{2}\frac{\omega_0^2}{2c_0\varepsilon_0 k_0}\sum_{j=1}^{4} P_j(z_n, t) \\
E^{(2)}(t) &= \exp\left[-i\frac{\Delta z}{4}\omega_0\varepsilon_0 n_0 n_2 |E^{(1)}(t)|^2\right] E^{(1)}(t) \\
E^{(3)}(t) &= \mathcal{F}^{-1}\left\{\exp -i\frac{k_2\Delta z}{2}\omega^2 \mathcal{F}\left\{E^{(2)}(t)\right\}\right\} \\
E^{(4)}(t) &= E^{(3)}(t) - i\frac{\Delta z}{2}\frac{\omega_0^2}{2c_0\varepsilon_0 k_0}\sum_{j=1}^{4} P_j(z_n, t) \\
E(z_{n+1}, t) &= \exp\left[-i\frac{\Delta z}{4}\omega_0\varepsilon_0 n_0 n_2 |E^{(4)}(t)|^2\right] E^{(4)}(t).
\end{aligned}
$$

Remark 27. *The free or linear Schrödinger equation $i\frac{\partial E}{\partial z} = \mathcal{D}(E)$ is easily solved in the frequency domain, wherefore numerical solutions can be obtained by using the fast Fourier transform. Essentially, this is equivalent to using spectral methods to solve the free Schrödinger equation. To solve $i\frac{\partial E}{\partial z} = \mathcal{N}(E)$, one uses the fact that the absolute value $|E(z,t)|$ remains unchanged along a solution trajectory.*

To illustrate the solution behavior, we simulate the amplification of a single measured 10 nJ pulse from a typical source with a pulse width of roughly 600 fs. The required initial population is chosen as a steady state of the pump model, i.e., the amplifier is fully charged and exhibits extremely high gains. Additionally, we do not apply any input shaping, i.e., $G_{\mathrm{F}}(\omega) = 1$.

As shown in Figure A.2, the amplification process successively extracts energy from the laser medium and the populations deplete with each round-trip. Since the extraction rate rises with the energy of the pulse propagating through the medium (see Figure A.3), the larger part of the population inversion is actually extracted in the last few round-trips. In the absence of saturation effects, the pulse energy rises exponentially with the number of round-trips, while real amplifiers reach a point at which the round-trip gain is equal to the losses the pulse experiences during one round-trip and the output energy reaches its maximum value, see Section 5.2. Increasing the number of round-trips beyond that point reduces the energy of the circulating pulse as shown in Figure A.3. A comparison between the input and output pulse is given in Figure A.4. Due to the strongly inhomogeneous gain profile, the resulting narrowing of the pulse spectrum, and the nonlinear

Die approbierte Originalversion dieser Dissertation ist in der TU Wien Bibliothek verfügbar.
The approved original version of this doctoral thesis is available at the TU Wien Bibliothek.
TU Bibliothek WIEN Your knowledge hub

phase components due to the Kerr nonlinearity, the compressor is not able to fully recompress the pulse and the resulting power density of the output pulse is greatly reduced.

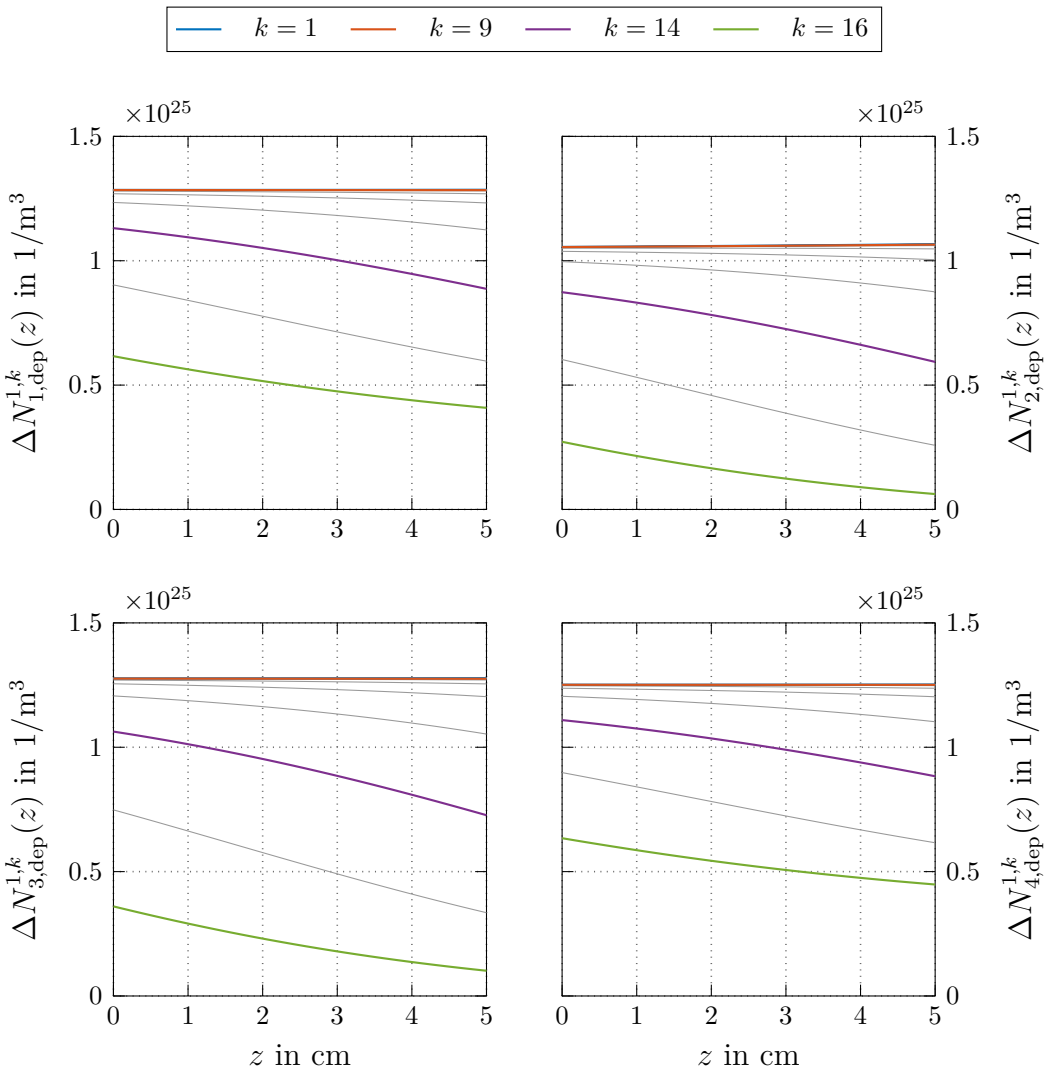

Figure A.2: Successive depletion of the population inversion at the end of one round-trip $\Delta N^{1,k}_{j,\mathrm{dep}}(z)$. The amplification process extracts increasing amounts of energy due to the growing pulse energy. As a result, only the last few round-trips contribute significantly to the total gain saturation.

Die approbierte Originalversion dieser Dissertation ist in der TU Wien Bibliothek verfügbar.
The approved original version of this doctoral thesis is available at the TU Wien Bibliothek.
TU WIEN Bibliothek Your knowledge hub

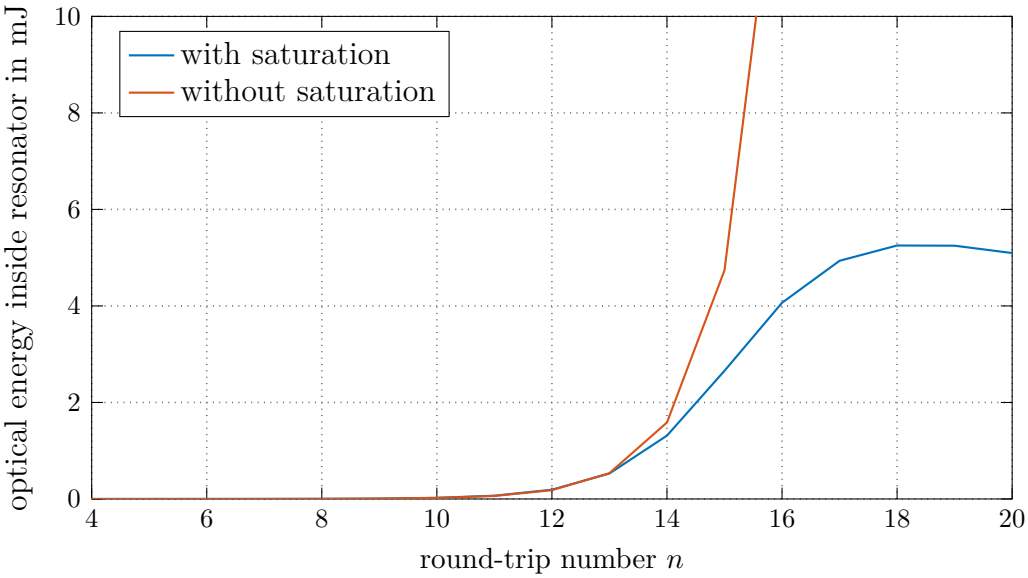

Figure A.3: Evolution of the pulse energy inside the resonator cavity for a real amplifier and for an idealized amplifier without any saturation of the population inversion, respectively.

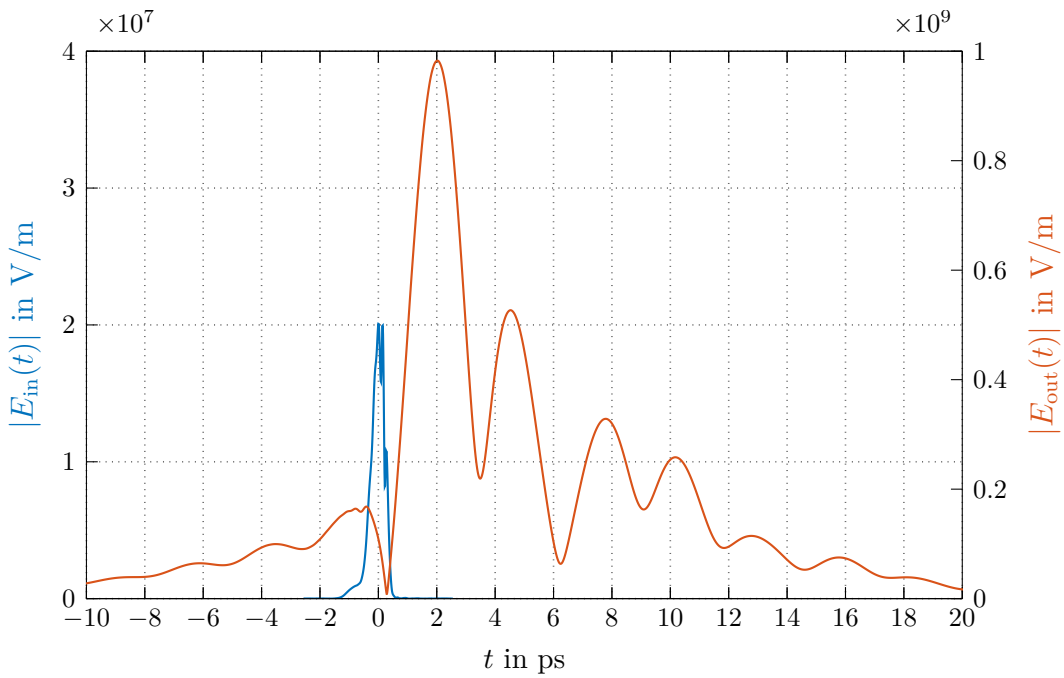

Figure A.4: Comparison between input and output pulses for the unshaped case $G_{\mathrm{F}}(\omega) = 1$ after 12 round-trips.

Die approbierte Originalversion dieser Dissertation ist in der TU Wien Bibliothek verfügbar.
The approved original version of this doctoral thesis is available at the TU Wien Bibliothek.
TU WIEN Bibliothek Your knowledge hub

Die approbierte Originalversion dieser Dissertation ist in der TU Wien Bibliothek verfügbar.
The approved original version of this doctoral thesis is available at the TU Wien Bibliothek.

APPENDIX B

Parameter identification strategies for CPAs

The mathematical model of the chirped pulse amplifier (CPA) derived in Chapter 2 contains a rather large number of parameters, most of which are either given by geometry (e.g., the length of the resonator cavity L, the coefficients of the pulse stretcher and the pulse compressor $\varphi_{\mathrm{S},i}$ and $\varphi_{\mathrm{C},i}$), can be measured with high precision (e.g., the optical properties n_0, n_2 and k_2 of the aluminium-yttrium crystal) or can be estimated (e.g., the resonator losses η_{RC}).

Significantly more troublesome is the identification of suitable parameters of the doped laser atoms like the relaxation rates γ_{ij} between the individual energy levels and the resonance frequencies ω_j, the corresponding transition cross sections σ_j, and the line width $\Delta\omega_j$ of each resonant transition. To make things more complicated, usually the only available data sets are corresponding input-output measurements of steady-state pulses. Thus, the recorded pulse profiles are a result of the population densities N_j arriving at an equilibrium between the extraction due to the amplification process and the regeneration due to the pumping process, i.e., according to Figure 2.5 a steady state is given by $N_{j,in}^{n}(z) = N_{j,in}^{n+1}(z) = N_j^s(z)$. Contrary to the simplified, spectrally homogeneous model used in Chapter 5 and Chapter 6, a direct calculation of the steady-state populations $N_j^s(z)$ is quite difficult. For the considered stable operational regimes, it is thus customary to simply calculate the steady-state populations by iterative simulation of the complete model, which is rather time-consuming due to the model's inherent complexity. Thus, using a direct optimization-based identification approach results in an enormous simulation effort and is thus virtually unfeasible in practice. Trying to adjust the parameters manually, on the other hand, is a quite tedious task as the individual parameters are strongly interconnected. For example, the observed amplification due to a single resonant transition is determined by the product of its transition cross section σ_j and the corresponding population inversion $\Delta N_j(z)$,

Die approbierte Originalversion dieser Dissertation ist in der TU Wien Bibliothek verfügbar.
The approved original version of this doctoral thesis is available at the TU Wien Bibliothek.
TU WIEN Bibliothek Your knowledge hub

which in turn depends on all relaxation rates and *all* transition cross sections. This ambiguity can only be resolved - at least to some extent - by assessing the individual saturation behavior of each transition.

As a result, we will approximately split the full system identification into two partial dynamics: the population dynamics and the propagation dynamics. The population dynamics can be simplified by reducing the number of (free) parameters while the propagation dynamics can be approximated by a linear model which serves as a solid basis for the application of optimation-based identification strategies. Combining both yields a semi-automatic identification algorithm that is able to produce meaningful parameters within a required model fidelity. A complete set of all parameters of the CPA system is given in Table E.1.

B.1 Partial decoupling of the population dynamics by parameter reduction

Using input-output measurements to extract values for all relaxation parameters γ_{ij} is clearly a rather hopeless endeavor. To still reproduce the observed behavior, we will therefore start be reducing the number of parameters by assuming that the contribution to the total population relaxation due to the "inner" transitions can be neglected, i.e., $\gamma_{12} = \gamma_{21} = \gamma_{23} = \gamma_{32} = \gamma_{34} = \gamma_{43} = 0$. Since the population densities obey a Boltzmann distribution at thermal equilibrium, we assume that the upward and downward oriented relaxation rates between the inner energy states and the ground state are connected by the ratio [30, p. 76]

$$\frac{\gamma_{0i}}{\gamma_{i0}} = \mathrm{e}^{\left(-\frac{E_i - E_0}{kT}\right)} \tag{B.1}$$

with the Boltzmann constant k and the temperature T. From fluorescence measurements it is known that the life time of the upper state E_5 is approximately $\tau_5 = 8\,\mathrm{ms}$. Assuming that all relaxation transitions contribute in a roughly similar way, the downward relaxation rates leaving the upper state can be approximated as $\gamma_{5j} = 1/(5\tau_5) = 25/\mathrm{s}$. This leaves only four remaining parameters γ_{j0} with $j = 1, \ldots, 4$, which we will collect in a single parameter vector $\boldsymbol{\theta}_1 = [\gamma_{10}, \ldots, \gamma_{40}]^{\mathrm{T}}$ for convenience. All energy levels still interact with the ground level E_0, wherefore the dynamics of the individual energy levels are not fully decoupled. Since this affects all energy levels in the same way, we can adjust the relative saturation behavior of the j-th energy level using γ_{j0}.

B.2 Linear propagation model

The spectral properties of chirped pulse amplifiers are essentially given by the parameters $\boldsymbol{\theta}_2 = [\omega_1, \ldots, \omega_4, \Delta\omega_1, \ldots, \Delta\omega_4, \sigma_1, \ldots, \sigma_4]^{\mathrm{T}}$, describing the shape and

Die approbierte Originalversion dieser Dissertation ist in der TU Wien Bibliothek verfügbar.
The approved original version of this doctoral thesis is available at the TU Wien Bibliothek.
TU WIEN Bibliothek Your knowledge hub

strength of each resonant transition. Trying to describe the amplifier's gain in an approximate way can be approached similar to Chapter 4. Assuming that the Kerr effect has only a minor influence on the observed spectral gain, i.e., the spectral broadening due to self-phase modulation, and the depletion of the population densities *during one* passage of the laser medium can be neglected, one obtains the linear relation analogous to (4.14) in Chapter 4. For a given population inversion of the n-th pulse and k-th round-trip $\Delta\mathbf{N}^{n,k}(z) = \left[\Delta N_{51}^{n,k}(z), \ldots, \Delta N_{54}^{n,k}(z)\right]^{\mathrm{T}}$, one obtains

$$\hat{E}_{\mathrm{out,RA}}^{n,k}(\omega) = G_{\mathrm{sp}}\left(\omega, \boldsymbol{\theta}_2; \overline{\Delta\mathbf{N}^{n,k}}\right) \hat{E}_{\mathrm{in,RA}}^{n,k}(\omega) \tag{B.2}$$

with the transfer function of a single passage

$$G_{\mathrm{sp}}\left(\omega, \boldsymbol{\theta}_2; \overline{\Delta\mathbf{N}^{n,k}}\right) = \exp\left[-\frac{iL}{2}\left(k_2\omega^2 + \frac{\omega_0^2}{c_0^2\varepsilon_0 k_0}\sum_{j=1}^{4}\chi_j\left(\omega, \boldsymbol{\theta}_2; \overline{\Delta N_{5j}^{n,k}}\right)\right)\right] \tag{B.3}$$

and the susceptibilities

$$\chi_j\left(\omega, \boldsymbol{\theta}_2; \overline{\Delta N_{5j}^{n,k}}\right) = \frac{-\kappa_j\overline{\Delta N_{5j}^{n,k}}}{i\omega(\Delta\omega_j + 2i\omega_0) + \omega_j^2 + i\omega_0\Delta\omega_j - \omega_0^2} \tag{B.4}$$

where $\kappa_j = \frac{\omega_j\varepsilon_0 c_0\Delta\omega_j\sigma_j}{\omega_0}$. The mean population inversions are given by the spatial mean over the length of the laser medium

$$\overline{\Delta N_{5j}^{n,k}} = \frac{1}{L}\int_0^L \Delta N_{5j}^{n,k}(z)\mathrm{d}z. \tag{B.5}$$

If we have knowledge of the steady-state population inversions $\overline{\Delta\mathbf{N}^{s,k}}$ of each round-trip $k = 1, \ldots, N_{\mathrm{RT}}$ using a simulation of the full mathematical model, we can approximate the behavior of the CPA in the vicinity of the chosen parameters $\boldsymbol{\theta}_1$ and $\boldsymbol{\theta}_2$ by

$$\hat{E}_{\mathrm{out}}^{s}(\omega) = \underbrace{\eta G_{\mathrm{F}}^{s}(\omega)\prod_{k=1}^{N_{\mathrm{RT}}} G_{\mathrm{sp}}\left(\omega, \boldsymbol{\theta}_2; \overline{\Delta\mathbf{N}^{s,k}}\right)}_{=G(\omega,\boldsymbol{\theta}_2)} \hat{E}_{\mathrm{in}}^{s}(\omega), \tag{B.6}$$

with the accumulated loss factor $\eta = \eta_{\mathrm{S}}\eta_{\mathrm{C}}\eta_{\mathrm{RC}}^{N_{\mathrm{RT}}-1}$. This simple expression can be used to determine suitable "spectral" parameters $\boldsymbol{\theta}_2$ as a solution of the optimization problem

$$\boldsymbol{\theta}_{2,\mathrm{opt}} = \underset{\boldsymbol{\theta}_2}{\operatorname{argmin}}\|\hat{E}_{\mathrm{out}}^{s}(\omega) - G(\omega, \boldsymbol{\theta}_2)\hat{E}_{\mathrm{in}}^{s}(\omega)\|_2. \tag{B.7}$$

The assumptions above are particularly valid for low energy pulses, wherefore we can expect that the optimization problem (B.7) yields a good approximation of such pulses.

Die approbierte Originalversion dieser Dissertation ist in der TU Wien Bibliothek verfügbar.
The approved original version of this doctoral thesis is available at the TU Wien Bibliothek.
TU Bibliothek WIEN Your knowledge hub

B.3 Semi-automatic identification algorithm

Building on the two approximate models of the previous subsections, we can provide a simple identification procedure for a set of steady-state input and output pulses with varying pulse energies, i.e., for a different number of round-trips or varying pumping powers. Thereby, a given set of parameters $\boldsymbol{\theta}_1$ and $\boldsymbol{\theta}_2$ is successively improved in an alternating fashion until the mathematical model matches the measured input-output behavior with sufficient precision. The adaption procedure is based on the following steps:

1. Calculate a steady-state solution of the population inversions $\Delta\mathbf{N}^{s,k}(z)$ for a given input pulse $E^s_{\text{in}}(t)$ and the current parameter sets $\boldsymbol{\theta}_1$ and $\boldsymbol{\theta}_2$ by iterative simulation of the full mathematical model according to Section 2.2.3

2. Adjust one set of parameters $\boldsymbol{\theta}_1$ or $\boldsymbol{\theta}_2$ by

   (a) Manual adaption of $\boldsymbol{\theta}_1$ to improve the saturation behavior for varying pulse energies

   (b) Solution of the optimization problem (B.7) using the calculated mean population inversions $\overline{\Delta\mathbf{N}^{s,k}}$ due to (B.5) for the data set with the lowest pulse energies

Remark 28. *In principle, one could use the separation of the system dynamics as presented above with an automatic adaption of the saturation behavior as well. However, since this requires gradient-free optimization algorithms with a rather high number of evaluations of the cost function which in turn implies calculation of steady-state population densities for a large number of operating points, it is computationally very demanding and we refrained from applying such an approach for the moment.*

As shown in Figure 2.6, the parameter set obtained by this semi-automatic identification algorithm (see Table E.1) reproduces the measured data quite well. Obviously, four resonant transitions cannot fully explain the observed amplification, which is particularly apparent for low wavelengths $\lambda \leq 2090\,\text{nm}$, where the deviations indicate a minor contribution due to higher energy levels. This results in an approximately constant multiplicative error of the output energies as shown in Figure 2.7 while the saturation behavior itself is reproduced quite well. Due to the increasing extraction of excited states, the steady-state inversion before the following laser pulse $\overline{\Delta N^s_{5\text{j,reg}}}$ is slowly depleting with the number of round-trips N_{RT} as illustrated in Figure 2.8.

Die approbierte Originalversion dieser Dissertation ist in der TU Wien Bibliothek verfügbar.
The approved original version of this doctoral thesis is available at the TU Wien Bibliothek.
TU Bibliothek Your knowledge hub WIEN

APPENDIX C

Extensions of the dynamic model to multi-pass pumping and linear cavities

The dynamical model of regenerative amplifiers derived in Section 5.1 as well as the more complicated model presented in Chapter 2 represent the simplest case of end-pumped regenerative amplifiers using a ring cavity design with a pumping beam that is fed through the laser medium once. Alternatively, one can use a linear cavity[1] where the pulse is trapped between two mirrors bouncing back and forth. While both designs have significant differences regarding their modal stability [127, 128], i.e. the geometric conditions upon which injected light stays inside the cavity, the effect on the amplifier's dynamics is less significant, as we will argue below.

While the pumping beam is propagating through the gain medium it is gradually absorbed and its energy is transformed into excited states of the doped atoms (see Figure 5.4). As the beam is absorbed, the regions of the medium being farther away from the laser source observe declining excitation rates that ultimately result in a very inhomogeneous population inversion throughout the laser rod. As this inhomogeneous population inversion is causing thermal stress to the crystal, laser engineers are usually inclined to achieve more homogeneous profiles by feeding the remaining pump light exiting the laser rod back into the crystal.

In the following, we want to consider an end-pumped regenerative amplifier with a linear cavity and continuous pumping where the pumping beam is fed through the crystal twice. A drastically simplified schematic of such an amplifier

[1] Sometimes also called *standing wave* cavity as continuous beams ultimately form a standing wave pattern inside the resonator. Since we consider pulsed operation only, the term linear cavity seems more natural.

Die approbierte Originalversion dieser Dissertation ist in der TU Wien Bibliothek verfügbar.
The approved original version of this doctoral thesis is available at the TU Wien Bibliothek.
TU WIEN Bibliothek Your knowledge hub

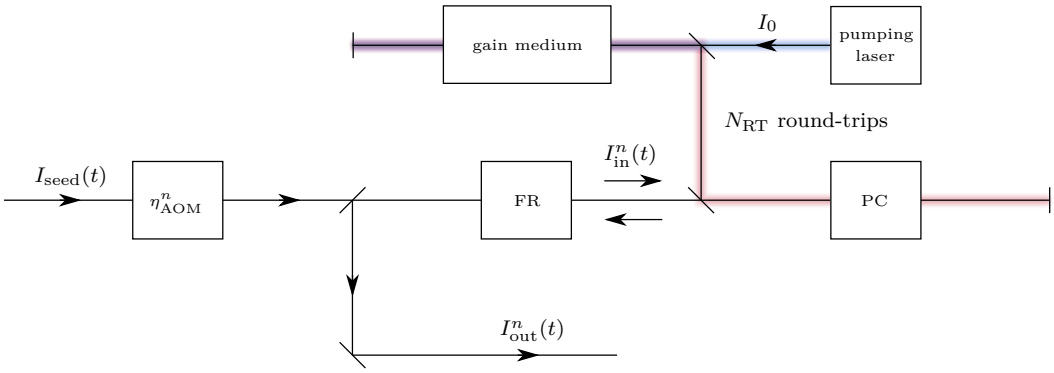

Figure C.1: Exemplary schematic of a regenerative amplifier in an end-pumped configuration (blue) using a linear resonator cavity (red). The seed pulse $I_{\mathrm{seed}}(t)$ passes an acousto-optic modulator (AOM) and a Faraday rotator (FR) befor entering the cavity denoted by $I^n_{\mathrm{in}}(t)$. After N_{RT} round-trips, the pulse is ejected by switching the Pockel's cell (PC). Accounting for additional losses yields the final output pulse $I^n_{\mathrm{out}}(t)$.

is given in Figure C.1. The seed pulses $I_{\mathrm{seed}}(t)$ can be damped by means of an acousto-optic modulator (AOM). The resulting pulse is than fed through a Faraday rotator (FR) to separate input and output pulses by introducing a rotation of the polarisation axis. Analogous to Section 5.1, the resulting pulse $I^n_{\mathrm{in}}(t)$ is then entering the cavity. Merging all losses into η_{in} and the damping due to the AOM into η^n_{AOM}, the input pulse $I^n_{\mathrm{in}}(t)$ is again given by (5.1). The injected pulse is then bouncing back and forth inside the cavity (illustrated by a red shading in Figure C.1) for N_{RT} round-trips until it is again released by switching the Pockels cell (PC) with the output pulse given by (5.2) and the concentrated extraction losses η_{out}. Inside the cavity, it is again assumed that the losses can be considered concentrated as a single round-trip loss factor η_{RT}.

While all developments in this chapter are illustrated for the energy-based model derived in Section 5.1, they can be directly applied to the pulse burst formation presented in Chapter 6 and even the complex CPA model derived in Chapter 2.

C.1 Differences for linear cavities

The most obvious difference compared to ring cavities is that pulses traverse the gain medium twice per round-trip in alternating directions. In particular, the left and right propagating pulses can exhibit some temporal overlap if the spatial distance between the gain medium and the reflecting mirror is shorter than the spatial width of the laser pulses. For coherent light, the envelope of the

Die approbierte Originalversion dieser Dissertation ist in der TU Wien Bibliothek verfügbar.
The approved original version of this doctoral thesis is available at the TU Wien Bibliothek.
TU Bibliothek WIEN Your knowledge hub

superposition of two pulses shows a rapidly oscillating spatial behavior that cannot be described by the simple intensity-based model used in Chapter 5. However, while this effect is significant for continuous-wave amplifiers and may lead to so-called spatial hole burning [39, 129], the broad bandwidth of laser pulses and their movement through the crystal tends to wash out such coherent effects. This would in some cases allow a treatment as presented in [130] to account for the residual gain saturation effects, although their influence is on the total pulse energy is very small. Additionally, since pulses with 1 ps duration exhibit a spatial width of approximately 0.3 mm, the overlap can only occur for very narrowly placed mirrors. Thus, we will neglect any effects due to temporal overlap.

Under these assumptions, one round-trip inside the cavity splits up into two passages of a pulse according to the pulse model presented in Section 5.1.3. Strictly speaking, the second passage of the pulse is in the opposite direction of the first passage and thus the initial population inversion of the second round-trip is given by the spatially reversed remaining population after the first passage, i.e., $\Delta N_{\mathrm{in},2}(z) = \Delta N_{\mathrm{out},1}(L - z)$. Since the analytical solution only depends on the spatial average of the population inversion, one can easily see that the effect of a single round-trip inside the linear cavity is given by

$$\begin{bmatrix} G^{n,k+1} \\ H_{\mathrm{in}}^{n,k+1} \end{bmatrix} = \mathbf{f}_{\mathrm{DP}} \left(\begin{bmatrix} G^{n,k} \\ H_{\mathrm{in}}^{n,k} \end{bmatrix} \right) \tag{C.1}$$

analogous to (5.28) with[2]

$$\mathbf{f}_{\mathrm{DP}} \left(\begin{bmatrix} G^{n,k} \\ H_{\mathrm{in}}^{n,k} \end{bmatrix} \right) = \begin{bmatrix} f_{\mathrm{dep}} \left(f_{\mathrm{dep}}(G^{n,k}, H_{\mathrm{in}}^{n,k}) \, , \, f_{\mathrm{gain}}(G^{n,k}, H_{\mathrm{in}}^{n,k}) \right) \\ \eta_{\mathrm{RT}} f_{\mathrm{gain}} \left(f_{\mathrm{dep}}(G^{n,k}, H_{\mathrm{in}}^{n,k}) \, , \, f_{\mathrm{gain}}(G^{n,k}, H_{\mathrm{in}}^{n,k}) \right) \end{bmatrix} . \tag{C.2}$$

The resulting dynamics are thus given by (5.31) by replacing the iterated function (5.29) with

$$\mathbf{f}_{\mathrm{MP}} = \mathbf{f}_{\mathrm{DP}}^{(N_{\mathrm{RT}})} . \tag{C.3}$$

C.2 Description of multi-pass pumping

According to Figure C.1, the pumping laser produces a continuous intensity $I_0 = {}^{4P_{\mathrm{pump}}}/_{d_{\mathrm{P}}^2 \pi}$ with the optical pumping power P_{pump} and the diameter of the pumping beam d_{P} that is fed through the gain medium twice. Feeding the remaining pump light back into the gain medium, the superposition of the left and right travelling components of the pump beam can lead to significant interference effects due to its coherent nature as illustrated in Figure C.2. In light of (5.24b), the rapid modulations of the pumping intensity will result in a similarly modulated

[2]Notice that $\mathbf{f}_{\mathrm{DP}} = \mathbf{f}_{\mathrm{SP}} \circ \mathbf{f}_{\mathrm{SP}}$ is only valid for $\eta_{\mathrm{RT}} = 1$ since the definition of $\mathbf{f}_{\mathrm{SP}}$ in (5.28) includes the round-trip losses.

Die approbierte Originalversion dieser Dissertation ist in der TU Wien Bibliothek verfügbar.
The approved original version of this doctoral thesis is available at the TU Wien Bibliothek.
TU Bibliothek Your knowledge hub WIEN

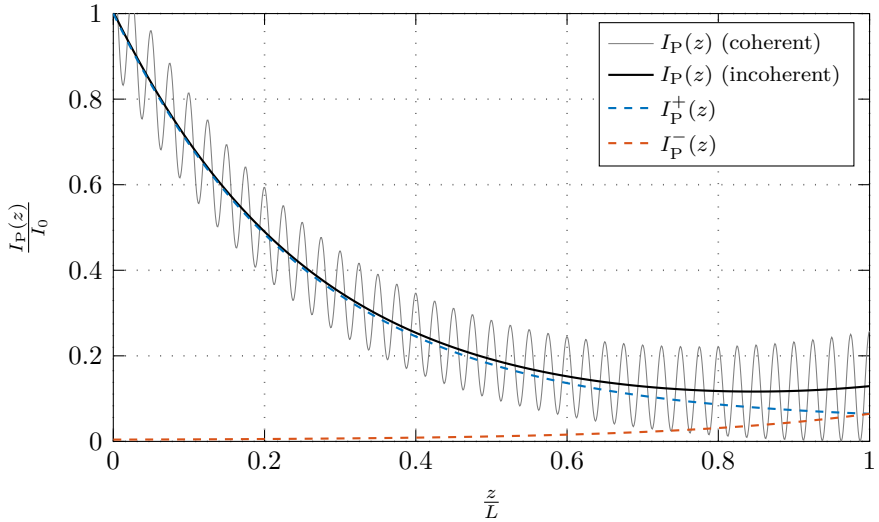

Figure C.2: Illustration of the stationary forward- and backward-propagating beams $I_P^+(z)$ and $I_P^-(z)$ and their coherent and incoherent superposition $I_P(z)$.

spatial distribution of the total population inversion. Similar to the discussion in the previous section, the gain of the amplifiers only depends on the total population inversion and not on its spatial distribution, see (5.16). While the altered spatial profile of $I_P(z)$ might have some effects on the evolution of the total population inversion, we assume for the following that an incoherent description is sufficient.

Using singular perturbation theory analogous to Section 5.1.4, the case of incoherent double-pass pumping can be described by

$$\frac{\partial I_P^+}{\partial z} = -\sigma_P \frac{(f_0 f_2 - f_3 f_1) N_{dop} - (f_0 + f_3)\Delta N}{f_1 + f_2} I_P^+ \tag{C.4a}$$

$$\frac{\partial I_P^-}{\partial z} = \sigma_P \frac{(f_0 f_2 - f_3 f_1) N_{dop} - (f_0 + f_3)\Delta N}{f_1 + f_2} I_P^- \tag{C.4b}$$

$$\begin{aligned}\frac{\partial \Delta N}{\partial t} &= -\gamma_{21} f_2 (f_1 N_{dop} + \Delta N) \\ &\quad + \frac{\sigma_P (I_P^+ + I_P^-)}{\hbar \omega_P} \left((f_0 f_2 - f_3 f_1) N_{dop} - (f_0 + f_3)\Delta N \right),\end{aligned} \tag{C.4c}$$

with the initial condition $\Delta N(z,0) = \Delta N_{in}(z)$ and the left boundary condition $I_P^+(0,t) = I_0$. Assuming that the losses in the mirror can be neglected, the right boundary condition is given by $I_P^-(L,t) = I_P^+(L,t)$. Proceeding as in Section 5.1.4, the evolution of the total population inversion is given by

$$\frac{\mathrm{d}}{\mathrm{d}t} N_{tot}(t) = -\gamma_{21} f_2 (f_1 N_{dop} L + N_{tot}(t)) + \tag{C.5}$$

Die approbierte Originalversion dieser Dissertation ist in der TU Wien Bibliothek verfügbar.
The approved original version of this doctoral thesis is available at the TU Wien Bibliothek.
TU Bibliothek WIEN Your knowledge hub

$$\frac{f_1+f_2}{\hbar\omega_\mathrm{P}}\left[-I_\mathrm{P}^+(L,t)+I_\mathrm{P}^+(0,t)+I_\mathrm{P}^-(L,t)-I_\mathrm{P}^-(0,t)\right].$$

Using the solutions of (C.4a) and (C.4b), i.e.,

$$\ln\left[\frac{I_\mathrm{P}^\pm(L,t)}{I_\mathrm{P}^\pm(0,t)}\right]=\mp\int_0^L\sigma_\mathrm{P}\frac{(f_0f_2-f_3f_1)N_\mathrm{dop}-(f_0+f_3)\Delta N}{f_1+f_2}\mathrm{d}z \tag{C.6}$$

together with the boundary conditions above, $\kappa_1=\frac{f_0f_2-f_1f_3}{f_1+f_2}$, and $\kappa_2=\frac{f_0+f_3}{f_1+f_2}$, one finally obtains

$$\begin{aligned}\frac{\mathrm{d}}{\mathrm{d}t}N_\mathrm{tot}(t)=&-\gamma_{21}f_2(f_1N_\mathrm{dop}L+N_\mathrm{tot}(t))\\&+I_0\frac{f_1+f_2}{\hbar\omega_\mathrm{P}}\left[1-\exp\left(-2\sigma_\mathrm{P}(\kappa_1N_\mathrm{dop}L-\kappa_2N_\mathrm{tot}(t))\right)\right],\end{aligned} \tag{C.7}$$

which is in fact almost identical to the simpler case (5.25) except for the factor of two. Under the given assumptions, using a double-pass pumping scheme effectively yields the exact same dynamics as the known single-pass scheme but with $\sigma_\mathrm{P}\to 2\sigma_\mathrm{P}$. Analogous results can be derived for higher-order schemes.

Die approbierte Originalversion dieser Dissertation ist in der TU Wien Bibliothek verfügbar.
The approved original version of this doctoral thesis is available at the TU Wien Bibliothek.
TU Bibliothek WIEN Your knowledge hub

Die approbierte Originalversion dieser Dissertation ist in der TU Wien Bibliothek verfügbar.
The approved original version of this doctoral thesis is available at the TU Wien Bibliothek.

APPENDIX D

Proof of Identity (3.35)

To show that the identity (3.35) is valid, we proceed analogously to [75, Claim 1] and multiply the right-hand side with its inverse. Using $\mathbf{\Phi} = \mathbf{G}_w \mathbf{S}_{ww} \mathbf{G}_w^H + \mathbf{S}_{nn}$ and $\mathbf{L}^k$ from (3.32a), we get

$$\begin{aligned}
&\left(\mathbf{I} - \mathbf{L}^k \mathbf{G}_u\right)\left[\mathbf{I} + \mathbf{S}_{\nu\nu}^k \mathbf{G}_u^H \left(\mathbf{G}_w \mathbf{S}_{ww} \mathbf{G}_w^H + \mathbf{S}_{nn}\right)^{-1} \mathbf{G}_u\right] \\
&= \mathbf{I} - \mathbf{S}_{\nu\nu}^k \mathbf{G}_u^H \left(\mathbf{G}_u \mathbf{S}_{\nu\nu}^k \mathbf{G}_u^H + \mathbf{\Phi}\right)^{-1} \mathbf{G}_u + \mathbf{S}_{\nu\nu}^k \mathbf{G}_u^H \mathbf{\Phi}^{-1} \mathbf{G}_u \\
&- \mathbf{S}_{\nu\nu}^k \mathbf{G}_u^H \left(\mathbf{G}_u \mathbf{S}_{\nu\nu}^k \mathbf{G}_u^H + \mathbf{\Phi}\right)^{-1} \mathbf{G}_u \mathbf{S}_{\nu\nu}^k \mathbf{G}_u^H \mathbf{\Phi}^{-1} \mathbf{G}_u. \qquad \text{(D.1)}
\end{aligned}$$

Applying the well-known Sherman-Morrison-Woodbury inversion formula, i.e.

$$\left(\mathbf{G}_u \mathbf{S}_{\nu\nu}^k \mathbf{G}_u^H - \mathbf{\Phi}\right)^{-1} = \mathbf{\Phi}^{-1} + \mathbf{\Phi}^{-1} \mathbf{G}_u \left(\left(\mathbf{S}_{\nu\nu}^k\right)^{-1} + \mathbf{G}_u^H \mathbf{\Phi}^{-1} \mathbf{G}_u\right)^{-1} \mathbf{G}_u^H \mathbf{\Phi}^{-1} \qquad \text{(D.2)}$$

one can rewrite (D.1) as

$$\begin{aligned}
&\mathbf{I} + \mathbf{S}_{\nu\nu}^k \mathbf{G}_u^H \mathbf{\Phi}^{-1} \mathbf{G}_u \left[\left(\mathbf{S}_{\nu\nu}^k\right)^{-1} + \mathbf{G}_u^H \mathbf{\Phi}^{-1} \mathbf{G}_u\right]^{-1} \mathbf{G}_u^H \mathbf{\Phi}^{-1} \mathbf{G}_u \\
&\quad - \mathbf{S}_{\nu\nu}^k \mathbf{G}_u^H \mathbf{\Phi}^{-1} \mathbf{G}_u \mathbf{S}_{\nu\nu}^k \mathbf{G}_u^H \mathbf{\Phi}^{-1} \mathbf{G}_u + \mathbf{S}_{\nu\nu}^k \mathbf{G}_u^H \mathbf{\Phi}^{-1} \mathbf{G}_u \\
&\quad \times \left[\left(\mathbf{S}_{\nu\nu}^k\right)^{-1} + \mathbf{G}_u^H \mathbf{\Phi}^{-1} \mathbf{G}_u\right]^{-1} \mathbf{G}_u^H \mathbf{\Phi}^{-1} \mathbf{G}_u \mathbf{S}_{\nu\nu}^k \mathbf{G}_u^H \mathbf{\Phi}^{-1} \mathbf{G}_u \\
&= \mathbf{I} + \mathbf{S}_{\nu\nu}^k \mathbf{G}_u^H \mathbf{\Phi}^{-1} \mathbf{G}_u \\
&\times \underbrace{\left[\left(\left(\mathbf{S}_{\nu\nu}^k\right)^{-1} + \mathbf{G}_u^H \mathbf{\Phi}^{-1} \mathbf{G}_u\right)^{-1} \left(\mathbf{I} + \mathbf{G}_u^H \mathbf{\Phi}^{-1} \mathbf{G}_u \mathbf{S}_{\nu\nu}^k\right) - \mathbf{S}_{\nu\nu}^k\right]}_{=\mathbf{0}} \\
&\times \mathbf{G}_u^H \mathbf{\Phi}^{-1} \mathbf{G}_u = \mathbf{I}, \qquad \text{(D.3)}
\end{aligned}$$

which proves the stated equality.

Die approbierte Originalversion dieser Dissertation ist in der TU Wien Bibliothek verfügbar.
The approved original version of this doctoral thesis is available at the TU Wien Bibliothek.
TU Bibliothek Your knowledge hub WIEN

Die approbierte Originalversion dieser Dissertation ist in der TU Wien Bibliothek verfügbar.
The approved original version of this doctoral thesis is available at the TU Wien Bibliothek.

APPENDIX E

Parameter values

The investigations presented in this thesis are directly related to research questions known from specific experimental systems at the Photonics Institute at TU Wien and are the product of an ongoing collaboration. At the time the underlying research was conducted, those experimental setups were either already fully functional or under construction. To retain this direct link to the experimental setups, all simulation scenarios are prepared using a set of parameters with a specific amplifier in mind. The simulation scenarios presented in Chapter 2 and Chapter 4 are performed using a set of parameters given in Table E.1. Parts of these parameters were identified by the method described in Appendix B using measurement data of a CPA system previously presented in [15] based on a holmium-dopend yttrium-aluminium garnet (Ho:YAG). The developments presented in Chapter 5 and Chapter 6 are concerned with different amplifier setups including a pre-amplifier [35] and a dedicated power amplifier using an ytterbium-doped calcium fluoride (Yb:CaF2) crystal. For convenience, all simulation scenarios in both chapters were performed using the same parameters listed in Table E.3 for a regenerative amplifier with a linear cavity employing a double-pass pumping scheme as described in Appendix C. The experimental results presented in Section 5.5 were measured at the Yb:CaF2 power amplifier operated at $N_{\mathrm{RT}} = 184$ round-trips. Finally, some relevant physical constants used throughout this thesis are given in Table E.2.

Die approbierte Originalversion dieser Dissertation ist in der TU Wien Bibliothek verfügbar.
The approved original version of this doctoral thesis is available at the TU Wien Bibliothek.
TU Bibliothek Your knowledge hub WIEN

Parameter name	Symbol	Value	Unit	Parameter name	Symbol	Value	Unit
carrier wavelength	λ_0	$2093 \cdot 10^{-9}$	m	pump wavelength	λ_P	$1910 \cdot 10^{-9}$	m
transition wavelengths	λ_1	$2090.24 \cdot 10^{-9}$	m	transition wavelengths	λ_2	$2092.15 \cdot 10^{-9}$	m
	λ_3	$2095.16 \cdot 10^{-9}$	m		λ_4	$2097.66 \cdot 10^{-9}$	m
atomic line widths	$\Delta\omega_1$	$1.03 \cdot 10^{12}$	rad/s	atomic line widths	$\Delta\omega_2$	$8.19 \cdot 10^{11}$	rad/s
	$\Delta\omega_3$	$4.14 \cdot 10^{12}$	rad/s		$\Delta\omega_4$	$1.06 \cdot 10^{12}$	rad/s
atomic transition rates	γ_{10}	$5 \cdot 10^{5}$	1/s	atomic transition rates	γ_{20}	$1 \cdot 10^{2}$	1/s
	γ_{30}	$1 \cdot 10^{4}$	1/s		γ_{40}	$2 \cdot 10^{2}$	1/s
	γ_{50}	25	1/s		γ_{51}	25	1/s
	γ_{52}	25	1/s		γ_{53}	25	1/s
	γ_{54}	25	1/s		γ_{01}	$1.2 \cdot 10^{4}$	1/s
	γ_{02}	2	1/s		γ_{03}	170	1/s
	γ_{04}	3.4	1/s		γ_{12}	0	1/s
	γ_{21}	0	1/s		γ_{23}	0	1/s
	γ_{32}	0	1/s		γ_{34}	0	1/s
	γ_{43}	0	1/s				
cross sections	σ_1	$1.43 \cdot 10^{-24}$	m^2	cross sections	σ_2	$1.45 \cdot 10^{-24}$	m^2
	σ_3	$2.52 \cdot 10^{-24}$	m^2		σ_4	$1.09 \cdot 10^{-24}$	m^2
	σ_P	$1.25 \cdot 10^{-24}$	m^2				
length of the gain medium	L	$5 \cdot 10^{-2}$	m	length of ring cavity	L_{RC}	4	m
cavity efficiency coeff.	η_{RC}	0.975	1	repetition rate	f_{rep}	$1 \cdot 10^{3}$	Hz
beam cross section	A_B	$5.03 \cdot 10^{-7}$	m^2	refractive index	n_0	1.833	1
nonlinear refractive index	n_2	$3 \cdot 10^{-20}$	m^2/W	group velocity	v_g	$163.73 \cdot 10^{6}$	m/s
dispersion coefficient	k_2	$-7.97 \cdot 10^{-26}$	s^2/m	dopant density	N_{dop}	$3.15 \cdot 10^{25}$	$1/m^3$
stretcher efficiency coeff.	η_S	0.6	1	phase coeff.	$\varphi_{S,2}$	$-1.51 \cdot 10^{-22}$	s
compressor efficiency coeff.	η_C	0.75	1		$\varphi_{S,3}$	$1.05 \cdot 10^{-37}$	s

Table E.1: Given and identified parameter values of the matheamtical model of a CPA derived in Chapter 2 using measurement data from the experimental setup given in [15].

TU Bibliothek Your knowledge hub WIEN
Die approbierte Originalversion dieser Dissertation ist in der TU Wien Bibliothek verfügbar.
The approved original version of this doctoral thesis is available at the TU Wien Bibliothek.

Physical constant	Symbol	Value	Unit
speed of light in free space	c_0	$2.998 \cdot 10^{8}$	m/s
permittivity of free space	ε_0	$8.854 \cdot 10^{-12}$	A s m/V
reduced Planck constant	$\hbar$	$1.054 \cdot 10^{-34}$	J s
Boltzmann constant	k	$1.381 \cdot 10^{-23}$	J/K

Table E.2: Physical constants used in this thesis.

Parameter name	Symbol	Value	Unit
laser wavelength	λ	$1030 \cdot 10^{-9}$	m
pump wavelength	λ_{P}	$980 \cdot 10^{-9}$	m
laser beam diameter	d_{L}	$0.8 \cdot 10^{-3}$	m
pump beam diameter	d_{P}	$1.6 \cdot 10^{-3}$	m
lifetime of the exited states	τ	$2.4 \cdot 10^{-3}$	1/s
cross section of the lasing trans.	σ	$8.0 \cdot 10^{-25}$	m^2
cross section of the pumping trans.	σ_P	$9.0 \cdot 10^{-25}$	m^2
occupation factors	f_0	0.9736	1
	f_1	0.0264	1
	f_2	0.9217	1
	f_3	0.0783	1
dopant density	N_{dop}	$3.8 \cdot 10^{26}$	$1/\mathrm{m}^3$
length of the gain medium	L	$6 \cdot 10^{-3}$	m
length of resonator cavity	L_{RC}	4	m
cavity efficiency coeff.	η_{RC}	0.8	1
output efficiency coeff.	η_{out}	0.9	1
repetition rate	f_{rep}	$1 \cdot 10^{3}$	Hz

Table E.3: Parameter values for the simulation scenarios in Chapter 5 and Chapter 6. For the latter, $\eta_{\mathrm{RC,A}} = \eta_{\mathrm{RC,F}} = \eta_{\mathrm{RC}}$ was used for simplicity.

Die approbierte Originalversion dieser Dissertation ist in der TU Wien Bibliothek verfügbar.
The approved original version of this doctoral thesis is available at the TU Wien Bibliothek.
TU Bibliothek WIEN Your knowledge hub

Parameter name	Symbol	Value	Unit
laser wavelength	λ	$1030 \cdot 10^{-9}$	m
pump wavelength	λ_{P}	$980 \cdot 10^{-9}$	m
laser beam diameter	d_{L}	$890 \cdot 10^{-6}$	m
pump beam diameter	d_{P}	$890 \cdot 10^{-6}$	m
lifetime of the exited states	τ	$2.4 \cdot 10^{-3}$	1/s
cross section of the lasing trans.	σ	$4.3 \cdot 10^{-25}$	m^2
cross section of the pumping trans.	σ_P	$15.0 \cdot 10^{-25}$	m^2
occupation factors	f_0	0.9736	1
	f_1	0.0264	1
	f_2	0.9217	1
	f_3	0.0783	1
dopant density	N_{dop}	$2.44 \cdot 10^{26}$	$1/\mathrm{m}^3$
length of the gain medium	L	$10 \cdot 10^{-3}$	m
length of resonator cavity	L_{RC}	4	m
cavity efficiency coeff.	η_{RC}	0.947	1
output efficiency coeff.	η_{out}	0.3	1
repetition rate	f_{rep}	$1 \cdot 10^{3}$	Hz

Table E.4: Parameter values for the experimental results in Section 5.5.

Die approbierte Originalversion dieser Dissertation ist in der TU Wien Bibliothek verfügbar.
The approved original version of this doctoral thesis is available at the TU Wien Bibliothek.
TU Bibliothek WIEN Your knowledge hub

Bibliography

[1] M. Fox, *Quantum Optics: An Introduction*. Oxford: Oxford University Press, 2006.

[2] S. Haroche and J.-M. Raimond, *Exploring the quantum: Atoms, cavities and photons*. Oxford: Oxford University Press, 2010.

[3] M. Aspelmeyer, T. J. Kippenberg, and F. Marquardt, "Cavity optomechanics", *Reviews of Modern Physics*, vol. 86, no. 4, pp. 1391–1452, 2014.

[4] J. Vovrosh, M. Rashid, D. Hempston, J. Bateman, M. Paternostro, and H. Ulbricht, "Parametric feedback cooling of levitated optomechanics in a parabolic mirror trap", *Journal of the Optical Society of America B*, vol. 34, no. 7, pp. 1421–1428, 2017.

[5] T. H. Maiman, "Stimulated optical radiation in ruby", *Nature*, vol. 187, no. 4736, pp. 493–494, 1960.

[6] A. Ashkin, "Acceleration and trapping of particles by radiation pressure", *Physical Review Letters*, vol. 24, no. 4, pp. 156–159, 1970.

[7] D. J. Wineland, R. E. Drullinger, and F. L. Walls, "Radiation-pressure cooling of bound resonant absorbers", *Physical Review Letters*, vol. 40, no. 25, pp. 1639–1642, 1978.

[8] S. W. Hell and J. Wichmann, "Breaking the diffraction resolution limit by stimulated emission: Stimulated-emission-depletion fluorescence microscopy", *Optics Letters*, vol. 19, no. 11, pp. 780–782, 1994.

[9] C. Sayrin, I. Dotsenko, X. Zhou, B. Peaudecerf, T. Rybarczyk, S. Gleyzes, P. Rouchon, M. Mirrahimi, H. Amini, M. Brune, J.-M. Raimond, and S. Haroche, "Real-time quantum feedback prepares and stabilizes photon number states", *Nature*, vol. 477, no. 7362, pp. 73–77, 2011.

Die approbierte Originalversion dieser Dissertation ist in der TU Wien Bibliothek verfügbar.
The approved original version of this doctoral thesis is available at the TU Wien Bibliothek.
TU WIEN Bibliothek Your knowledge hub

[10] B. Latour, *Science in Action: How to Follow Scientists and Engineers Through Society*. Cambridge: Harvard University Press, 1987.

[11] A. Nordmann, *Technikphilosophie*. Hamburg: Junius, 2008.

[12] L. Daston and P. Galison, *Objectivity*. New York: Zone Books, 2007.

[13] F. Krausz and M. Ivanov, "Attosecond physics", *Reviews of Modern Physics*, vol. 81, no. 1, pp. 163–234, 2009.

[14] D. Goswami, "Optical pulse shaping approaches to coherent control", *Physics Reports*, vol. 374, no. 6, pp. 385–481, 2003.

[15] P. Malevich, G. Andriukaitis, T. Flöry, A. J. Verhoef, A. Fernández, S. Ališauskas, A. Pugžlys, A. Baltuška, L. H. Tan, C. F. Chua, and P. B. Phua, "High energy and average power femtosecond laser for driving mid-infrared optical parametric amplifiers", *Optics Letters*, vol. 38, no. 15, pp. 2746–2749, 2013.

[16] M. Kellert, K. Kruse, M. Pergament, G. Kulcsar, T. Mans, and M. J. Lederer, "High power femtosecond 1030nm burst-mode front-end and pre-amplifier for the european XFEL pump-probe laser development", in *2013 Conference on Lasers Electro-Optics Europe, International Quantum Electronics Conference*, Munich, May 2013, p. 1.

[17] S. Nolte, C. Momma, H. Jacobs, A. Tünnermann, B. N. Chichkov, B. Wellegehausen, and H. Welling, "Ablation of metals by ultrashort laser pulses", *Journal of the Optical Society of America B*, vol. 14, no. 10, pp. 2716–2722, 1997.

[18] H. K. Tönshoff, C. Momma, A. Ostendorf, S. Nolte, and G. Kamlage, "Microdrilling of metals with ultrashort laser pulses", *Journal of Laser Applications*, vol. 12, no. 1, pp. 23–27, 2000.

[19] L. Jiang, A.-D. Wang, B. Li, T.-H. Cui, and Y.-F. Lu, "Electrons dynamics control by shaping femtosecond laser pulses in micro/nanofabrication: Modeling, method, measurement and application", *Light: Science & Applications*, vol. 7, no. 2, p. 17 134, 2018.

[20] H. N. Chapman, P. Fromme, A. Barty, T. A. White, R. A. Kirian, A. Aquila, M. S. Hunter, J. Schulz, D. P. DePonte, U. Weierstall, R. B. Doak, f. R. N. C. Maia, A. V. Martin, I. Schlichting, L. Lomb, N. Coppola, R. L. Shoeman, S. W. Epp, R. Hartmann, D. Rolles, A. Rudenko, L. Foucar, N. Kimmel, G. Weidenspointner, P. Holl, M. Liang, M. Barthelmess, C. Caleman, S. Boutet, M. J. Bogan, J. Krzywinski, C. Bostedt, S. Bajt, L. Gumprecht, B. Rudek, B. Erk, C. Schmidt, A. Hömke, C. Reich, D. Pietschner, L. Strüder, G. Hauser, H. Gorke, J. Ullrich, S. Herrmann, G. Schaller, F. Schopper, H. Soltau, K.-U. Kühnel, M. Messerschmidt, J. D. Bozek, S. P. Hau-Riege, M. Frank, C. Y. Hampton, R. G. Sierra,

Die approbierte Originalversion dieser Dissertation ist in der TU Wien Bibliothek verfügbar.
The approved original version of this doctoral thesis is available at the TU Wien Bibliothek.
TU Bibliothek WIEN Your knowledge hub

D. Starodub, G. J. Williams, J. Hajdu, N. Timneanu, M. M. Seibert, J. Andreasson, A. Rocker, O. Jönsson, M. Svenda, S. Stern, K. Nass, R. Andritschke, C.-D. Schröter, F. Krasniqi, M. Bott, K. E. Schmidt, X. Wang, I. Grotjohann, J. M. Holton, T. R. M. Barends, R. Neutze, S. Marchesini, R. Fromme, S. Schorb, D. Rupp, M. Adolph, T. Gorkhover, I. Andersson, H. Hirsemann, G. Potdevin, H. Graafsma, B. Nilsson, and J. C. H. Spence, "Femtosecond x-ray protein nanocrystallography", *Nature*, vol. 470, no. 7332, pp. 73–77, 2011.

[21] W. Sekundo, K. Kunert, C. Russmann, A. Gille, W. Bissmann, G. Stobrawa, M. Sticker, M. Bischoff, and M. Blum, "First efficacy and safety study of femtosecond lenticule extraction for the correction of myopia: Six-month results", *Journal of Cataract & Refractive Surgery*, vol. 34, no. 9, pp. 1513–1520, 2008.

[22] W. H. Lowdermilk and J. E. Murray, "The multipass amplifier: Theory and numerical analysis", *Journal of Applied Physics*, vol. 51, no. 5, pp. 2436–2444, 1980.

[23] D. Strickland and G. Mourou, "Compression of amplified chirped optical pulses", *Optics Communications*, vol. 56, no. 3, pp. 219–221, 1985.

[24] E. Treacy, "Optical pulse compression with diffraction gratings", *IEEE Journal of Quantum Electronics*, vol. 5, no. 9, pp. 454–458, 1969.

[25] D. F. Hotz, "Gain narrowing in a laser amplifier", *Applied Optics*, vol. 4, no. 5, pp. 527–530, 1965.

[26] G. P. Agrawal and N. A. Olsson, "Self-phase modulation and spectral broadening of optical pulses in semiconductor laser amplifiers", *IEEE Journal of Quantum Electronics*, vol. 25, no. 11, pp. 2297–2306, 1989.

[27] M. D. Perry, T. Ditmire, and B. C. Stuart, "Self-phase modulation in chirped-pulse amplification", *Optics Letters*, vol. 19, no. 24, pp. 2149–2151, 1994.

[28] P. Kroetz, A. Ruehl, K. Murari, H. Cankaya, F. X. Kärtner, I. Hartl, and R. J. D. Miller, "Numerical study of spectral shaping in high energy ho:YLF amplifiers", *Optics Express*, vol. 24, no. 9, p. 9905, 2016.

[29] G. A. Reider, *Photonics: An Introduction*, 2nd ed. Springer, 2016.

[30] A. E. Siegman, *Lasers*. Mill Valley: University Science Books, 1986.

[31] M. Grishin, V. Gulbinas, and A. Michailovas, "Dynamics of high repetition rate regenerative amplifiers", *Optics Express*, vol. 15, no. 15, pp. 9434–9443, 2007.

[32] ——, "Bifurcation suppression for stability improvement in nd:YVO_4 regenerative amplifier", *Optics Express*, vol. 17, no. 18, pp. 15 700–15 708, 2009.

Die approbierte Originalversion dieser Dissertation ist in der TU Wien Bibliothek verfügbar.
The approved original version of this doctoral thesis is available at the TU Wien Bibliothek.
TU WIEN Bibliothek Your knowledge hub

[33] G. Andriukaitis, "Development and application of a kilohertz high energy femtosecond yb:CaF2 laser amplifier", PhD thesis, TU Wien, Vienna, Austria, 2012.

[34] T. Zhou, J. Ruppe, C. Zhu, I.-N. Hu, J. Nees, and A. Galvanauskas, "Coherent pulse stacking amplification using low-finesse gires-tournois interferometers", *Optics Express*, vol. 23, no. 6, pp. 7442–7462, 2015.

[35] T. Flöry, G. Andriukaitis, M. Barkauskas, E. Kaksis, I. Astrauskas, A. Pugžlys, A. Baltuška, R. Danielius, A. Galvanauskas, and T. Balčiunas, "High repetition rate fs pulse burst generation using the vernier effect", in *2017 Conference on Lasers and Electro-Optics*, San Jose, CA, Jun. 2017, pp. 1–2.

[36] A. M. Weiner, "Ultrafast optical pulse shaping: A tutorial review", *Optics Communications*, Special Issue on Optical Pulse Shaping, Arbitrary Waveform Generation, and Pulse Characterization, vol. 284, no. 15, pp. 3669–3692, 2011.

[37] P. Tournois, "Acousto-optic programmable dispersive filter for adaptive compensation of group delay time dispersion in laser systems", *Optics Communications*, vol. 140, no. 4, pp. 245–249, 1997.

[38] R. Trebino, K. W. DeLong, D. N. fittinghoff, J. N. Sweetser, M. A. Krumbügel, B. A. Richman, and D. J. Kane, "Measuring ultrashort laser pulses in the time-frequency domain using frequency-resolved optical gating", *Review of Scientific Instruments*, vol. 68, no. 9, pp. 3277–3295, 1997.

[39] C. L. Tang, H. Statz, and G. deMars, "Spectral output and spiking behavior of solid-state lasers", *Journal of Applied Physics*, vol. 34, no. 8, pp. 2289–2295, 1963.

[40] H. Statz, G. A. DeMars, D. T. Wilson, and C. L. Tang, "Problem of spike elimination in lasers", *Journal of Applied Physics*, vol. 36, no. 5, pp. 1510–1514, 1965.

[41] M. D. Skeldon, A. Babushkin, W. Bittle, A. V. Okishev, and W. Seka, "Modeling the temporal-pulse-shape dynamics of an actively stabilized regenerative amplifier", *IEEE Journal of Quantum Electronics*, vol. 34, no. 2, pp. 286–291, 1998.

[42] P. Dower, P. Farrell, and D. Nesic, "Extremum seeking control of cascaded raman optical amplifiers", *IEEE Transactions on Control Systems Technology*, vol. 16, no. 3, pp. 396–407, 2008.

[43] S. L. Brunton, X. Fu, and J. N. Kutz, "Extremum-seeking control of a mode-locked laser", *IEEE Journal of Quantum Electronics*, vol. 49, no. 10, pp. 852–861, 2013.

Die approbierte Originalversion dieser Dissertation ist in der TU Wien Bibliothek verfügbar.
The approved original version of this doctoral thesis is available at the TU Wien Bibliothek.
TU Bibliothek WIEN Your knowledge hub

[44] J. N. Kutz and S. L. Brunton, "Intelligent systems for stabilizing mode-locked lasers and frequency combs: Machine learning and equation-free control paradigms for self-tuning optics", *Nanophotonics*, vol. 4, no. 1, 2015.

[45] T. Baumeister, S. L. Brunton, and J. N. Kutz, "Deep learning and model predictive control for self-tuning mode-locked lasers", *Journal of the Optical Society of America B*, vol. 35, no. 3, pp. 617–626, 2018.

[46] A. Efimov, M. D. Moores, N. M. Beach, J. L. Krause, and D. H. Reitze, "Adaptive control of pulse phase in a chirped-pulse amplifier", *Optics letters*, vol. 23, no. 24, pp. 1915–1917, 1998.

[47] F. Omenetto, D. Reitze, B. Luce, M. Moores, and A. J. Taylor, "Adaptive control methods for ultrafast pulse propagation in optical fibers", *IEEE Journal of Selected Topics in Quantum Electronics*, vol. 8, no. 3, pp. 690–698, 2002.

[48] J. Prawiharjo, N. K. Daga, R. Geng, J. H. V. Price, D. C. Hanna, D. J. Richardson, and D. P. Shepherd, "High fidelity femtosecond pulses from an ultrafast fiber laser system via adaptive amplitude and phase pre-shaping", *Optics Express*, vol. 16, no. 19, pp. 15 074–15 089, 2008.

[49] D. N. Schimpf, J. Limpert, and A. Tünnermann, "Controlling the influence of SPM in fiber-based chirped-pulse amplification systems by using an actively shaped parabolic spectrum", *Optics Express*, vol. 15, no. 25, p. 16 945, 2007.

[50] D. N. Schimpf, C. Ruchert, D. Nodop, J. Limpert, A. Tünnermann, and F. Salin, "Compensation of pulse-distortion in saturated laser amplifiers", *Optics Express*, vol. 16, no. 22, p. 17 637, 2008.

[51] B. Ren, P. Frihauf, M. Krstic, and R. J. Rafac, "Laser pulse shaping via iterative learning control and high-dimensional extremum seeking", in *Proceedings of the ASME Dynamic Systems and Control Conference*, Arlington, USA, 2011, pp. 667–674.

[52] B. Ren, P. Frihauf, R. J. Rafac, and M. Krstic, "Laser pulse shaping via extremum seeking", *Control Engineering Practice*, vol. 20, no. 7, pp. 674–683, 2012.

[53] S. M. Webb, J. G. Ellison, S. R. Desbruslais, M. P. Fedoruk, and S. K. Turitsyn, "Adaptive pulse shaping through BER feedback", *Journal of Lightwave Technology*, vol. 27, no. 17, pp. 3765–3772, 2009.

[54] A. Deutschmann, P. Malevich, A. Baltuška, and A. Kugi, "Modeling and iterative pulse-shape control of optical chirped pulse amplifiers", *Automatica*, vol. 98, pp. 150–158, 2018.

Die approbierte Originalversion dieser Dissertation ist in der TU Wien Bibliothek verfügbar.
The approved original version of this doctoral thesis is available at the TU Wien Bibliothek.
TU Bibliothek WIEN Your knowledge hub

[55] A. Deutschmann, G. Stadler, and A. Kugi, "Stochastic iterative learning control for lumped- and distributed-parameter systems: A wiener-filtering approach", *Under review*, 2019.

[56] A. Deutschmann, P. Malevich, A. Baltuška, and A. Kugi, "Identifikation und simulation optischer verstärker für ultra-kurze laserpulse", *At - Automatisierungstechnik*, vol. 66, no. 1, pp. 66–78, 2018.

[57] T. Oksenhendler and N. Forget, "Pulse-shaping techniques theory and experimental implementations for femtosecond pulses", in *Advances in Solid State Lasers Development and Applications*, M. Grishin, Ed., London: InTech, 2010.

[58] B. E. A. Saleh and M. C. Teich, *Fundamentals of Photonics*, 2nd ed. Hoboken, NJ: Wiley, 2007.

[59] E. V. Vanin, A. I. Korytin, A. M. Sergeev, D. Anderson, M. Lisak, and L. Vazquez, "Dissipative optical solitons", *Physical Review A*, vol. 49, no. 4, pp. 2806–2811, 1994.

[60] C. Cohen-Tannoudji, *Quantum Mechanics*, 2nd ed. New York: Wiley, 1991.

[61] R. Shankar, *Principles of Quantum Mechanics*, 2nd ed. New York: Plenum Press, 1994.

[62] S. Rand, *Lectures on Light: Nonlinear and Quantum Optics using the Density Matrix*. Oxford: Oxford University Press, 2010.

[63] D. C. Brown, V. Envid, and J. Zembek, "Ho:YAG absorption cross sections from 1700 to 2200 nm at 83, 175, and 295 k", *Applied Optics*, vol. 51, no. 34, pp. 8147–8158, 2012.

[64] A. S. Fokas, A. A. Himonas, and D. Mantzavinos, "The nonlinear schrödinger equation on the half-line", *Transactions of the American Mathematical Society*, vol. 369, no. 1, pp. 681–709, 2016.

[65] G. Métivier, "The mathematics of nonlinear optics", in *Handbook of Differential Equations: Evolutionary Equations*, vol. 5, Amsterdam: Elsevier, 2009, pp. 169–313.

[66] L. M. Frantz and J. S. Nodvik, "Theory of pulse propagation in a laser amplifier", *Journal of Applied Physics*, vol. 34, no. 8, pp. 2346–2349, 1963.

[67] J. Dörring, A. Killi, U. Morgner, A. Lang, M. Lederer, and D. Kopf, "Period doubling and deterministic chaos in continuously pumped regenerative amplifiers", *Optics Express*, vol. 12, no. 8, pp. 1759–1768, 2004.

[68] W. He, T. Meng, D. Huang, and X. Li, "Adaptive boundary iterative learning control for an euler-bernoulli beam system with input constraint", *IEEE Transactions on Neural Networks and Learning Systems*, vol. 29, no. 5, pp. 1539–1549, 2017.

Die approbierte Originalversion dieser Dissertation ist in der TU Wien Bibliothek verfügbar.
The approved original version of this doctoral thesis is available at the TU Wien Bibliothek.
TU Bibliothek WIEN Your knowledge hub

[69] D. Huang, J.-X. Xu, X. Li, C. Xu, and M. Yu, "D-type anticipatory iterative learning control for a class of inhomogeneous heat equations", *Automatica*, vol. 49, no. 8, pp. 2397–2408, 2013.

[70] C. Xu, R. Arastoo, and E. Schuster, "On iterative learning control of parabolic distributed parameter systems", in *17th Mediterranean Conference on Control and Automation*, Thessaloniki, 2009, pp. 510–515.

[71] D. Huang, X. Li, J.-X. Xu, C. Xu, and W. He, "Iterative learning control of inhomogeneous distributed parameter systems—frequency domain design and analysis", *Systems & Control Letters*, vol. 72, pp. 22–29, 2014.

[72] N. Wiener, *Extrapolation, Interpolation, and Smoothing of Stationary Time Series*. Cambridge: MIT Press, 1964.

[73] R. C. Gonzalez, R. E. Woods, and S. L. Eddins, *Digital Image Processing Using MATLAB*. Upper Saddle River: Prentice Hall, 2003.

[74] A. V. Oppenheim and G. C. Verghese, *Signals, Systems & Inference*. Upper Saddle River: Prentice Hall, 2016.

[75] S. S. Saab, "A discrete-time stochastic learning control algorithm", *IEEE Transactions on Automatic Control*, vol. 46, no. 6, pp. 877–887, 2001.

[76] ——, "Stochastic p-type/d-type iterative learning control algorithms", *International Journal of Control*, vol. 76, no. 2, pp. 139–148, 2003.

[77] ——, "A stochastic iterative learning control algorithm with application to an induction motor", *International Journal of Control*, vol. 77, no. 2, pp. 144–163, 2004.

[78] ——, "On a discrete-time stochastic learning control algorithm", *IEEE Transactions on Automatic Control*, vol. 46, no. 8, pp. 1333–1336, 2001.

[79] V. Kučera, "Transfer-function solution of the kalman-bucy filtering problem", *Kybernetika*, vol. 14, no. 2, pp. 110–122, 1978.

[80] N. Amann, D. H. Owens, E. Rogers, and A. Wahl, "An h-infinity approach to linear iterative learning control design", *International Journal of Adaptive Control and Signal Processing*, vol. 10, pp. 767–781, 1996.

[81] M. Norrlöf and S. Gunnarsson, "Time and frequency domain convergence properties in iterative learning control", *International Journal of Control*, vol. 75, no. 14, pp. 1114–1126, 2002.

[82] J. Ghosh and B. Paden, "A pseudoinverse-based iterative learning control", *IEEE Transactions on Automatic Control*, vol. 47, no. 5, pp. 831–837, 2002.

[83] D. A. Bristow and B. Hencey, "A Q, L factorization of norm-optimal iterative learning control", in *47th IEEE Conference on Decision and Control*, Dec. 2008, pp. 2380–2384.

Die approbierte Originalversion dieser Dissertation ist in der TU Wien Bibliothek verfügbar.
The approved original version of this doctoral thesis is available at the TU Wien Bibliothek.
TU Bibliothek WIEN Your knowledge hub

[84] X. Ge, J. L. Stein, and T. Ersal, "Frequency-domain analysis of robust monotonic convergence of norm-optimal iterative learning control", *IEEE Transactions on Control Systems Technology*, vol. 26, no. 2, pp. 637–651, 2017.

[85] N. Amann, D. H. Owens, and E. Rogers, "Iterative learning control using optimal feedback and feedforward actions", *International Journal of Control*, vol. 69, no. 2, pp. 203–226, 1998.

[86] D. A. Bristow, M. Tharayil, and A. G. Alleyne, "A survey of iterative learning control", *IEEE Control Systems*, vol. 26, no. 3, pp. 96–114, 2006.

[87] D. A. Bristow, "Frequency domain analysis and design of iterative learning control for systems with stochastic disturbances", in *2008 American Control Conference*, Jun. 2008, pp. 3901–3907.

[88] A. V. Oppenheim and A. S. Willsky, *Signals and Systems*, 2nd ed. Upper Saddle River: Prentice Hall, 1996, 957 pp.

[89] S. Devasia, D. Chen, and B. Paden, "Nonlinear inversion-based output tracking", *IEEE Transactions on Automatic Control*, vol. 41, no. 7, pp. 930–942, 1996.

[90] T. Sogo, "On the equivalence between stable inversion for nonminimum phase systems and reciprocal transfer functions defined by the two-sided laplace transform", *Automatica*, vol. 46, no. 1, pp. 122–126, 2010.

[91] D. Bailey and P. Swarztrauber, "A fast method for the numerical evaluation of continuous fourier and laplace transforms", *SIAM Journal on Scientific Computing*, vol. 15, no. 5, pp. 1105–1110, 1994.

[92] D. H. Owens and J. Hätönen, "Iterative learning control — an optimization paradigm", *Annual Reviews in Control*, vol. 29, no. 1, pp. 57–70, 2005.

[93] D. H. Owens, C. T. Freeman, and B. Chu, "Multivariable norm optimal iterative learning control with auxiliary optimisation", *International Journal of Control*, vol. 86, no. 6, pp. 1026–1045, 2013.

[94] D. A. Bristow, "Optimal iteration-varying iterative learning control for systems with stochastic disturbances", in *2010 American Control Conference*, Baltimore, MD, Jun. 2010, pp. 1296–1301.

[95] O. V. Iftime, "A j-spectral factorization approach to h-infinity control problems", PhD thesis, University of Twente, Twente, 2002.

[96] T. Meurer and M. Zeitz, "Feedforward and feedback tracking control of nonlinear diffusion-convection-reaction systems using summability methods", *Industrial & Engineering Chemistry Research*, vol. 44, no. 8, pp. 2532–2548, 2005.

Die approbierte Originalversion dieser Dissertation ist in der TU Wien Bibliothek verfügbar.
The approved original version of this doctoral thesis is available at the TU Wien Bibliothek.
TU WIEN Bibliothek Your knowledge hub

[97] T. Utz, T. Meurer, D. Wild, and A. Kugi, "Inversion-based trajectory planning for the heat equation with temperature-dependent parameters and radiation boundary conditions", *PAMM*, vol. 7, no. 1, pp. 4 130 039–4 130 040, 2007.

[98] T. Meurer, "Flatness-based trajectory planning for diffusion–reaction systems in a parallelepipedon - a spectral approach", *Automatica*, vol. 47, no. 5, pp. 935–949, 2011.

[99] J. Schröck, T. Meurer, and A. Kugi, "Motion planning for piezo-actuated flexible structures: Modeling, design, and experiment", *IEEE Transactions on Control Systems Technology*, vol. 21, no. 3, pp. 807–819, 2013.

[100] M. O. Wagner, T. Meurer, and M. Zeitz, "K-summable power series as a design tool for feedforward control of diffusion–convection–reaction systems", in *6th IFAC Symposium on Nonlinear Control Systems*, vol. 37, Stuttgart, Germany, Sep. 2004, pp. 147–152.

[101] T. Glück, M. Blank, D. Büchl, and A. Kugi, "Convex constrained iterative learning control using projection: Application to a smart power switch", *IEEE Transactions on Control Systems Technology*, vol. 26, no. 5, pp. 1818–1825, 2017.

[102] A. Tikan, S. Bielawski, C. Szwaj, S. Randoux, and P. Suret, "Single-shot measurement of phase and amplitude by using a heterodyne time-lens system and ultrafast digital time-holography", *Nature Photonics*, vol. 12, no. 4, pp. 228–234, 2018.

[103] D. Mueller, A. Giesen, and H. Huegel, "Picosecond thin disk regenerative amplifier", in *14th International Symposium on Gas Flow, Chemical Lasers, and High-Power Lasers*, Wroclaw, Nov. 10, 2003, pp. 281–287.

[104] M. W. P. Strandberg and J. R. Shane, "General properties of thermal-relaxation rate equations", *Physical Review B*, vol. 7, no. 11, p. 4809, 1973.

[105] P. V. Kokotovic, R. E. O'Malley, and P. Sannuti, "Singular perturbations and order reduction in control theory - an overview", *Automatica*, vol. 12, no. 2, pp. 123–132, 1976.

[106] K. Ikeda, "Multiple-valued stationary state and its instability of the transmitted light by a ring cavity system", *Optics Communications*, vol. 30, no. 2, pp. 257–261, 1979.

[107] T. Hansson and S. Wabnitz, "Dynamics of microresonator frequency comb generation: Models and stability", *Nanophotonics*, vol. 5, no. 2, pp. 231–243, 2016.

Die approbierte Originalversion dieser Dissertation ist in der TU Wien Bibliothek verfügbar.
The approved original version of this doctoral thesis is available at the TU Wien Bibliothek.
TU Bibliothek WIEN Your knowledge hub

[108] W. Hahn, „Über die anwendung der methode von ljapunov auf differenzengleichungen“, *Mathematische Annalen*, vol. 136, no. 5, pp. 430–441, 1958.

[109] H. Freeman, *Discrete-Time Systems*. Hoboken, NJ: Wiley, 1965.

[110] A. Stamati and J. Tsinias, “Sufficient conditions for local asymptotic stability and stabilization for discrete-time varying systems”, *IEEE Transactions on Automatic Control*, vol. 56, no. 3, pp. 643–649, 2011.

[111] S. Huang, M. R. James, D. Nesic, and P. M. Dower, “Analysis of input-to-state stability for discrete time nonlinear systems via dynamic programming”, *Automatica*, vol. 41, no. 12, pp. 2055–2065, 2005.

[112] D. Kazakos and J. Tsinias, “The input-to-state stability condition and global stabilization of discrete-time systems”, *IEEE Transactions on Automatic Control*, vol. 39, no. 10, pp. 2111–2113, 1994.

[113] N. Bof, R. Carli, and L. Schenato, “Lyapunov theory for discrete time systems”, *ARXIV:1809.05289 [math]*, 2018.

[114] H. Khalil, *Nonlinear Systems*, 3rd ed. New Jersey: Prentice Hall, 2002.

[115] D. J. Leith and W. E. Leithead, “Survey of gain-scheduling analysis and design”, *International Journal of Control*, vol. 73, no. 11, pp. 1001–1025, 2000.

[116] C. Kerse, H. Kalaycıoğlu, P. Elahi, B. Çetin, D. K. Kesim, Ö. Akçaalan, S. Yavaş, M. D. Aşık, B. Öktem, H. Hoogland, R. Holzwarth, and F. Ö. Ilday, “Ablation-cooled material removal with ultrafast bursts of pulses”, *Nature*, vol. 537, no. 7618, pp. 84–89, 2016.

[117] S. Zhou, F. W. Wise, and D. G. Ouzounov, “Divided-pulse amplification of ultrashort pulses”, *Optics Letters*, vol. 32, no. 7, pp. 871–873, 2007.

[118] I. Astrauskas, E. Kaksis, T. Flöry, G. Andriukaitis, A. Pugžlys, A. Baltuška, J. Ruppe, S. Chen, A. Galvanauskas, and T. Balčiūnas, “High-energy pulse stacking via regenerative pulse-burst amplification”, *Optics Letters*, vol. 42, no. 11, pp. 2201–2204, 2017.

[119] P. Stellnberger, “Adaptive pulse-shaping for nonlinear dispersive media: An iterative learning approach”, diploma thesis, TU Wien, Vienna, Austria, 2019.

[120] T. J. Kippenberg, R. Holzwarth, and S. A. Diddams, “Microresonator-based optical frequency combs”, *Science*, vol. 332, no. 6029, pp. 555–559, 2011.

[121] Y. K. Chembo and C. R. Menyuk, “Spatiotemporal lugiato-lefever formalism for kerr-comb generation in whispering-gallery-mode resonators”, *Physical Review A*, vol. 87, no. 5, p. 53 852, 2013.

Die approbierte Originalversion dieser Dissertation ist in der TU Wien Bibliothek verfügbar.
The approved original version of this doctoral thesis is available at the TU Wien Bibliothek.
TU Bibliothek WIEN Your knowledge hub

[122] T. Meurer, *Control of Higher-Dimensional PDEs: Flatness and Backstepping Designs*. Berlin: Springer, 2013.

[123] J. M. Beckers, P. Lena, O. Lai, P.-Y. Madec, G. Rousset, M. Sechaud, M. J. Northcott, F. Roddier, J.-L. Beuzit, F. Rigaut, and D. G. Sandler, *Adaptive optics in astronomy*, F. Roddier, Ed. Cambridge: Cambridge Univ. Press, 1999.

[124] B. Cichy, P. Augusta, K. Gałkowski, A. Rauh, H. Aschemann, E. Rogers, and B. Rehák, "Modeling and iterative learning control of a circular deformable mirror", in *20th IFAC World Congress*, vol. 50, Toulouse, Jul. 2017, pp. 3117–3122.

[125] G. P. Agrawal, *Nonlinear fiber Optics*, 5th ed. Boston: Academic Press, 2012.

[126] W. Bao, S. Jin, and P. A. Markowich, "On time-splitting spectral approximations for the schrödinger equation in the semiclassical regime", *Journal of Computational Physics*, vol. 175, no. 2, pp. 487–524, 2002.

[127] L. Casperson, "Mode stability of lasers and periodic optical systems", *IEEE Journal of Quantum Electronics*, vol. 10, no. 9, pp. 629–634, 1974.

[128] V. Magni, "Multielement stable resonators containing a variable lens", *Journal of the Optical Society of America A*, vol. 4, no. 10, pp. 1962–1969, 1987.

[129] F. X. Kärtner, B. Braun, and U. Keller, "Continuous-wave mode-locked solid-state lasers with enhanced spatial hole burning", *Applied Physics B*, vol. 61, no. 6, pp. 569–579, 1995.

[130] M. Li, X. M. Zhang, Z. G. Wang, X. D. Cui, X. W. Yan, X. Y. Jiang, J. G. Zheng, W. Wang, and M. Li, "Analytical and numerical solutions to the amplifier with incoherent pulse temporal overlap", *Optics Communications*, vol. 382, pp. 49–57, 2017.

Die approbierte Originalversion dieser Dissertation ist in der TU Wien Bibliothek verfügbar.
The approved original version of this doctoral thesis is available at the TU Wien Bibliothek.
TU Bibliothek WIEN Your knowledge hub